

Michael Manfred Hirtz

Surface Structuring by Bottom-Up and Top-Down Approaches

Experimentelle Physik

Surface Structuring by Bottom-Up and Top-Down Approaches

Inaugural-Dissertation
zur Erlangung des Doktorgrades
der Naturwissenschaften im Fachbereich Physik
der Mathematisch-Naturwissenschaftlichen Fakultät
der Westfälischen Wilhelms-Universität Münster

vorgelegt von
Michael Manfred Hirtz
aus Coesfeld

- 2009 -

Dekan:	Prof. Dr. Johannes Peter Wessels
Erster Gutachter:	Prof. Dr. Lifeng Chi
Zweiter Gutachter:	Prof. Dr. Harald Fuchs
Tag der mündlichen Prüfung:	02.10.2009
Tag der Promotion:	02.10.2009

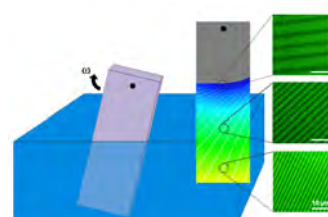
“Not all treasure is silver and gold...”

Captain Jack Sparrow, Pirates of the Carribean

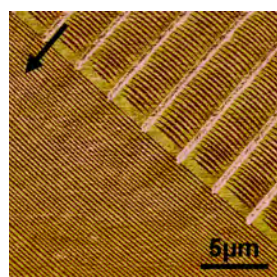
To my Parents and Bastian

Abstract

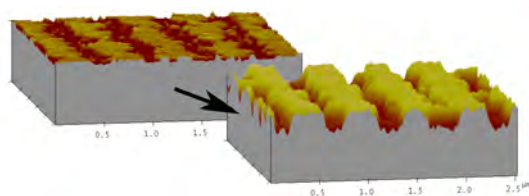
In the course of the present work new strategies for the structuring of surfaces utilizing different “top-down” and “bottom-up” methods were developed. The central “bottom-up” element in this endeavor was the phenomenon of self-organized pattern formation in monolayers of phospholipids during Langmuir-Blodgett transfer onto solid substrates originally discovered by *Gleiche* et. al. in our group. At first the influence of different substrate treatments as well as the role of heat and humidity on pattern formation and stability was analyzed (Chapter 3). To further increase the complexity of achievable patterns a novel type of Langmuir-Blodgett transfer was established. In this Langmuir-Blodgett rotating transfer the substrate is rotated out of the subphase as compared to the conventional vertical withdrawing (Chapter 4). It was shown that gradient surface structures over large areas can be generated by this approach.



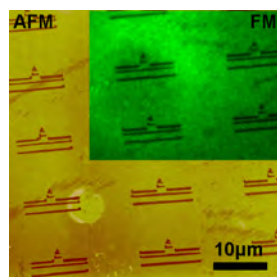
Another way of increasing the complexity of the obtained patterns as well as getting additional insights into the process of pattern formation was realized by introducing prestructures on the substrates by electron beam lithography (Chapter 5). The results of these experiments underline the importance of ultrathin water layers on the substrate during pattern formation. The influence of admixings of different chemical compounds on pattern formation was examined (Chapter 6) and it was demonstrated that this is a feasible approach for achieving diverse functionalizations of



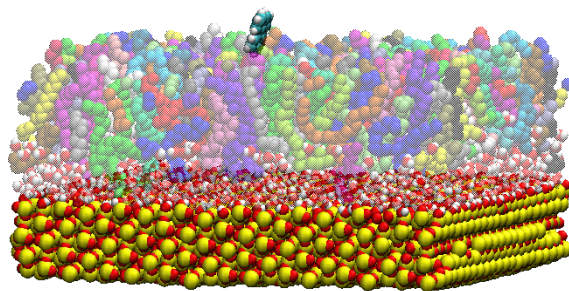
surfaces. As an outstanding example the structured transfer of an initiator molecule for surface induced polymerization was chosen and the growth of different kinds of structured polymer brushes on large-area substrates was



realized (Chapter 7). The mechanical stability of the polymer brushes inspired structuring of homogeneous polymer brush films by atomic force microscope lithography (Chapter 8). The lithography properties of the polymer brushes proved to be superior compared to comparable spin-coated polymer films. Additionally, the covalent binding of the polymer brushes enabled wet-chemical subsequent processing of the structured surfaces. This allowed for the site-selective immobilization of different



dyes and thus a further functionalization of the surfaces. In the last part of the present work molecular dynamics simulations were utilized to gain a better understanding of two different self-assembled systems: two distinct structures were observed in the self-assembly of two-dimensional crystals of adenine-C₂₀ on graphite with different heat stabilities among those two domains. The modelling by molecular dynamics simulations enabled an assessment of the different structural proposals for the observed domains and established a mechanism for the distinct stability on heating (Chapter 9). Finally the simulation of phospholipids monolayers on a solid substrate with subsequent examination of the diffusion of organic molecules on these (Chapter 10) enabled the development of an atomistic picture of the mechanisms behind the site-selective deposition of organic molecules onto phospholipid stripe patterns.

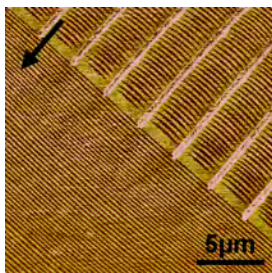
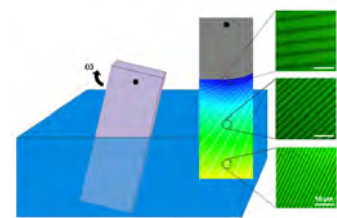


Description of illustrations (in order of appearance):

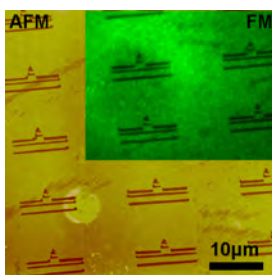
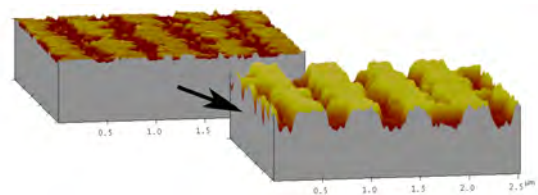
1. Scheme of Langmuir-Blodgett rotating transfer, insets show fluorescence microscopy images of marked positions on the sample.
2. DPPC stripe pattern formed on a prestructured substrate.
3. Mixed DPPC/initiator stripe pattern before and after polymerization of styrene.
4. AFM image of a polymer brush structured by AFM lithography. Inset shows a fluorescence microscopy of the sample after immobilization of dye into the polymer brush.
5. Snapshot of a molecular dynamics simulation of the diffusion of perylene on a DPPC film supported by a solid substrate.

Zusammenfassung

Im Rahmen der vorliegenden Arbeit wurden neue Strategien zur Strukturierung von Oberflächen unter Einbeziehung verschiedener „top-down“ und „bottom-up“ Methoden entwickelt. Das zentrale „bottom-up“ Element war dabei das ursprünglich von *Gleiche* et. al. entdeckte Phänomen selbstorganisierter Musterbildung in Phospholipidmonolagen bei Langmuir-Blodgett Transfer auf ein festes Substrat. Zunächst wurde der Einfluss verschiedener Substratbehandlungen sowie die Rolle von Hitze und Luftfeuchte auf die Musterbildung und -stabilität untersucht (Kapitel 3). Um die Komplexität der erzeugbaren Muster weiter zu steigern wurde eine neuartige Art der Langmuir-Blodgett Transfers entwickelt, bei dem das Substrat aus der Subphase herausrotiert anstatt vertikal herausgezogen wird (Kapitel 4). Dies ermöglicht die Erstellung gradienter Oberflächenstrukturen über große Flächen. Ein anderer Weg die Komplexität der erhaltenen Muster zu steigern, sowie weitere Einblicke in den Musterbildungsprozess zu gewinnen, wurde durch die Vorstrukturierung der Substrate

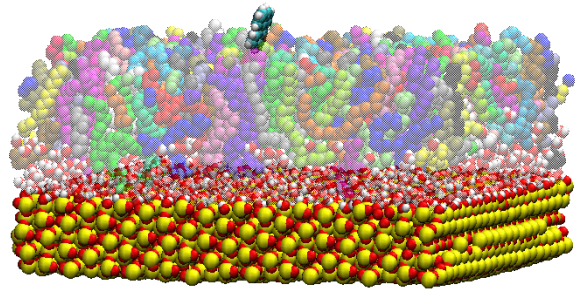


mittels Elektronenstrahlolithographie verwirklicht (Kapitel 5). Die erhaltenen Ergebnisse untermauern zusätzlich die Rolle ultradünner Wasserfilme auf dem Substrat während der Musterbildung. Der Einfluss von Beimischung verschiedener chemischer Verbindungen auf die Musterbildung wurde untersucht (Kapitel 6) und gezeigt, dass sich auf diese Weise sehr unterschiedliche Funktionalisierungen von Oberflächen realisieren lassen. Als herausragendes Beispiel wurde hier das strukturierte Aufbringen eines Initiatormoleküls für die oberflächeninduzierte Polymerisation gewählt und mittels dieser Methode das Aufwachsen verschiedener Arten von strukturierten Polymerbürsten auf großflächigen Substraten realisiert (Kapitel 7).



Die mechanische Stabilität dieser Polymerbürsten inspirierte den Versuch homogene Polymerbürstenfilme mittels Rasterkraftmikroskopolithographie zu strukturieren (Kapitel 8). Die Lithographieeigenschaften der Polymerbürsten erwiesen sich dabei als den vergleichbarer rotationsbeschichteter Polymerfilme als überlegen. Zudem ermöglicht die kovalente Anbindung der Polymerbürsten eine nasschemische

Weiterbehandlung der strukturierten Oberflächen, die eine selektive Anbindung verschiedener Farbstoffe und somit eine weitere Funktionalisierung der Oberfläche möglich macht. Im letzten Teil der Arbeit wurden Molekulardynamiksimulationen eingesetzt um ein besseres Verständnis zweier unterschiedlicher selbstassemblierter Systeme zu erhalten: Bei der Selbstassemblierung zweidimensionaler Kristalle aus Adenin-C₂₀ Molekülen auf Graphit wurden zwei unterschiedliche Strukturen, sowie eine unterschiedliche Hitzestabilität dieser verschiedenen Domänen beobachtet. Die Modellierung mittels Molekulardynamiksimulationen ermöglichte eine Einschätzung der verschiedenen Strukturvorschläge für die vorgefundenen Domänen, sowie eines Mechanismus für die unterschiedliche Hitzestabilität (Kapitel 9). Die Simulation von Phospholipidmonolagen auf einem festen Substrat mit der anschließenden Untersuchung der Diffusion organischer Moleküle auf diesen (Kapitel 10) ermöglichte schließlich die Entwicklung einer atomistischen Vorstellung der Prozesse die zur ortsselektiven Ablagerung organischer Moleküle auf Phospholipidstreifenmustern führen.



Beschreibung der Bilder (Reihenfolge wie im Text):

1. Schematische Darstellung des Langmuir-Blodgett Rotationstransfer, die kleinen Bilder zeigen Fluoreszenzmikroskopaufnahmen der markierten Stellen auf der Probe.
2. DPPC Streifenmuster auf einem vorstrukturierten Substrat.
3. DPPC/Initiator Mischfilm vor und nach der Polymerisation von Styren.
4. Rasterkraftmikroskopaufnahme einer durch Lithographie mittels Rasterkraftmikroskop strukturierten Polymerbürste. Das eingefügte Bild zeigt eine Fluoreszenzmikroskopaufnahme der Probe nach der Immobilisierung eines Farbstoffes in die Polymerbürste.
5. Momentaufnahme einer Molekulardynamiksimulation der Diffusion von Perylen auf einem DPPC Film auf einem festen Substrat.

Table of Contents

1	Introduction	1
1.1	Why Surface Structuring?	1
1.2	Top-Down Approaches	2
1.3	Bottom-Up Approaches.....	4
1.4	Scope of This Thesis	5
2	General Methodology.....	7
2.1	Langmuir-Blodgett Technique	7
2.1.1	Introduction	7
2.1.2	The Langmuir-Blodgett Trough.....	8
2.1.3	π -A Isotherms.....	10
2.1.4	Langmuir-Blodgett Transfer	11
2.2	Brewster Angle Microscopy.....	13
2.3	Fluorescence Microscopy.....	15
2.4	Atomic Force Microscopy.....	17
2.5	Electron Beam Lithography	19
2.6	Molecular Dynamics with GROMACS	20
2.6.1	Introduction	20
2.6.2	General MD Algorithm	21
2.6.3	Used Interaction Function and Force Field	23
3	Substrate Treatment and Self-Organized Pattern Formation	33
3.1	Introduction	33
3.2	Preparations of the Samples	34
3.3	Pattern Formation on the Different Treated Substrates.....	34
3.4	Surface Energy Measurements.....	38
3.5	Effect of Sample Heating	39
3.6	Discussion	41
3.7	Conclusion.....	42
4	A Device for Rotational Langmuir-Blodgett Transfer.....	45
4.1	Introduction	45
4.2	Conventional and Rotational Langmuir-Blodgett Transfer	46
4.3	Description of the LB Rotator.....	49
4.4	Demonstration Experiment Results and Discussion	51

4.5	Summary and Conclusion	54
5	Self-Organized DPPC Patterns on Prestructured Substrates	57
5.1	Introduction	57
5.2	Materials and Experimental Details	58
5.3	Results and Discussion.....	59
5.4	Summary and Outlook	68
6	Admixing of Functional Compounds in LB Transfer	71
6.1	Introduction	71
6.2	Materials and Experimental Details	71
6.3	Results and Discussion.....	72
6.4	Summary	84
7	Structured Polymer Brushes by LB-Transfer.....	85
7.1	Introduction	85
7.2	Synthesis of an Amphiphilic Initiator	86
7.3	LB Transfer of a DPPC/Initiator Film.....	87
7.4	SIP of Structured Polymer Brushes.....	88
7.5	Results and Discussion.....	89
7.6	Summary and Conclusion	92
8	AFM Lithography on Polymer Brushes	93
8.1	Introduction	93
8.2	Preparation of Polymer Brushes.....	94
8.3	General Lithography Procedure	95
8.4	Lithography Results	96
8.5	Immobilization of Dyes.....	100
8.6	Summary and Outlook	102
9	MD Simulation of Adenin-C ₂₀ on Graphite	107
9.1	Introduction	107
9.2	The Experimental System	107
9.3	Modelling of the System in GROMACS	110
9.4	Simulation Results and Discussion	112
9.5	Summary	121
10	MD Simulation of Molecular Diffusion on DPPC.....	123
10.1	Introduction	123
10.2	The Experimental System	123

10.3	Modelling of the System in GROMACS	125
10.4	Simulation Results and Discussion	130
10.5	Summary and Outlook	138
11	Closing Remarks	139
	References	141
	Publications	149
	Acknowledgements	153
	Lebenslauf	157

1 Introduction

1.1 Why Surface Structuring?

The structuring of surfaces on a micro and nanoscale has become one of the most active fields in the nano-sciences over the last decades. This is not surprising since control over matter at the micro- and nano-scale potentially gives one control about the many processes that are rooted in these length scales or enables miniaturization of existing technologies for enhanced performance. Miniaturization was the driving force in electronic devices like micro processors in the last 50 years most arrestingly depicted by Moore's law which states that the number of transistors in commercial integrated circuits grows exponentially doubling about every two years.^[1] It also enabled new integrated devices in the field of opto-electronics or even the integration of whole "lab-on-a-chip" systems and other micro-electro-mechanical systems (MEMS). Up to now the miniaturization of already existing major structures has been done with rather conventional top-down methods in particular optical lithography which have been enhanced constantly over the years. Moore's law is thought to continue for some more years even with "simple" enhancement of existing technologies, but ultimately there has to be some new method for generating the ever smaller structures needed and at some point even new concepts of transistors will be necessary. Surface structuring also plays an important role in microbiology where one can gain control over cell growth, migration, adhesion or even differentiation by aly preparations of surfaces.^[2] Surface structuring at the micro- and even nano-scale can also lead to new macroscopic properties making structuring methods of huge relevance to the material sciences, too. The most prominent application – at least in the awareness of the general public – is superhydrophobicity and therefore self-cleaning properties by altering the wetting behavior of surfaces by carefully designed structuring, the so called lotus effect.^[3] Another interesting possibility is the generation of so-called meta-materials with electromagnetic properties that are not available in natural materials (e.g., a negative refractive index). These are opening up completely new potentials for optical devices.^[4]

The methods for the structuring of surfaces are usually divided into two main groups, so called "top-down" (from big to small, starting from bulk material and breaking it down) and "bottom-up" (from small to big, building up a desired structure from smaller often molecular

building blocks) methods. Top-down methods are usually characterized by the application of externally-controlled tools that shape the preparation system into the desired structure. In contrast bottom-up methods start with small building blocks (usually of molecular size) and then rely onto the chemical properties of these building blocks to either directly build some useful structure by self-assembly or self-organization or achieve a functional structure by selective assembly onto desired position. In the latter top-down and bottom-up approaches are often mixed with each other, when, e.g., a top-down method is used for the preparation of active sites that then allow for a selective assembly of molecules in a bottom-up process. Another example for mixed bottom-up and top-down approaches is when in contrast to the aforementioned procedure a self-assembled monolayer (bottom-up) is used as a substrate for subsequent structuring by a top-down method.^[5-7]

1.2 Top-Down Approaches

A list of common top-down approaches and typical length scales accessible by the respective method as well as a comparison of the size of natural and artificial objects is given in Figure 1. The accessible length scales of the different methods span from millimeter to sub-nanometer resolution.

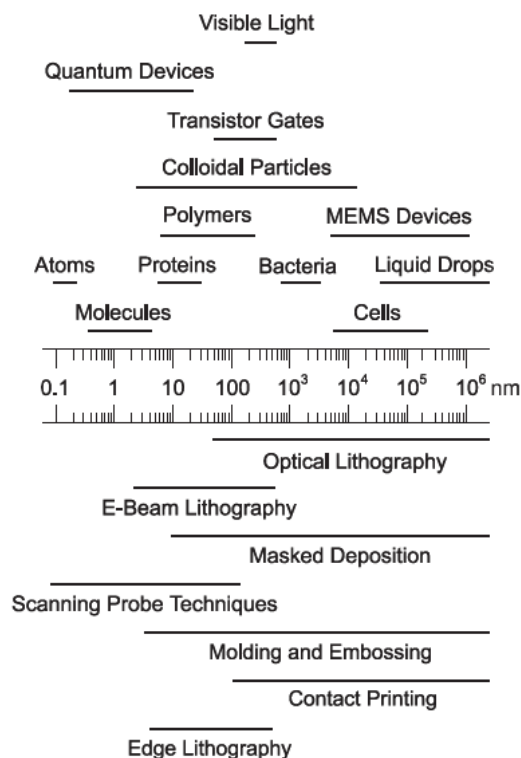


Figure 1. Accessible length scales by top-down methods (below ruler) compared to common structural length scales of specific natural and artificial objects (above ruler). Taken from reference.^[8]

By far the most common top-down technique is the optical lithography which is extensively used in the manufacturing of microelectronic devices like processors or memory chips.^[9] Optical lithography is based on the exposure of a photosensitive resist layer to spatially modulated UV light. The structured resist layer is then used as a mask or sacrificial layer for subsequent process steps to generate the desired structures. In commercial manufacturing feature sizes of 45 nm are well-established and 32 nm are projected for the near future. In electron beam lithography the UV light is replaced by a focused electron beam. This allows for a highly improved resolution with features below 10 nm but unfortunately has the implication of a much lower throughput. This is because in electron beam lithography there is no mask that allows for a parallel exposure of large areas as with optical lithography but every structure must be written sequentially by the electron beam. Scanning Probe Microscopy (SPM) techniques, like lithography with Atomic Force Microscopes (AFM) or Scanning Tunneling Microscopes (STM) reach the ultimate resolution limit by enabling the interaction with and movement of single molecules and atoms. The precise positioning of single atoms into arbitrary patterns by STM was first demonstrated in 1990^[10] and led to the famous “quantum corral” a few years later.^[11] STMs can also be used to induce chemical reactions on atomic scales.^[12] Another SPM based approach in top-down patterning is the so-called Dip Pen Nanolithography (DPN). In this method an AFM tip is “inked” with a suitable substance and then scanned over the surface in the desired pattern, leaving the substance on the surface similar to a fountain-pen.^[13] All scanning probe techniques are sequential methods so they exhibit the same drawbacks with respect to achievable throughput (although this may be compensated to some extent by parallelization through cantilever arrays). Alternative methods like micro- or nanocontact printing (μ CP/NCP) are especially useful in the chemical patterning of surfaces and are often used to print “ink” molecules that form self-assembled monolayers (thus somehow combining again top-down and bottom-up methods). They can be used in the patterning of chemical compounds that may not be stable enough for other lithographic methods (like many proteins) and can be employed in mass production even cheaper than optical lithography.^[14] Another promising emerging structuring method is nanoimprint lithography (NIL).^[15] In this method the patterns are transferred from a mask by mechanical deformation of an imprint resist often combined with a curing with UV light or heat during the imprint process. What makes this method very promising is that it potentially features a very high resolution while still having a considerable throughput, therefore, being much cheaper than for example electron beam lithography. The remaining problem in this approach is that still another conventional method (e.g., optical lithography or electron beam

lithography) is needed for manufacturing the mask for the imprint process which may be prohibitive for a broad commercial usage at the present time.

1.3 Bottom-Up Approaches

“Bottom-up” means to use smaller often molecular size building blocks and rely on their specific interactions with each other or prestructured substrates to form desired functional structures by self-assembly or self-organization*. Therefore, these approaches are often essentially of chemical nature because of the need for specific design in and synthesis of the molecular building blocks. The key feature of bottom-up approaches is the molecular self-assembly most prominently known in the case of self-assembled monolayers (SAMs).^[16] SAMs are organized monomolecular films consisting of bipolar molecules that have one end with a special affinity to the substrate and the other free for functionalization with desired chemical groups. SAMs can be used to alter surface properties, e.g., the wetting behavior or induce new chemical functionalities to a surface like the polymerization of polymer brushes. Other examples of self-assembly giving rise to pattern formation can be found in many different systems and on many different length scales like phase-separating block copolymers,^[17] two dimensional molecular crystals on surfaces,^[18] DNA network structures,^[19] and the generation of close packed structures of latex beads^[20] to mention only a few in the multitude of reported approaches.^[21] An obvious example for extreme self-organization is the growth of biological organism (although most basic assembly processes in cells may be based on self-assembly).^[22,23] Other examples are the pattern formation in chemical reactions^[24] or the pattern formation in Langmuir-Blodgett films.^[25,26] Many of these pattern producing processes are used in bottom-up approaches by utilizing them as templates to guide further self-assembled positioning of functionalized building blocks for later applications.^[27] The main fascination in bottom-up approaches is found in their potential of providing nanoscale structuring and functionalization over arbitrary sized areas combined with low cost and low time consumption. The problems in controlling these processes may

* The terms “self-assembly” and “self-organization” are often used synonymously. However “self-assembly” is more precisely used for processes where the ordered structure is formed while the system approaches thermodynamic equilibrium minimizing its free energy. In contrast “Self-organization” often appears far away from equilibrium and may need constant supply of energy to occur. For example one could call the growth of a highly ordered crystal as a simple form of self-assembly whereas a growing biological organism is an extreme form of self-organization.

seem enormous but we should not forget that the most sophisticated “machines” known to men are biological systems and these rely entirely on bottom-up approaches.

1.4 Scope of This Thesis

This thesis mainly deals with the endeavor to utilize the self-organized pattern formation of DPPC during Langmuir-Blodgett transfer for novel approaches of chemical and structural surface patterning. This type of self-organization being a typical bottom-up approach is combined but also contrasted with typical top-down methods as electron beam lithography and lithography by an atomic force microscope. Last but not the least the use of molecular dynamic simulations for elucidating pattern formation in self-assembly systems is demonstrated.

The thesis is structured into eleven chapters of which eight (Chapter 3 - 10) deal with experimental results. After the introduction (Chapter 1) a short overview on the methods employed is given (Chapter 2). The first chapter on experimental results (Chapter 3) deals with the influence of substrate treatment on the self-organized pattern formation of DPPC during Langmuir-Blodgett transfer and the impact of environmental humidity and temperature on the pattern. In Chapter 4 the development of a novel device that allows for a new variation of Langmuir-Blodgett transfer is described. It is shown that by this “rotational” Langmuir-Blodgett transfer complex pattern of gradient structure can be obtained. Striving for another way of deliberately influencing the self-organized DPPC patterning the interaction of prestructures introduced by electron beam lithography with the patterning process is examined (Chapter 5). One approach for the functionalization of the self-organized DPPC pattern is the admixing of compounds with desired functionality into the Langmuir film prior to the transfer onto a solid substrate. The feasibility of this approach for different kind of compounds and the impact of the admixing onto pattern formation and phase transition are demonstrated in Chapter 6. One class of the previously examined compounds that is functionalized for polymerization is used in the generation of structured polymer brushes, the results being described in Chapter 7. The mechanical properties of the polymer brushes were inspiring the use of these in lithography by an atomic force microscope, thus coming back to the realm of top-down methods. Chapter 8 is about the outcome of the lithographic process in comparison to spin-coated polymer films and some interesting application in the selective patterning of chemical compounds into the structured polymer brushes. Finally Chapter 9

and 10 deal with the modeling and simulation of self-organization and self-assembly processes with the means of molecular dynamics. Chapter 9 features a stability analysis of a system consisting of adenine-C₂₀ molecules on a graphite substrate that self-assemble into two different domain structures. The molecular dynamics simulation can shed some light onto the possible molecular packing structure and the mechanism behind their different stability on heating of the substrate. In Chapter 10 molecular dynamics simulation are utilized to discover the possible molecular mechanism behind the selective deposition process taking place in the evaporation of 3(5)-(9-anthryl) pyrazole and perylene onto structured DPPC pattern. Chapter 11 then gives some conclusions regarding the thesis as a whole and for some closing remarks.

The fact that most of the present work either has already been published or is in preparation for publication in scientific journals reflects in the structure of the single chapters. They can be read independently although the order is intentional because most of them rely in one way or the other on the results and achievements of the previous chapters.

2 General Methodology

2.1 Langmuir-Blodgett Technique

2.1.1 Introduction

The Langmuir-Blodgett technique (in short LB technique) deals with the preparation and investigation of insoluble monolayers at the air-water interface (usually termed as Langmuir films) as well as the transfer of such films onto solid substrates (then called LB films). Probably the earliest documented scientific observation related to the emergence of the LB technique was made as early as 1773 by *Benjamin Franklin* who “stilled the waves” by dropping a teaspoon full of oil into a pond.^[28] Over a century later *Lord Rayleigh* realized that *Franklin* had actually generated a monolayer of oil on the ponds surface that was calming down the surface movement and calculated the thickness of such a monolayer as well as used these calculations to confirm the Avogadro number.^[29] The progenitor of today’s LB trough (actually an ordinary kitchen sink) was introduced by *Agnes Pockels*. She experimented on the influence of oil monolayers and the compression of these through barriers on the water surface tension.^[30] Based on this setup *Irving Langmuir* developed the instrument that has come to be known as Langmuir trough and opened up a whole new scientific field.^[31] Together with his assistant *Katherine Blodgett** he later did the groundbreaking works in the transfer of Langmuir films onto solid substrates^[32-34] and finally established what is today known as Langmuir-Blodgett technique. Starting in the 1960s the LB technique gained growing interest for the generation of functional molecular arrangement on solid substrates with specifically designed molecules, advanced especially by *Hans Kuhn* and his colleagues.^[35] Although the LB technique is already a mature field with a century-long history it still constitutes an active research area with many recent applications in a broad variety of fields like molecular electronics,^[36,37] optoelectronics,^[38] sensor devices,^[39,40] generation of ordered arrangement of particles,^[41-43] and even the processing of graphene.^[44]

* An interesting side note is that although the general (non-scientific) public has never reached a state of wide awareness about LB technique *Katherine Blodgett* nevertheless had an appearance in the famous animation show “*The Simpsons*” (episode 2 of season 17, GABF16) when *Lisa* talked her family into a trip to the newly opened local stamp museum.



2.1.2 The Langmuir-Blodgett Trough

The essential piece of equipment for the LB technique the LB trough has come a long way from the more improvised kitchen sink used by *Pockels* over the first dedicated troughs designed by *Langmuir* to modern commercially available LB troughs. Although a variety of different setups exist^[45] LB troughs commonly consist of the same basic constituents. A typical setup realized in one of the commercial troughs used during the course of the present work is shown in Figure 2.

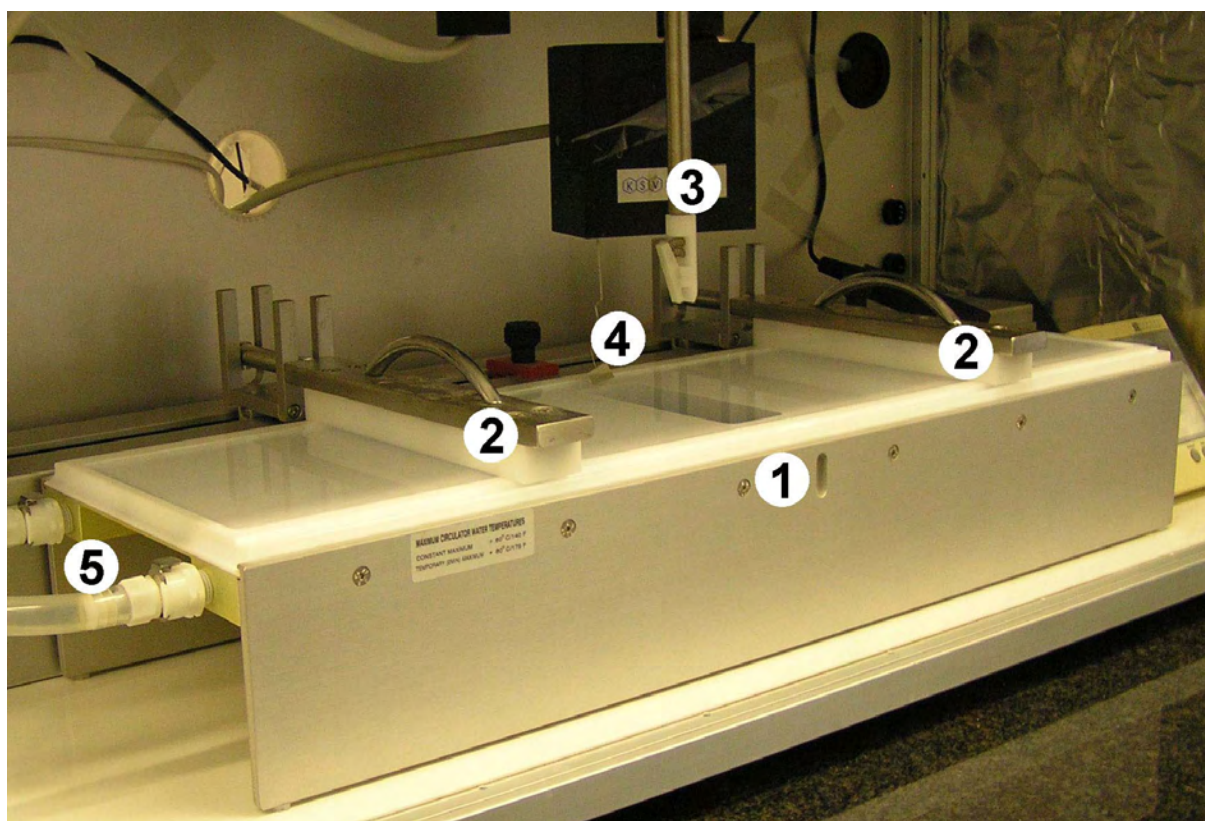


Figure 2. Image of a commercial Langmuir-Blodgett trough consisting of (1) the basin (2) symmetric movable barriers (3) dipper (4) Wilhelmy plate and (5) connectors for the thermostat.

This typical setup consists of a basin (1) to hold the subphase on which the monolayers are to be spread. This basin is made of Teflon which has the advantage of being chemically inert to a wide range of compounds and is hydrophobic, hence easy to clean. Incorporated into the basin is a network of tubes to allow temperature control of the subphase by a thermostat. The symmetric movable barriers (2) are made from Teflon, too, and are used to adjust the surface area of the floating monolayer. The dipper (4) is utilized to move a sample vertically into or out off the subphase in order to transfer a floating monolayer onto a solid substrate. The Wilhelmy plate (4) is used to measure the change in surface tension during experiments that is

usually translated into the lateral surface pressure, a key parameter for the characterization of the state of a floating monolayer. The plate used in this setup is made of platinum but other materials (glass, mica, and even filter paper) can be used, too. Connectors for a thermostat (5) enable a temperature control of the subphase.

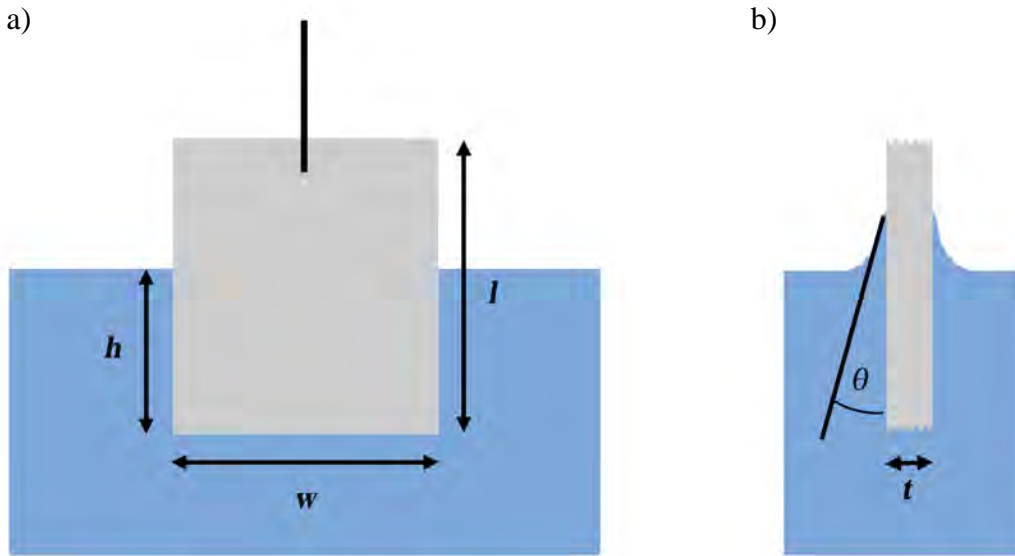


Figure 3. Schematic view of a Wilhelmy plate in (a) front view and (b) side view.

When a rectangular plate (Figure 3) with the dimensions l , w , and t made from a material with a density ρ_P is immersed up to a depth h into a liquid of density ρ_L it will experience a force F given by

$$F = \rho_P g l w t + 2\gamma(t + w)\cos\theta - \rho_L g t w h \quad (1)$$

with g being the acceleration of gravity, γ the surface tension of the liquid and θ the contact angle of the liquid on the plate. If the plate is completely wetted ($\theta = 0^\circ$), sufficiently thin ($t \ll w$), and stationary during the experiment the change in surface tension $\Delta\gamma$ due to a floating monolayer is related to a change in force acting onto the plate ΔF by the simple expression

$$\Delta\gamma = \frac{\Delta F}{2(t + w)} \approx \frac{\Delta F}{2w} \quad (2)$$

The surface pressure π is then defined by

$$\pi = \gamma_0 - \gamma = -\Delta\gamma = -\frac{\Delta F}{2w} \quad (3)$$

where γ_0 is the initial surface tension of the pure subphase and γ is the surface tension in the presence of a floating monolayer.

2.1.3 π -A Isotherms

A floating monolayer at the air-water interface can be described as a two-dimensional gas. In analogy to the thermodynamics of three-dimensional gasses a lateral pressure π (as defined above by the drop in surface tension of the subphase due to the floating monolayer) assumes the role of the pressure p in the three-dimensional case and instead of the volume V the molecular area A (defined by the surface area available in the monolayer per molecule) is used for characterization of the thermodynamic state. The molecular area A for a floating monolayer in a LB trough can be adjusted by restricting the available surface area with moving barriers. For a constant temperature a π -A isotherm can be recorded for the Langmuir film by progressive compression and simultaneously measuring the lateral pressure π . A generalized π -A isotherm of a Langmuir film of fatty acid is shown in Figure 4.

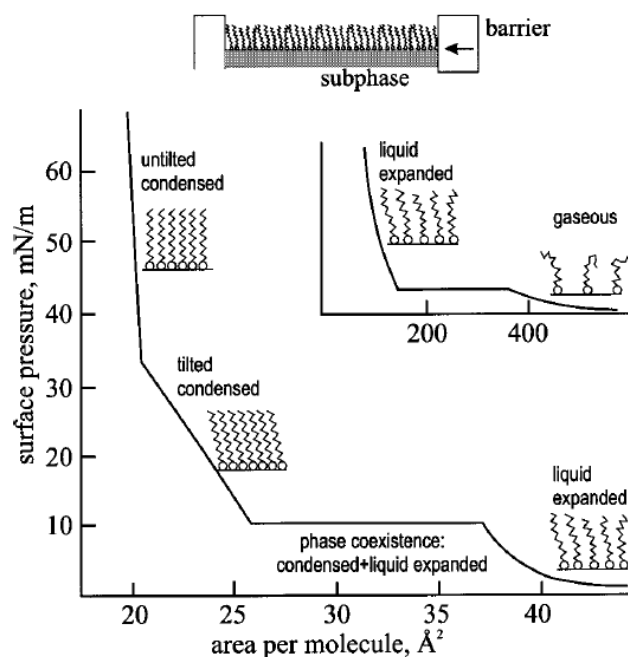


Figure 4. A generalized π -A isotherm of a Langmuir film of a fatty acid (taken from reference^[46]).

In a very dilute state with molecular areas of hundreds of square angstroms the monolayer is well described as being in a gaseous state. Upon compression there will be a transition into what is traditionally called the liquid expanded phase. Both aforementioned phases do not exhibit any measurable order; the molecule's headgroups are translationally disordered and the carbon chain tails are conformationally disordered. Further compression leads to an increase in surface pressure until a plateau region is reached, indicating a first-order transition from the liquid expanded phase to a condensed phase (meaning that now the film exhibits translational and conformational order to some extent when examined by, e.g., x-ray-diffraction methods). The condensed phase is less compressible than the liquid expanded phase; therefore the rise in surface pressure upon compression is steeper. At some point usually a kink in the isotherm can be observed that denotes the transition into another condensed phase. This kink was observed and interpreted as an additional phase transition as early as 1922^[47] before structural data was available. Therefore, the phases after the main phase transition from the liquid expanded phase were traditionally termed liquid condensed and solid phase. Later obtained structural data implies that the translational order in both of these phases is alike and the transition is essentially a change in the tilt angle of the hydrocarbon chains with respect to the water surface, so it would be more appropriate to refer to both of these phases as condensed and denote the difference by the prefix tilted or untilted, respectively. Nevertheless, the use of the terms "liquid condensed phase" and "solid phase" is still common due to described historical reasons. Monolayers of the phospholipid DPPC, the prominent system in the LB related parts of the current work, exhibit a first-order transition between liquid expanded and liquid condensed phase, too. This transition plays a crucial role in the self-organized patterning of DPPC during LB transfer.

2.1.4 Langmuir-Blodgett Transfer

The Langmuir-Blodgett transfer was introduced by *Langmuir* and *Blodgett* in the 1930s^[32-34] and is still the most common method to transfer a floating monolayer onto a solid substrate. Most of the transfers carried out in the current work use this method, too. A schematic transfer procedure for the case of a hydrophilic substrate is shown in Figure 5.

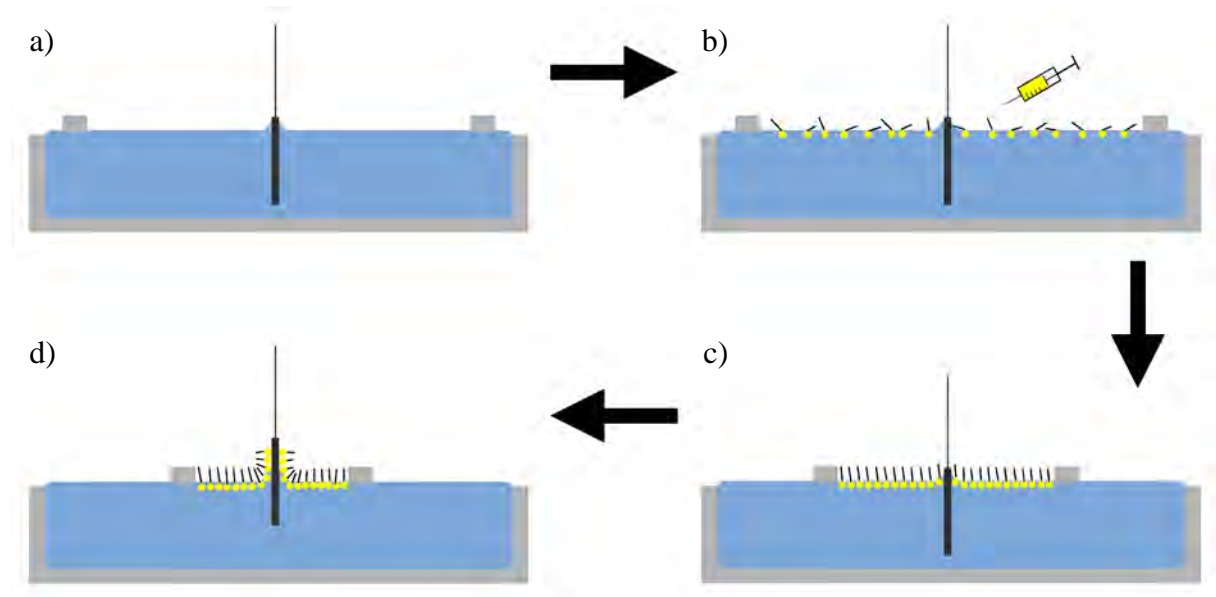


Figure 5. Schematic procedure for a Langmuir-Blodgett transfer onto a hydrophilic substrate.

The hydrophilic substrate is submerged into the water subphase (a) then a monolayer is spread (b) and compressed to the desired surface pressure (c). Finally the substrate is withdrawn from the subphase and the monolayer transfers onto the solid substrate at the three-phase contact line, the line on the sample where air, water and the solid substrate converge (d). Usually the surface pressure is kept constant during transfer by a feedback loop that compresses the film by movement of the barriers as soon as the surface pressure drops due to the transfer of molecules onto the solid substrate.

The detailed processes in the vicinity of the three-phase contact line during LB transfer are still poorly understood. The contact angle θ of a liquid resting on a solid substrate is governed by Young's equation:^[48]

$$\cos \theta_e = \frac{\gamma_{SV} - \gamma_{SL}}{\gamma_{LV}} \quad (4)$$

with γ_{SV} , γ_{SL} , and γ_{LV} being the surface tensions at the solid/vapor, solid/liquid, and liquid/vapor interface, respectively. For the case of a vertical wall immersed in a liquid at the equilibrium state the then static meniscus is described by^[49]

$$\theta_e = \arcsin\left(1 - \frac{\rho g Z^2}{2\gamma}\right) \quad (5)$$

where ρ is the density of the liquid, g the acceleration of gravity, Z the capillary height and γ the surface tension of the liquid. However, in the case of the solid substrate being withdrawn from a subphase that is additionally covered with a floating monolayer that will alter itself the wetting properties during transfer the description becomes much more complicated. One approach based on a combined molecular-hydrodynamic model obtained following equation for the description of the meniscus shape during transfer:^[50,51]

$$\cos(\theta_r) = \frac{nk_b T}{\sigma} \operatorname{arcsinh}\left(\frac{v}{2K\lambda}\right) + \cos(\theta_e) \quad (6)$$

This model was applied with some success for the description of the self-organized DPPC patterning.^[52]

2.2 Brewster Angle Microscopy

Brewster Angle Microscopy (BAM) was introduced independently and almost simultaneously by two groups *Hönig* and *Möbius*^[53] and *Hénon* and *Meunier*^[54] in 1991. It is a potent tool for the direct visualization of monolayers at the air-water interface. The basic phenomenon that is exploited by the BAM is the so called Brewster angle (after *Sir David Brewster* who discovered it in 1811). This is the angle of incidence at which only the s-polarized part of the light shining on an interface between two media of different refractive index is reflected:

$$\theta_B = \arctan\left(\frac{n_2}{n_1}\right) \quad (7)$$

The Brewster angle for an air-water interface ($n_1 \approx 1$, $n_2 \approx 1.33$) is approximately 53° . In a BAM setup p-polarized light is used to illuminate the air-water interface in a LB trough under the Brewster angle. Because only s-polarized light is reflected when the Brewster angle condition is fulfilled there will be no reflection from the trough surface. However if a floating monolayer covers the air-water interface the Brewster angle condition will be slightly violated

giving rise to a small amount of reflection that can be detected and translated into an image of the monolayer morphology (Figure 6).

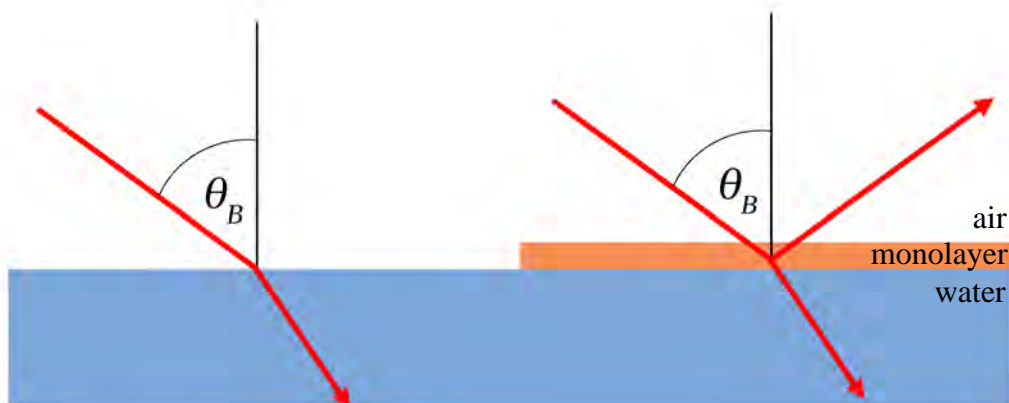


Figure 6. Scheme of the signal generation in BAM.

Since the reflected signal is only a tiny fraction of the incoming light intensity (usually in the order of 10^{-6}) lasers are used as light sources and the reflected signal is collected by CCD cameras or similar devices. A typical BAM setup as it was also used in the present work is shown in Figure 7.

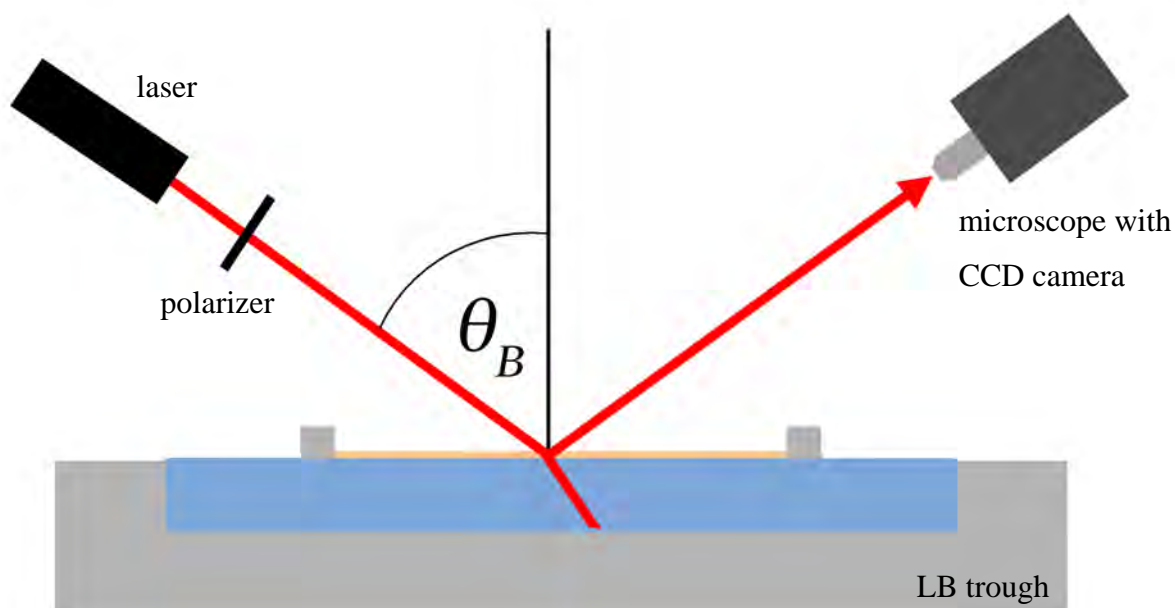


Figure 7. Schematic setup of a Brewster angle microscope.

A laser source (Nd-YAG laser in our setup) is filtered by a polarizer yielding p-polarized light shining on the LB trough under the Brewster angle θ_B . Since a floating monolayer is present part of the incoming light is reflected and collected by a microscope equipped with a sensitive CCD camera. The BAM usually yields a resolution of about 1 to 2 μm and enables the direct optical observation of domain growths in Langmuir films without the need of adding fluorescent probes that may itself influence the behavior of the examined system.

2.3 Fluorescence Microscopy

Fluorescence Microscopy (FM) is a special form of conventional light microscopy where a sample is studied by the fluorescence (or phosphorescence) of either naturally occurring fluorophores inside the sample or deliberately added fluorescent dyes. It has become extremely useful especially in the life sciences because biological structures can be selectively labeled by different fluorescent dyes. In the simplest form of fluorescence light of a certain wavelength is absorbed by an atom or molecule (the fluorophore) leaving it in an excited state that later decays under emission of light with longer wavelength. In fluorescence microscopy light matching the excitation spectra of the used fluorophores evokes fluorescence inside the sample that is then observed. A set of filters in the excitation and observation light path ensures that only fluorescence coming from the sample is observed while mere reflection of the exciting light is blocked. By an intelligent choice of fluorophores with different excitation and emission characteristics multi-color and selective observations of dye species are possible. A typical setup for an (epi-)fluorescence microscope is given in Figure 8.

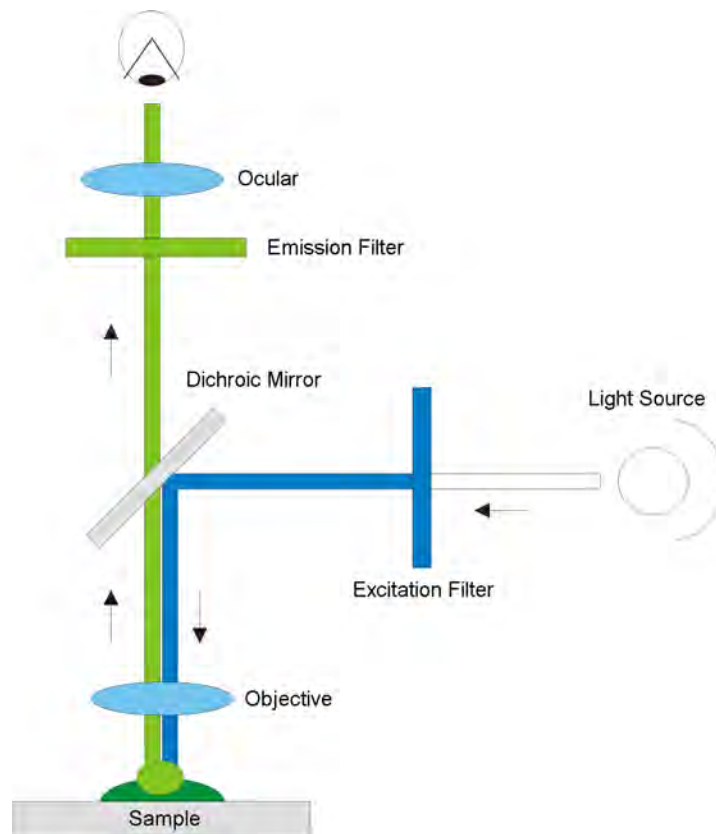


Figure 8. Schematic setup of an epi-fluorescence microscope.

The emitted light from a bright light source (usually a xenon or mercury lamp) is filtered by an excitation filter to a narrow spectrum suitable for the excitation of the used fluorophore. The excitation light is then reflected onto the sample by a dichroic mirror that is matched to reflect the excitation light while letting pass the emitted fluorescent light from the sample. The fluorescent compounds inside the sample are excited by the incoming light and the resulting fluorescent emission is passed through the dichroic mirror and is filtered once again by an emission filter matched for the emission spectra of the used dye before reaching the objective where it can be observed directly or captured with a camera. The resolution limits of fluorescence microscopy are in principal similar to conventional microscopy (i.e., about half the wavelength of the used light) but advanced methods evolved based on fluorescence techniques, e.g., confocal laser scanning microscopy (CLSM), 4Pi microscopy, stimulated emission depletion (STED) and more that can reach resolutions even beyond the Abbe limit.^[55,56]

2.4 Atomic Force Microscopy

Atomic Force Microscopy (AFM) is an excellent tool for exploring surfaces and measuring tiny forces at the nanometer scale. The first AFM was introduced by *Gerd Binnig, Calvin Quate* and *Christoph Gerber* in 1986.^[57] Whereas imaging in atomic scale resolution on conducting surfaces was achieved before by scanning tunneling microscopy (STM)^[58,59] the advent of AFM provided a similar high resolution for the wide range of non-conductive samples (especially the most organic and biological materials). A scheme of a basic AFM setup is shown in Figure 9.

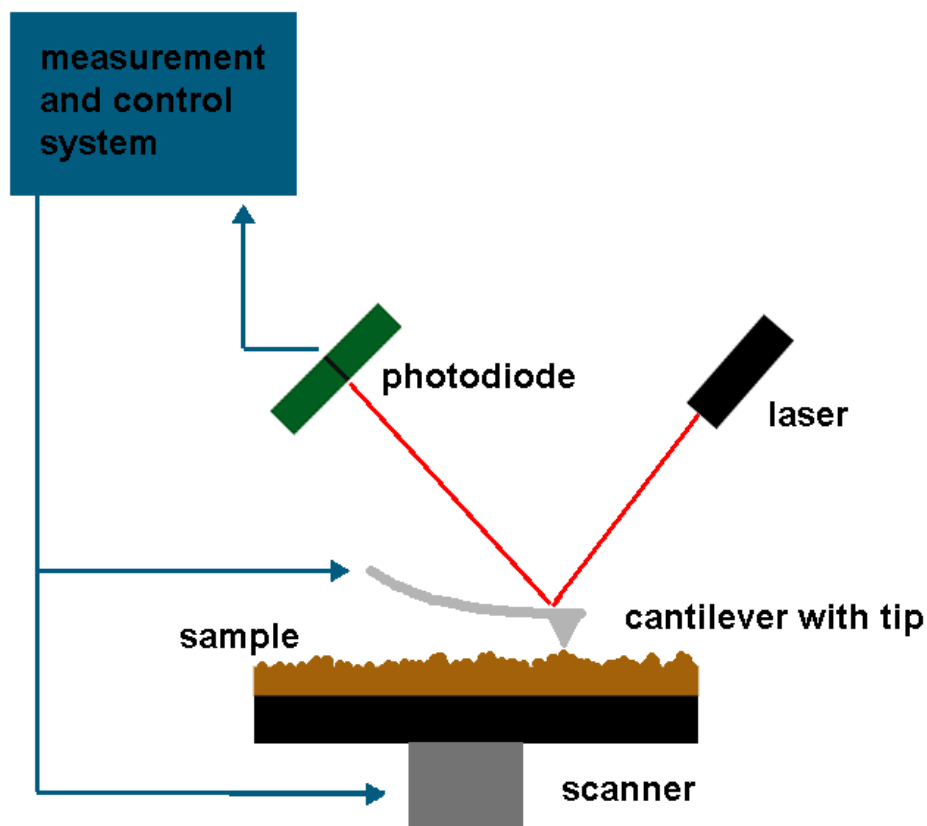


Figure 9. Schematic basic AFM setup.

The image generation by AFM is done by scanning a sharp tip (with apex radii of only several nanometers) attached to a cantilever over the surface to be examined. The scanning is either done by moving the sample or the cantilever usually by piezo crystal units for the movement in lateral (x - y) and vertical (z) direction. The interactions between tip and sample will bend the cantilever which is then detected by the instrument (usually by a Laser that is reflected by the cantilever onto a split photodiode) and translated into a topographic image of the surface.

Three modes of operation can be distinguished depending on how the cantilever is scanned over the sample:

(1) Contact mode: in this mode the tip is in direct mechanical contact with the sample surface which means that strong repulsive forces are acting. There is a further distinction between constant height mode where the z-position is not altered during scanning and the constant force mode where the z-position is updated during scanning in a way that keeps the bending of the cantilever constant (which means a constant force is acting upon the tip). In the first case the current deflection of the cantilever is converted into a topographic image of the surface, in the latter case the topographic image is obtained by recording the current z-position of the cantilever.

(2) Non-contact or dynamic mode: here the cantilever is excited to oscillate and the tip is scanned over the sample far away from the surface (about 100 nm). Long-range forces acting between sample and cantilever shift the resonance frequency of the oscillating cantilever which is then detected as measurement signal.

(3) Tapping or intermittent mode: when applying this mode the cantilever is oscillating, too, but is scanning so close to the sample surface that the tip reaches the repulsive forces regimen in the lower dead centre of the oscillation. The tip is therefore not in constant mechanical contact with the sample surface but is just tapping on the sample regularly. The feedback signal in this mode is usually the oscillation amplitude. When the distance (hence the force) between oscillating cantilever and the sample surface changes the resonance frequency of the cantilever will change and therefore the oscillation amplitude (because the excitation frequency will not exactly match the resonance frequency any more). The feedback loop will then adjust the z-position of the cantilever until the oscillation amplitude reaches the old magnitude again. Generally two measurement signals are generated regularly: the z-position of the cantilever is used to generate a topographic image. As a second source of information the phase shift between excitation oscillation and the actual oscillation of the cantilever is recorded and translated into a phase image of the surface.

All three modes have advantages and drawbacks with respect to resolution, mechanical strain on tip and sample, and stability and complexity of the setup itself. While the contact mode was the first one to be implemented historically it is also the one with the strongest forces

acting on tip and sample. This may not be a problem on hard samples but for soft surfaces (like most biological samples) scanning in contact mode will considerably alter or even damage the scanned object. The non-contact mode exerts the lowest force onto the sample but high-vacuum conditions are needed for a feasible application. Therefore, the most common mode today for the examination of soft matter samples (like most samples in the current work) is the tapping mode that yields good results even under ambient conditions as long as molecular or even atomic resolution is not necessary. When used for lithographic purposes the AFM is most often operated in contact mode because relatively high forces are to be generated but the intermittent mode can also be used in the right setup and for soft materials.^[60-64]

2.5 Electron Beam Lithography

In electron beam lithography (EBL) a focused electron beam is scanned over a sample covered with a resist layer (e.g., PMMA) sensitive to electron irradiation to generate a pattern of exposed and non exposed areas that can be later selectively removed by solvents. The structures generated in the resist layer by this process can then be transferred onto the sample, e.g., by evaporating of metals and subsequent removal of the remaining resist layer. A typical schematic process as it was used to generate the prestructures in the present work is depicted in Figure 10.

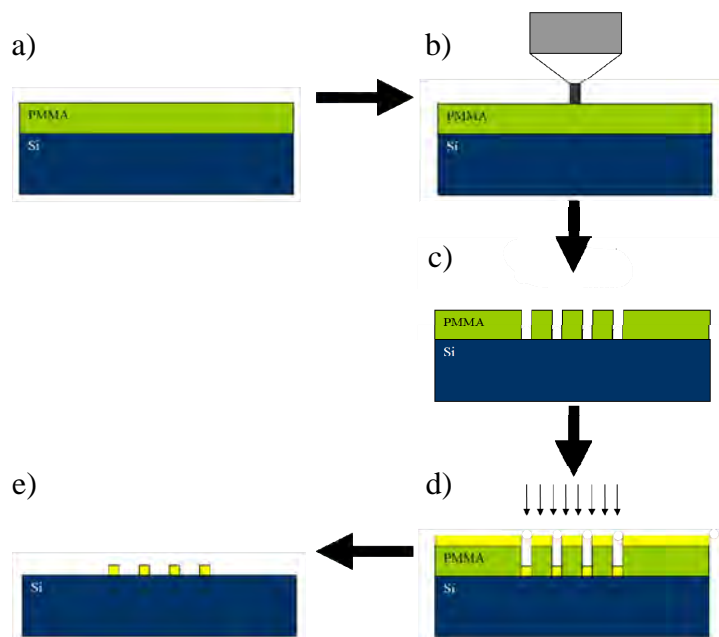


Figure 10. Scheme of a typical EBL process: (a) a sample with resist layer (b) exposure to an electron beam (c) selective solvolysis of exposed areas (d) evaporating of metal (e) removal of residual resist layer.

A silicon sample is covered with a resist layer (a) in a typical case 300 nm of PMMA. The sample is then scanned by an electron beam to expose the desired pattern (b). The electron beam induces chain breaks in the exposed areas of the resist layer thus lowering the molecular weight of the PMMA in these areas. Since the solubility of PMMA is strongly dependant on the molecular weight for some solvents the exposed pattern can be dissolved selectively (c) by washing the sample with an appropriate solvent (e.g., MIBK). Metals can then be applied to the sample for example by thermal evaporation (d) and after a final lift off process in that the residual resist layer is completely removed (e.g., by washing with acetone) the exposed pattern remains as a metal structure on the sample (e). Since EBL can generate structure way beyond the diffraction limit it has become widely used in the area of nanotechnology and related fields. Dedicated EBL systems can reach feature sizes down to 10 nm and for systems (that are more common in research setups) that are built upon a conventional electron microscope (like used in the present work) still features down to 20 nm are reported. Although EBL is superior to photolithographic approaches in terms of resolution it has the problem of being a serial technique: the electron beam has to scan the whole pattern and dwell long enough in each position to reach the exposure dose needed for development of the resist. Therefore EBL is limited to the patterning of relatively small areas in feasible time scales and only used in areas where the improved resolution makes up for the extensive fabrication time (e.g., mask production for later photolithographic processes) or only small area patterning is needed as is often the case in research settings.

2.6 Molecular Dynamics with GROMACS

2.6.1 Introduction

Molecular dynamics (MD) refers to a method of computer simulation where a system of atoms or molecules is allowed to evolve for a period of time (usually) under Newtonian physics. This means that in contrast to Monte Carlo (MC) simulations the trajectories of the constituents are not based on random movements but rather dictated by the forces calculated from approximations of know interactions within the system (e.g., coulomb forces, van der Waals forces). The first MD simulations were performed in the late 50s^[65] and since then the method was constantly improved. With the advances in computer technology and therefore constantly increasing computing power the simulation of ever more complex and larger systems have become feasible. Recently, even a MD simulation of a whole virion with a complete set of RNA and viral proteins in atomistic details (about one million atoms) for a

period of 50 ns was achieved.^[66] Another development enabling simulations of larger systems for longer timescales is the use of coarse grained (CG) models in which several atoms are combined into one model particle to reduce the overall numbers of particles for that the forces and resulting trajectories must be calculated. By current implementations of this method, e.g., the MARTINI force field^[67] for GROMACS, time scales in the range of microseconds for big systems like phospholipid bilayers on a solid support^[68] or phospholipid monolayers on water^[69] (with over 200,000 particles representing over 2,400,000 atoms) can be reached if atomistic details are not necessary. Nowadays MD simulation has become a powerful tool and is often referred to as “molecular microscope”. It is broadly used in the biochemical sciences to investigate the properties of proteins, the interaction of proteins with small molecules, or other proteins in water and within biomembranes. There are several software suites available that provide efficient MD codes and standardized force fields. This opens up the use of MD simulation to a broader audience that generally does not have the resources to develop simulation programs from scratch: among the most widespread simulation suites are AMBER^[70], CHARMM^[71-73], GROMACS^[74,75] and NAMD^[76]. For the simulations in the present work we chose GROMACS because it is broadly used in the simulation of phospholipid systems, highly efficient, and freely available.

2.6.2 General MD Algorithm

A general flow chart of a simulation in the GROMACS suite (as well as of most classical MD simulations) is given in Figure 11. As an input the simulation requires the position and speed of all constituents of the system (i.e., the system’s starting configuration) as well as all parameters that describe the bonded and non-bonded interactions within the system namely the topology that describes which atoms in the system are bound together to molecules (and in which way) and the force field that provides the parameters for calculating the interaction forces. Given all of this information the software can determine the forces acting upon each constituent of the system by calculating the force between each pair of non-bonded constituents plus the forces due to bonded interaction. Afterwards the configuration is updated by calculating the movement of each constituent for the period of one time step by numerically solving Newton’s equation of motion. During the duration of a time step the forces are postulated to remain constant, therefore it is very important to choose the steps short enough in order to prevent artifacts. Usually time steps in the order of 1 to 4 fs are applied, depending on the fastest occurring motions (e.g., oscillations of bound hydrogen

atoms) in the simulated system. When the new position and velocity of each system constituent are determined they can be logged together with other system parameters

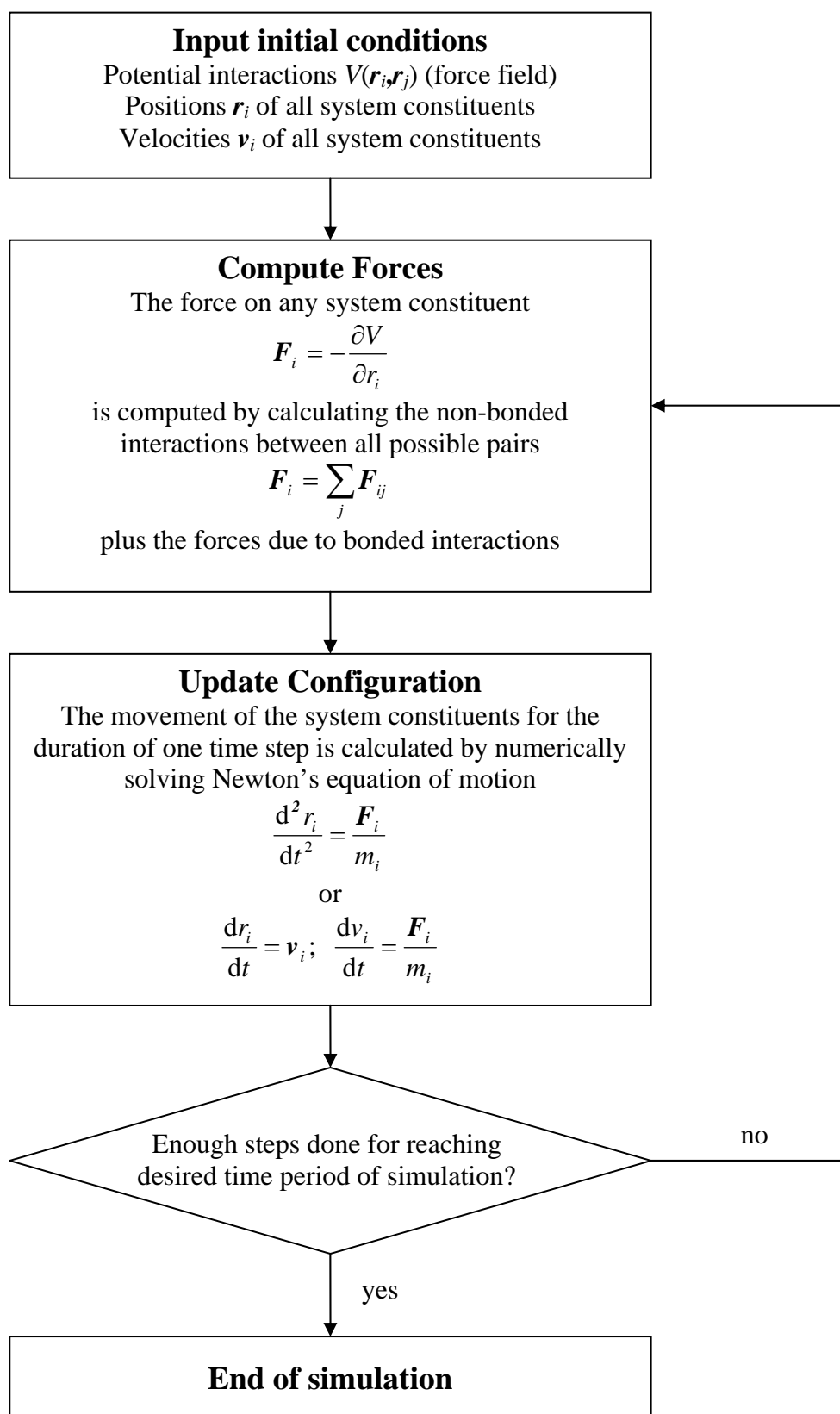


Figure 11. Flow chart of a classical MD algorithm (adapted from GROMACS manual^[77]).

of interest (e.g., potential and kinetic energies and pressure tensors) that can be derived from the calculation. After each time step it is checked whether the desired simulation time has already been reached. If not the algorithm starts over with calculating the forces on each system constituent based upon their new positions and then updates the configuration again until the desired simulation time is reached.

2.6.3 Used Interaction Function and Force Field

The interactions between the constituents of a simulated system can be divided into non-bonded and bonded interactions. GROMACS offers various functions and methods to calculate the interaction forces in order to be easily adaptable to a lot of different set of force field parameters from external sources as well as personal preferences of the users. This chapter covers only the options used and relevant to this work. For a full account of possible choices and more detailed information refer to the GROMACS manual^[78] and the description of the GROMOS96 force field.^[79]

All non-bonded interactions in GROMACS are pair-additive as well as centro-symmetric:

$$V(\mathbf{r}_1, \dots, \mathbf{r}_N) = \sum_{i < j} V_{ij}(\mathbf{r}_{ij}) \quad (8)$$

$$\mathbf{F}_i = -\sum_j \frac{dV_{ij}(\mathbf{r}_{ij})}{d\mathbf{r}_{ij}} \frac{\mathbf{r}_{ij}}{r_{ij}} = -\mathbf{F}_j \quad (9)$$

The non-bonded interactions contain a repulsion and dispersion term that are combined into a Lennard-Jones (or 6-12 interaction) term and a Coulomb term. Additionally (partially) charged constituents act through the Coulomb term.

The Lennard-Jones potential V_{LJ} is given by

$$V_{LJ}(\mathbf{r}_{ij}) = \frac{C_{ij}^{(12)}}{r_{ij}^{12}} - \frac{C_{ij}^{(6)}}{r_{ij}^6} \quad (10)$$

The term derived from this potential is

$$\mathbf{F}_i(\mathbf{r}_{ij}) = \left(12 \frac{C_{ij}^{(12)}}{r_{ij}^{13}} - 6 \frac{C_{ij}^{(6)}}{r_{ij}^7} \right) \frac{\mathbf{r}_{ij}}{r_{ij}} \quad (11)$$

Alternatively V_{LJ} can be written in the form of

$$V_{LJ}(\mathbf{r}_{ij}) = 4\varepsilon_{ij} \left(\left(\frac{\sigma_{ij}}{r_{ij}} \right)^{12} - \left(\frac{\sigma_{ij}}{r_{ij}} \right)^6 \right) \quad (12)$$

The parameters $C_{ij}^{(12)}$ and $C_{ij}^{(6)}$ depend on each respective pair of the system constituent. Therefore, it is necessary to calculate these parameters for all possible types of pairs within the simulated system. This is done once before the start of the simulation and the results are stored into a LJ-parameter matrix to be used whenever needed. The combination rules to determine the combined parameters from the self-interaction parameters given by the force field are either to use geometric means for both parameters:

$$\begin{aligned} C_{ij}^{(6)} &= (C_{ii}^{(6)} C_{jj}^{(6)})^{1/2} \\ C_{ij}^{(12)} &= (C_{ii}^{(12)} C_{jj}^{(12)})^{1/2} \end{aligned} \quad (13)$$

or alternatively use an arithmetic average for the σ_{ij} and geometric average for the ε_{ij} :

$$\begin{aligned} \sigma_{ij} &= \frac{1}{2} (\sigma_{ii} + \sigma_{jj}) \\ \varepsilon_{ij} &= (\varepsilon_{ii} \varepsilon_{jj})^{1/2} \end{aligned} \quad (14)$$

the latter known as the Lorentz-Berthelot rules.^[80]

The Coulomb interaction between two charged particles is given by:

$$V_C(\mathbf{r}_{ij}) = \frac{1}{4\pi\varepsilon_0\varepsilon_r} \frac{q_i q_j}{r_{ij}} \quad (15)$$

Hence the derived force term is:

$$\mathbf{F}_i(\mathbf{r}_{ij}) = \frac{1}{4\pi\epsilon_0\epsilon_r} \frac{q_i q_j}{r_{ij}^2} \frac{\mathbf{r}_{ij}}{r_{ij}} \quad (16)$$

In order to save computing time usually the non-bonded forces are not accounted for if the pair of beheld system constituents is farther away from each other than a certain cutoff radius. Introducing such a simple cutoff will produce a discontinuity in the experienced forces just at the cutoff radius which can result in serious simulation artifacts.^[81] To remove the artificial leap in force at the cutoff radius shift functions can be used that smoothen out the discontinuity. For a pure Coulomb interaction $F(r) = F_\alpha(r) = r^{-(\alpha+1)}$ the shifted force $F_s(r)$ can generally be written as

$$\begin{aligned} F_s(r) &= F_\alpha(r) & r < r_1 \\ F_s(r) &= F_\alpha(r) + S(r) & r_1 \leq r < r_c \\ F_s(r) &= 0 & r_c \leq r \end{aligned} \quad (17)$$

Here two new parameters r_1 and r_c are introduced. The shifted force is identical to the unshifted force up to a radius of r_1 . Then the shifting function $S(r)$ is added in order to bring the force smoothly down to zero until radius r_c is reached. For bigger r the shifted force is set to zero. The corresponding shifted Coulomb potential is

$$V_s(r_{ij}) = \frac{1}{4\pi\epsilon_0\epsilon_r} \Phi_s(r_{ij}) q_i q_j \quad (18)$$

with

$$\Phi_s(r) = \int_r^\infty F_s(x) dx \quad (19)$$

Because the shifted force function should be smooth at r_1 and r_c and additionally become zero at r_c the following boundary conditions are imposed:

$$\begin{aligned} S(r_1) &= 0 \\ S'(r_1) &= 0 \\ S(r_c) &= -F_\alpha(r_c) \\ S'(r_c) &= -F'_\alpha(r_c) \end{aligned} \quad (20)$$

A third degree polynomial like

$$S(r) = A(r - r_1)^2 + B(r - r_1)^3 \quad (21)$$

can fulfill these requirements. A and B are determined by the boundary conditions to:

$$A = -\frac{(\alpha + 4)r_c - (\alpha + 1)r_1}{r_c^{\alpha+2}(r_c - r_1)^2} \quad (22)$$

$$B = \frac{(\alpha + 3)r_c - (\alpha + 1)r_1}{r_c^{\alpha+2}(r_c - r_1)^3} \quad (23)$$

The shifted force function in the range between r_1 and r_c is therefore

$$F_s(r) = \frac{\alpha}{r^{\alpha+1}} + A(r - r_1)^2 + B(r - r_1)^3 \quad (24)$$

and the corresponding potential

$$\Phi(r) = \frac{1}{r^\alpha} - \frac{A}{3}(r - r_1)^3 - \frac{B}{4}(r - r_1)^4 - C \quad (25)$$

with

$$C = \frac{1}{r_c^\alpha} - \frac{A}{3}(r_c - r_1)^3 - \frac{B}{4}(r_c - r_1)^4 \quad (26)$$

When r_1 is set to zero the modified Coulomb force function becomes

$$F_s(r) = \frac{1}{r^2} - \frac{5r^2}{r_c^4} + \frac{4r^3}{r_c^5} \quad (27)$$

and is identical to the parabolic force function recommended to be used as a short-range function in conjunction with a Poisson solver for the long-range part.^[82] The corresponding Coulomb potential is

$$\Phi(r) = \frac{1}{r} - \frac{5}{3r_c} + \frac{5r^3}{3r_c^4} - \frac{r^4}{r_c^5} \quad (28)$$

The use of shift functions and cutoffs has only minor implications for the Lennard-Jones forces but will obviously reduce the long-range Coulomb forces drastically. Negligence of the long-range Coulomb forces by not applying a suitable correction may result in simulation artifacts.^[83] To account for the decline in Coulomb force due to the exclusion of charges farther away than the cutoff radius a method named Ewald summation can be used:

Generally the total electrostatic energy of N particles and their periodic images is

$$V_c = \frac{1}{8\pi\epsilon_0\epsilon_r} \sum_{n_x} \sum_{n_y} \sum_{n_z} \sum_i^N \sum_j^N \frac{q_i q_j}{r_{ij,n}} \quad (29)$$

For $n_x = n_y = n_z = 0$ (i.e., the box vector \mathbf{n} becomes the zero vector) the exception must be made that terms with $i = j$ are omitted to avoid self-interaction within the base simulation cell. The distance $r_{ij,n}$ is the true distance between two particles and not the nearest-image distance. This sum conditionally converges but does so very slowly. To ease the calculation of long-range interactions of the periodic images in crystals the Ewald summation was introduced.^[84]

The basic idea is to split up the slowly converging sum into two faster converging and a constant term:

$$V_c = V_{dir} + V_{rec} + V_0 \quad (30)$$

$$V_{dir} = \frac{1}{8\pi\epsilon_0\epsilon_r} \sum_{i,j}^N \sum_{n_x} \sum_{n_y} \sum_{n_z} q_i q_j \frac{\text{erfc}(\beta r_{ij,n})}{r_{ij,n}} \quad (31)$$

$$V_{rec} = \frac{1}{8\pi^2\epsilon_0\epsilon_r V} \sum_{i,j}^N q_i q_j \sum_{m_x} \sum_{m_y} \sum_{m_z} q_i q_j \frac{e^{-\left(\frac{\pi m}{\beta}\right)^2 + 2\pi i m \cdot (r_i - r_j)}}{m^2} \quad (32)$$

$$V_0 = -\frac{\beta}{4\pi^{3/2}\epsilon_0\epsilon_r} \sum_i^N q_i^2 \quad (33)$$

The parameter β determines the relative weight between the direct sum V_{dir} and the reciprocal sum V_{rec} . By this approach relative short cutoffs in the direct space sum (in the order of 1 nm) and in the reciprocal space sum (e.g., 10 wave vectors in each direction) can be used. Still, there remains a problem in efficiency: the computing cost of the reciprocal sum increases as N^2 which (by better implemented algorithms) can be cut down only to $N^{3/2}$. This makes the approach prohibitive for bigger system sizes. To circumvent this problem GROMACS usually utilizes a refined method named particle-mesh Ewald (PME).^[85,86] In this method the charges are assigned to a grid by cardinal B-spline interpolation. Then the grid is Fourier transformed with a 3D-FFT and the complete reciprocal energy term is obtained by a single sum over the grid in k-space instead of directly summing the wave vectors. The potential at the grid points is obtained by an inverse transformation and by using the interpolation factors the forces on each system constituent is gained. The computing cost of the PME algorithm scales as $N \log(N)$ and is therefore considerable faster than simple Ewald summation for medium to larger systems; though on very small systems simple Ewald summation may perform better.

In addition to the non-bonded interactions there are several bonded interactions that apply to all systems constituents that are bound to each other. The total bonded interaction on a given constituent is a sum of forces due to a bond stretching potential, angle potential, dihedral potentials and some cross term.

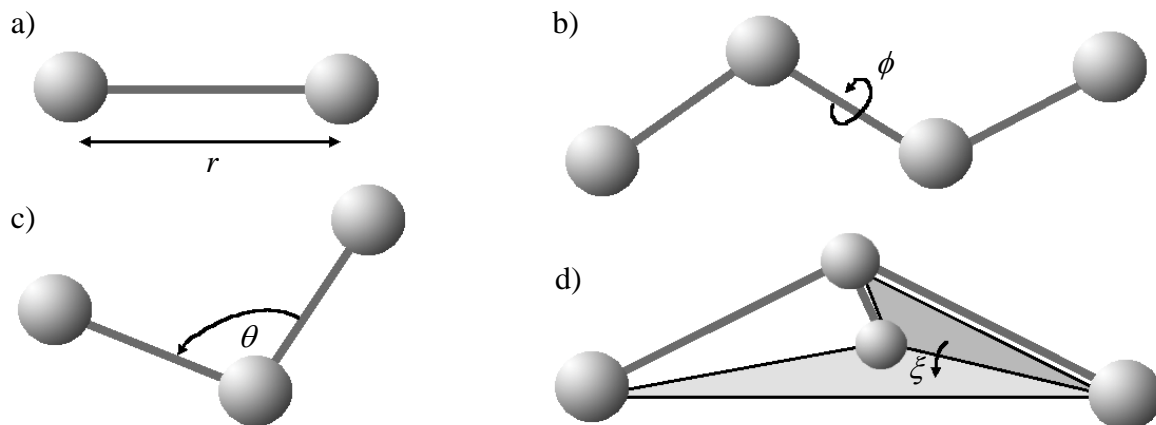


Figure 12. Naming conventions for the bonded interactions: (a) bond stretching, (b) proper dihedral angle, (c) bond angle, and (d) improper dihedral angle.

The bond stretching between two covalently bound atoms i and j is usually modeled by a harmonic potential

$$V_b(r_{ij}) = \frac{1}{2} k_{ij}^{b, \text{harm}} (r_{ij} - b_{ij})^2 \quad (34)$$

with $k_{ij}^{b, \text{harm}}$ being the bond stretch force constant and b_{ij} the equilibrium bond length. This potential results in a force given by

$$\mathbf{F}_i(\mathbf{r}_{ij}) = k_{ij}^{b, \text{harm}} (r_{ij} - b_{ij}) \frac{\mathbf{r}_{ij}}{r_{ij}} \quad (35)$$

To gain computing efficiency a fourth power bond potential is used within the GROMOS96 force field.^[79]

$$V_b(r_{ij}) = \frac{1}{4} k_{ij}^b (r_{ij}^2 - b_{ij}^2)^2 \quad (36)$$

The resulting force term becomes

$$\mathbf{F}_i(\mathbf{r}_{ij}) = k_{ij}^b (r_{ij}^2 - b_{ij}^2) \mathbf{r}_{ij} \quad (37)$$

The relation of this form of potential's force constant to the usual harmonic one is

$$2k_{ij}^b b_{ij}^2 = k_{ij}^{b,harm} \quad (38)$$

Most of the force constants are derived by this relation from the harmonic ones used in the GROMOS-87 force field.^[87] The gain in computing efficiency (no need for the evaluation of square roots) is paid for by a conceptually more complex design. One particular disadvantage is that due to the non-harmonic form the average energy of a single bond does not equal $\frac{1}{2}kT$ as one would expect for a usual harmonic potential.

The vibration of the bond angle between a triplet ijk of atoms is also usually represented by a harmonic potential with the equilibrium angle θ_{ijk}^0 :

$$V_a(\theta_{ijk}) = \frac{1}{2} k_{ijk}^{\theta,harm} (\theta_{ijk} - \theta_{ijk}^0)^2 \quad (39)$$

The corresponding forces on each atom can be derived by the chain rule:

$$\begin{aligned} \mathbf{F}_i &= -\frac{dV_a(\theta_{ijk})}{d\mathbf{r}_i} \\ \mathbf{F}_k &= -\frac{dV_a(\theta_{ijk})}{d\mathbf{r}_k} \quad \text{with} \quad \theta_{ijk} = \arccos\left(\frac{\mathbf{r}_{ij} \cdot \mathbf{r}_{kj}}{r_{ij} r_{kj}}\right) \\ \mathbf{F}_j &= -\mathbf{F}_i - \mathbf{F}_k \end{aligned} \quad (40)$$

Within the GROMOS96 force field a simplified function represents the angle vibrations:

$$V_a(\theta_{ijk}) = \frac{1}{2} k_{ijk}^{\theta} (\cos(\theta_{ijk}) - \cos(\theta_{ijk}^0))^2 \quad (41)$$

where now

$$\cos(\theta_{ijk}) = \frac{\mathbf{r}_{ij} \cdot \mathbf{r}_{kj}}{r_{ij} r_{kj}} \quad (42)$$

The corresponding forces can be obtained by partial differentiation with respect to the atomic positions. The relationship between the harmonic force constant $k_{ijk}^{\theta, harm}$ and the cosine form is given by

$$k_{ijk}^{\theta} \sin^2(\theta_{ijk}^0) = k_{ijk}^{\theta, harm} \quad (43)$$

A much more complicated temperature dependent relationship is given in the GROMOS96 manual^[79] but the formulas are equivalent at 0 K and show only minor deviations (about 0.1% to 0.2% at 300 K). Therefore, the use of this conversion is feasible for virtually all applications.

In addition to the pure bond and angle potentials two terms originating from crosstalk between the stretching of neighboring bonds (bond-bond cross term) and the stretching of bonds by angle deformation (bond-angle cross term) are included.^[88]

For three particles i, j and k forming bonds between i and j respectively k and j the bond-bond cross term is given by:

$$V_{rr'} = k_{rr'} \left(|\mathbf{r}_i - \mathbf{r}_j| - r_{1e} \right) \left(|\mathbf{r}_k - \mathbf{r}_j| - r_{2e} \right) \quad (44)$$

$k_{rr'}$ is the force constant, r_{1e} and r_{2e} are the equilibrium bond length of i - j and k - j respectively.

This correction potential results in a force

$$\mathbf{F}_i = -k_{rr'} \left(|\mathbf{r}_k - \mathbf{r}_j| - r_{2e} \right) \frac{\mathbf{r}_i - \mathbf{r}_j}{|\mathbf{r}_i - \mathbf{r}_j|} \quad (45)$$

on particle i . To obtain the force on particle k it is sufficient to interchange the indices i and k in (45). Because the sum of internal forces should be zero the force on particle j is given by the simple relationship

$$\mathbf{F}_j = -\mathbf{F}_i - \mathbf{F}_k \quad (46)$$

The bond-angle cross term for the same three particles accounting for the bond deformations occurring when the angle between the bonds i - j and k - j is changed is

$$V_{r\theta} = k_{r\theta} \left(|\mathbf{r}_i - \mathbf{r}_k| - r_{3e} \right) \left(|\mathbf{r}_i - \mathbf{r}_j| - r_{1e} + |\mathbf{r}_k - \mathbf{r}_j| - r_{2e} \right) \quad (47)$$

where $k_{r\theta}$ is the force constant r_{1e} and r_{2e} apply again to the equilibrium bond lengths and r_{3e} stands for the equilibrium distance between the non-bonded particles i and k . The force resulting on particle i is given by

$$\mathbf{F}_i = -k_{r\theta} \left[\left(|\mathbf{r}_i - \mathbf{r}_k| - r_{3e} \right) \frac{\mathbf{r}_i - \mathbf{r}_j}{|\mathbf{r}_i - \mathbf{r}_j|} + \left(|\mathbf{r}_i - \mathbf{r}_j| - r_{1e} + |\mathbf{r}_k - \mathbf{r}_j| - r_{2e} \right) \frac{\mathbf{r}_i - \mathbf{r}_k}{|\mathbf{r}_i - \mathbf{r}_k|} \right] \quad (48)$$

Proper dihedral angles are defined in compliance with IUPAC/IUB convention:^[89] ϕ is defined as the angle between the ijk and jkl planes, a ϕ of zero corresponds to the cis configuration (i.e., i and l are located on the same side). The proper dihedral potential function is given by

$$V_d(\phi_{ijkl}) = k_\phi (1 + \cos(n\phi - \phi_s)) \quad (49)$$

In order to keep planar groups (e.g., aromatic rings) flat improper dihedrals are introduced with an additional harmonic potential:


$$V_{id}(\xi_{ijkl}) = \frac{1}{2} k_\xi (\xi_{ijkl} - \xi_0)^2 \quad (50)$$

Since the potential is harmonic there will be a kink at some point of the potential when it also should exhibit a 360° periodicity. To prevent any problems that could arise of this the placement of the discontinuity is chosen at a distance of 180° from ξ_0 (i.e., as far away as possible from equilibrium configuration).

3 Substrate Treatment and Self-Organized Pattern Formation

3.1 Introduction

Micro and nanoscale patterning of surfaces is of importance in wide areas of research fields and applications including biology, material, and medical science. There are two main strategies in surface patterning: the top-down approach like e-beam lithography and the bottom-up approach that utilizes self-assembly and self-organization of molecules or simple basic building blocks in order to achieve regular structures. The main advantage of most top-down strategies is the precise control over the structuring process. Very delicate structures like those found in modern micro processors are implemented by means of typical top-down strategies like photo or UV-lithography and electron beam lithography. The disadvantage of most top-down strategies is that they are very elaborate and usually time consuming. Most bottom-up strategies that use self-assembly are much simpler and can often pattern over arbitrary sized areas during the process. Stripe patterning during LB transfer was observed in the early 1990's^[90] and later our group proposed an easy way of patterning large mica surfaces with regular stripe patterns with submicron resolution^[25]. Recently, mixed component transfers yielding luminescent stripe patterns^[91] or initiator patterns for polymer brushes^[92] could be shown. Many other applications were demonstrated for this self-organized patterning process. A full review can be found in the literature.^[27] Many more fields of application like chemical modification, etching and imprinting were opened up by switching to silicon substrates. It was observed that the periodicity of the stripe pattern was generally much smaller when using silicon substrates. Also due to the natural hydrophobicity of silicon additional cleaning and pretreatment steps were necessary in order to prepare the silicon and render it hydrophilic. This motivated us to systematically investigate the influence of different surface chemistry on the pattern formation by preparations of the substrate with different cleaning treatments.

* The work presented in this chapter is a direct continuation of my diploma thesis^[209] and was published partly ibidem and in a peer reviewed paper.^[208] 

3.2 Preparations of the Samples

Before transfer the Silicon substrates (2 x 5 cm²) were sonicated consecutively in a bath of chloroform, isopropanol and pure water (15 minutes each). Two different treatments were applied after this pre-cleaning procedure: Either 2 minutes of O₂-plasma etching at 1 mbar and 300 watts or 25 minutes in a mixture of ammonium hydroxide, hydrogen peroxide and pure water (ratio 5:1:1) known as RCA-1. The RCA-treated samples were sonicated in pure water for an additional 10 minutes after treatment. Both types of substrate were stored under pure water after treatment and used within one hour. The mica substrates used for the heating experiments were cleaved freshly and rinsed with purified water directly before transfer.

The general procedure for the preparation of self-organized DPPC patterns is already described extensively elsewhere^[27].

The LB-Transfers were conducted under clean room conditions (class 10.000). The subphase-thermostat was kept at 29 °C yielding a temperature of about 26 °C at the air-water interface. The room temperature was kept at 22 °C and humidity was constant at about 37%. After the DPPC-solution was spread onto the surface the solvent was allowed to evaporate for 10 minutes. The resulting monolayer was then compressed up to a lateral pressure of 6.0 mN/m and allowed to rest for another 20 minutes. The trough barriers were kept fixed during the actual withdrawal of the substrate. Therefore, the lateral pressure dropped down during the transfer resulting in a pressure gradient from top to bottom on the substrate, a technique later termed “continuously varying surface pressure” (COVASP) by other authors.^[93] The lateral pressure was recorded with respect to the dipper position to allow a reference of the position on the samples to a specific lateral pressure.

3.3 Pattern Formation on the Different Treated Substrates

After the preparation of the samples was completed AFM was used to investigate the LB-films. A typical result of our LB-transfers can be seen in Figure 13. When the lateral pressure during transfer is higher (here 3.5 mN/m) a homogeneous monolayer of DPPC will be transferred onto the substrate (top). As the pressure drops the monolayer will break up and channel-like structures will emerge, first parallel (not shown here), then perpendicular to the withdraw direction (second from top). The channels parallel to the withdraw direction vanish with further decrease in lateral pressure and the perpendicular channels become very regular

(middle) before the pattern becomes irregular again and the condensation stops (lower two). This general behavior for different pressure ranges is observed on all samples and is in good agreement with the previous work.^[27]

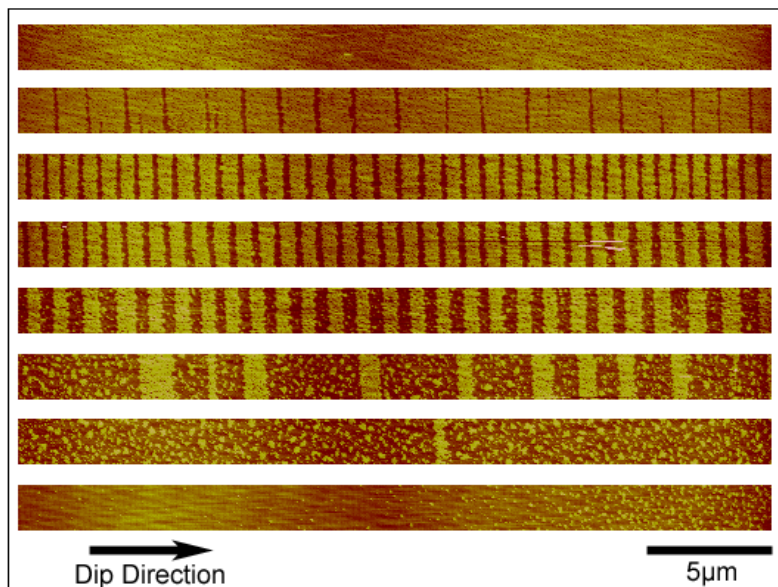


Figure 13. AFM-micrographs of different areas on a silicon surface (plasma treated) after LB-transfer with a transfer speed of 32mm/min. The corresponding lateral pressures from top to bottom are: 3.5 mN/m, 3.0 mN/m, 2.5 mN/m, 2.3 mN/m, 2.0 mN/m, 1.5 mN/m, 1.0 mN/m and 0.5 mN/m.

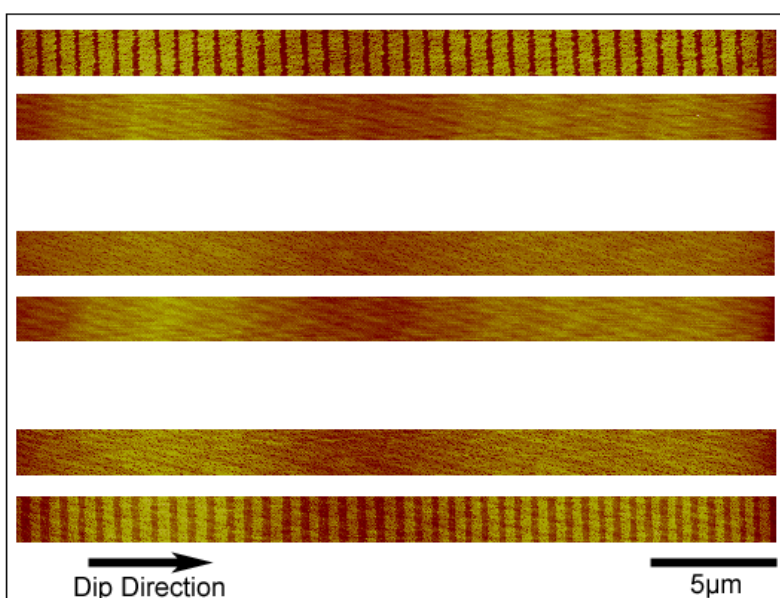


Figure 14. Direct comparison of transferred monolayers on plasma-treated (in each case upper image) and RCA-treated (in each case lower image) at same transfer pressures. The transfer pressure was 2.5 mN/m for the upper images, 3.5 mN/m for the middle images and 5.0 mN/m for the lower ones. Transfer speed was 32mm/min for all images.

In a direct comparison to the plasma-treated substrates the whole pattern formation is shifted towards higher lateral pressures on the RCA-treated substrates. The upper picture in Figure 14 shows the samples at a lateral pressure of 2.5 mN/m. There is a regular stripe pattern formed on the plasma-treated substrate but no visible condensation at all on the RCA-treated substrate. In the middle images the lateral pressure is 3.5 mN/m. Here the monolayer on the plasma-treated sample is almost compact already (except for some lines parallel to the withdraw direction) whereas the RCA-treated still shows no visible condensation. Finally, in the lower pictures ($p = 5.0$ mN/m) the stripe patterning on the RCA-treated substrate is very regular whereas the monolayer on the plasma-treated sample is absolutely compact. Table 1 summarizes the pressure ranges for stripe patterning on the different treated substrates and for different withdrawal speeds. The transfer pressure at which the stripe patterning starts is for all withdraw speeds about 2.5 mN/m higher on the RCA-treated sample than on the plasma-treated. Also the transfer pressure at which the transition to a compact monolayer occurs is about 2.0 mN/m to 2.4 mN/m higher on the RCA-treated samples as compared to the plasma-treated.

Table 1. Transfer pressure ranges for patterning on different treated substrates and for different withdrawal speeds.

Transfer speed (mm/min)	16		32		64	
Treatment	Plasma	RCA	Plasma	RCA	Plasma	RCA
Pressure (mN/m) at						
Start of patterning	1.3	3.7	1.5	4.1	1.7	4.3
Most regular pattern	2.0	4.2	2.3	5.0	2.5	5.2
Transition to compact monolayer	2.7	4.7	3.3	5.7	3.7	5.9

The pressure drop graphs are recorded during the transfer to enable a correlation of certain positions on the samples with the momentary transfer pressure. They can also be used to quantify the amount of material transferred onto the substrates. Figure 15 shows a typical transfer pressure versus sample position graph used to derive the transfer pressure at a given sample position during AFM measurements. The current lateral pressure and the relative dipper position are recorded by the LB trough control software during transfer. The point of no further decrease of the lateral pressure corresponds to the bottom of the sample because from this point on there is no more transfer of DPPC onto the sample (sample left water phase

completely). By adjusting the recorded relative dipper position to zero at this point and plotting the pressure data against the adjusted position we obtain the desired graph that gives us information about the current transfer pressure on a given sample position.

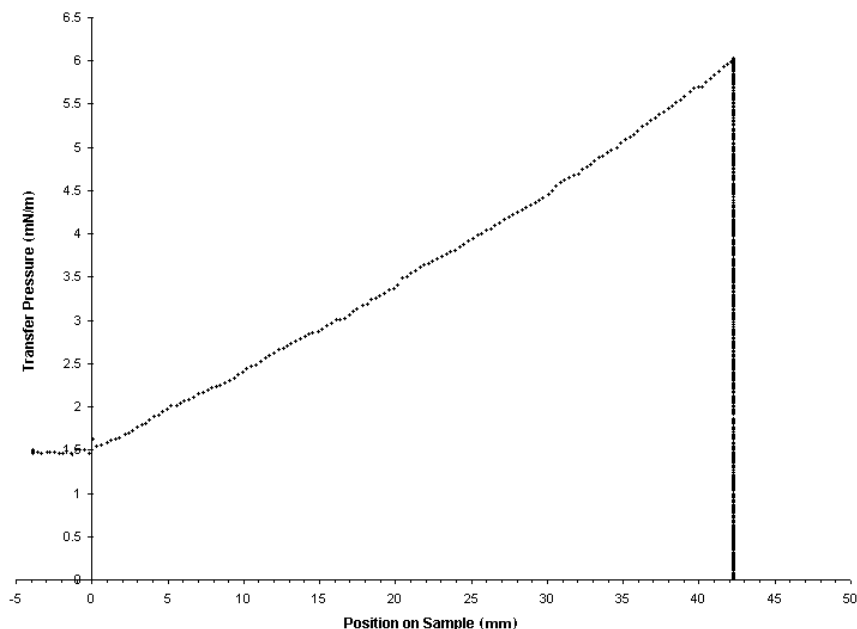


Figure 15. Typical transfer pressure vs. sample position graph.

The amount of transferred material (indicated by the slope of the surface pressure vs. dipper position graph) stays almost constant over the whole transfer, although it decreases a bit at lower surface pressures. The average slope is a little bit higher on plasma treated samples for all transfer speeds (Table 2) indicating a slightly higher DPPC transfer compared to RCA treated samples. Note that there is still transfer of DPPC onto the substrate in areas where there is no DPPC film visible on the sample by AFM. This is explained by two different phases on the substrate (see discussion).

Table 2. Average slopes of transfer pressure vs. dipper position graphs at different transfer speeds.

Transfer speed (mm/min)	Plasma	RCA
	slope (N/m ²)	Slope (N/m ²)
16	0.144	0.128
32	0.111	0.107
64	0.133	0.119

When we consider the periodicity and the width of stripes and channels with respect to the transfer pressure there is also a common trend visible at all transfer speeds regardless of the substrate treatment. Figure 16 shows this behavior for a plasma treated substrate and a transfer speed of 32 mm/min (a) and for the same transfer speed on a RCA treated sample (b). The width of stripes increases whereas the width of channels decreases with increasing transfer pressure. This yields a minimum in the periodicity (about 800 nm for plasma treated and 750 nm for RCA treated samples at this transfer speed). The most regular stripe pattern occurs for all transfer speeds and for both treatments always at the respective minimum in periodicity.

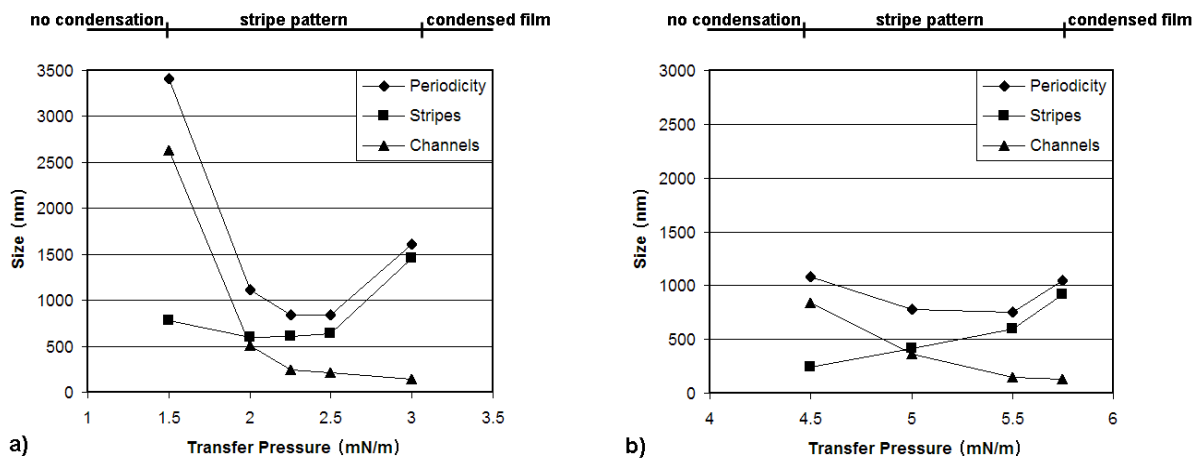


Figure 16. Periodicity stripe and channel width at a transfer speed of 32mm/min with respect to transfer pressure for (a) plasma treated and (b) RCA treated samples.

3.4 Surface Energy Measurements

As a first step to understand the cause of the difference in pattern formation on the differently treated substrates surface energy consideration were done. The surface energies of the naked different treated substrates were determined by a modified sessile drop method as proposed by Schultz et. al.^[94,95]. The static contact angles of droplets of pure water under a bulk phase of different alkenes (hexane, octane, decane, hexadecane) were measured with a commercial instrument (Contact Angle Measuring System G2, Krüss). The surface energy for cleaved mica was also determined in the same fashion for comparison and to confirm validity of the current method. The results are presented in Table 3. The surface energy of mica was determined to check the validity of our measurements and is in good agreement with literature. Regardless of treatment the silicon samples were shown to have lower surface energies than

mica (especially the non-polar part γ_s^D which is one half for RCA treated and one tenth for plasma treated).

Table 3. Surface energies of the different substrates.

	γ_s^D (mN/m)	γ_s^P (mN/m)	γ_s (mN/m)
Mica	33.3 ± 3.0	89.7 ± 0.8	123.0 ± 3.8
Mica (Schultz et. al.) ^[95]	30 ± 2.5	90	120 ± 2.5
Silicon (Plasma)	3.2 ± 1.5	85.1 ± 0.4	88.3 ± 1.9
Silicon (RCA)	17.4 ± 2.5	88.1 ± 0.6	105.5 ± 3.1

The trend in the observed surface energies for the differently treated silicon samples is in compliance with the higher density of OH groups on the RCA-treated surfaces^[96] that should yield a higher surface energy as compared to the plasma treated ones.

3.5 Effect of Sample Heating

We proposed that micro water films on the substrate surface may play a crucial role to influence the pattern formation. To test this notion subsequent heating of mica substrates covered with DPPC patterns was conducted for 1 h at 80°C in a dry (~0% RH) or wet (~100% RH) environment. Typical results are shown in Figure 17.

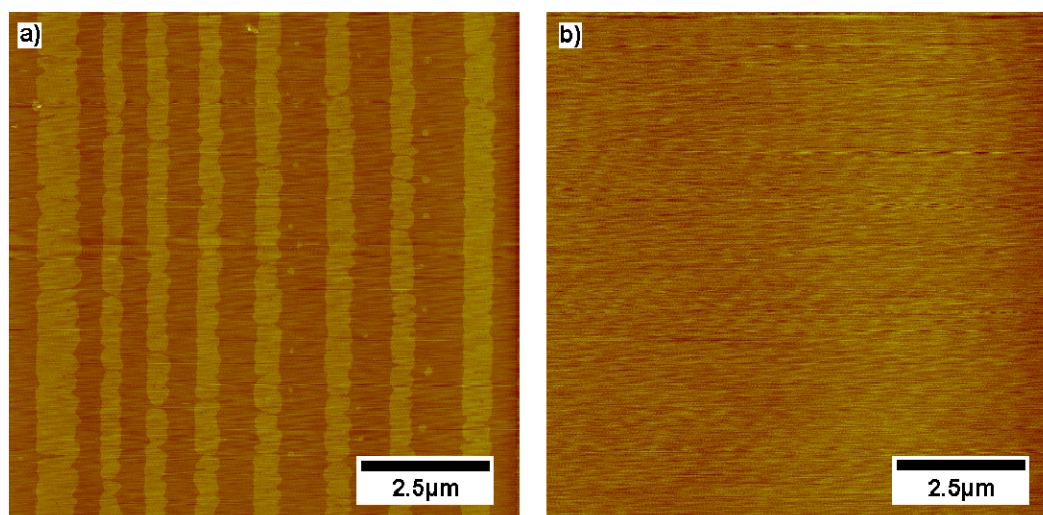


Figure 17. Patterned mica substrate after heating for 1h at 80°C in (a) dry environment (b) wet environment.

The pattern survives heating in a dry environment whereas the topography pattern is destroyed by heating in a wet environment. Note that the effects seen here are not due to diffusion of the DPPC molecules under the wet conditions: in the case of mixed transfer dye patterns (where the DPPC molecules in the channels are labeled by fluorescent dye) the fluorescent pattern remains unaltered although the topography pattern is destroyed. The images in Figure 18 show such a sample with a fluorescent stripe pattern on mica consisting of alternating DPPC LC/LE stripes and a fluorescent dye in the LE phase stripes (preparation details of fluorescent stripes can be found in the literature^[91]). After preparation the sample was cut into three pieces of which two were heated to 80 °C for 1 h, one in a dry oven (~0% RH), the other in a closed Petri dish with abundant water for yielding high humidity (~100% RH) but without liquid water coming in direct contact with the sample. The third part of the sample was kept untreated for reference.

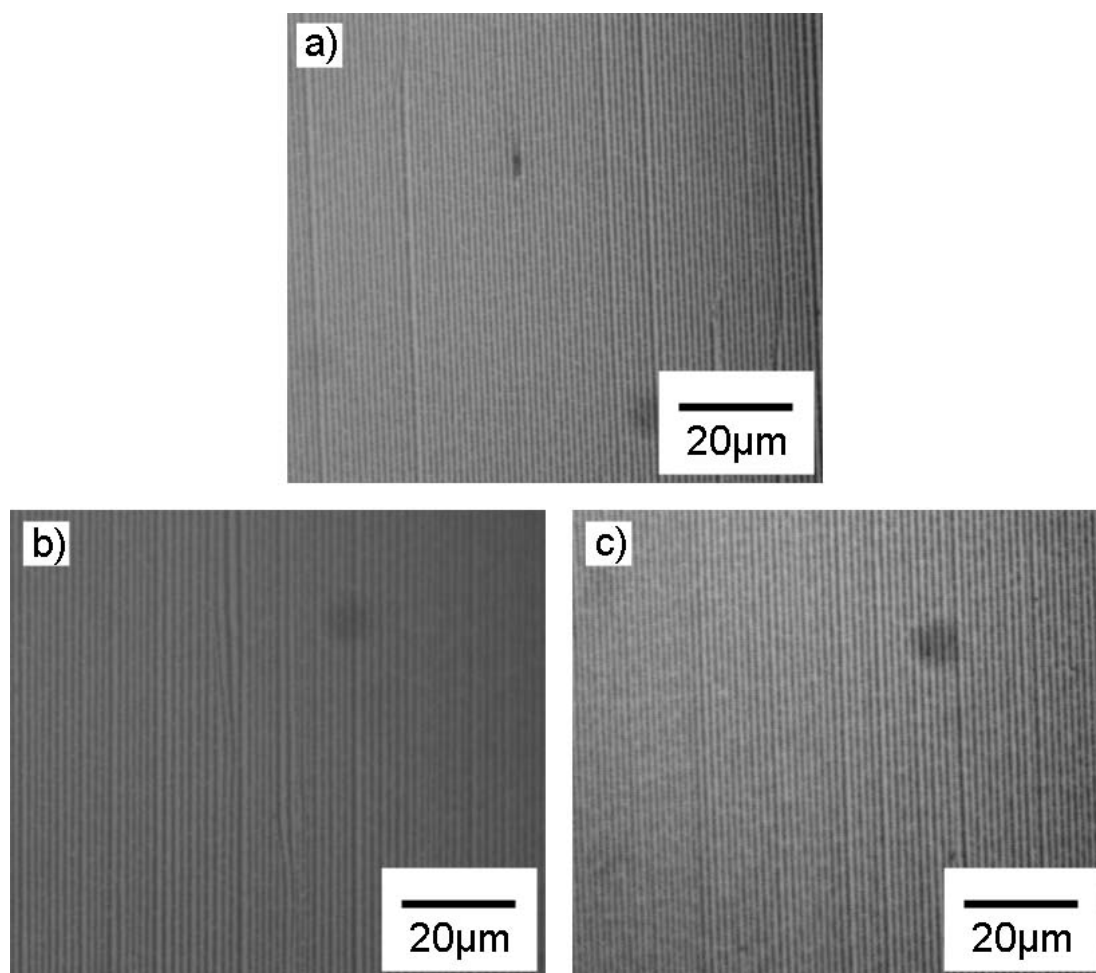


Figure 18. Fluorescence microscope images of (a) untreated DPPC pattern, (b) sample heated in dry environment, and (c) sample heated in humid environment.

Although the topography of the pattern was totally destroyed for the sample heated under humid conditions (Figure 17), there is no visible change in the luminescence pattern between the untreated sample (a), the sample heated in dry environment (b), and the sample heated in humid environment (c). This implies a phase change of the DPPC film during heating in humid conditions rather than diffusion on the sample, which should result in a disturbed fluorescence pattern, too. Therefore, it can be concluded that individual DPPC molecules remain more or less in place during heating. The DPPC film appears to undergo a phase transition (from a liquid condensed phase to a liquid expanded phase) rather than diffuse.

3.6 Discussion

In order to understand the experimental findings we utilize a model of equivalent states as proposed by Peterson^[97]. He and his co-workers separate the surface pressure into an interfacial term that describes the interaction between the monolayer and the substrate and an internal pressure term. Thus, the total surface pressure experienced by a monolayer will change during transfer onto substrates depending on the difference in monolayer-substrate interfacial energy. In our experiments all transfers are conducted at transfer pressures lower than the critical pressure for the DPPC monolayer to undergo the phase transition from a liquid expanded (LE) to condensed phase. Assuming a sufficiently higher interfacial mediated pressure between the monolayer and silicon compared to that between the monolayer and water, it follows that there is a condensed phase monolayer on the substrates at sufficiently high transfer pressures although the monolayer is in LE phase on the water before transfer. At low transfer pressures the difference in the interfacial pressure is not sufficient to evoke the phase transition so the LE phase is present on the silicon substrate after transfer. We assume that the LE phase is normally not visible with AFM under ambient conditions due to a lack of contrast. The recorded drop in surface pressure during transfer indicates ongoing transfer of DPPC even in areas of the sample where there is no AFM observable DPPC layer and supports this notion. Additional XPS measurements* showed an almost uniform average concentration on the whole sample. The pressure shift ~ 2.5 mN/m between the RCA and plasma treated silicon substrates indicates a higher interfacial mediated pressure on the plasma treated silicon. The trend of increasing pressure p_c for phase transfer $p_{c,\text{water}} > p_{c,\text{RCA}} > p_{c,\text{Plasma}}$ fits well to what one would expect from chemistry. Since RCA-treated silicon exhibits

* done by Dr. Andreas Schäfer (nanoAnalytics GmbH)

more hydroxyl groups on the surface than plasma treated^[96] it should adsorb more ambient water vapor and interact more “water-like” with the DPPC film. This behavior can not be explained by examining only the respective surface energies alone. The explorative heating experiments shed light on the influence of thin water films in the micro to nanometer range on the pattern formation process. They indicated a water film is crucial for the potential of phase transition of the DPPC film. Another possible explanation for the differences between plasma and RCA-treated substrates may relate to the amount of water adsorbed on the surface during LB transfer although in all cases there is no water visible to the naked eye.

The results also have some interesting implications on the supposed mechanism for the stripe patterning. The stripes parallel to transfer direction occurring at high transfer pressures can be explained by the Maragoni Effect fingering instabilities and were successfully modelled.^[52] The exact cause for the stripe patterns perpendicular to the transfer direction is yet unclear as the proposed stick-slip-models need to introduce some ad-hoc assumptions to account for these patterns. The results presented here strongly suggest that the channels separating the stripes are not bare substrate but rather filled with DPPC in LE phase while the stripes are DPPC in condensed phase (Figure 19b). The areas transferred at lower transfer pressure than necessary for pattern formation are covered completely with LE phase (Figure 19a). This conclusion has been supported recently by direct AFM observation of different height steps in stripe pattern defects.^[98] This implies that models that employ pressure oscillations at the meniscus^[99] may account for this behavior.

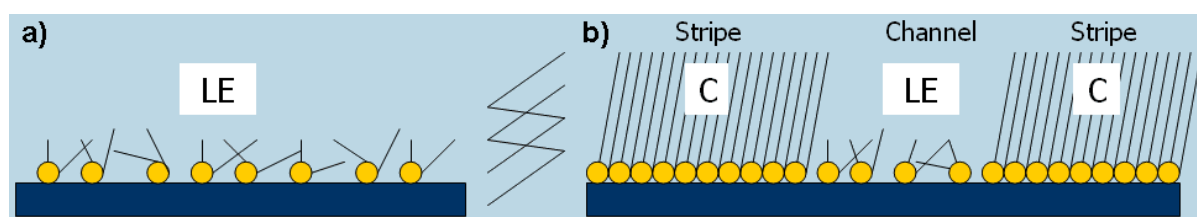


Figure 19. Scheme of DPPC Langmuir Blodgett film on a substrate transferred (a) at very low pressure (b) at a higher pressure suitable for stripe pattern formation.

3.7 Conclusion

In this chapter a systematic study of the influence of substrate treatment on DPPC stripe pattern formation was performed. The results obtained can be explained in terms of equivalent states. The data gives some interesting insights into stripe pattern formation and strongly

suggests an alternating LE / LC phase sequence as the pattern morphology. This should lead to more detailed consideration of meniscus pressure oscillation models for stripe pattern formation. Furthermore, this work motivates future experiments to investigate the experimental parameters surrounding stripe pattern formation on other substrates (e.g., gold or other metal films or polymers), because in this study experimental parameters were shown to play a major role in pattern formation on different surfaces. Also the role of the micro or nano water films was shown to influence pattern formation and should be taken into account by performing experiments with humidity controlled transfers.

4 A Device for Rotational Langmuir-Blodgett Transfer

4.1 Introduction

Substrate-bound molecular gradients (chemical gradients) obtained in a well-controlled fashion offer an *in vitro* model to study the biological phenomena that occur *in vivo*, for instance, axon guidance, cell signaling, and proliferation.^[100] It has been demonstrated that chemical gradients on surfaces can influence the function and development of cells, biological recognition, and interaction.^[101,102] Different approaches to produce chemical gradients on surfaces have been reported, for instance, microfluidic systems,^[103-105] controlled diffusion of reactive substances,^[106-108] and microcontact printing.^[109-111] Similarly, generating continuous gradient micro/nanostructures on surfaces (topographical or pattern gradients) would be interesting for the study of cell motility and adhesion, cell mechanotransduction,^[112] and micro/nano analysis systems.^[113] However, the fabrication of structure gradients on surfaces has been much less frequently addressed than that of concentration gradients. This can be explained with the difficulty and expensiveness of fabricating continuous-gradient micro/nanostructures on surfaces over the distances required for biological studies (at least a few hundred micrometers) on the basis of only top-down techniques, e.g., scanning probe lithography^[114] or optical lithography.^[113] This inspires the search for bottom-up techniques based on self-assembly due to their simplicity, high yield, and ease of implementation over large areas.^[8,115] Here we report a simple yet novel method based on the Langmuir-Blodgett (LB) technique to achieve a continuous gradient mesostructure in a well-ordered fashion over large areas. The key improvement over the standard LB transfer technique is the transfer of a monolayer onto a solid substrate by rotating the substrate rather than vertically pulling the substrate. As a result, LB patterns with different dimensions and orientations that depend on the transfer velocity^[52,116] can be generated simultaneously. The varying orientation of the three-phase contact line during rotating transfer opens up opportunities for complex patterning not achievable solely by transfer speed variations (COVASP^[93]) principally capable of yielding gradient structures, too. These new possibilities can also be interesting for

* The work presented in this chapter was done together with Dr. Xiaodong Chen who also performed the experiments to test the capability of complex patterning with the rotational Langmuir-Blodgett transfer. The results were already published^[128] and a patent for the method has been filed (GB 2444036 A).



other patterning methods depending on the orientation of the three-phase contact line, e.g., in the patterning of nanocrystals by LB-transfer.^[41,42,117]

4.2 Conventional and Rotational Langmuir-Blodgett Transfer

The typical geometry during LB-transfers is shown in Figure 20a: a substrate is fixed in a sample holder and can be moved up and down in z-direction.

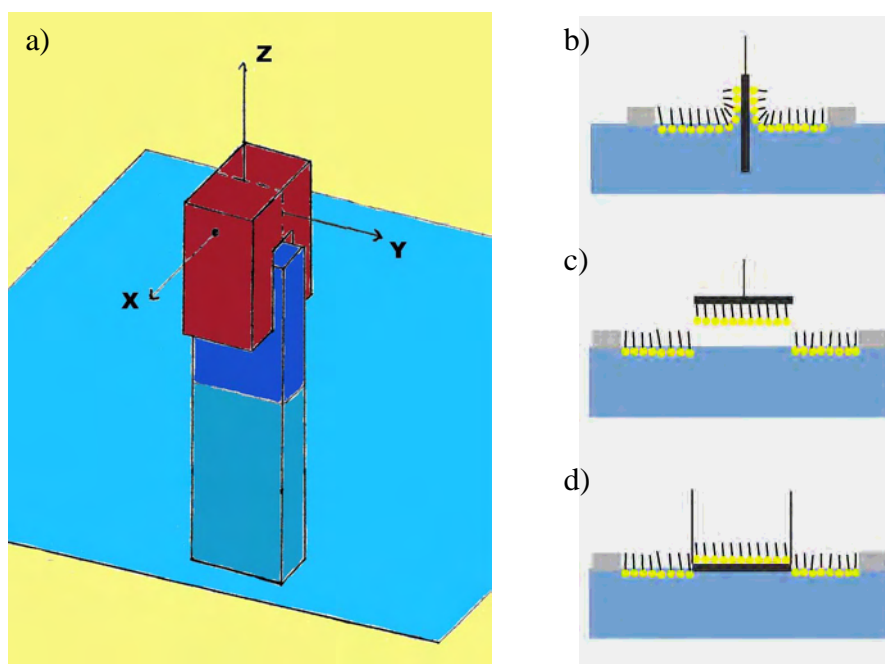


Figure 20. Typical geometry during LB-transfers: (a) definition of axes, (b) conventional Langmuir-Blodgett transfer, (c) Langmuir-Schaefer transfer, (d) horizontal scooping-up transfer.

This setup gave rise to three widespread modes for the transfer of a floating monolayer to a solid substrate. The first one and by far the most common mode (Figure 20b) is the conventional vertical transfer introduced by *Blodgett* and *Langmuir*^[32-34] where a hydrophilic substrate is withdrawn from a fluid subphase, dewetting at the three-phase contact line where the floating monolayer is transferred onto the substrate. In a variation of this method hydrophobic substrates can be used to transfer the monolayer during the downstroke of the substrate. Multilayers can be transferred by repeating up and downstrokes with the accompanying film transfer as desired. The second transfer method the horizontal lifting transfer (Figure 20c) also termed Langmuir-Schaefer transfer, was introduced by *Langmuir* and *Schaefer*.^[118] Here a flat hydrophobic substrate is placed parallel to the air-subphase interface covered by the monolayer. Then the substrate is lowered to the point of touching the

floating monolayer. Finally it is withdrawn together with the monolayer which is now attached to the substrate. The third less often used method is the horizontal scooping-up method (Figure 20d). A hydrophilic substrate is submerged into the subphase into a position parallel to and just beneath the air-subphase interface before the monolayer to be transferred is spread. For the transfer the substrate is either slowly raised through the monolayer allowing the subphase to flow off or the subphase level is decreased by suction or evaporation until the substrate emerged completely. Which way of transfer has to be favored depends strongly on the monolayer to be transferred, the substrate properties, and the desired film morphology.

All three transfer methods described above rely on the movement of the substrate along the z -direction. Our approach for the creation of gradient and more complex patterns by rotating LB-transfer incorporates another degree of freedom: the substrate is rotated along the x -axis (i.e., the axis parallel to the air-subphase interface and perpendicular to the substrate). This yields on the one hand a varying velocity field over different areas of the substrate and on the other hand a changing alignment of the three-phase contact line in regard to the substrate in the course of the transfer. To clarify these new features we will discuss the geometrical conditions of this setup.

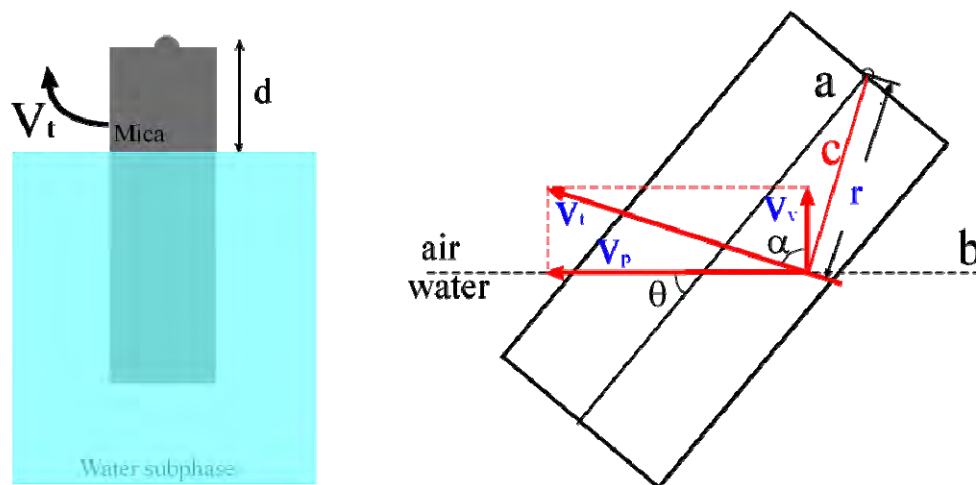


Figure 21. Geometric setup of the rotating LB transfer and naming conventions.

The basic geometric setup during a rotating transfer and naming for all entities relevant to the discussion is given in Figure 21. The rotation speed v_t and the distance d of the rotational axis from the air-subphase can be chosen by the experimenter. Since the pattern formation in our system is dependent on the vertical withdrawal speed v_v we should consider the split up of v_t in its components vertical and parallel to the three-phase contact line.

$$v_t = 2\pi \times \omega \times r \quad (51)$$

$$v_v = v_t \cos \alpha \quad (52)$$

The angle α at a given position with the distance r to the rotational axis is determined by geometrical relations as

$$\alpha = \arctan\left(\frac{d}{\sqrt{r^2 - d^2}}\right) \quad (53)$$

The key parameter for the alignment of the pattern (which emerges in our system as stripes either parallel or perpendicular to the three-phase contact line) is defined by the angle θ between the sample and the three-phase contact line at a given position on the sample. Along line a the angle θ is given by the simple expression

$$\theta = \arcsin\left(\frac{d}{r}\right) \quad (54)$$

θ will be constant along line b (i.e., the three-phase contact line). To get an impression of the overall distribution of v_v and θ on the sample we developed a simulation program that plots color maps based on the given substrate dimensions and the chosen setup for d and rotation speed.

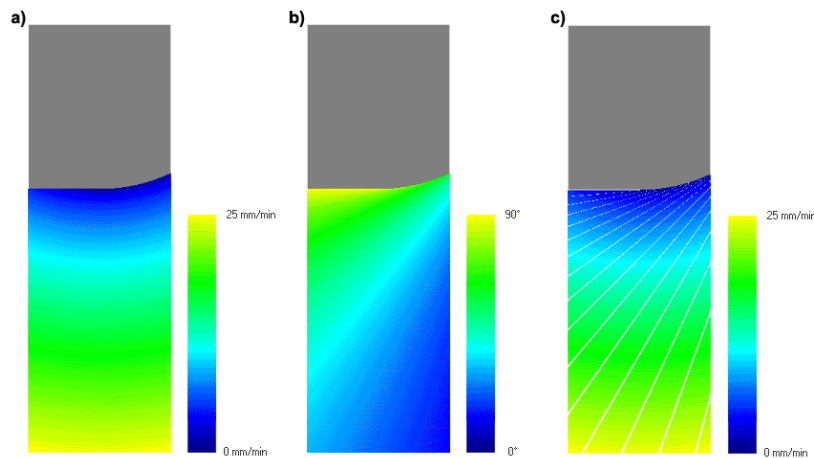


Figure 22. Simulation of the (a) velocity field for v_v , (b) angle field for θ and (c) velocity field with overlaid lines of same θ (i.e., three-phase contact line). Sample width 20 mm, length 60 mm, $d = 22$ mm and a rotation speed of 0.07 rpm.

Figure 22 shows color maps for a typical setup. In this case vertical speeds from 0 mm/min up to 25 mm/min occur (Figure 22a). The pattern alignment in the case of a line pattern emerging parallel to the three-phase contact line is denoted in Figure 22c by an overlay of white lines with same θ .

4.3 Description of the LB Rotator

Figure 23 shows the actual LB rotator sample holder prototype.

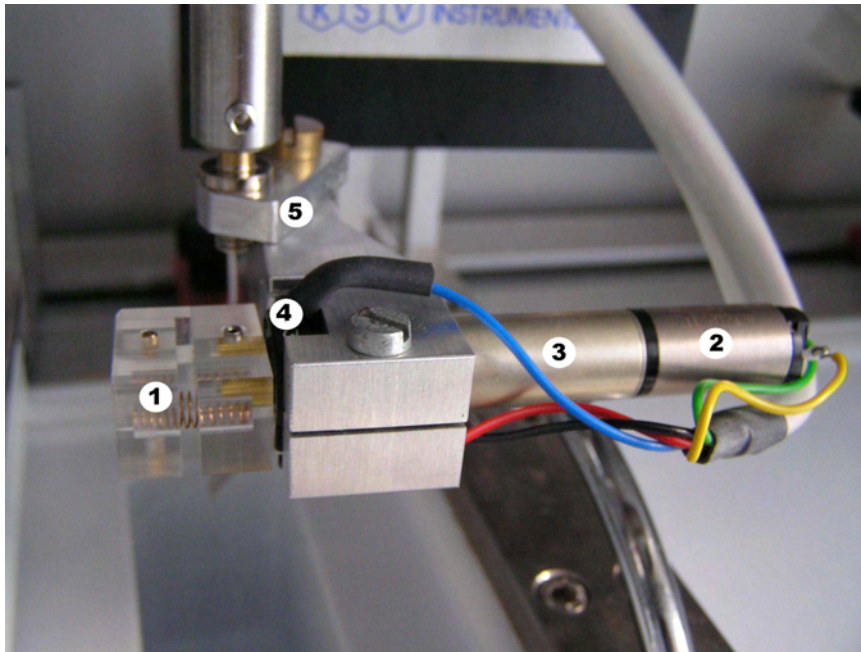


Figure 23. Close up of the LB Rotator: (1) sample holder clamp, (2) DC motor, (3) gears, (4) angular position control, and (5) frame and connector to conventional dipper.

The LB rotator consists of the following main parts: the sample holder clamp (1) is made from plexiglass and is connected by a strong spring that enables a secure and stable fixing mica substrates as well as heavier silicon substrates. The DC motor (2), a very smooth running electric motor (Faulhaber 1224 012 S), is connected with a high reduction gear (3) (Faulhaber 12/3, reduction 68,608:1) yielding the very low rotational speeds needed for our system but still assuring a very smooth movement not achievable by step motors. The angular position control (4) consists of a potentiometer that generates a voltage drop proportional to the angular position of the sample holder clamp that can be evaluated by the control interface. The frame (5) holds together all pieces of the LB rotator, guarantees for a decent damping of

4 A Device for Rotational Langmuir-Blodgett Transfer

vibrations, and connects the whole device to the conventional z-direction LB dipper allowing a convenient positioning of our LB rotator in a conventional commercial LB trough setup.

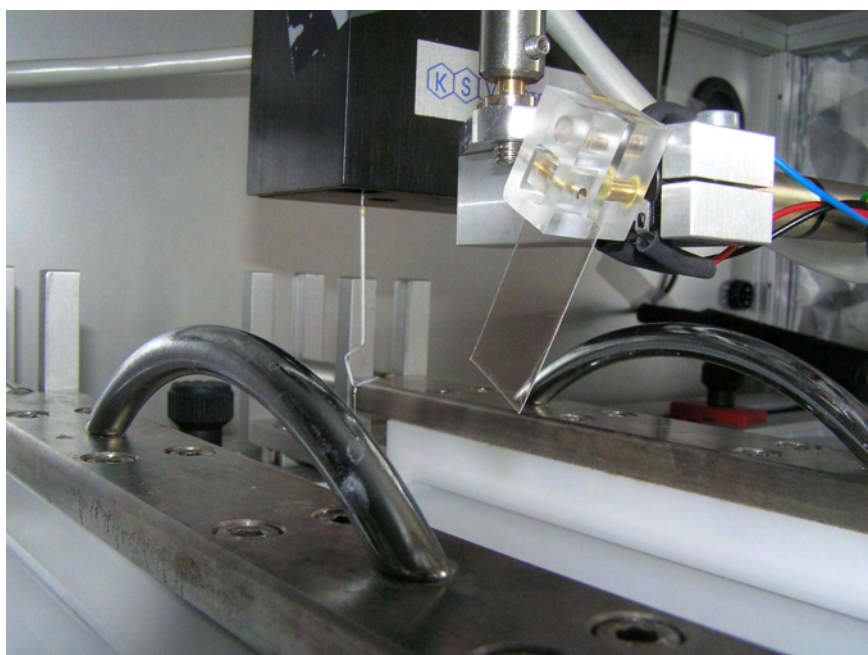


Figure 24. LB rotator attached to commercial LB trough with a clamped mica sample.

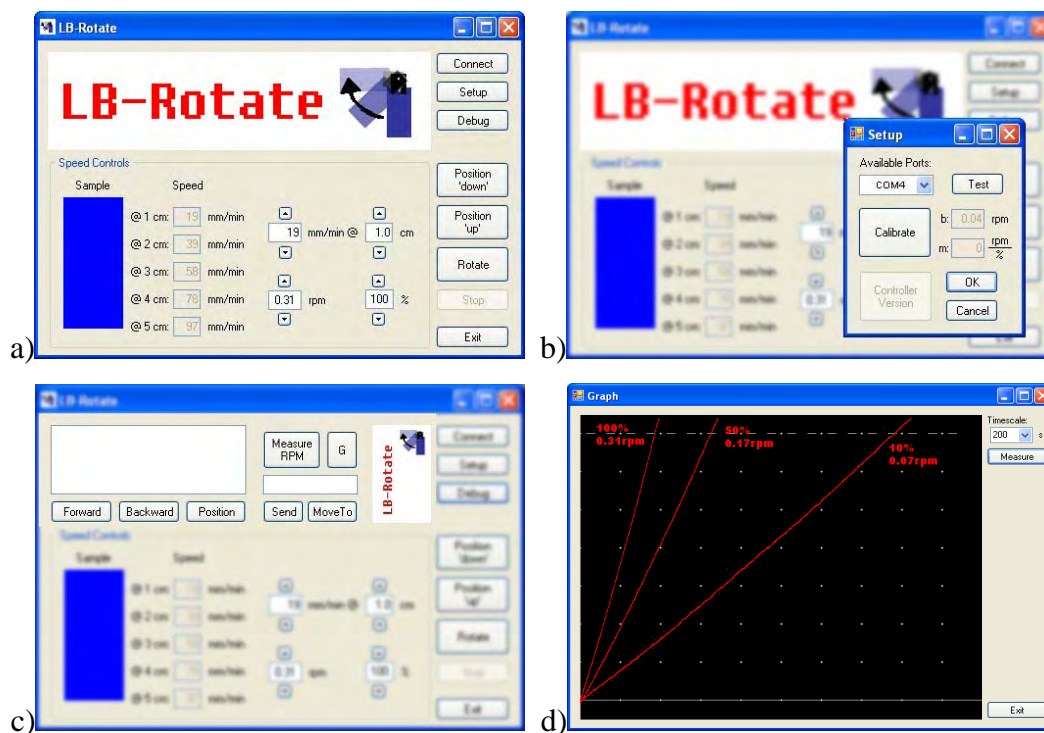


Figure 25. The interface software used to control the LB rotator: (a) control-mode, (b) setup-mode, and (c), (d) debug-mode.

The whole device is connected to a standard personal computer by a commercial interface that can digitize voltages (for the angular position control) and generates the pulse width modulation (PWM) signal needed for the speed control of the electric motor. The control software is written in Visual Basic (the programming environment was Microsoft Visual Studio 2005) and is split into three parts: control, setup and debug-mode (Figure 25).

In the control-mode one can set the rotation speed of the sample in specified distances from the rotation axis or in rotations per minutes. The dipper can be moved to defined positions “up” (sample parallel to the air-water surface) and “down” (sample perpendicular to the air-water surface) and the dipping process can be initiated by control buttons. In setup-mode one can choose the COM port for connecting the rotator interface, test this connection, and run the calibration to get the required values to calculate the speed readings in control mode. In debug-mode one has direct access to the actual angular position and one can move to any desired position and measure the actual rotation speed as well as record graphs of the position versus time to check the rotator’s status.

4.4 Demonstration Experiment Results and Discussion

We use the transfer of a mixed DPPC/NBD (2 mol%) monolayer as a model system to demonstrate the feasibility of LB rotating transfer for complex patterning and to test our theoretical consideration. We chose this system because it is already known to yield large area luminescent patterns easily observed by fluorescent microscopy^[91] which would be needed to check the complex pattern generated by LB rotating transfer extending over the whole substrate. The mixed monolayer was transferred onto mica at a surface pressure of 2 mN/m with an angular velocity of 0.07 rpm. The obtained sample was measured by a fluorescence microscopy (Olympus BX41). According to the principle of LB rotating and the mechanism for DPPC stripe pattern formation we can expect a pattern similar to Figure 26 (generated by the simulation software mentioned above).

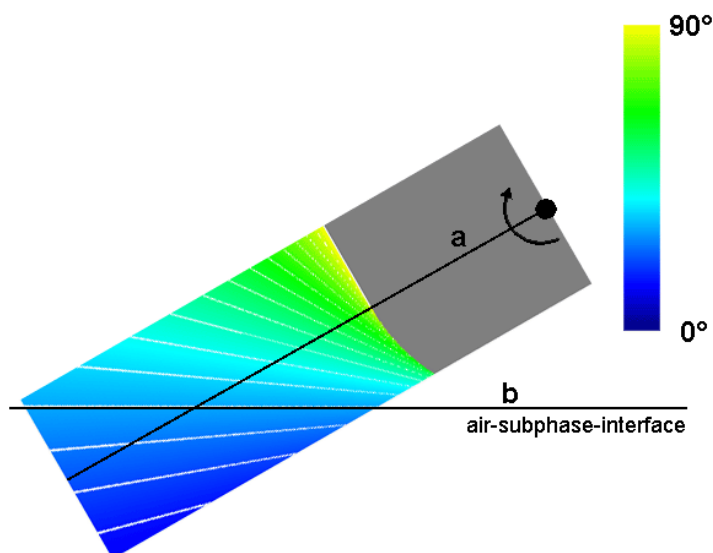


Figure 26. Scheme of the expected pattern generated by the experiment and definition of line a and b. The color map shows the local θ angle, white lines denote the local stripe pattern direction.

However, it is not feasible to measure all the points on the whole substrate. Therefore, we select two typical scenarios. One scenario is the points along line a. In this case, θ is equal to α , i.e., line a and line c (of Figure 21) are superposed and θ is changing with the position on line a. The second scenario is the points along line b. Here θ stays constant but α (and therefore also v_v) is different for different points.

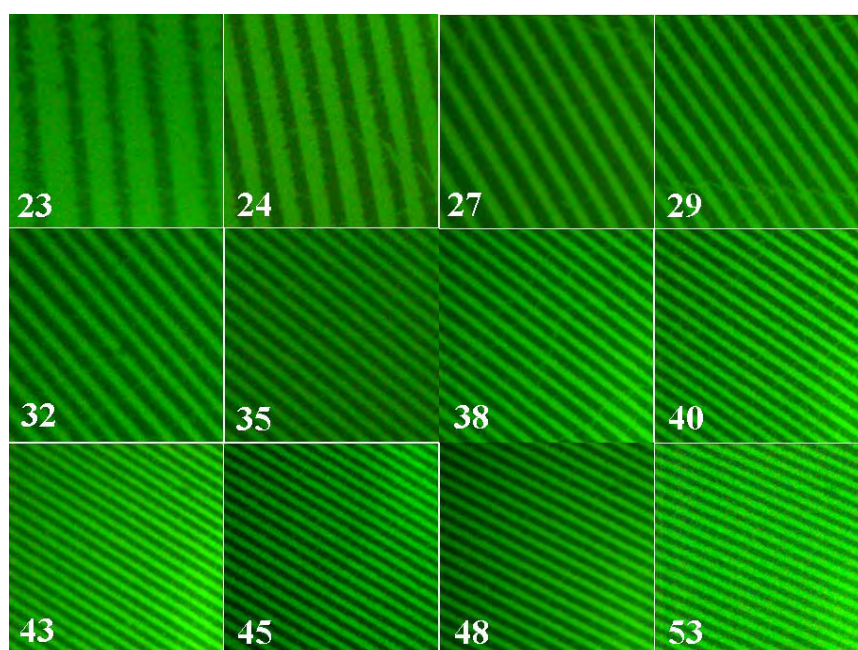


Figure 27. Fluorescence microscopy images ($30 \times 30 \mu\text{m}^2$) for the pattern along line a. The number in the images denotes the distance to the rotational axis in mm.

Figure 27 illustrates the fluorescence microscopy images of gradient stripe patterns along line a. The changing alignment of the pattern with increasing distance r from the rotational axis is clearly visible. Additionally, the lateral width of the stripe pattern decreases with increasing r (which also means increasing v_v). The angle of θ was determined for the different points on line a. The experimental data for the relationship between θ and r is shown in Figure 28a, which could be fitted well by the theoretical expectation derived from Formula (54). Figure 28b and c summarize the lateral width of the luminescent stripes, the dark stripes and the overall periodicity as a function of radius r and vertical transfer velocity v_v . One observes that the lateral width of luminescent stripe and the periodicity strongly depend on the radius, mono-exponential decreasing with the radius increasing. In other words, the pattern was gradient rather than repetitive in a substrate which is different to the stripe pattern published before.^[25,91,116,119-121]

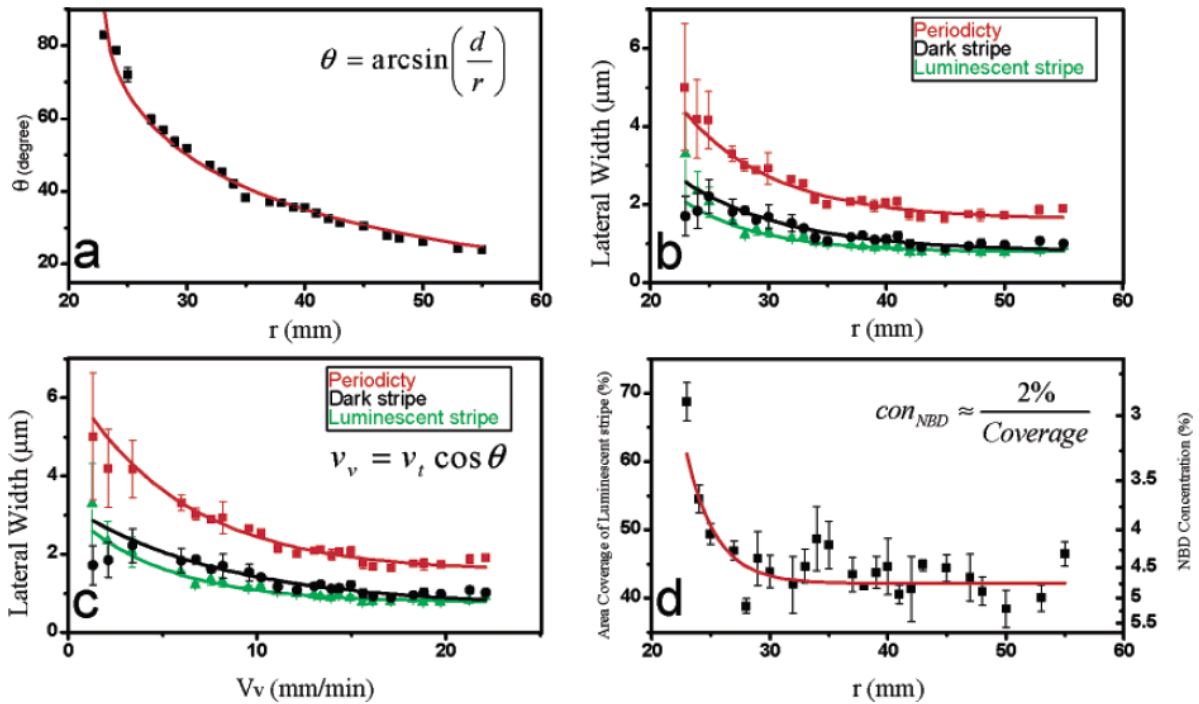


Figure 28. (a) Dependence of θ on the radius with fit from Formula (54). (b) Dependence of the lateral width of the luminescent stripe and dark stripe and periodicity of the gradient pattern on the radius and (c) linear velocity perpendicular to the three-phase contact line. (d) Area coverage of the luminescent stripe and NBD concentration as a function of the radius. All data in b-d is fitted by mono-exponential decay.



Figure 29. Fluorescence microscopy images ($30 \times 30 \mu\text{m}^2$) for the pattern along line b ($\theta = 35^\circ$). The number in the images denotes the distance to the rotational axis in mm.

Fluorescence microscopy images of gradient stripe patterns along line b for an angle of $\theta = 35^\circ$ are shown in Figure 29. The dependence of lateral width on the radius r (or v_r) is more complicated (as compared to the latter case along line a). Primarily, the lateral width decreases with the radius increasing. However, at some point the lateral width tends to increase with the radius increasing yielding an additional gradient in the overall pattern.

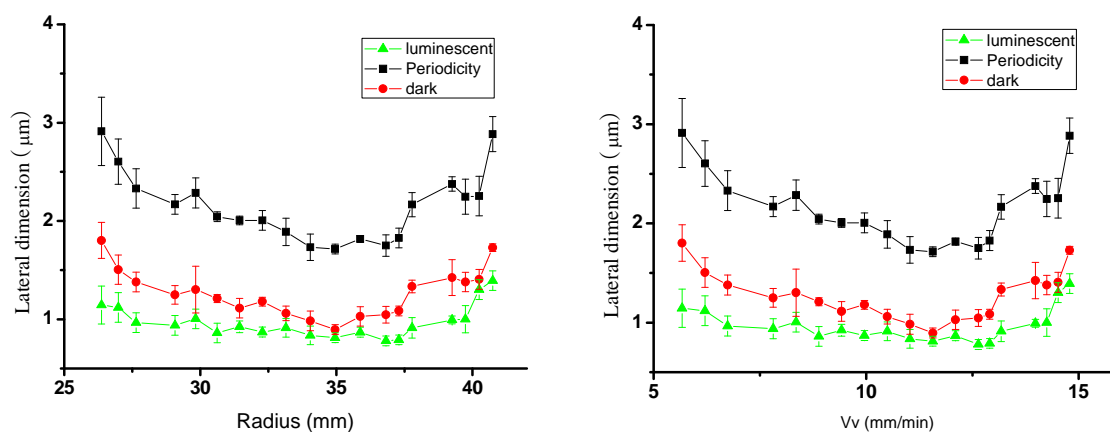


Figure 30. The dependence of the lateral width of luminescent stripes, dark stripes, and pattern periodicity along line b ($\theta = 35^\circ$) on the radius and v_r respectively.

4.5 Summary and Conclusion

In summary, we put forth a new idea of monolayer transfer onto solid substrate, i.e., LB rotating transfer which extends the application of LB patterning. We found that this new

transfer technique can be used to transfer DPPC/NBD mixed monolayer onto mica to achieve complex patterns. This simple yet novel approach enables one to produce and organize surface patterns in a well-ordered gradient fashion. We expect that combining vertical and rotating transfers would further enrich the transfer way and achieve more complex pattern. It is easy to extrapolate the ideas presented here to other systems, such as nanocrystals,^[41,42,117] or lipopolymer.^[122] Moreover, this kind of transfer could be easily used to test the experimental conditions for exploring the pattern formation of other systems.

5 Self-Organized DPPC Patterns on Prestructured Substrates

5.1 Introduction

For the formation of DPPC stripe patterns on mica the substrate is cleaved prior to LB transfer to obtain an atomic flat and clean area. Although atomically flat surfaces over areas of square centimeters are accomplished regularly, often places with terraces can be found on the samples, too, where the mica is cleaved at different crystal layers. This usually unwanted phenomenon also gave rise to the observation of the interaction of the stripe pattern formation with structural defects in the substrate. Figure 31 shows a typical result of a pattern formation on stepped mica terraces.

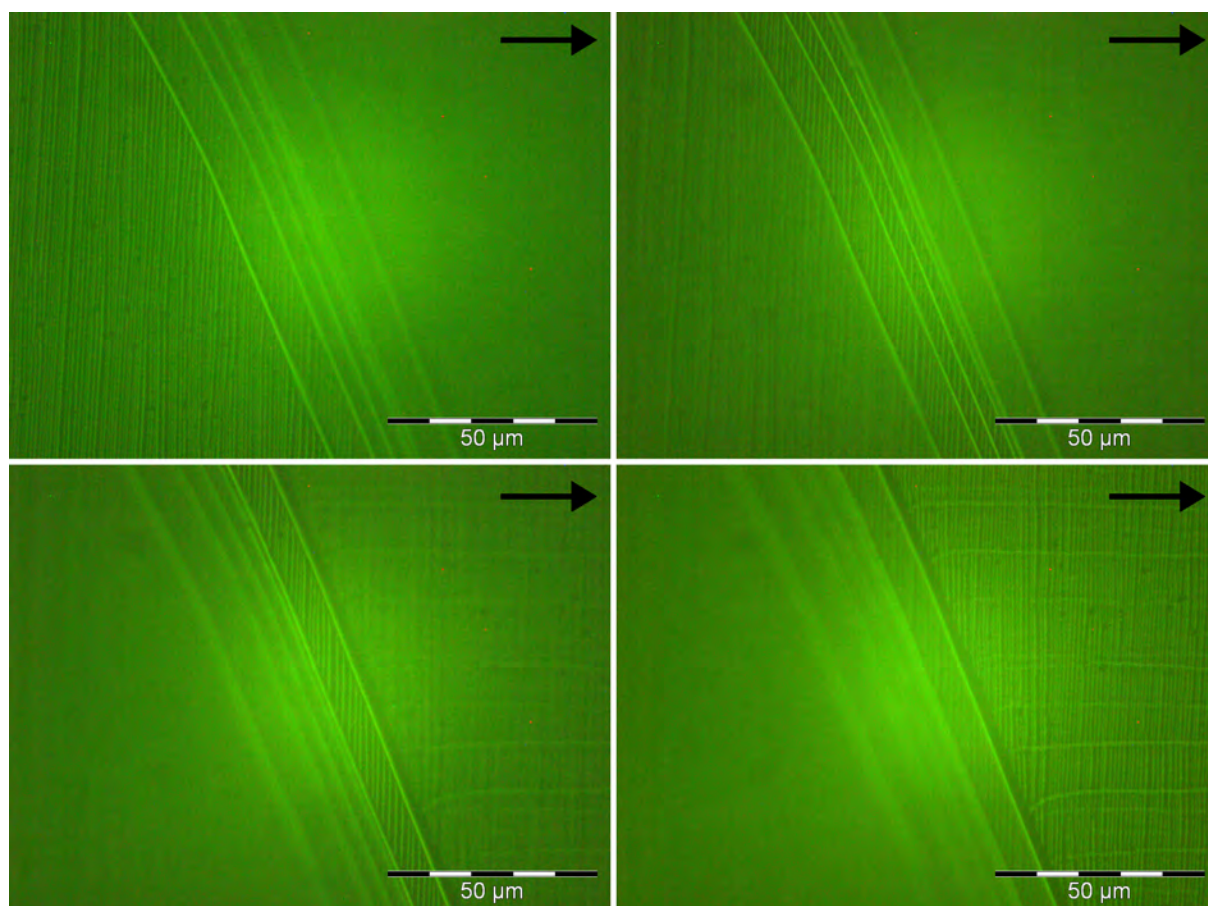


Figure 31. DPPC stripe pattern on mica over different substrate terraces. The focal plane is on the highest terrace in upper left image and is then lowered subsequently to the lowest terrace in the lower right image. Black arrows denote the direction of withdrawal during LB transfer.

The images show a pattern created by a mixed DPPC/NBD-PC film as reported before.^[91] It is clearly visible that the different edge steps of the terraces disrupt the continuity of pattern formation but without inhibiting it. Even the smaller terraces are covered with stripe pattern, the stripes being sometimes continuous sometimes uncoupled over the terrace edges. All in all the observation of substrate defects on mica with the corresponding stripe pattern formations lead to the clear notion that the observed deviation originate in the guiding and pinning of the water meniscus during transfer but for a more detailed picture it would be nice to design arbitrary defect structures instead of the limited and accidentally generated defects on mica. Therefore we decided to switch silicon substrates where electron beam lithography could be employed to introduce prestructures onto the samples and study the impact on pattern formation.

5.2 Materials and Experimental Details

Silicon wafers with a native oxide layer were cut into $2 \times 2 \text{ cm}^2$ pieces, cleaned by rinsing and sonication in acetone and covered with a resist layer of 300 nm thickness for electron beam lithography. The desired prestructures were then written into fields of $150 \times 150 \mu\text{m}^2$ each. Three to six of these fields were written onto one sample by electron beam lithography in distances of several millimeters so that several different patterns could be examined within one LB transfer assuring exactly same transfer conditions for all fields while still providing independence due to the large distances of the fields on the sample. The line patterns spacings ranged from 500 nm to 10 μm and additional fields filled with arrays of squares and circles were written to study point defects. All lithographic procedures were done on an Elphy 100 system attached to a LEO 1530 VP Gemini electron microscope. After development of the exposed resist layers 2 nm of chrome was evaporated onto the sample as a sticking layer followed by the evaporation of gold until the desired structural height (ranging from 10 to 50 nm) was reached. The evaporation was done in an Edwards system at a residual pressure of $2 \cdot 10^{-4}$ Pa. After the lift off process (submerging into acetone at 70 °C for 60 minutes followed by rinsing with acetone) the samples were cleaned in the usual way for LB transfer of DPPC stripe patterns by subsequent sonication in chloroform, isopropanol and pure water (DI, resistance of 18.2 M Ω cm) for 10 minutes each. After this the samples were exposed for 2 minutes to an oxygen plasma of 300 W at a pressure of 1 mbar and stored under pure water until the LB transfer took place. A DPPC solution with an addition of 2 mol-% of NBD-PC was used for the LB transfers since the small admixing improves patterning stability. All

transfers were done with a withdrawal speed of 30 mm/s and with a controlled subphase temperature of 25 °C. Since the air temperature and humidity varied over the different experiments (in the range from 22 to 25 °C and 40% to 60% RH, respectively) the lateral pressure for transfer was fine-tuned for the best patterning in the vicinity of 4.0 mN/m by test transfers onto unstructured silicon substrates prior to transfer onto the structured samples. After transfer the samples were allowed to rest for about 24 hours before AFM images were acquired.

5.3 Results and Discussion

Despite the prestructuring and the accompanying substrate treatment with resist layers and metal evaporation surfaces clean enough for DPPC stripe pattern formation could still be obtained. The pattern formation far away (about hundred micrometer or more) from the prestructured areas is unaffected and is in accordance with conventional transfers under similar conditions. Figure 32 shows the impact of single topographic lines (actually an array of lines in 6 μm distance in case of the Figure 32a) on the pattern formation.

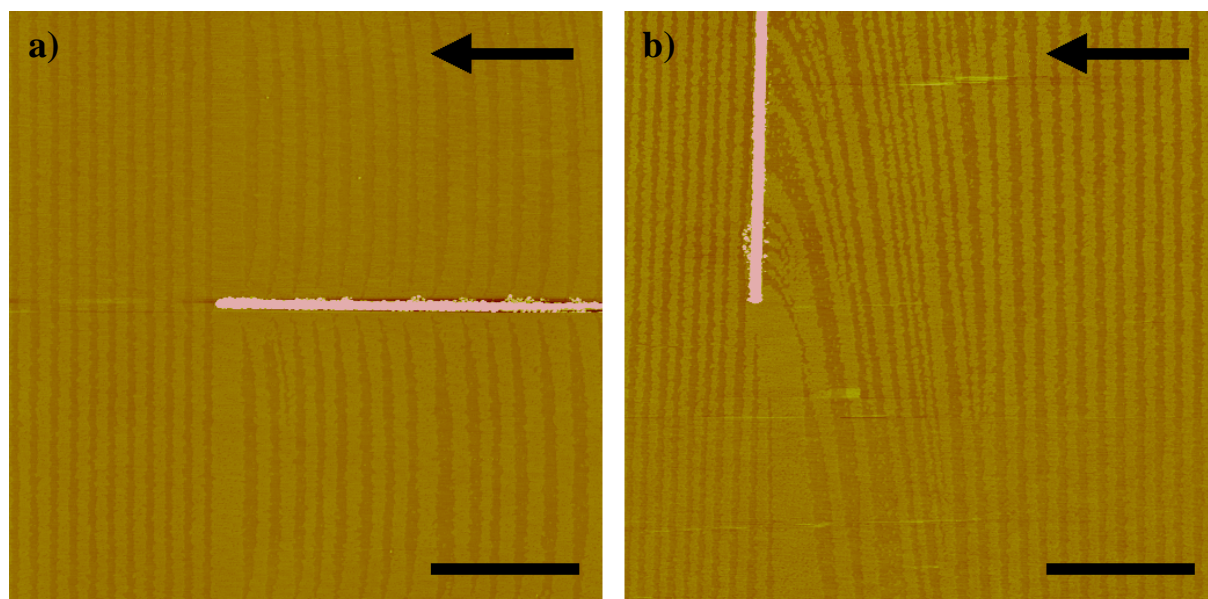


Figure 32. AFM images of topographic lines (height 20 nm) running (a) parallel and (b) perpendicular to the withdrawal direction during LB transfer (indicated by black arrow). Black bar equals 2.5 μm .

The line in Figure 32a runs parallel to the withdrawal direction (that is indicated by the black arrow) and has a height of 20 nm. The undisturbed pattern on the left is disrupted by a thicker stripe directly at the beginning of the line which is most probably caused by some pinning

effect of the line array on the flowing meniscus. The width of this “stop stripe” is dependent on the spacing between the lines and discussed later in this chapter. After the broader stripe the patterning immediately sets in again with almost the same periodicity. The shape of the stripes is distorted to some extent and becomes sickle-shaped. The shape matches what one would expect from a water meniscus flowing through a hydrophilic channel: the receding waterfront is lagging at the walls giving rise to the observed crescent shape. The impact of a line lying perpendicular to the withdrawal direction (Figure 32b) is more pronounced. There is again some broader stripe at the position of the interfering prestructure indicating pronounced pinning of the receding three phase contact line but since the waterfront is not divided into several channels for a continuous flow like in the latter case it will now run into the space behind from the edges of the flow-obstructing line (rather than just jumping over it). Since the waterfront will recede normally in the areas left and right of the line a pattern of strongly distorted stripes will result with normal parallel stripes at the areas left and right of the obstacle line that bend to connect in an almost perpendicular angle behind the line at its edges and with a decreasing angle towards the middle of the line. After the waterfronts emerging from the edges of the line meet each other at the middle of the line the receding waterfront is finally detached from the line completely and the normal patterning sets in again, in this particular case the pattern returns to normal about $3\ \mu\text{m}$ after being disturbed by the line. A sketch of the proposed flow of the receding meniscus in the two discussed cases is given in Figure 33.

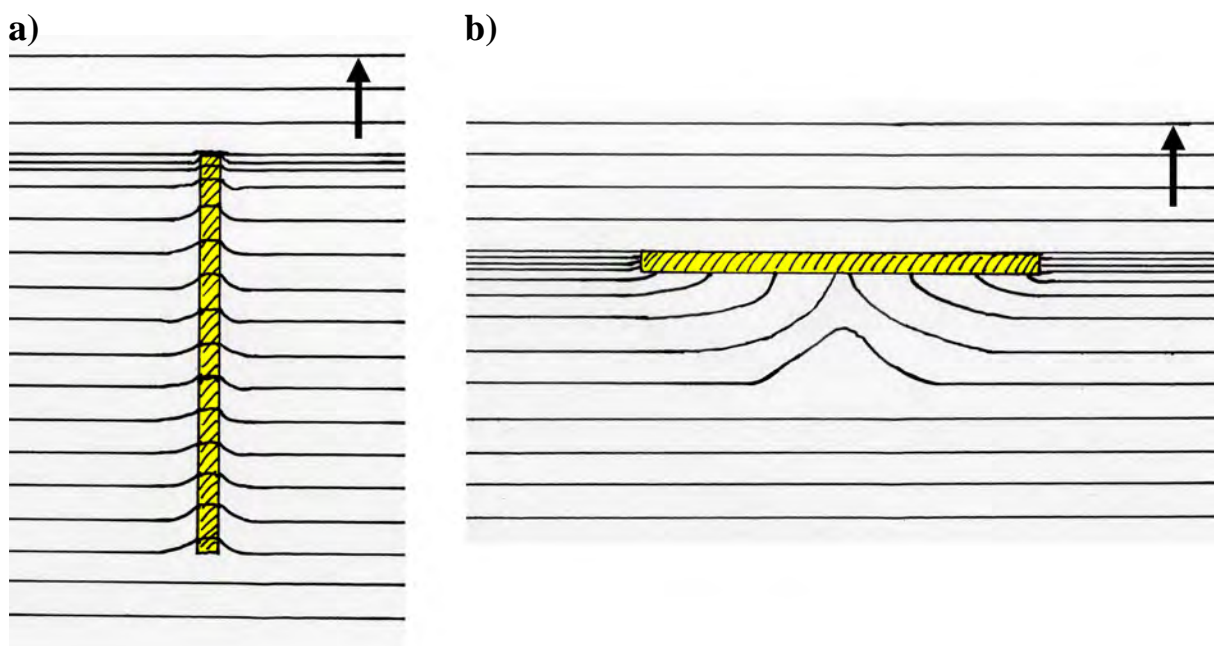


Figure 33. Proposed flow of the three phase contact line in the case of a line running (a) parallel and (b) perpendicular to the withdrawal direction during LB transfer (denoted by black arrow).

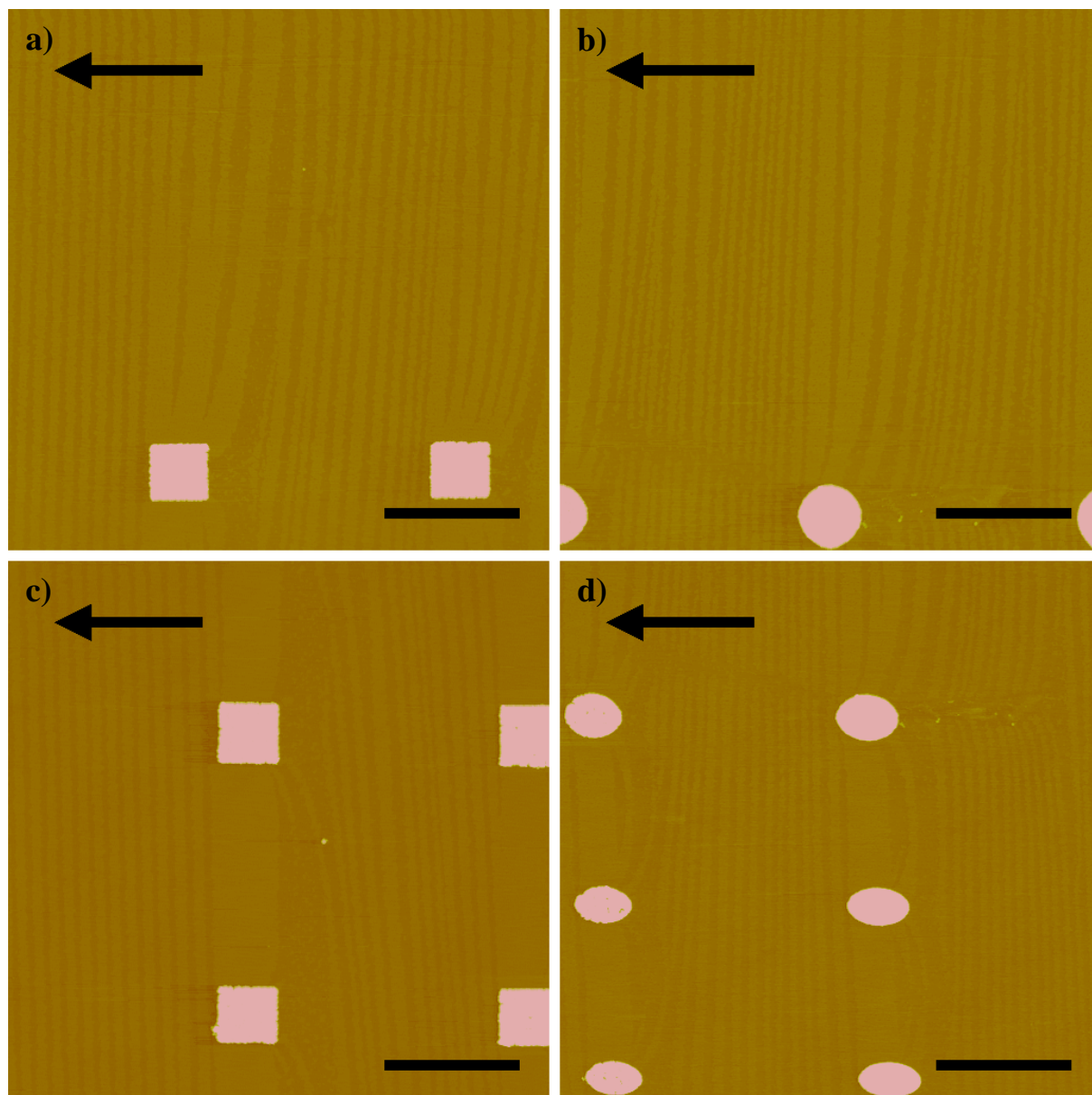


Figure 34. AFM images of self organized DPPC pattern on arrays of squares (edge length $1\ \mu\text{m}$) at (a) the edge of the array and (c) in the middle of the array and of circles (diameter $1\ \mu\text{m}$) at (b) the edge of the array and (d) in the middle of the array (distortions by defect of scanner in y-direction). All prestructures are $25\ \text{nm}$ in height. Black arrow denotes the direction of withdrawal during LB transfer, black bar equals $2.5\ \mu\text{m}$.

The meniscus pinning effect also becomes nicely visible in the case of prestructured point defects (Figure 34). The prestructures in this experiment consist of squares with a side length of $1\ \mu\text{m}$ and circles of $1\ \mu\text{m}$ diameter, respectively, in a regular array with $3\ \mu\text{m}$ spacing in between the structures that have a height of $25\ \text{nm}$. The square shaped point defects in the middle of the array are connected by a “stop stripe” similar to that observed before, almost as broad as the defects itself (Figure 34c). This stripe is followed by an area of about $1\ \mu\text{m}$ width where almost no stripes are found (only some bent stripes indicating the longest lasting

pinning of the meniscus at the corners of the squares) but are filled mainly with small DPPC LC domains. This area looks like a sample that has been either transferred at too high withdrawal speed or too low lateral pressure for pattern formation. Thus, the observed patterns suggest a rapid motion of the receding water front after the pinning at the square defects to catch up with the undisturbed receding water front far away from the prestructured area of the sample which would emulate an alternating lower (when pinned) and higher (while catching up) withdrawal speed than in the unstructured areas of the sample with a steady-speed receding water front. Directly after this area of small domains the patterning returns to a regular pace until it is stopped again by the next row of defects. At the edges of the structured area (Figure 34a) it becomes obvious that the pronounced “stop stripe” is a collective effect of the repetitive defect structure: although the broad stripe connects even the outmost square to the next neighbor in direction to the array bulk (next neighbor is not visible in this image) it is much less pronounced in the direction of the unstructured substrate area, breaks up into several smaller stripes and the overall pattern has a bent shape that blends into the undisturbed pattern over some tens of micrometers away from the prestructured area. In the case of the circular point defects a quite similar pattern can be found although there are some distinct differences. The observation of a “stop stripe” connecting the prestructures is also repeated for the circular defects inside the array (Figure 34d). Interestingly the area without stripes behind the broad stripe is much smaller and interspersed with sickle-shaped stripes spanning from one prestructure to the next or sometimes also blending into the reappearing regular pattern after the disturbance. This is most likely a result of the more streamline form of the circular defects promoting a flow of the water front around the shape of the defects and an easier detachment at the end of the circular defect structure leading to a more regular flow of the water front as compared to the square shape case. This is also supported by the smaller width of the “stop stripe” that does not form as broad as the whole circular defect but only about three quarters of it again indicating less pronounced pinning and smoother detachment of the receding water front compared to the square shape defects. At the edge of the circular defect array (Figure 34b) the pattern looks quite similar to the square shaped case. The “stop stripes” may be even less pronounced but the overall effect of a quite rapid blending of the stripes into the regular undisturbed ones by splitting and bending towards the unstructured area of the sample is in full accordance to the square shaped case.

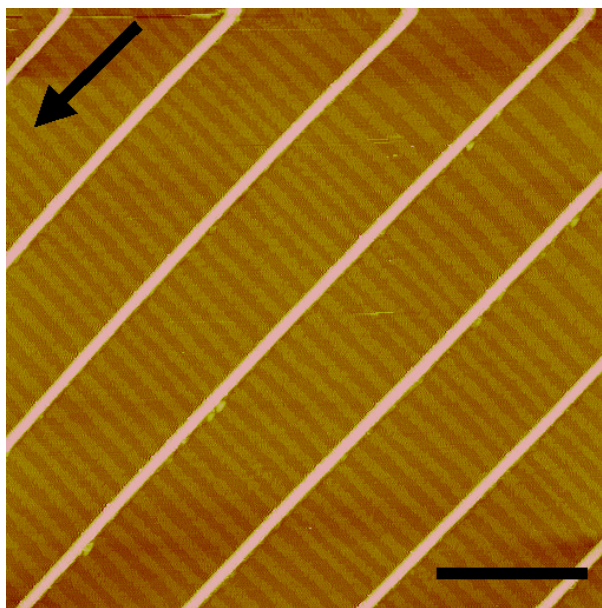


Figure 35. AFM image of a DPPC stripe pattern on a prestructured line array with a height of 6 nm. Black arrow denotes the withdrawal direction, black bar represents 2.5 μm .

The influence of regularly spaced line arrays on the pattern formation depends crucially on the prestructure's height and the spacing in between the prestructure's lines. Figure 35 shows an image of a completely undisturbed pattern formation on a prestructured substrate with a line height of 6 nm and a line spacing of 2 μm . The spacing should be narrow enough to have a pronounced influence on the stripe pattern formation but obviously the height of only 6 nm is not enough to have a noticeable influence on the receding waterfront. The DPPC stripes are absolutely continuous and synchronous over the lines; this becomes especially obvious when the stripe and channel widths vary over the course of the pattern like in the top right part of the image. A much higher and narrower prestructure is shown in Figure 36. Here the structure height is 30 nm and the line spacing is 500 nm. The undisturbed pattern far away from the prestructured areas is shown in Figure 36c. The other images show (with respect to the withdrawal direction) the top right corner (Figure 36a), the bottom right corner (Figure 36b) and the bottom left corner (Figure 36d) of the prestructured field (with an overall size of 150 \times 150 μm^2).

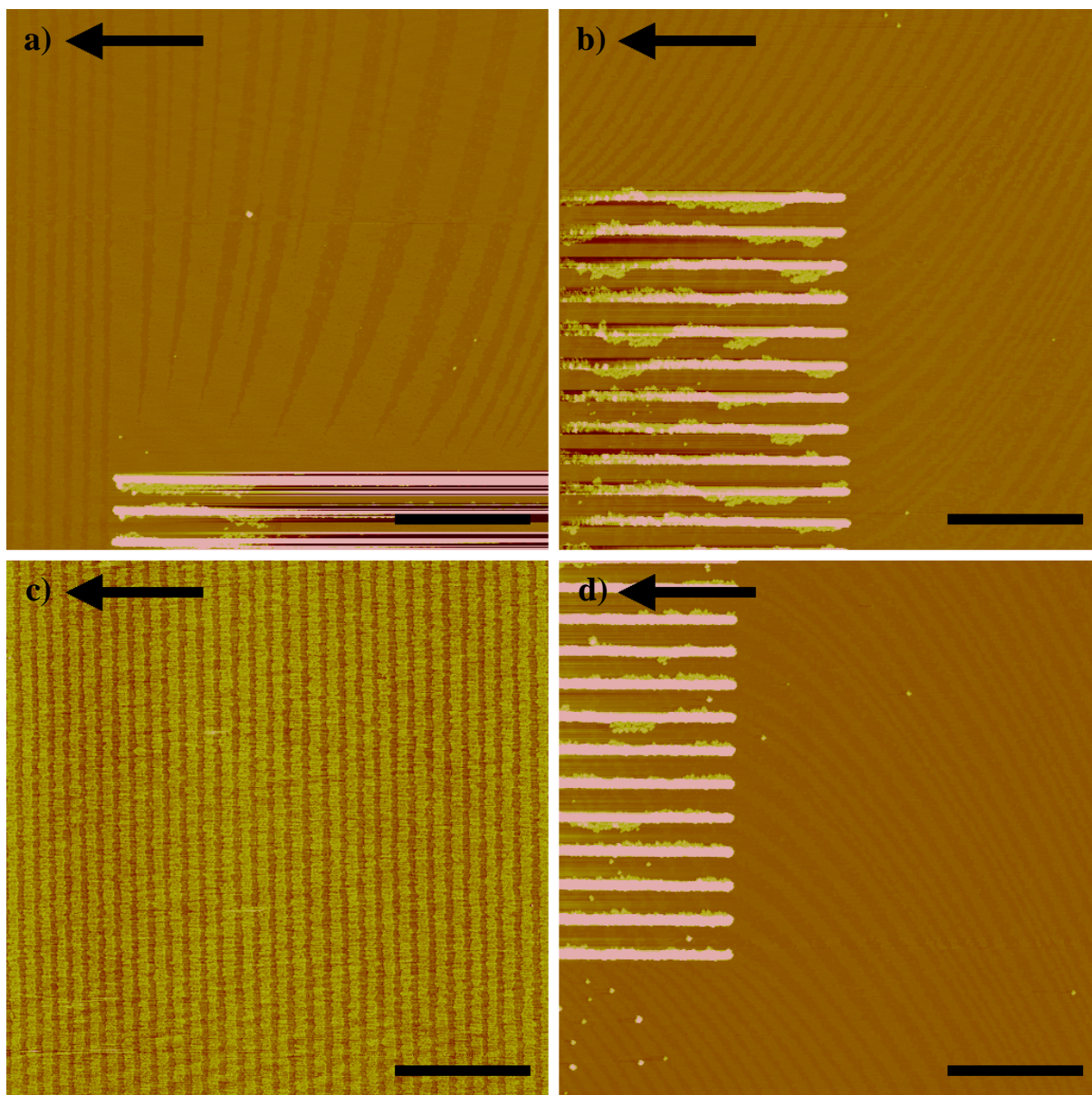


Figure 36. AFM images of a DPPC stripe pattern on a substrate with a 500 nm spacing line pattern of 30 nm height parallel to the withdrawal direction (indicated by black arrow) at (a) the top right corner, (b) bottom right corner, and (d) the top left corner of the prestructured area (relative to the withdrawal direction); (c) shows an area far away from the prestructured area for comparison. Black bar equals 2.5 μm .

With the undisturbed pattern coming from the right again the aforementioned “stop stripe” can be observed at the beginning of the prestructured area (Figure 36a). In between the lines of the prestructure the LC phase stripe extends for more than 10 μm but on the outside edge of the prestructure it quickly breaks into smaller stripes that bend and blend into the surrounding undisturbed DPPC stripe pattern. At the bottom end of the prestructure (Figure 36b and d) the stripe pattern is still bent towards the prestructured area but the pattern periodicity and regularity is similar to the undisturbed pattern owing to a new balance between the

undisturbed receding waterfront and the one flowing over the prestructure that may still flow with some delay but after a while inevitably with the same speed because of the comparatively large size of the prestructured area or otherwise it would detach from the undisturbed waterfront and be trapped on the sample which would then be incompatible with the observed continuous pattern formation. At the bottom end of the prestructured area (Figure 36b and d) the pattern looks similar to the case of the single line perpendicular to the withdrawal direction case: the stripes bend strongly yielding an almost 90 degree angle directly at the corners of the prestructured area and this angle is decreasing towards the middle of the prestructure indicating again a receding waterfront from the corners of the prestructured area to the middle where it finally detaches and catches up with the undisturbed receding waterfront of the unstructured surrounding substrate.

Varying the spacing in between the prestructure's lines has a profound influence on the width of the "stop stripe" at the beginning of the prestructured area. Figure 37 shows AFM phase images of DPPC stripe patterns on substrates with line prestructures of 50 nm height and different spacing in between the lines. The two images in the top (Figure 37a/b) show the same prestructure, once at the top of the prestructured area and once in the middle of it (with regard to the withdrawal direction during transfer). At the top of the prestructured area (Figure 37a) it can be nicely observed that the previously undisturbed pattern reacts with a broad "stop stripe" exactly when the receding water front reaches the prestructured line pattern most probably arising by the pinning or at least slowing down of the receding meniscus due to the prestructure. Directly after this broader stripe the regular stripe patterning returns in a form of sickle-shaped stripes clearly reflecting the shape of the receding waterfront in the channels created by the prestructure's lines as side walls and as expected for a receding waterfront through a hydrophilic channel. For a proposed flow of the waterfront over the prestructure see Figure 38. The sickle-shaped stripes continue over the rest of the prestructured area as seen in Figure 37b. It is interesting to note that although the stripe patterning within the different channels of the prestructure is almost perfectly synchronized with variations in the stripe size usually appearing in all channels at parallel the patterning itself seems to be decoupled in between the different channels because defects in one channel (like the two successive broader stripes in Figure 37b marked by the red arrow) do not necessarily spread to adjacent channels. These findings are in line with a two region model of the meniscus shape for the receding waterfront as proposed in theoretical modelling before:^[52] a thicker "macroscopic" meniscus that will not split up by the prestructure into independently receding waterfronts

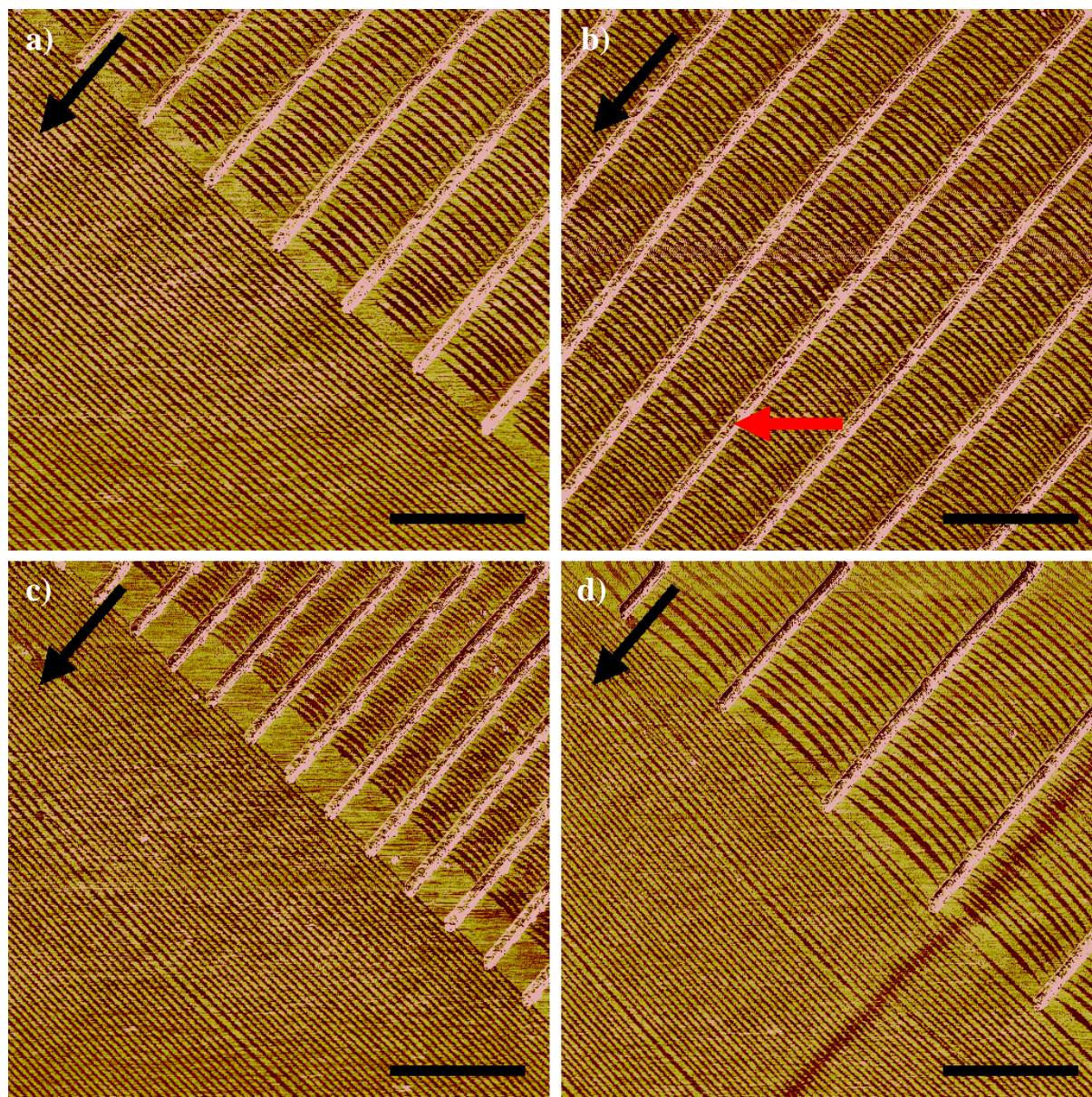


Figure 37. AFM images (phase) of a DPPC stripe pattern on prestructures with different line spacing. The image (a) shows the start of a prestructured area with $3\ \mu\text{m}$ line spacing, (b) the same sample in the middle of the prestructure. The red arrow indicates an incidence of uncoupled patterning in the channels created by the line array prestructure. The other two images show the beginning of prestructures with (c) $1\ \mu\text{m}$ and (d) $5\ \mu\text{m}$ line spacing. All prestructures have a height of $50\ \text{nm}$. The black arrows denote the withdrawal direction, black bars equal $5\ \mu\text{m}$.

will lead to a general synchronization of the pattern formation in the channels with global variations in the pattern induced by, e.g., irregularities in the withdrawal speed, vibrations of the sample or similar influences. A second much thinner precursor water film in which the actual stripe formation will occur is significantly influenced or even ruptured by the prestructure giving rise to the possibility of defects in the pattern formation in one channel (induced, e.g., by a irregularity in the channels sidewall) that is not translating to the

neighboring channels. While the aforementioned macroscopic water film should be much thicker than the prestructures (hence at least hundreds of nanometers) to be not severely influenced by the underlying prestructures a better range estimate can be given for the thinner precursor water film based on the impact of prestructures with different height on the pattern formation: here we would conclude a thickness in the order of 10 to 20 nm since the low prestructures with 6 nm (Figure 35) do not disturb the pattern formation at all while prestructures with a height of 20 nm already show an profound impact on pattern formation.

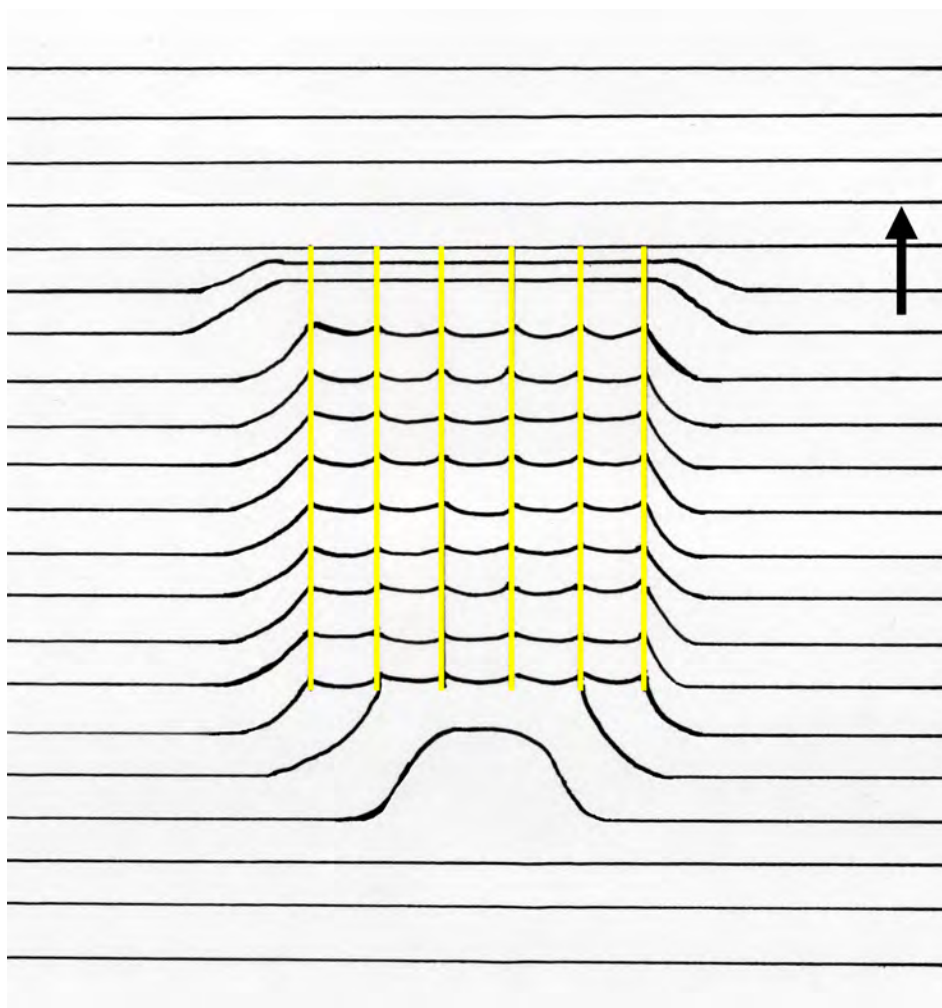


Figure 38. Proposed flow of the receding waterfront over the line array prestructure during LB transfer (transfer direction denoted by black arrow).

A plot of the width of the “stop stripe” width against the line spacing of the prestructure for different prestructure’s height is given in Figure 39. In general the “stop stripe” width increases dramatically when the spacing between the lines of the prestructure drops below 4 μm . For similar line spacings the “stop stripe” width increases with increasing height of the

prestructure. The obtained data points for the different prestructures could be fitted empirically by a power function of the form

$$f(x) = \frac{a}{x^{1.2}} \quad (55)$$

With $a = 4$ for the 50 nm height prestructure, $a = 3.2$ for 30 nm and $a = 2.2$ for 20 nm structural height.

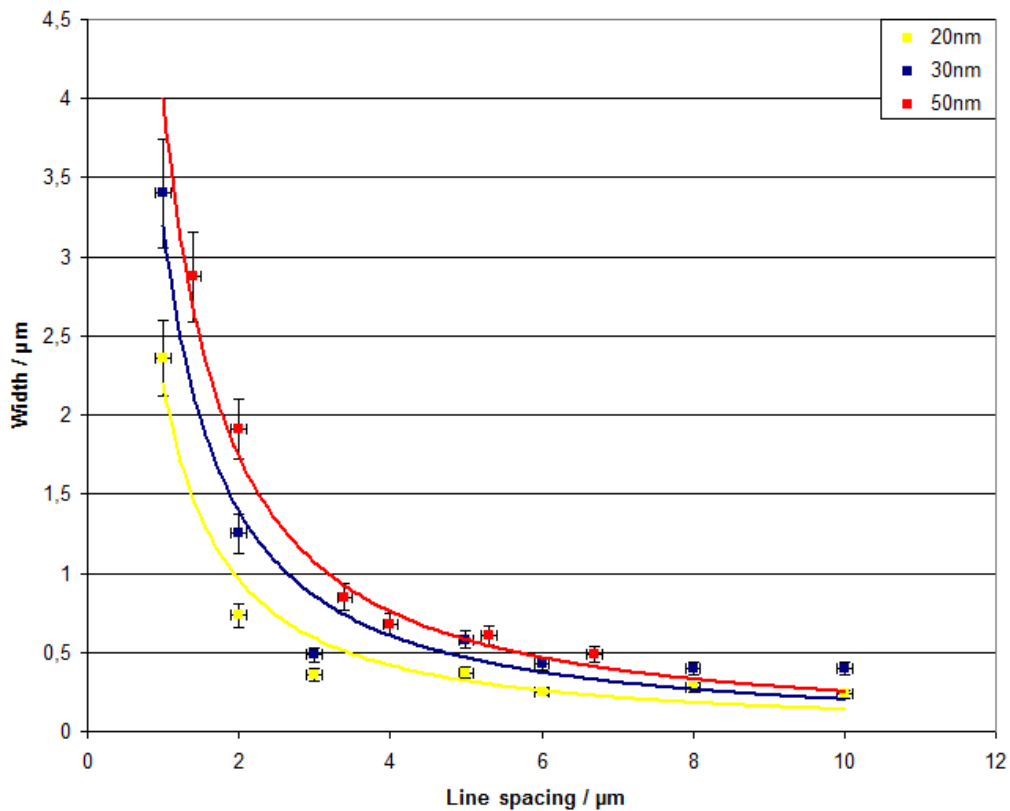


Figure 39. Width of the “stop stripe” versus line spacing of the prestructure for prestructures of different height.

5.4 Summary and Outlook

DPPC stripe patterns were successfully obtained on substrate with prestructured areas patterned by electron beam lithography. The resulting patterns enabled a profound insight in the meniscus flow during pattern formation and could affirm the theoretical proposed partition of the meniscus into a (thick) macroscopic part and a thin precursor water film. The thickness of the precursor film could be estimated to be in the range of 10 to 15 nm. Since the influence of the prestructure on the pattern formation is mediated by shaping, pinning, and guiding the

receding waterfront future experiments should aim at altering the local wetting properties on the sample to directly target the meniscus shape and flow of water during LB transfer. It would be also interesting to generate prestructures with continuously varying height (e.g., by electron or ion-beam induced metal deposition from precursor gasses) to further clarify the role of the precursor film and macroscopic meniscus during pattern formation. Another interesting conceivable application that should be probed in future experiments is inspired by the works of *Moraille* and *Badia* on the templated assembly of proteins on the DPPC stripe pattern.^[123] They showed that the preferred assembly of the protein human albumin (HSA) is dependent not only of the general phase state (LE or LC) but also on the packing density (that still can vary within a phase state). The concerted modulation of the meniscus flow could enable such density variations within the general LE/LC pattern and yield a route for additional control on the absorption of proteins.

6 Admixing of Functional Compounds in LB Transfer

6.1 Introduction

The DPPC stripe pattern was shown to be useful as a template to guide the self-assembly of nanoparticles^[124,125] and can be modified for further chemical patterning^[121] enabling, e.g., etching of the pattern into silicon^[119,126] or electrodeposition of copper wires.^[127] All these patterning methods take place after the LB-transfer of pure DPPC. Since experiments have shown that other lipids (that are also normally part of phospholipid-membranes in biological systems) can be directly transferred with DPPC and will affect but not inhibit pattern formation.^[116] In experiments with admixtures of fluorescent labelled dyes or even pure dye (i.e., not bound to a lipid) to the DPPC monolayer a phase separation leaving the admixed compound mainly in the LE-phase stripes of the pattern was observed yielding fluorescent stripe patterns.^[91,128] These results raise the question whether other functional compounds (especially non-lipid ones) can be generally patterned with this approach which would enable another rapid patterning technique for big surface areas.

6.2 Materials and Experimental Details

The chemical structures of the different compounds used in our experiments are shown in Figure 40. All compounds were synthesized in the group of Prof. Studer (by Julia Hederer and Dr. Marion Brinks) and checked for purity by means of mass spectrometry.

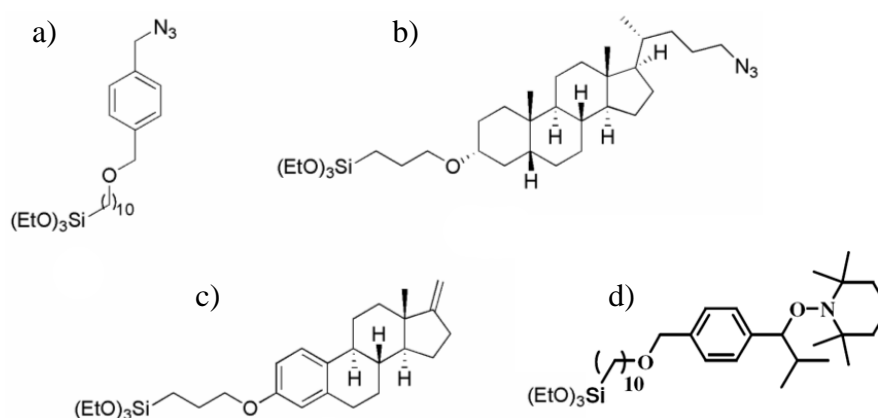


Figure 40. Molecular structure of (a) the azide, (b) lithocholic acid, (c) estrone derivative, and (d) the alkoxyamine N.

For each experiment fresh solutions of DPPC and the respective compound in HPLC grade chloroform at concentrations around 1 mg/ml were prepared. The DPPC solution was then divided into six parts and to each an appropriate amount of the respective compound was added to reach admixing of 2.5 mol-%, 5.0 mol-%, 7.5 mol-%, 10.0 mol-%, 12.5 mol-%, and 15.0 mol-%. As substrates silicon wafers with a native oxide layer were cut into pieces of about 5×2 cm² that were subsequently cleaned by 10 minutes of sonication each in chloroform, isopropanol and pure water (DI, resistance of 18.2 M Ω cm) and finally exposed to a 300 W oxygen plasma at a pressure of 1 mbar for 2 minutes. The substrates were stored under pure water and used for the transfer within 3 hours. The subphase temperature for all experiments was fixed at 25 °C, the relative humidity varied in between 50 % to 60 % between transfers. After a substrate was submerged into the subphase the respective solution was spread onto the air-water interface and the chloroform was allowed to evaporate for about 10 minutes, additional 50 minutes were waited for in the case of the acid and alkoxyamine to allow for hydration of the triethoxy anchors to enable a later covalent binding to the substrate. The monolayer is then compressed to a lateral pressure of 5 mN/m and another 10 minutes were allowed to pass so that the film could equilibrate. The substrate was then lifted through the monolayer with a velocity of 10 mm/min. The substrate were kept under ambient conditions at room temperature for one day and then studied by AFM to observe the resulting patterning.

For the monolayer with alkoxyamine admixings additionally Brewster angle microscopy was performed. For this the solution with the respective amount of admixture was spread onto a water subphase fixed at a temperature of 25 °C in a trough equipped with a Brewster angle microscope. After allowing the chloroform to evaporate for about 10 minutes an isotherm was recorded and images were acquired from the Brewster angle microscope in regular intervals during compression.

6.3 Results and Discussion

All four compounds could be transferred together with DPPC without inhibiting pattern formation. Detailed compilations of images of a typical transfer for a given admixing as well as data on stripe width, channel width and overall periodicity are given for the estrone derivative (Figure 41, Figure 42), lithocholic acid (Figure 43, Figure 44) and the azide (Figure 45, Figure 46).

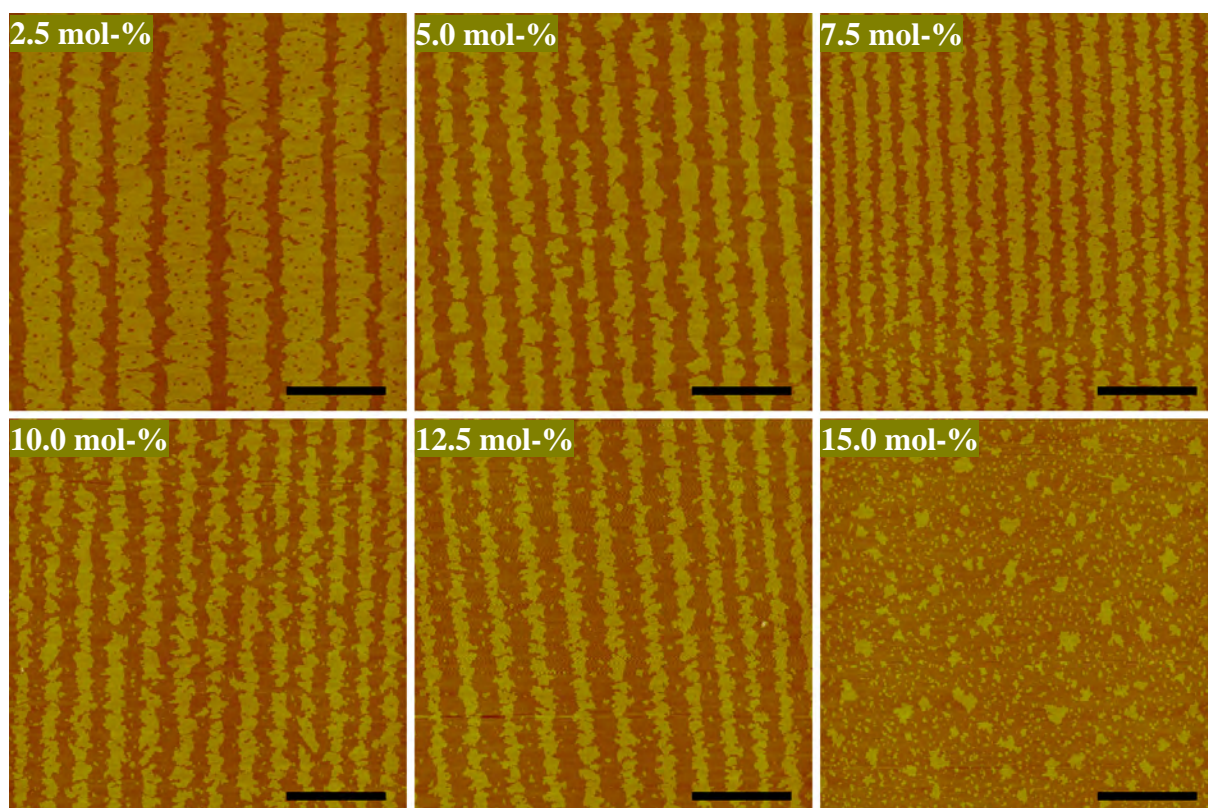


Figure 41. Obtained patterns after LB transfer with admixing of the estrone derivative (insets indicate added concentration, scale bar equals 2.5 μm).

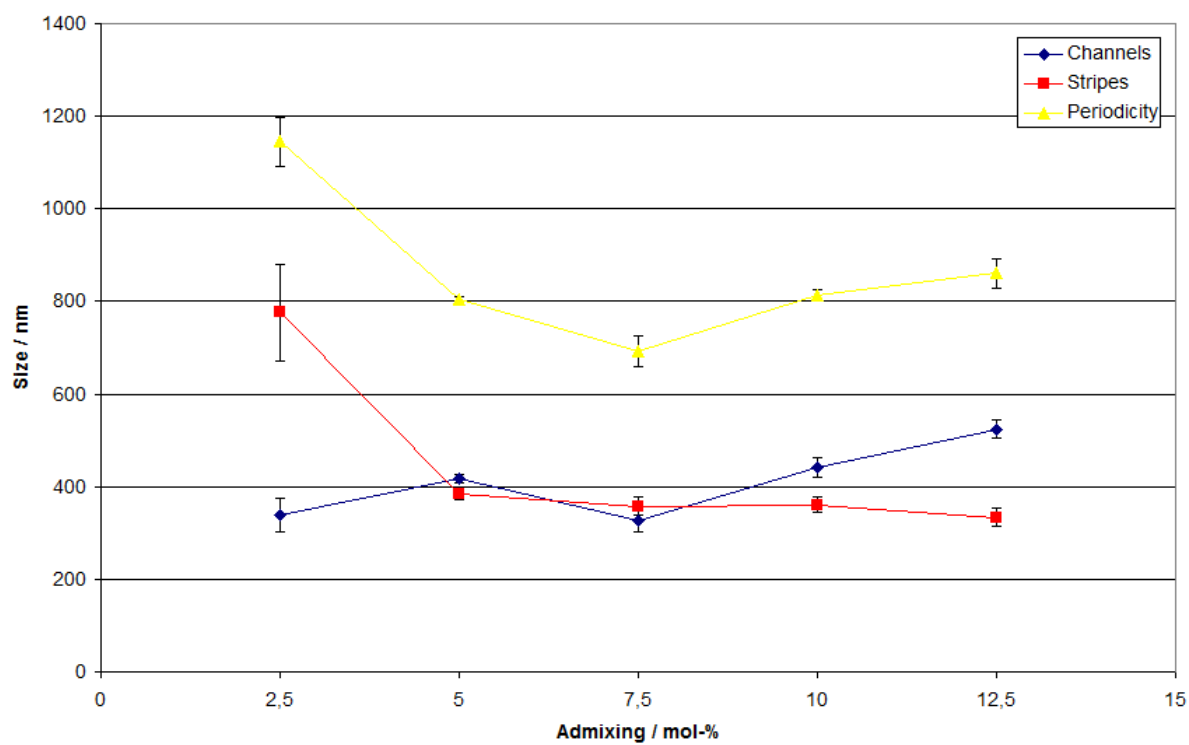


Figure 42. Size of the stripes, channels and overall periodicity versus admixing of the estrone derivative.

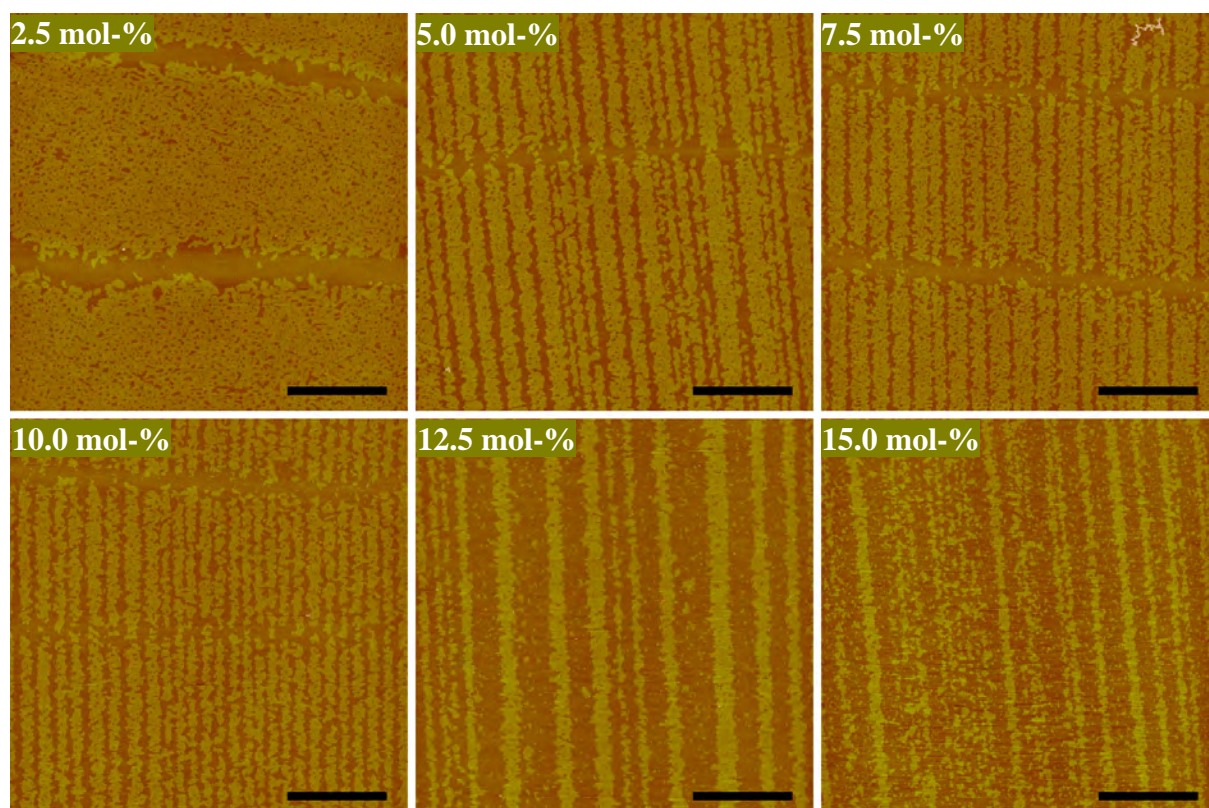


Figure 43. Obtained patterns after LB transfer with admixing of lithocholic acid (insets indicate added concentration, scale bar equals 2.5 μm).

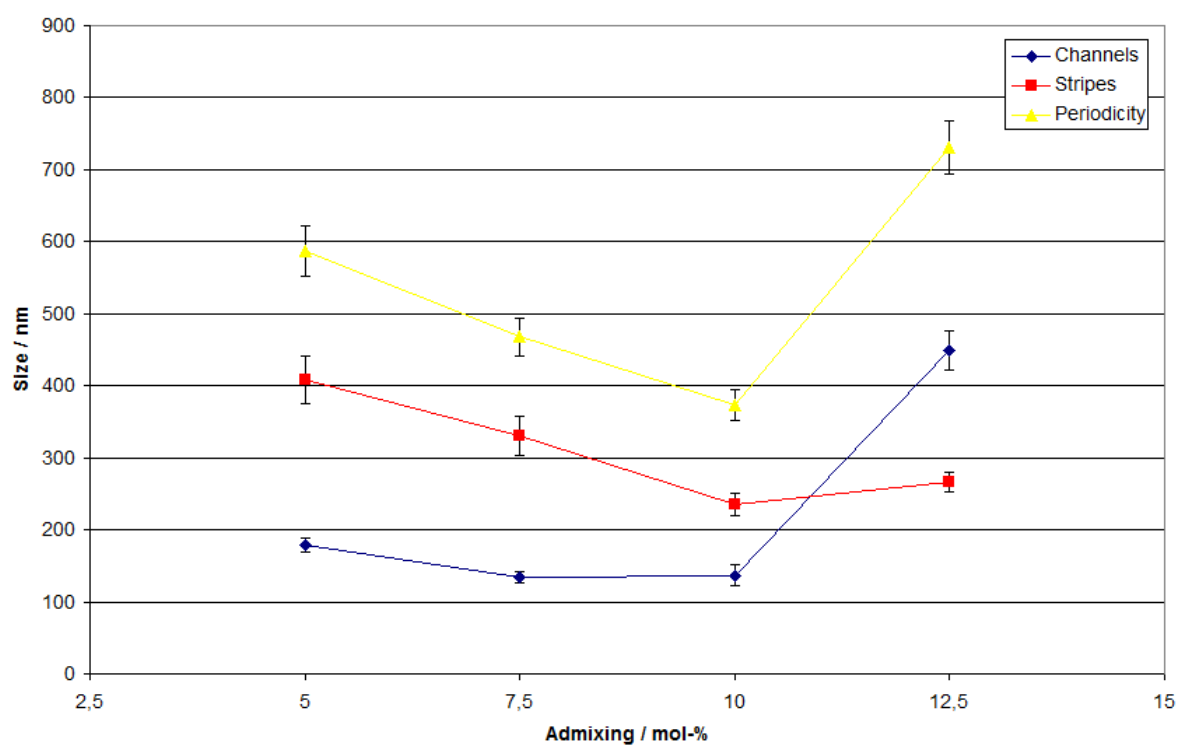


Figure 44. Size of the stripes, channels and overall periodicity versus admixing of lithocholic acid.

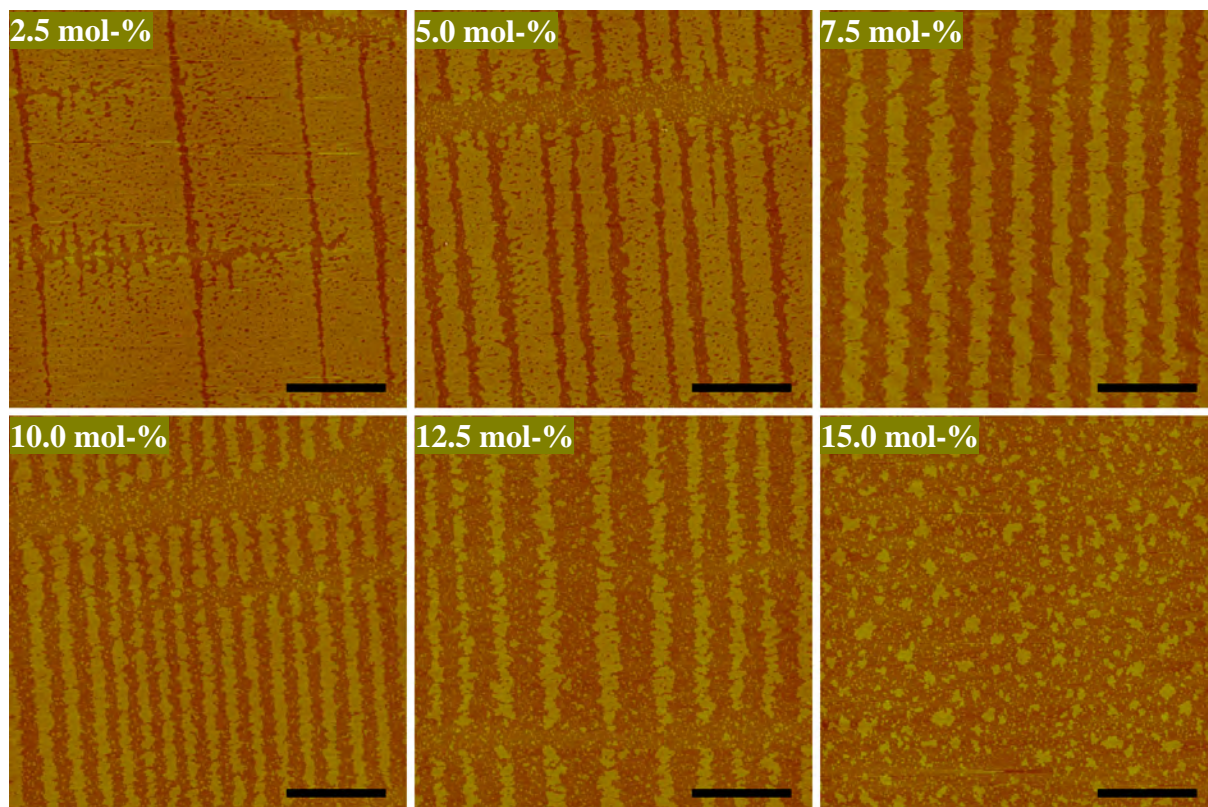


Figure 45. Obtained patterns after LB transfer with admixing of the azide (insets indicate added concentration, scale bar equals 2.5 μm).

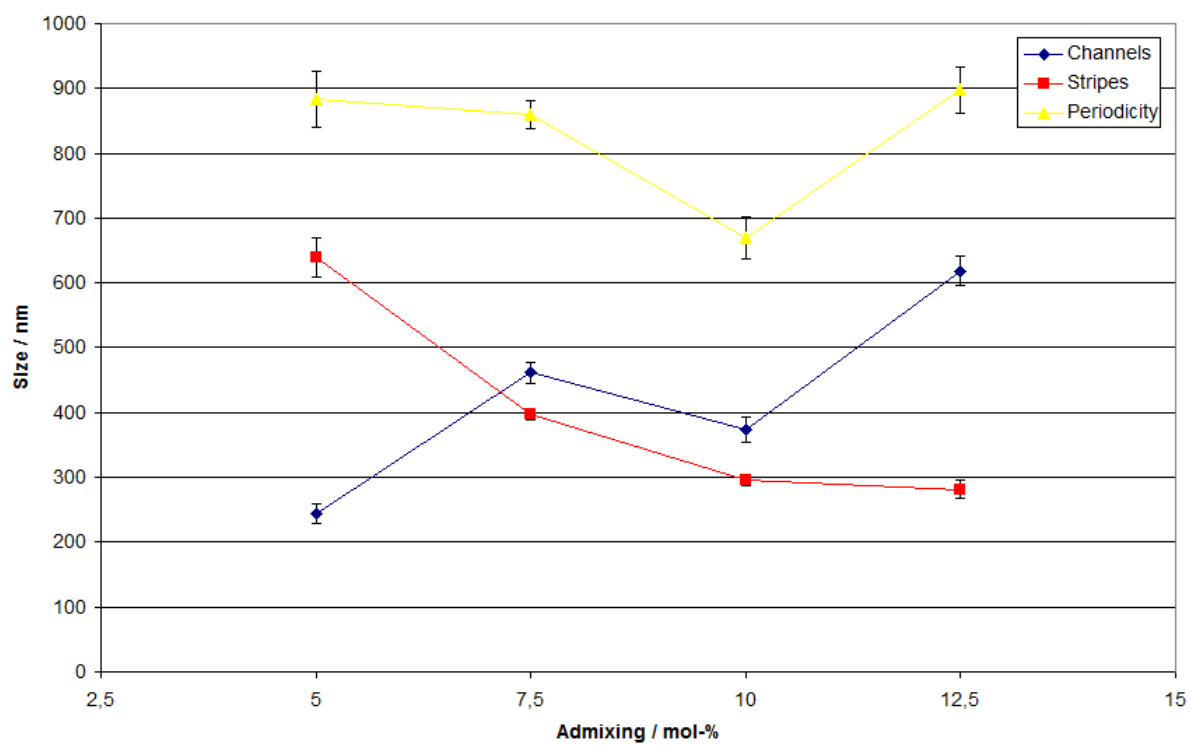


Figure 46. Size of the stripes, channels and overall periodicity versus admixing of the azide.

There are some similar trends observed in all patterned films after transfer with an admixing. All in all the stripe edges of the transferred patterns look more rugged as compared to that of pure DPPC transfers (c.f. rugged domains in BAM images, see below). Moreover the pattern dimensions become significantly smaller as compared to the transfer of pure DPPC: in the current experiment the overall periodicity varies from 1.2 μm down to under 400 nm depending on the amount and type of admixing whereas transfers of pure DPPC usually yield periodicity way above 1 μm under similar transfer velocities. Under the current transfer parameters all systems lose the patterning with an admixing of 15 mol-%, although patterning may be still possible by altering the transfer parameters to higher lateral pressures. With admixing of 2.5 mol-% only the DPPC/estrone derivate mixture still exhibit a regular stripe patterning. The other compounds form more or less complete LC phase films as would be expected for pure DPPC under current transfer conditions. All transferred systems show a pronounced minimum in the overall periodicity (at 7.5 mol-% for the estrone derivative, at 10.0 mol-% for the lithocholic acid and the azide). In general the stripe size decreases while the channel size increases with increasing of admixing which concurs with the intuition that (since the admixing tends to accumulate in the LE phase channels) a more of admixing should enlarge the channels. In case of the lithocholic acid admixing there is also a slight increase in channel size with decreasing admixing from 7.5 mol-% to 5.0 mol-%. This somehow counterintuitive behavior was also observed in the previous experiments with dye admixing^[91] and leads to the conclusion that under some circumstances a lower concentration of admixing can have an even bigger effect on the condensation behavior than a higher admixing. Another general observation is that a higher lateral transfer pressure is needed for the patterning of films with admixing. LB transfer of pure DPPC monolayers under a pressure around 5 mN/m would lead to a complete and unstructured LC phase coverage on the silicon substrates. This can be understood by the rise in the coexistence plateau of the isotherms with admixing. The condensation is hindered by the admixing therefore requiring a rise in lateral pressure to occur.

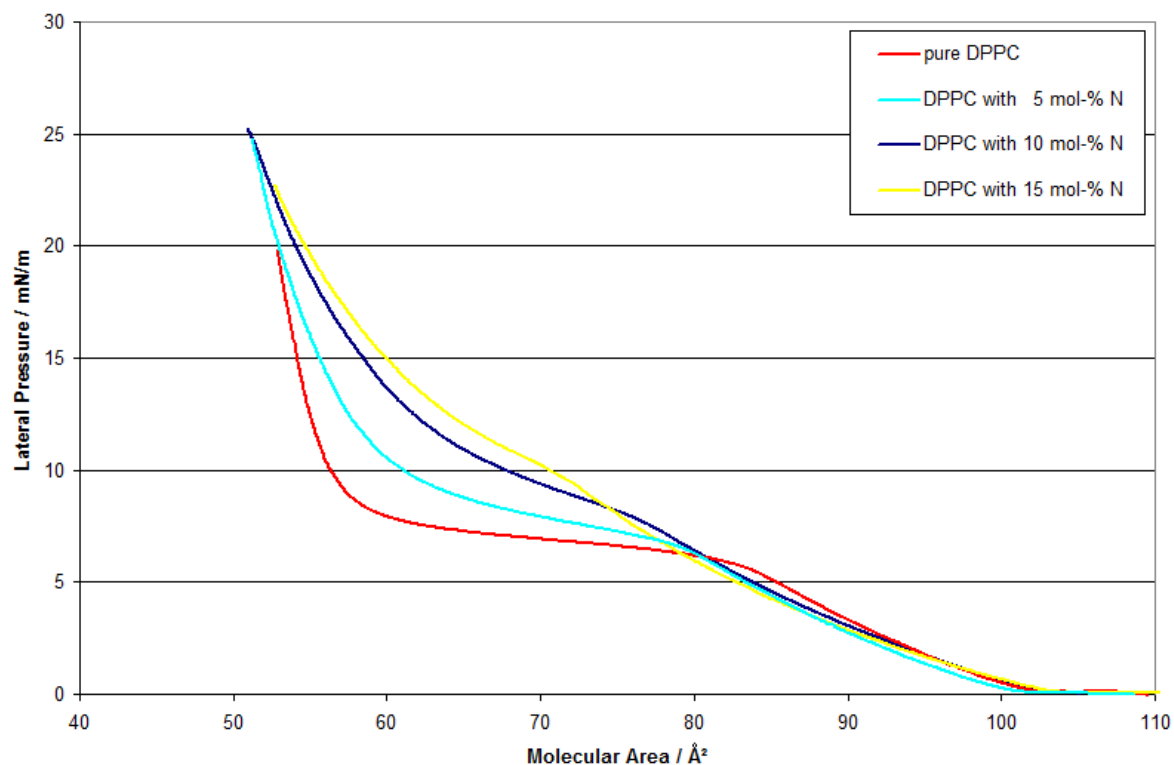


Figure 47. Isotherms for pure DPPC and different admixing of the alkoxyamine N.

The isotherms of DPPC with different amounts of admixed alkoxyamine N and that of pure DPPC for comparison are shown in Figure 47. With increasing admixing the plateau of LC/LE phase coexistence is shifted to higher pressures and twisted in a way that the transition of LE to LC phase is less pronounced. There is no substantial influence on the onset and slope of the LE phase domain of the isotherm by the admixing. For the LC phase domain a decrease in slope with increasing admixing is observed. With admixing of 10 mol-% and 15 mol-% there is no clear distinguishing mark between LC phase and the coexistence domain, only a kink in the isotherm between LE phase and the coexistence domain is still discernible. The following series of images shows Brewster angle microscopy (BAM) micrographs captured during the recording of the isotherms with different admixing and grouped into images with similar lateral pressure.

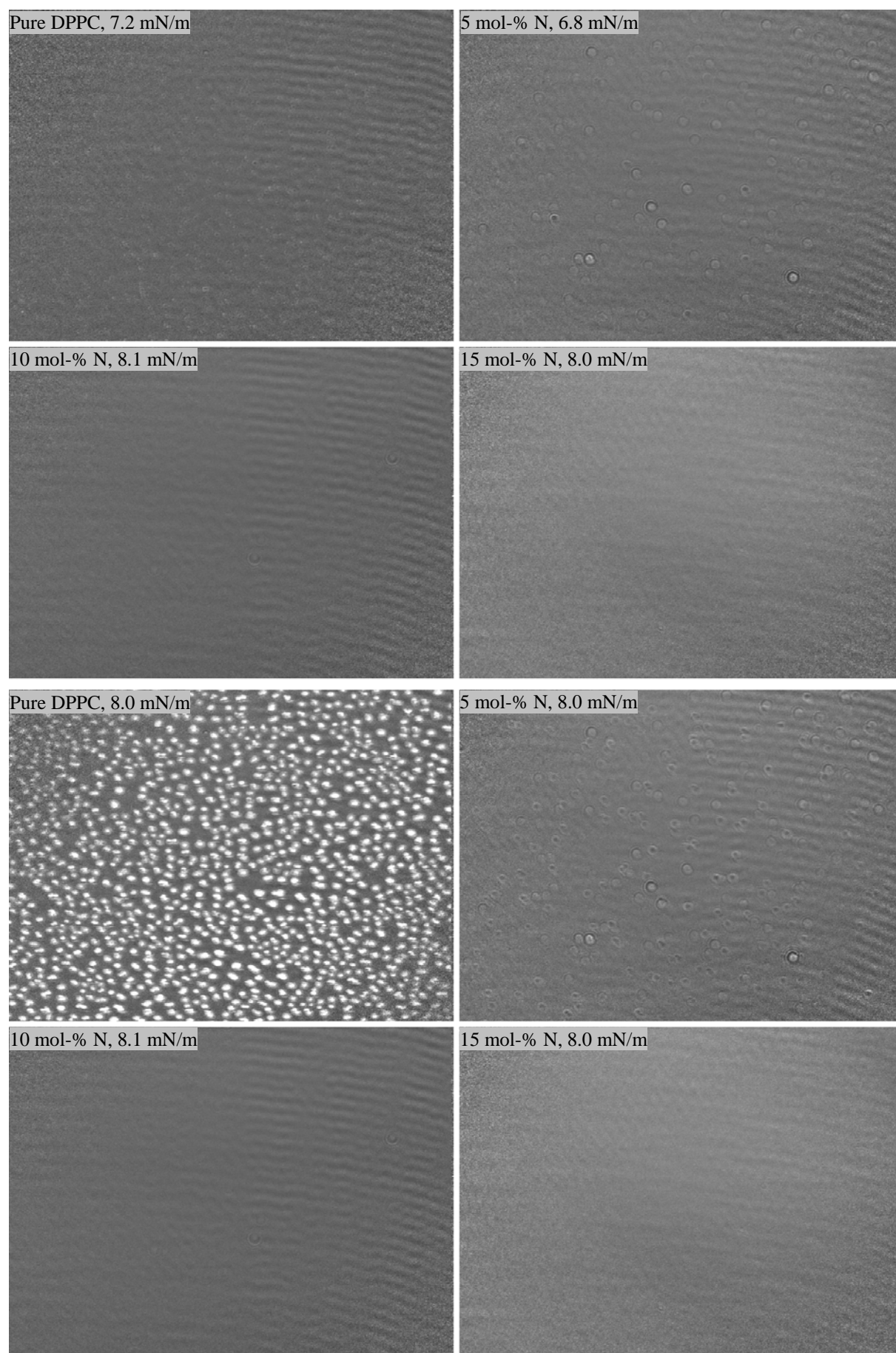


Figure 48. BAM images with different admixing amounts of alkoxyamine N (image width 430 μ m).

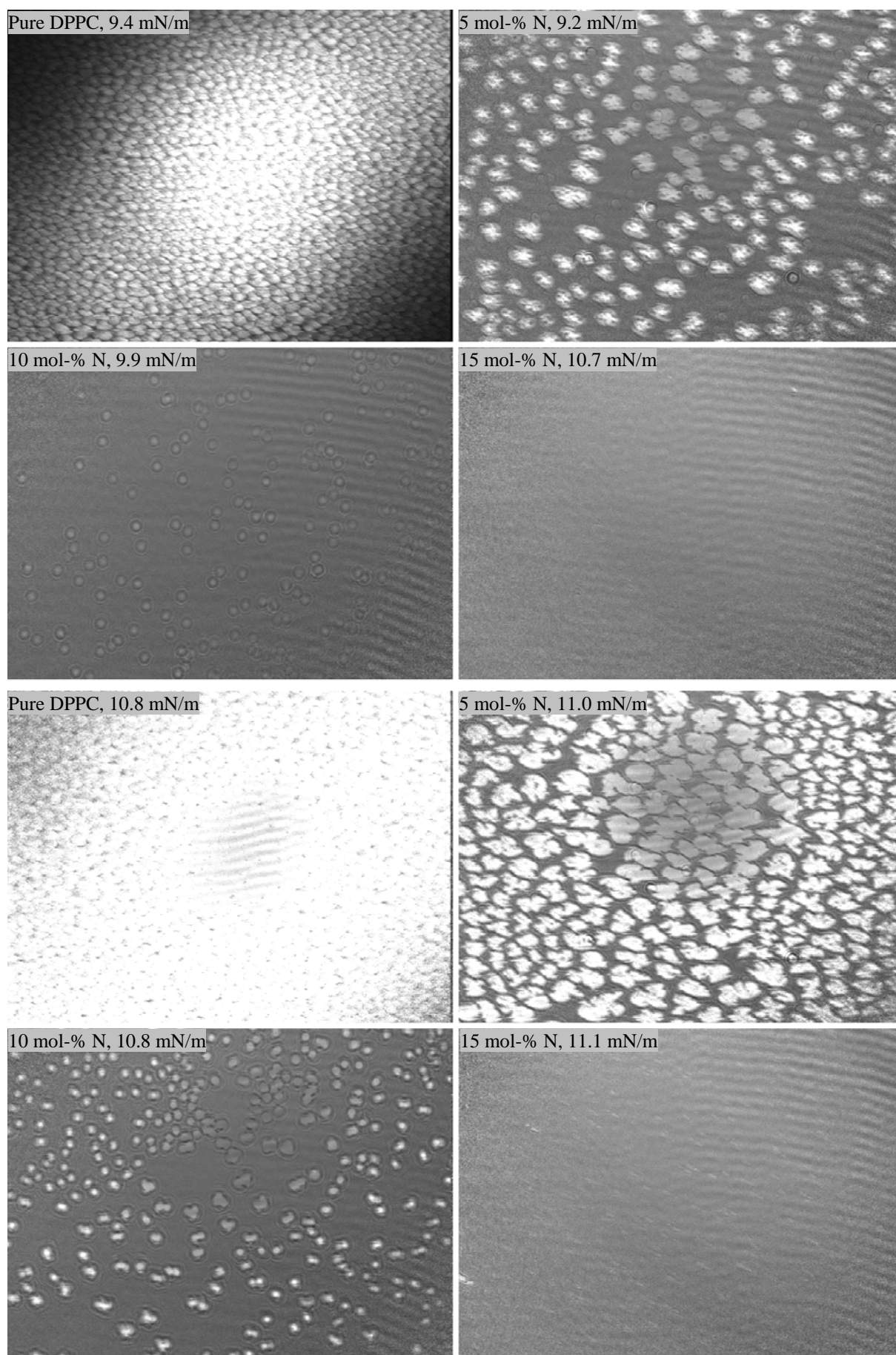


Figure 49. BAM images with different admixing amounts of alkoxyamine N (image width 430 μ m).

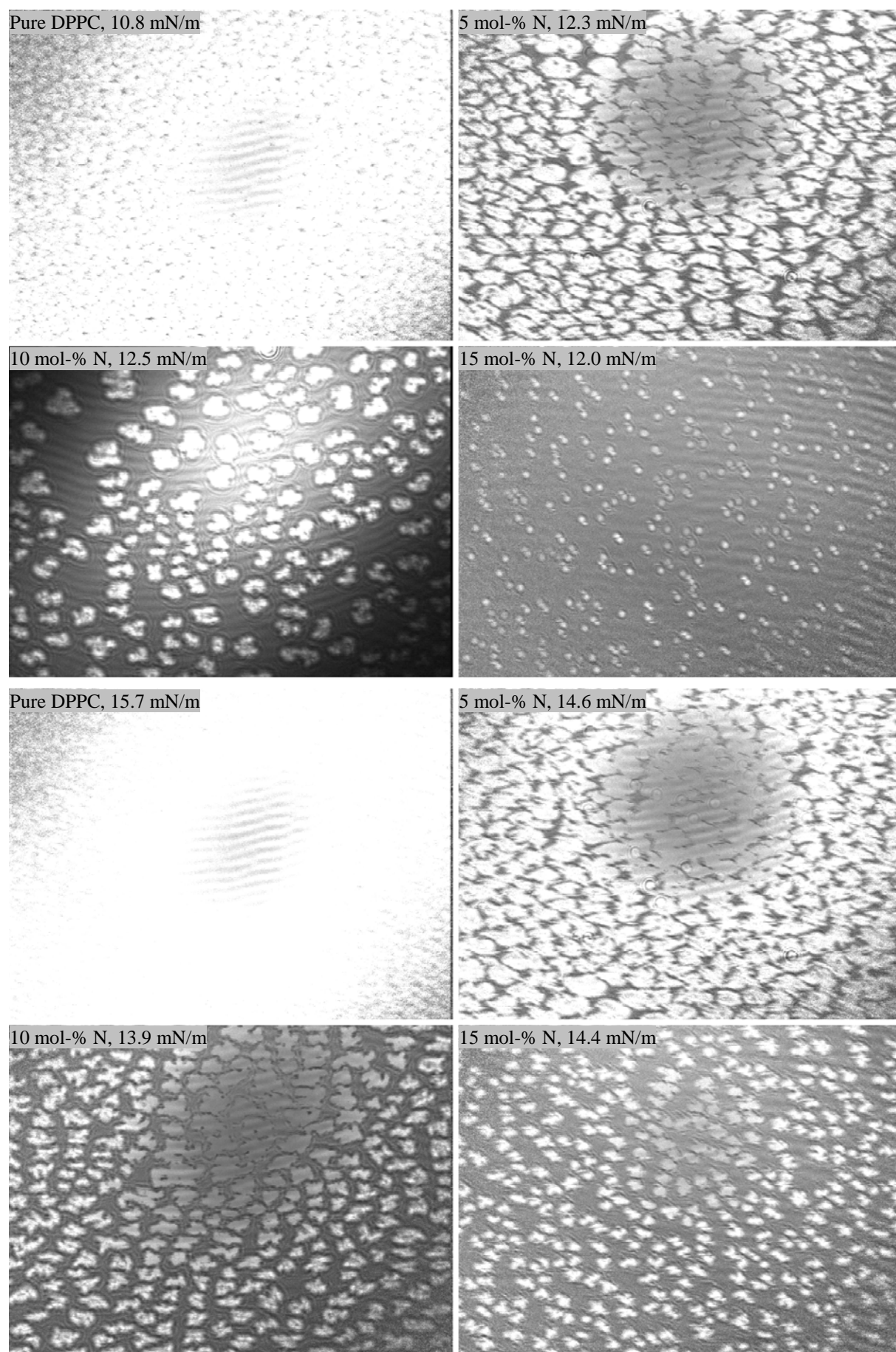


Figure 50. BAM images with different admixing amounts of alkoxyamine N (image width 430 μ m).

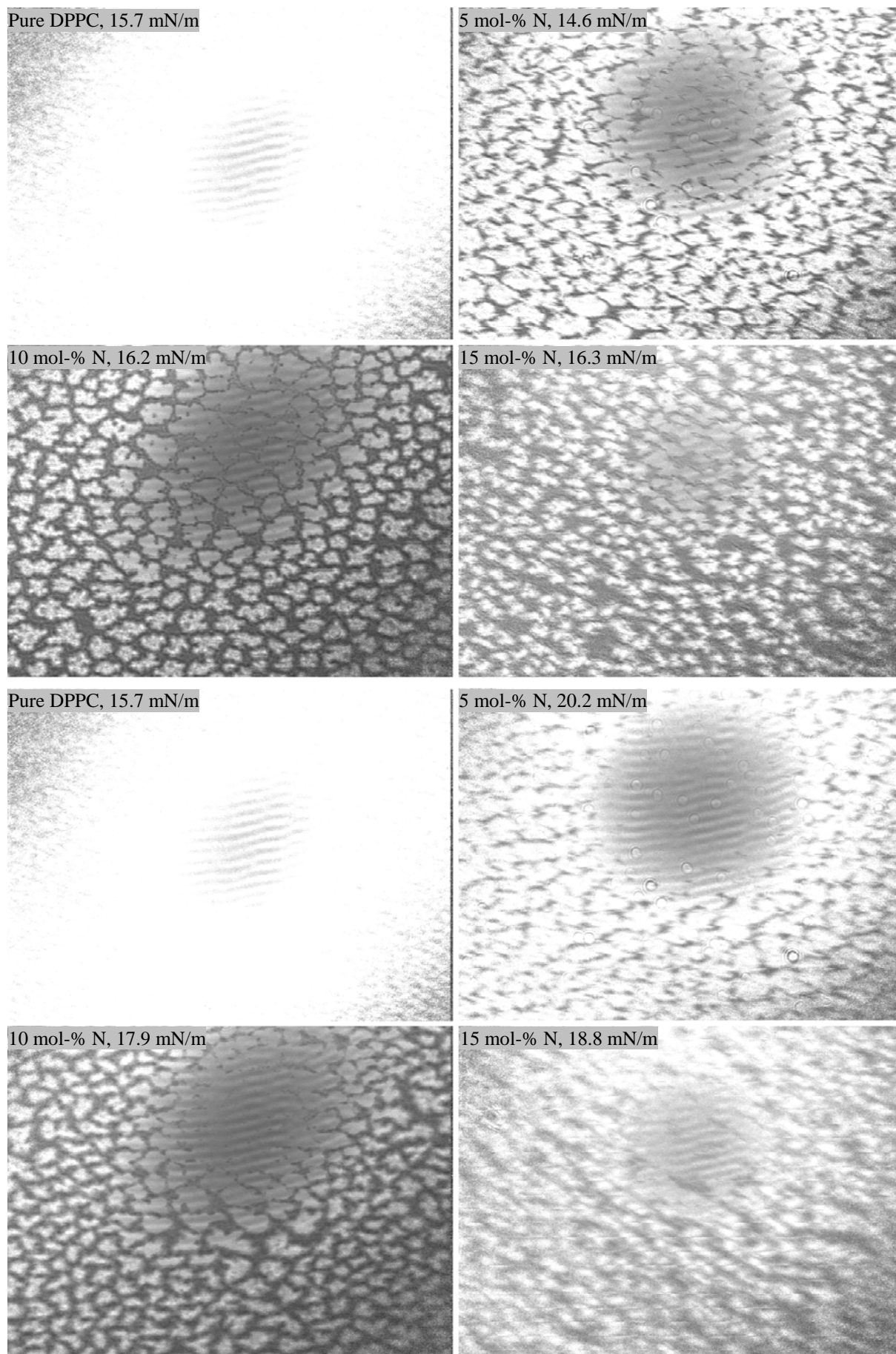


Figure 51. BAM images with different admixing amounts of alkoxyamine N (image width 430 μ m).

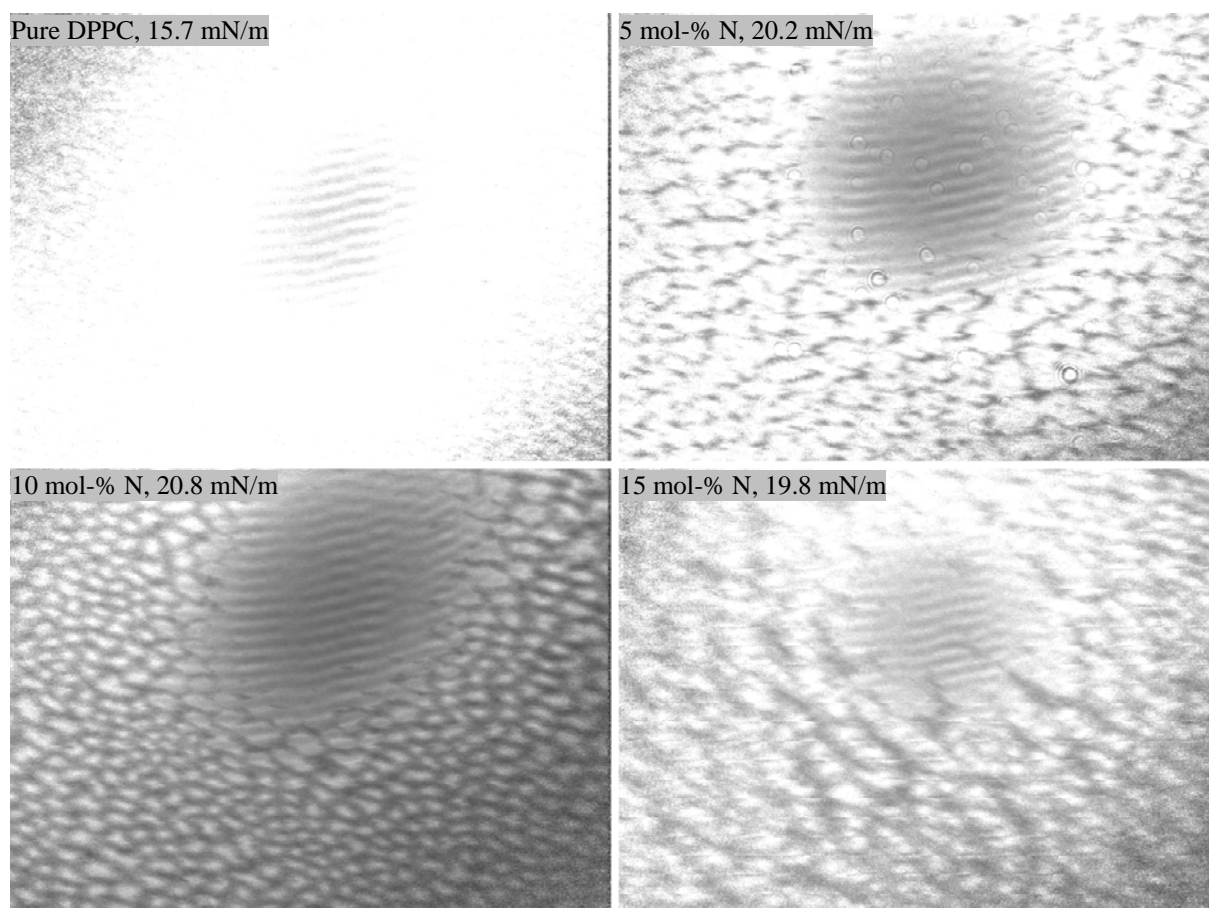


Figure 52. BAM images with different admixing amounts of alkoxyamine N (image width 430 μ m).

While the lateral pressure is increasing the nucleation of LC domains sets in, first in the pure DPPC, then later in the films with admixed alkoxyamine more delayed with increasing amount of admixing. The lateral pressure at the moment where the first LC domains become visible is a little bit higher as it would be indicated by the kink between LE and phase coexistence domain of the corresponding isotherm. This can be understood by taking into account that the LC domains need to grow to a specific size before they can be observed by the BAM, therefore the observed nucleation corresponds well to the recorded isotherms. For further evaluation the relative coverage of the images by LC domains was determined by image processing with self developed software. For this the images were converted into black and white images by a threshold optimized on the intensity of the LE background and then the relative amount of white pixels to black pixels was calculated. Figure 53 shows the resulting graph of relative coverage versus lateral pressure. Looking at images with different amounts of admixing but similar relative coverage a clear difference in domain size and shape can be seen for pure DPPC and DPPC with admixed alkoxyamine: the LC domains of the pure DPPC film grow in a round shape, almost circular (the domains look oval in the BAM images

because they are not corrected for the tilted view angle of the BAM) while the LC domains in the monolayers with admixed alkoxyamine grow very irregular with branches or even small inclusions of LE phase. At the same relative coverage the LC domains of the pure DPPC are smaller and more numerous compared to the domains in films with admixed alkoxyamine.

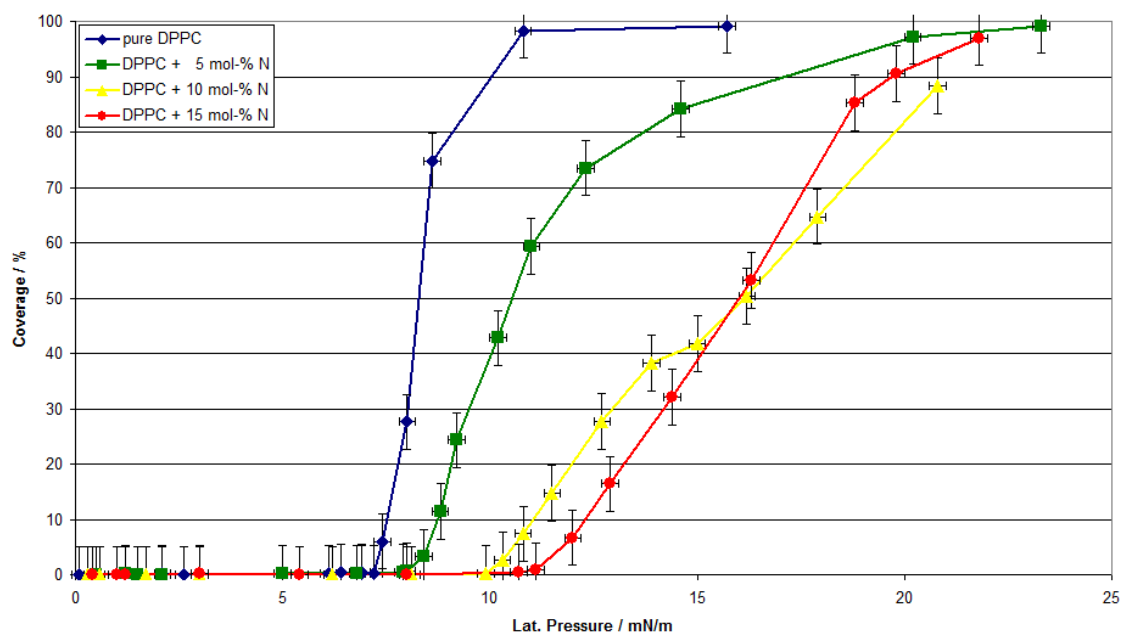


Figure 53. Relative coverage with LC domains in the BAM images versus lateral pressure for different amounts of admixing.

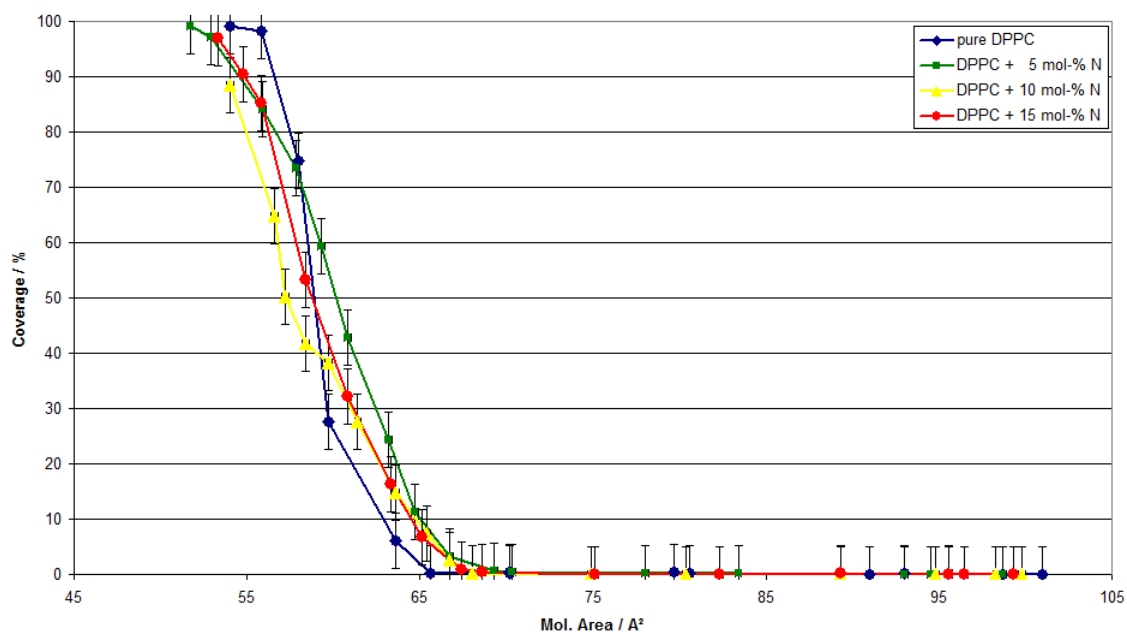


Figure 54. Relative coverage with LC domains in the BAM images versus molecular area for different amounts of admixing.

The graph of relative coverage versus lateral pressure (Figure 53) shows again the delayed onset of nucleation for the films with admixed alkoxyamine. Although the graph for the 10 mol-% looks distorted the overall trend is still clearly visible. The relative coverage rises very quickly for the case of pure DPPC. This abrupt transition is smeared out severely in the case of admixed monolayers. Plotting the relative coverage against the molecular area (Figure 54) reveals another interesting point: although the overall characteristics of all curves are quite similar it can be observed that all curves corresponding to monolayers with admixing have a broadened transition leading to an onset of nucleation at higher molecular areas as compared to pure DPPC with completion of the transition to LC phase at lower molecular area than for pure DPPC at the same time. An interesting point is that the shift in the curve is most pronounced for the 5 mol-% admixing leaving the 10 mol-% and 15 mol-% admixing curves more similar to pure DPPC than the one with the lower admixing. This could correspond to the observation of a minimum in the channel size in the transferred films of other compounds because this also implies that low concentration of admixing can sometimes have bigger implications on the pattern formation than higher ones (within certain borders). This behavior could be mediated by the change in interaction force between the DPPC and the admixing. Smaller amounts of admixing may be integrated into the DPPC film up to a certain concentration when the interaction within the molecules of the admixing also may play a crucial role and therefore lead the film back to more DPPC like behavior.


6.4 Summary

By transferring DPPC monolayers with admixing of different test compounds we further established that this approach constitutes a valid method of patterning a broad variation of chemical compounds onto solid substrates. The mixed layer LB transfer seems feasible for many types of molecules as long as they can form stable monolayers at the air water interface (i.e., are amphiphilic or insoluble in water). Of the examined compounds especially the alkoxyamine offers a route to interesting further experiments due to its intended use as a polymerization initiator.

7 Structured Polymer Brushes by LB-Transfer

7.1 Introduction

Growth of polymers from surfaces has been successfully conducted to tune surface properties such as wettability, bioadhesion and surface activity.^[129-131] Polymer brushes are successfully prepared via covalent attachment of a polymerization initiator onto the surface with subsequent surface initiated polymerization (SIP) via the “grafting from” approach.^[132,133] Atom transfer radical polymerization (ATRP),^[134] nitroxide mediated radical polymerization (NMP)^[135,136] and reversible addition fragmentation transfer polymerization (RAFT)^[137] were used in SIP. Site specific surface polymerization affords spatially controlled polymer brushes. Nanometer-sized structures are of increasing importance in various fields of nanoscale science. Microcontact printing,^[138-141] photo lithography,^[142-144] electron-beam lithography^[145-148] and other techniques were successfully used to spatially control covalent surface binding of the initiator. These techniques belong to the top-down strategies. Alternatively, self-assembly and self-organization offer interesting routes to patterned structures via a bottom-up approach.^[8] Block-copolymer lithography^[149] and nanosphere lithography^[150] belong to this category. Herein we present the use of self-organization to spatially control initiator attachment for the formation of regular stripes of polymer brushes using Langmuir-Blodgett (LB)-lithography.^[25,119] The width and the periodicity of the stripes can be controlled. Moreover, LB-lithography is performed using inexpensive equipment and large areas (several cm²) can be patterned. We have previously shown that mixed monolayers of L- α -dipalmitoyl-phosphatidylcholine (DPPC) and dyes can be transferred onto a mica surface in regular stripes consisting of dyes with submicrometer lateral dimensions by LB-technique.^[91,151] The challenge for the present work was to find a polymerization initiator which a) forms LB-films and b) is transferred to surfaces periodically from mixed monolayers with DPPC and c) contains a reactive functional group for covalent attachment of the polymer initiator onto a Si-wafer (Figure 55). For polymerization technique we chose NMP.^[134,152] The synthesis of the alkoxyamine initiator **4**, which should fulfill all the requirements mentioned above, is depicted in Figure 56.

* This chapter's work was done in close collaboration with the group of Prof. Studer. Dr. Marion Brinks, former PhD student in that group was responsible for the synthesis of the initiator and the polymerization of the brushes. Most of the results were already published in a peer reviewed paper.^[92,210] 

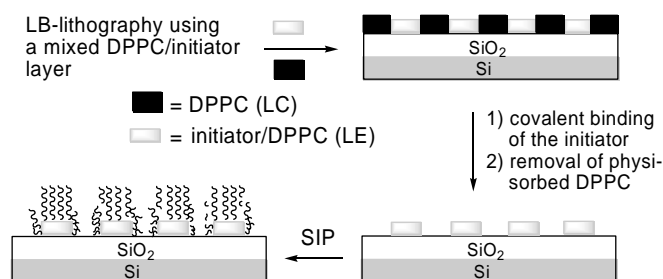


Figure 55. Formation of patterned polymer brushes – the concept (LC = liquid condensed phase, LE = liquid expanded phase).

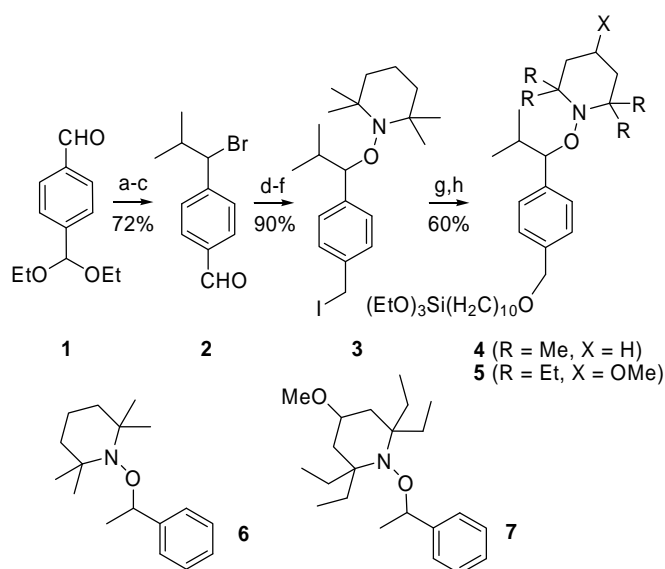


Figure 56. (a) $i\text{PrMgCl}$, Et_2O ; (b) aq. HCl ; (c) HBr (33% in AcOH), CH_2Cl_2 ; (d) TEMPO , Cu , $\text{Cu}(\text{OTf})_2$ (cat), 4,4'-bis-*tert*-butylpyridine (cat), Ph-H ; (e) LAH , THF ; (f) TMSCl , NaI , CH_3CN ; (g) NaH , $\text{CH}_2=\text{CH}(\text{CH}_2)_8\text{OH}$, THF ; (h) $\text{HSi}(\text{OEt})_3$, Karstedt-cat.

7.2 Synthesis of an Amphiphilic Initiator

Reaction of **1** with $i\text{PrMgCl}$ followed by acetal cleavage and subsequent bromination provided bromide **2** (72%). Transformation of **2** into the corresponding alkoxyamine was achieved using 2,2,6,6-tetramethylpiperidine-1-oxy radical (TEMPO) and Cu-catalysis.^[153] Aldehyde reduction (LAH) and iodination with TMSCl/NaI delivered **3**. Etherification using $\text{CH}_2=\text{CH}(\text{CH}_2)_8\text{OH}/\text{NaH}$ and hydrosilylation with Karstedt-catalyst in $\text{HSi}(\text{OEt})_3$ gave **4**. Alkoxyamine **5** bearing a sterically more demanding nitroxide moiety^[154,155] was prepared in an analogous way.

Pleasingly, **4** forms stable monolayers in the mixture with DPPC at the air/water interface.^[156] For the measurement of isotherms 20 μl of the respective solvent was spread onto the water surface and then allowed to evaporate for about 15 min. After that isotherms were measured with a maximum barrier speed of 10 mm/min. The surface pressure area (π -A) isotherms of a pure solution of **4**, of DPPC as well as of a mixture of **4** and DPPC are given in Figure 57.

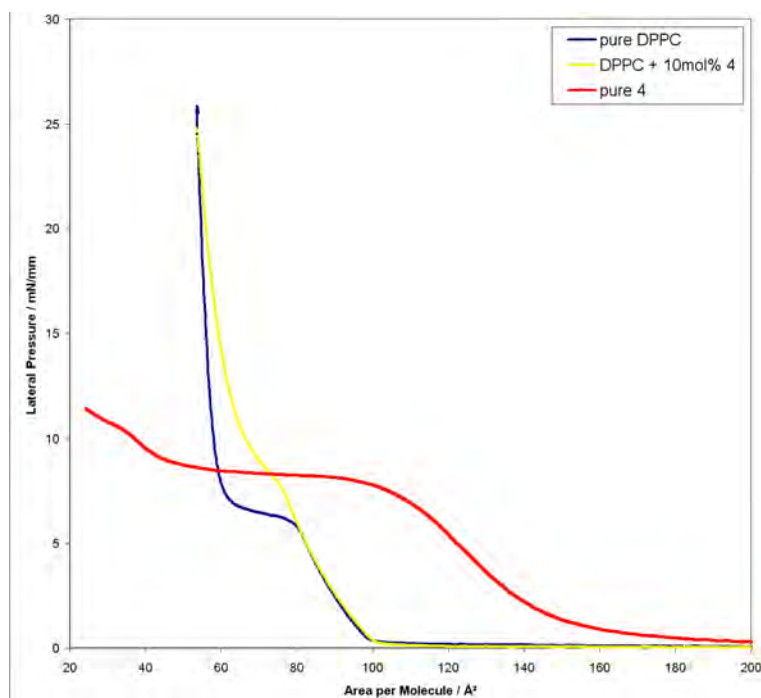


Figure 57. Surface pressure-molecular area (π -A) isotherms of **4**, DPPC and mixed DPPC/**4** (10 mol-% of **4**) monolayers at the air/water interface at room temperature.

7.3 LB Transfer of a DPPC/Initiator Film

In the LE-phase region, the mixed monolayers [DPPC/**4** (2.5 – 15 mol-%)] were transferred to an oxidized Si-wafer by the LB technique. All experiments were conducted in a commercial LB trough (KSV 3000). The subphase (MilliQ DI Water, 18.2 M Ω cm) was temperature controlled at $(24.0 \pm 0.1)^\circ\text{C}$ and the air temperature varied between 24.0 and 24.5 $^\circ\text{C}$. A DPPC solution in chloroform as well as chloroform solutions of **4** and **5** at a concentration of 1 mg/ml were prepared. The DPPC solution was then parted and mixed with a solution containing appropriate amounts of **4** and **5** to yield DPPC solutions with 2.5 mol-%, 5 mol-%, 7.5 mol-%, and 10 mol-% **4**, respectively 10 mol-% **5**. The silicon substrates for the transfer (Si 100, natural oxide layer) were cut into 5 \times 2 cm² pieces and then cleaned subsequently for 10 min each step in chloroform, isopropanol, and DI water (as above) and then treated

with an oxygen plasma (TePla 100-E, 300 W) for 2 min. The substrates were then submerged into the trough and 20 μl of mixed solutions were spread. After waiting for 1 h to allow hydrolyzation of the triethoxy functions of **4** respectively **5** the film was compressed to a lateral pressure of 5.0 mN/m with a maximum barrier speed of 30 mm/min and let rest again for about 10 min to stabilize. Then the substrate was lifted with a speed of 15 mm/min while the lateral pressure was kept constant by further compression. As an example for the typical result of such a procedure the AFM image of a covered Si-wafer prepared with 10 mol-% **4** showing regular stripes of DPPC (width = $0.27 \pm 0.01 \mu\text{m}$) with channels (width = $0.26 \pm 0.02 \mu\text{m}$) consisting of DPPC and **4** is presented in Figure 58a. The height difference between LC stripes and the LE channels is measured to be ca. 1 nm as reported earlier.^[91,151]

7.4 SIP of Structured Polymer Brushes

The covered wafer was then dried at 0.01 bar and at 80 °C under vacuum for 2 h to covalently bind **4** respectively **5** onto the wafer. The physisorbed DPPC was eventually removed by washing with CHCl_3 . To produce PS brushes on surfaces covered with **4** SIP was performed in a Schlenk tube charged with 2,2,6,6-tetramethyl-1-(1-phenyl-ethoxy)-piperidine (**6**) (5.4 mg, 21 μmol , 0.2 mol-%) sacrificial polymerization regulator and styrene (1.18 ml, 10.3 mmol, 1.00 eq).^[134] The tube was subjected to three freeze-thaw cycles. Then the structured silicon wafer containing immobilized alkoxyamine initiator **4** was added and sealed off under argon. The polymerization was carried out under argon at 125 °C for 24 h. The resulting mixture was cooled to room temperature and dissolved in CH_2Cl_2 . The wafer was taken out of the solution and continuously extracted with CH_2Cl_2 for at least 14 h before AFM measurements were carried out. CH_2Cl_2 was removed from the styrene/polystyrene solution under reduced pressure and residual monomer was removed in a vacuum-drying cabinet at 60 °C for 12 h. Conversion was evaluated gravimetrically; molecular weight and polydispersity index (PDI) were determined by size exclusion chromatography yielding a conversion of 73%, $M_n = 32300 \text{ g/mol}$, PDI = 1.30. Initiator **4** is somewhat limited to the polymerization of styrene. On the contrary initiator **5** is capable of polymerizing styrene as well as acrylates.^[134] The SIP procedures for surfaces covered with **5** are similar to the one stated above with the difference that 2,2,6,6-tetraethyl-4-methoxy-1-(1-phenyl-ethoxy)-piperidine (**7**) (6.4 mg, 18 μmol , 0.2 mol-% for styrene, 5.3 mg, 15 μmol , 2mol-% for the acrylate) was used as sacrificial polymerization regulator. The polymerization of styrene (1.06 ml, 9.21 mmol, 1.00 eq) and n-butyl acrylate (1.09 ml, 7.63 mmol, 1.00 eq) was also

done under argon for 24 h but the temperature (105 °C) was slightly lower than in the case of **4**. The post-polymerization procedure was the same as already given for **4** (Conversion = 76%; $M_n = 29400$ g/mol; PDI = 1.21 for styrene, Conversion = 67%; $M_n = 43800$ g/mol; PDI = 1.21 for acrylate).

7.5 Results and Discussion

AFM images of the polymerized surfaces show the formation of regular stripes of polymer brushes. For instance, using 10 mol-% of **4** after LB-lithography and SIP resulted in PS brushes with 0.20 ± 0.02 μm channel width and 0.26 ± 0.03 μm stripe width. The height of the stripes increased to 8.0 ± 0.2 nm (Figure 58b).

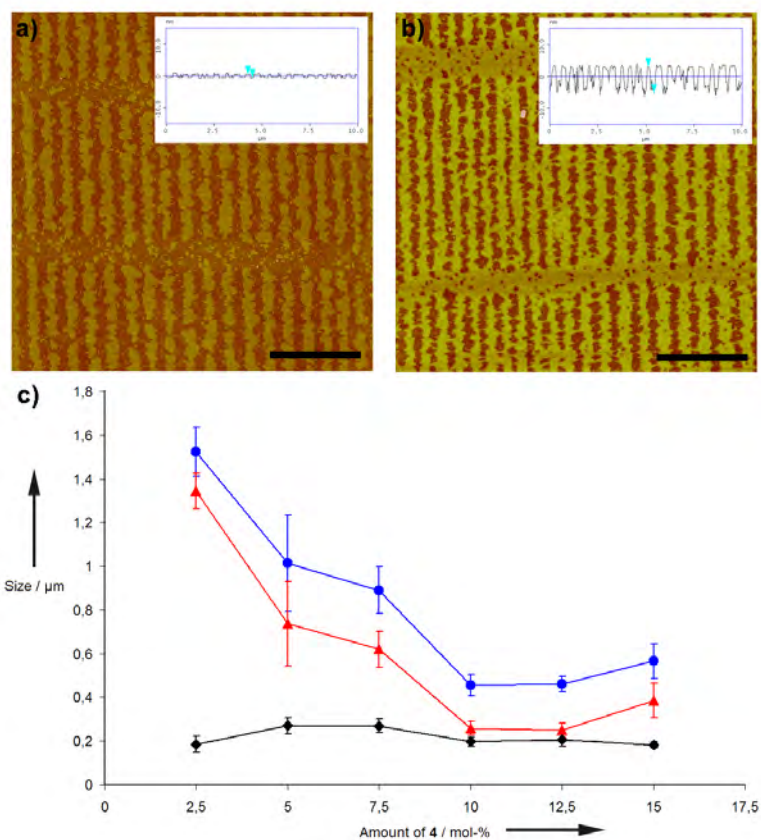


Figure 58. AFM image of a sample prepared with 10 mol-% of **4** (a) before and (b) after SIP of styrene (insets show sections, black bar equals 2.5 μm). (c) Periodicity (sum of stripe and channel size, blue circles), the size of stripes (red triangles) and the size of channels (black diamonds) depending on the amount of **4**. To visualize the trends, experimentally determined values are interconnected.

Smallest stripes were obtained for the 10 and 12.5 mol-% experiments. Lowering as well as increasing the amount of **4** provided wider stripes while the channel width remained nearly constant (Figure 58c).

To characterize the polymer brushes further the density of the chains on the wafer can be determined from the brush height and the number-average molecular weight (M_n) of the surface bound polymer.^[157] The graft density σ was estimated from

$$\sigma = L\rho N_A/M_n \quad (56)$$

where L is the thickness of graft layer (determined by AFM-measurements), ρ is the bulk density of the polymer (0.906 g/cm³ for styrene), N_A is the Avogadro number and M_n is the number-average molecular weight.^[158] M_n is determined on the polymer synthesized in solution with the sacrificial alkoxyamine initiator.^[157] The calculated graft densities σ of the polystyrene chains prepared from immobilized alkoxyamine initiator **4** are presented in Table 4.

Table 4. Chain densities of the structured wafers derived from immobilized alkoxyamine initiator **4**.

percentage of admixing of 4 [%]	height L [nm]	M_n [g/mol] of polymer synthesized in solution (PDI)	chain density σ [nm ²]
2.5	4.5 ± 0.1	22 850 (1.28)	0.11
5.0	3.7 ± 0.2	22 000 (1.23)	0.09
7.5	6.8 ± 0.2	32 900 (1.28)	0.11
10.0	8.0 ± 0.2	32 300 (1.30)	0.14
12.5	7.0 ± 0.2	31 400 (1.23)	0.12
15.0	10.0 ± 0.2	40 400 (1.35)	0.14

Densities ranging from 0.09 to 0.14 chains/nm² were calculated which proves that the brushes are in the semi-diluted regime.^[158] The brush heights obtained are typical for dry polymer brushes in the semi-diluted regime. Due to the rather low density brush thickness cannot be further increased upon increasing the reaction time.^[157]

It is known that NMP using TEMPO as a mediator is restricted to styrene derivatives.^[134] To employ our methodology to acrylic acid derivatives we conducted the surface modification

with **5** bearing a nitroxide which is able to control acrylate polymerization.^[154,155] LB lithography was performed using a mixed DPPC/**5**-monolayer containing 10 mol-% of **5**. The regularity of stripe pattern improved significantly indicating a better compatibility of **5** with DPPC. Also vertical stripes appearing with mixtures of **4** in higher concentrations decreased. SIP in neat styrene containing sacrificial **7** for 2 h delivered regular styrene stripes with an average height of 5.3 ± 0.2 nm (Figure 59a). We also performed n-butyl acrylate SIP in neat n-butyl acrylate containing **7** at 105 °C for 24 h. After rinsing, regularly patterned *poly*-n-butyl acrylate brushes were obtained (height = 4.7 ± 0.2 nm, stripe width = 0.18 ± 0.03 μm, channel width = 0.29 ± 0.05 μm, Figure 59b).

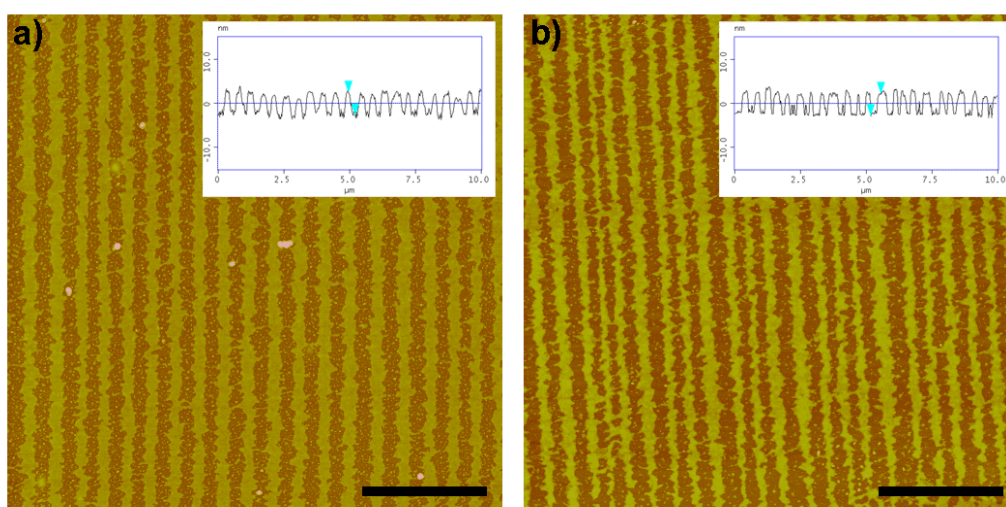


Figure 59. (a) AFM image after SIP of styrene using **5**. (b) AFM image after SIP of n-butyl acrylate using **5** (insets show sections, black bar equals 2.5 μm).

The DPPC stripe patterns can generally extend over large surface areas^[91]. Here the typical dimension of the substrates used during LB deposition was 5×2 cm². Unfortunately a quick large area survey by optical means was not feasible for our system because of the small periodicity and the thin film thickness. Alternatively AFM images were taken at several different positions all over the substrate to make sure that the whole substrate was covered uniformly by the stripe pattern. These random sample images show a complete coverage of the substrate by the alternating DPPC (LE) mixed with alkoxyamine initiator / DPPC (LC) stripe pattern over the whole sample surface. The primary substrates were then cut into smaller pieces (10×5 mm²) for the SIP. After the SIP once again several locations all over each sample were checked to ensure the uniformity of the polymerized pattern. A typical sample image is shown in Figure 60.

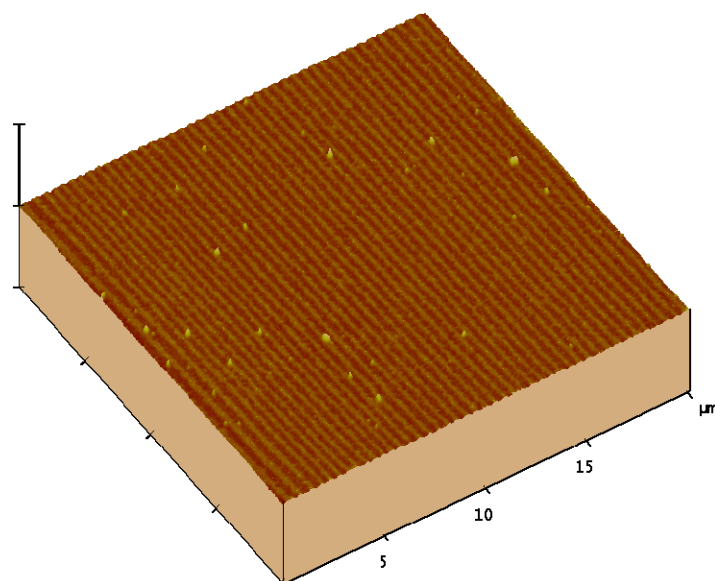


Figure 60. 20×20 μm² AFM image of a sample with 10 mol-% of **5** after SIP of styrene.

7.6 Summary and Conclusion


In conclusion LB-lithography based on dynamic self-assembly can be used for site specific covalent immobilization of radical initiators on a Si-wafer. Nitroxide mediated SIP delivers regular stripes of polystyrene and polyacrylate brushes. The polymer stripe width can be adjusted ranging from about 0.2 to 1.3 μm. This technique can be performed using inexpensive equipment and large surface areas up to square centimeters can readily be patterned.

8 AFM Lithography on Polymer Brushes

8.1 Introduction

Structured polymer surfaces have gained increased attention in various research fields during the past few years. By structuring of polymer surfaces, in particular of polymer brushes, functional surfaces with defined properties, e.g., for the study of cell adhesion^[159,160] and of cell alignment^[161,162] have been prepared. Moreover, patterning of polymer brushes allows to alter and to control their wetting properties.^[163] Patterned polymer brushes can be obtained by different methods including top down approaches such as electron beam chemical lithography (EBCL),^[145,5,6] photo lithography,^[164] dip-pen lithography^[165] or microcontact printing (μ CP)^[138,166] and bottom up methods such as Langmuir-Blodgett (LB) lithography.^[92] These methods mainly rely on a “grafting from” approach in which lithography is used to site selectively initiate a polymerization process or to site selectively install a polymerization initiator. In the latter case, subsequent polymerization eventually leads to structured polymer brushes. In addition, studies on the mechanical manipulation (nanoscratching/nanoshaving) of polymer films prepared by spin-coating,^[167] as well as SAMs^[7,168,169] and the nanowear of different polymer film architectures^[170] have been performed and even heated AFM tips were used for lithographic processes on polymer films^[171].

Herein we present an alternative approach to obtain structured polymer brushes by mechanical nanoscratching with AFM lithography. We will show that this method works very well for structuring polymer brushes whereas moderate results are obtained by nanoscratching of spin-coated polymer films. To the best of our knowledge, intentional scratching of polymer brushes by an AFM tip has not been reported to date whereas AFM lithography on spin-coated films is known.^[167] Furthermore, we will demonstrate that site selective immobilization of functionalized materials such as dyes (lissamine rhodamine B derivatives and boron-dipyrromethene (BODIPY) derivatives) into these structured polymer brushes can be achieved.

* This chapter’s work was done in close collaboration with the group of Prof. Studer. Dr. Marion Brinks, former PhD student in that group was responsible for the polymerization of the brushes. Saskia Miele, one of Prof. Studer’s PhD students, synthesized/modified and applied the dyes and polymerized the PNIPAM brushes used in the experiments. The results were partly already published in a peer reviewed paper.^[211] 

8.2 Preparation of Polymer Brushes

Various controlled radical polymerization techniques such as atom transfer radical polymerization (ATRP),^[135,136] reversible addition-fragmentation chain transfer (RAFT)^[137] and nitroxide mediated polymerization (NMP)^[134,172,152] have been successfully applied for the preparation of polymer brushes by surface initiated radical polymerization (SIP). The thin films of brush polymer in the present studies were prepared by using NMP on oxidized silicon wafers containing a 300 nm oxide layer (Figure 61).

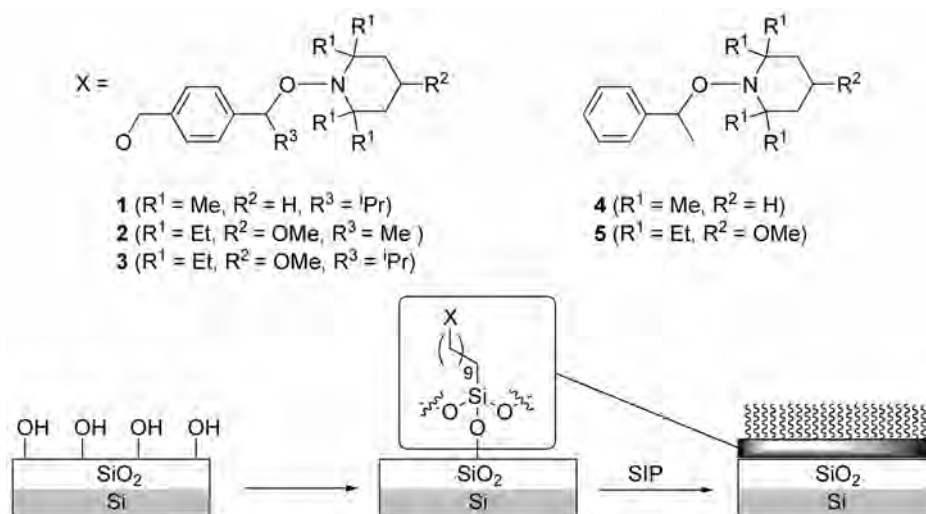


Figure 61. Immobilization of alkoxyamine initiators and surface initiated polymerization by using NMP.

Immobilization of the polymerization initiators **1-3** was achieved by transsilyletherification on the oxidized Si-wafer: therefore the silicon wafers were cleaned by sonication in solvents of increasing polarity (pentane, CH₂Cl₂, acetone, methanol, ultrapure water) for 5 min. The clean surfaces were oxidized with freshly prepared piranha solution (conc. H₂SO₄/H₂O₂ (30%) = 7:3) for 45 min. The surfaces were rinsed again with ultrapure water and blown dry with argon. The oxidized wafers were placed into a sealed tube and a solution of **1**, respectively **2** or **3**, was added (1.5 mL, 10 mmolar in abs. toluene). The mixture was allowed to stand at 60 °C (**1**), respectively room temperature (**2, 3**) for 3 days. The surfaces were purged with CH₂Cl₂ followed by soxhlet extraction for at least 14 h in CH₂Cl₂. After this procedure SIP was performed by placing the initiator covered wafer into neat styrene (125 °C, polystyrene (PS) brushes) or neat *n*-butyl acrylate (105 °C, poly *n*-butyl acrylate (PNBA) brushes) in the presence of a sacrificial alkoxyamine **4** or **5**, respectively. poly *N*-isopropylacrylamide (PNIPAM) brushes were obtained by SIP in a solution of NIPAM in C₆D₆ (125 °C). Basically the procedure was the same to the one for the polymer brush stripes

described in Section 7.4, only that the SIP took place on silicon wafers uniformly covered with the initiator. For control experiments polymers synthesized under standard NMP conditions were used for spin-coating. For a better comparison the polymers used in the spin-coating process had about the same molecular weight as the polymers of the brushes which are covalently bound to the wafer.

8.3 General Lithography Procedure

AFM lithography experiments were performed on a Dimension 3000 AFM equipped with silicon tapping mode cantilevers ($k \sim 42$ N/m) operating in contact mode and if not stated otherwise at a set-point of 5 V yielding a loading force of about 22 μ N. The lithographic pattern, as shown in Figure 62, consists of six single scan lines. The first on the left of the field is written from top to bottom consecutively followed by lines with decreasing distances in-between (2.0 μ m, 1.5 μ m, 1.0 μ m, 500 nm, 200 nm) and a 1 μ m x 1 μ m square that is written by 20 overlapping scan lines (line distance 50 nm, deviations are due to the drift of the microscope during lithography). After AFM lithography the structured wafers were washed with chloroform by using sonication to remove the scratched out polymer.

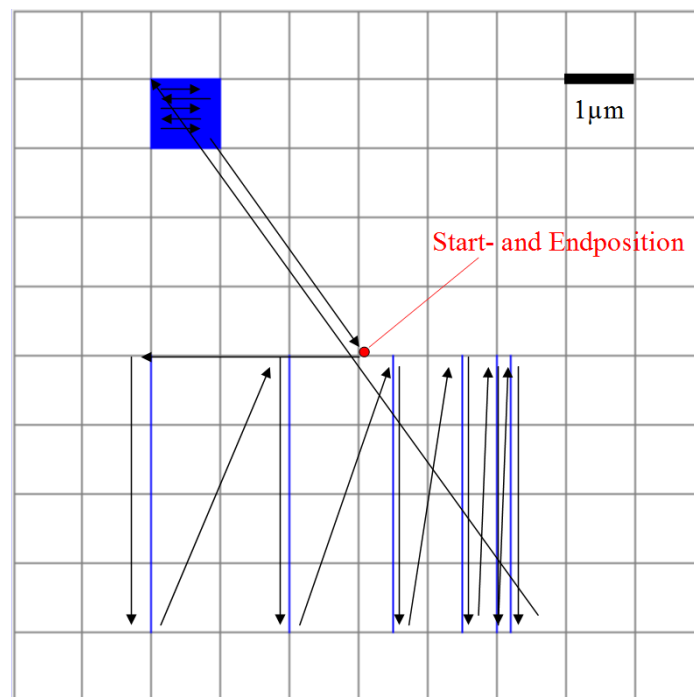


Figure 62. Schematic outline of the lithographic layout.

8.4 Lithography Results

Results of such a lithographic procedure on different polymer brushes and in comparison on spin-coated films are shown in Figure 63.

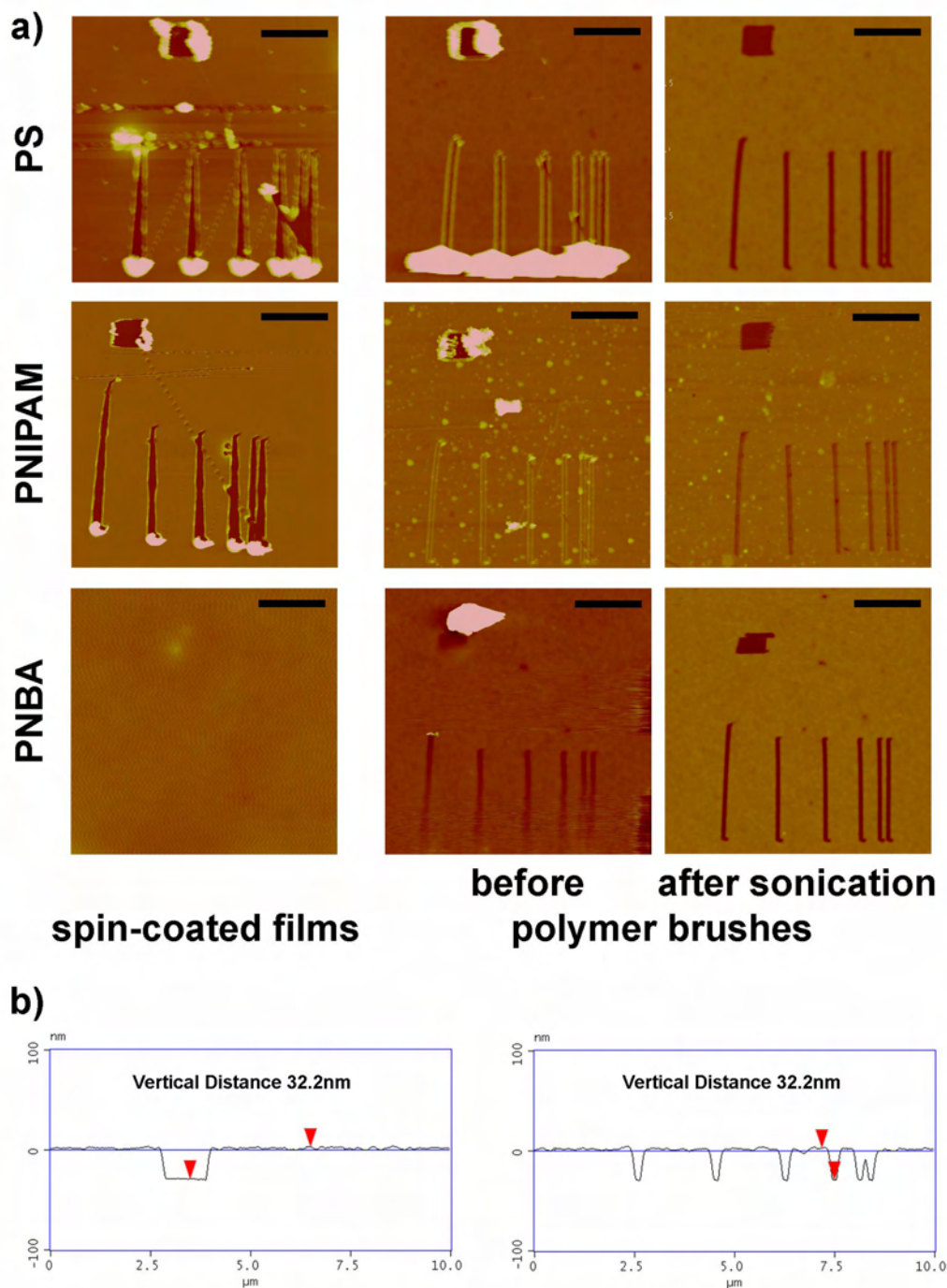


Figure 63. (a) Comparison of the different polymers (top row PS, middle row PNIPAM, bottom row PNBA) after lithography, either spin-coated film (left column) or polymer brushes before (middle column) and after (right column) sonication of 20 s in chloroform, film thicknesses around 25 nm (black bars represent 2.5 μm). (b) Sections of PS brush after sonication through the written square (left) and the single scan lines (right).

The comparison of lithography on spin-coated films and polymer brushes reveals obvious qualitative differences as shown in Figure 63a. The polymers investigated in this work can be categorized into two groups, the more crystalline PS and PNIPAM and the comparatively soft and viscous PNBA. Evidently the lithography results reflect these differences. The PS and PNIPAM systems show similar results in lithography. The single scan lines broaden in scan-direction by more than four times by going from polymer brushes to spin-coated wafers (from 100 nm to 450 nm) due to the dragging of polymer by the tip. The excavated material is clearly visible at the end of the grooves (Figure 63a, upper and middle image on the left). Overall, the scratch borders are not well defined and some material is also piled on the rim of the scratch on spin-coated films. No broadening of scan lines is observed on scratched PS and PNIPAM brushes although the scratched out material is clearly visible at the end and to a smaller extent at the rims of the groove. This implies a smaller adhesive force of the spin-coated films to the substrate than of the cohesive force within the polymer film, so that further material is dragged along with the moving tip. In the case of the polymer brushes the cohesive forces cannot overcome the binding of the brushes to the substrate, hence leaving the vicinity of the scratched areas intact. Another considerable advantage of the polymer brushes is the feasibility of cleaning the sample after lithography by sonication. While spin-coated films were washed away completely, only the material scratched out gets removed from the polymer brushes. The images in the right column of Figure 63a show the polymer brushes after sonication in chloroform for 20 seconds. The excavated material is removed completely at the end of the scan lines as well as at the rims leaving the clean lithographic pattern. In the case of PNBA covered wafers the difference between AFM lithography on spin-coated films and on polymer brushes is even more pronounced. Here lithography by AFM on the spin-coated film is impossible because the resulting scratches are immediately filled up again by the reflow of the previously scratched polymer (curing of the scratches, lower left image in Figure 63a). The lithographic pattern is however recognizable on the PNBA brush, although the pattern is partially filled with reflowing material (lower middle image in Figure 63a). After sonication this reflowing material is removed and the pattern becomes clearly visible (lower right image in Figure 63a).

The section analysis of the pattern on a PS brush shows that the square area as well as the single scan lines were written down to the substrate (silicon oxide layer). The footprint of the single scan lines is about 100 nm (Figure 63b). To demonstrate the stability and resolution of the lithographic process on polymer brushes, we used an altered pattern design consisting of

multiple single scan lines as shown in Figure 64a. Line structures in 200 nm periodicity were achieved. All lines are well defined showing no broadening. Due to the stability of the structure, even second writing over the existing scratched lines (perpendicular to the first scratch direction) is possible resulting in pillar structures shown in Figure 64b.

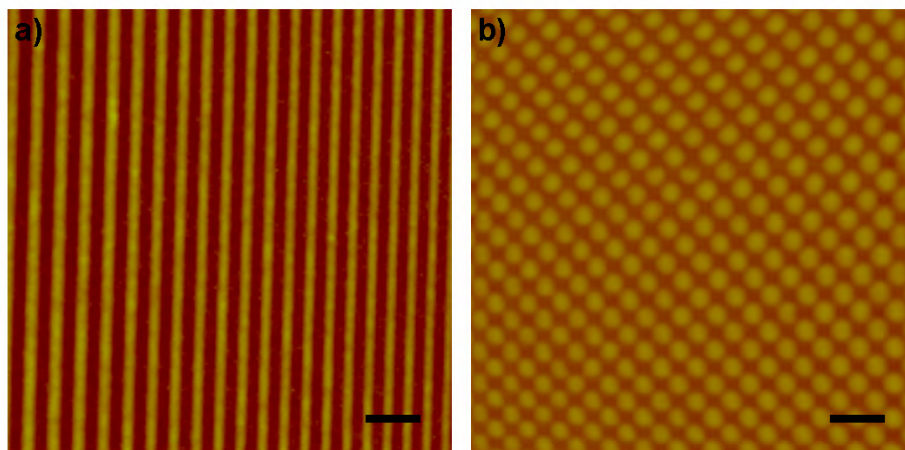


Figure 64. (a) Multiple single scan lines with periodicity of 200 nm on a PS brush. (b) Array of 200 nm diameter pillars achieved by perpendicular writing of single scan lines with 200 nm periodicity (32 nm thickness, black bars represent 600 nm).

The lithography process is highly reproducible and does not seem to depend crucially on the exact loading force or polymer film thickness as long as a certain threshold force is overcome. To clarify the threshold force needed, single scan lines with increasing and decreasing loading forces as shown in Figure 65 were written (in this case on a PS brush of 20 nm thickness).

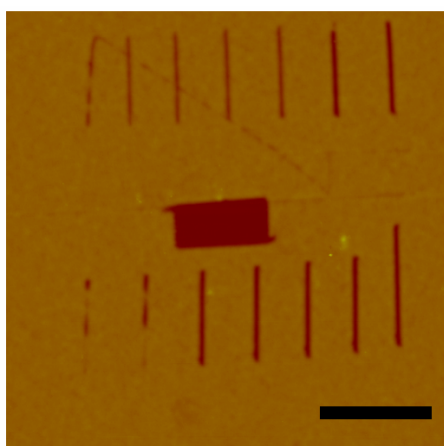


Figure 65. Single scan lines written with increasing (upper row) and decreasing (lower row) loading forces on a PS brush (20 nm thickness, black bar represents 2.5 μm).

The scan lines were prepared starting from left in the upper row with a low loading force of 1.3 μN . Six further scan lines were written with an increasing loading force of 2.6 μN , 4.0 μN , 5.3 μN , 6.6 μN , 7.9 μN , and 9.2 μN , respectively, followed by scratching of the lower seven scan lines, now beginning from the right with decreasing loading forces. A loading force of 1.3 μN causes only an incomplete scratching of the polymer brushes leaving a disconnected line. In the range of 2.6 to 6.6 μN continuous lines can be achieved, but the scratches do not penetrate the whole polymer film (only about half of it), probably resulting from partial polymer removal or thinning of the brush density. From 7.9 μN the substrate bottom (silicon oxide layer of the wafer) is reached. Higher loading forces (9.2 μN and higher) do not change the outcome of a single scan line. The line scans with decreasing loading force are stable and completely penetrate the polymer film down to a loading force of 4.0 μN . The scan lines were disconnected at lower loading forces. The hysteresis effects observed by increasing or decreasing loading forces can be understood by considering substantial modification of the tip at a force of 7.9 μN (Figure 66). The initially sharp tip applies a high pressure onto the substrate even with comparatively small loading forces due to its small contact area. Because this contact area is not well defined with changing tips and due to minor modification by wear within one tip the lithography results tend to be poorly reproducible in the middle loading force range. At a certain point the loading force becomes high enough to flatten the tip apex substantially yielding contact areas with a diameter of about 100 nm (Figure 67) corresponding to the observed width of single scan lines. Since the tip does not change to a great extent with even higher loading forces the lithography process becomes reproducible and reliable even after many subsequent pattern writings. Decreasing the loading force on such a modified tip results in reliable writing of single scan lines down to a loading force of about 4.0 μN .

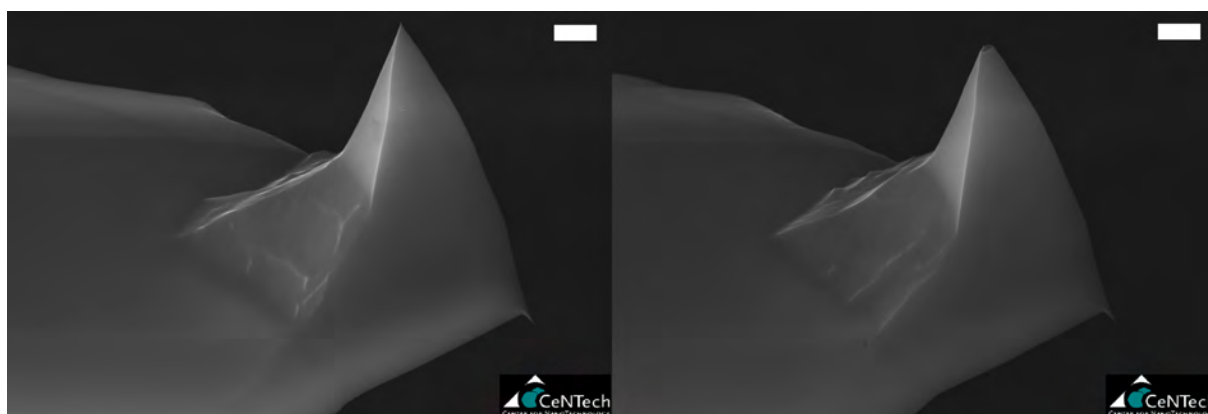


Figure 66. New cantilever (left) and used cantilever after lithography with an applied loading force of about 22 μN (right). White bar represents 2 μm .

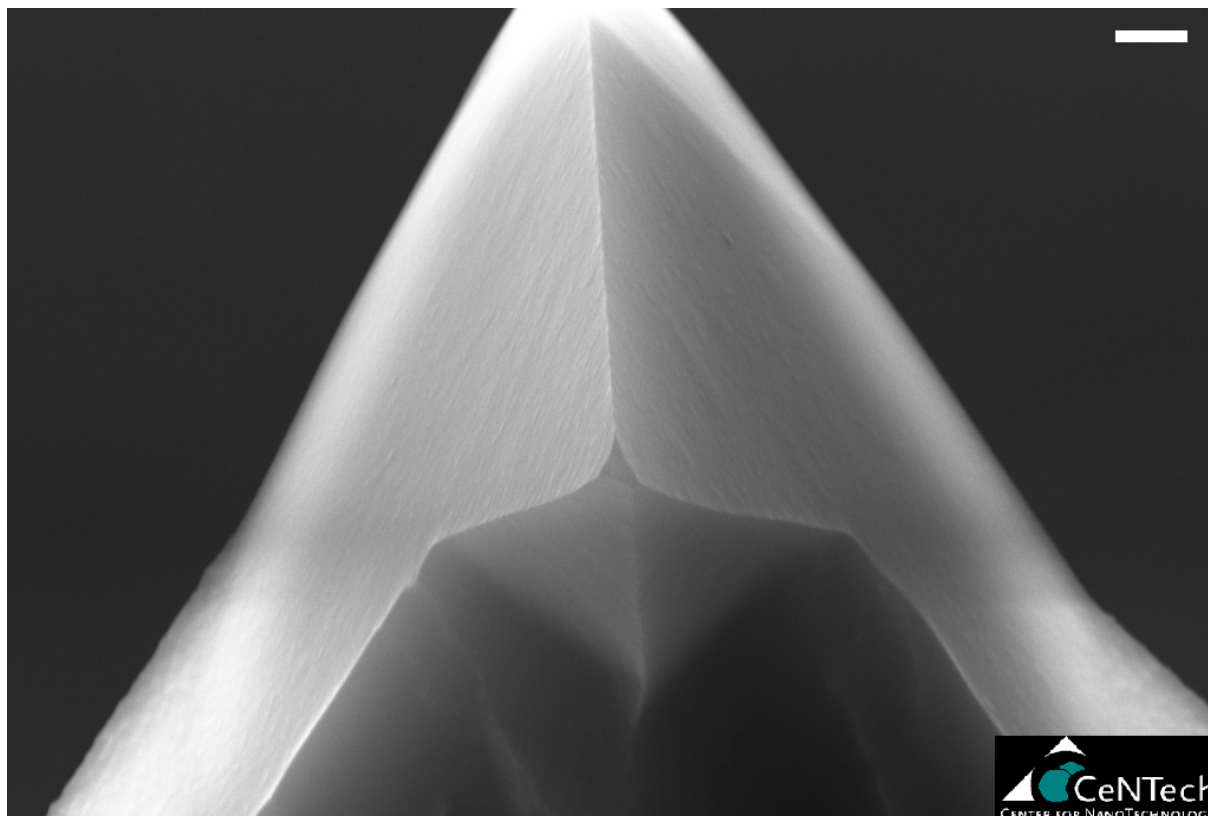


Figure 67. Cantilever after lithography with an applied loading force of about $22\mu\text{N}$. White bar represents $1\mu\text{m}$.

The size of the flattened area at the tip apex was found to be about $0.16\mu\text{m}^2$ on electron micrographs yielding estimated contact pressures of 49 GPa at the threshold force ($7.9\mu\text{N}$) and 25 GPa at $4.0\mu\text{N}$, respectively. Even for the high loading force of $22\mu\text{N}$ (approximately 138 GPa) used in the regular lithographic procedures no substantial modification of naked silicon oxide surfaces was observed. Overall the range of needed loading forces is comparable to preliminary studies of the removal of an alkyl silane monolayer by AFM lithography.^[173,174]

8.5 Immobilization of Dyes

The stability of the polymer brushes towards solvents allows us to further process the scratched brushes in solution (scheme depicted in Figure 68). This would not be possible on spin-coated polymer films. As an example we used the pink dye lissamine rhodamine B sulfonyl chloride **6** and alkyl chain conjugated derivatives thereof (**7-9**) to target the brushes or the scratched areas for selective deposition (structures given in Figure 69). Dye immobilization was performed by placing the structured wafer into a CH_2Cl_2 solution containing the dye (0.1mM) for 3 days. After removal of the dye solution the wafer was cleaned by sonication with CH_2Cl_2 and water five minutes each. An AFM image of the

lithographic pattern and fluorescent microscopy images of the resulting dye distribution on a patterned PS brush are shown in Figure 69a and b.

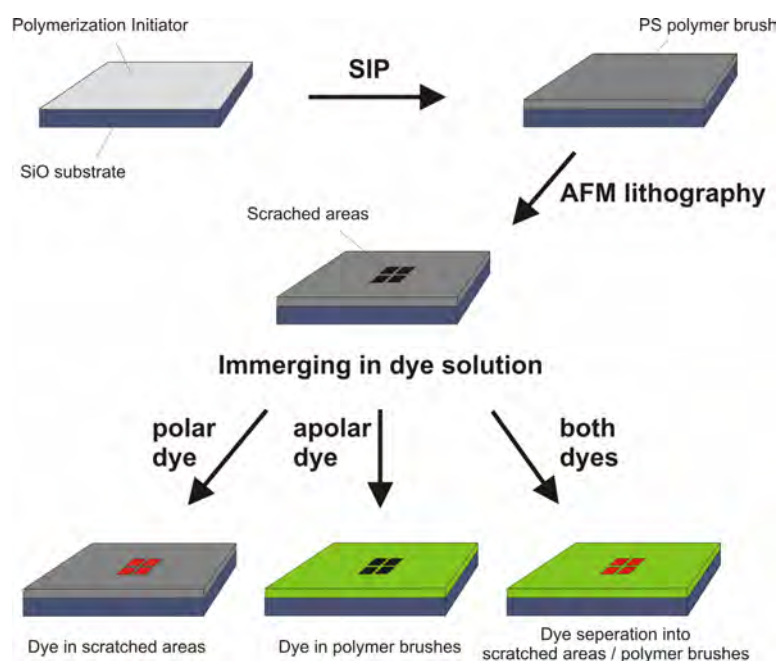


Figure 68. Schematic representation for the process of selective dye deposition onto the scratched areas or polymer brushes.

Interestingly, the polar dye **6** does not enter the polymer brushes. It selectively adsorbs to the scratched areas (Figure 69b, left image). However, when a C4 hydrocarbon chain is covalently bound to the dye (\rightarrow **7**) the interaction of the dye with the polymeric material becomes stronger, but **7** still adsorbs more in the scratched areas (stronger fluorescence). Attachment of a C7 hydrocarbon chain (\rightarrow **8**) further shifts the dye distribution towards the brush regime, but in the scratched areas dye is still clearly visible. Pleasingly, the dye with a hydrocarbon chain of 10 carbon atoms (\rightarrow **9**) selectively adsorbs on the polymer covered regions. In this case, at the scratched areas of the wafer which are free of polymer brushes no dye adsorption was observed. Hence, depending on the length of the alkyl chain attached to the polar chromophore, the immobilization of the dye molecules either at the brush polymer regime or in the scratched areas can be controlled and adjusted. The site specific dye immobilization is probably caused by intermolecular interactions of the alkyl chain of the dye with the polymer brushes (for **9**) or by hydrogen bonding of the Si-OH groups of the scratched areas with **6**.

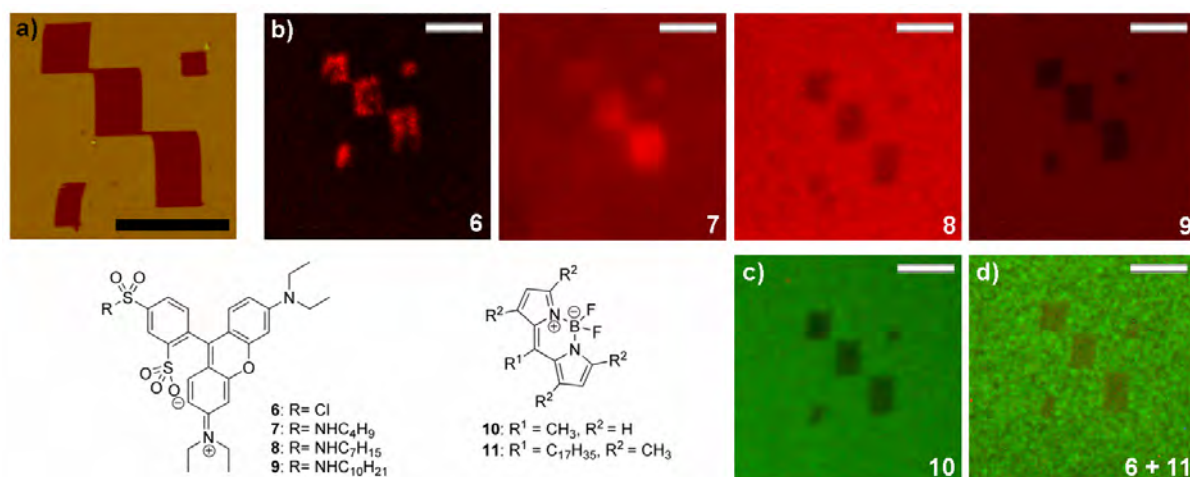


Figure 69. (a) AFM image of a lithographic pattern on a PS brush. Fluorescent microscopy images (b) after placing the structured wafer into a solution of lissamine rhodamine B dyes **6-9**, (c) after placing a structured wafer into a solution of BODIPY dye **10**, and (d) of selective deposition of **6** and **11** onto a PS brush respectively the structured area (bars represent 5 μm).

Furthermore we studied the immobilization of BODIPY dyes (hydrophobic dyes) **10** and **11** and found that both adsorb at the brush region (Figure 69c). Hence, for hydrophobic dyes long alkyl chains are obviously not necessary for immobilization into the brush area. Combining the two types of adsorption behaviors of the dye molecules, we further achieved the selective deposition of two different dyes (BODIPY derivative **11** and lissamine rhodamine B sulfonyl chloride **6**) into the polymer brushes and on the scratched areas on the same sample by exposing the wafer to a CH_2Cl_2 solution containing both dyes (Figure 69d). The hydrophobic BODIPY **11** adsorbs at the brush region and **6** is site specifically immobilized into the scratched area. We believe that this approach is highly promising for selective immobilization of chemical compounds into specific areas of structured brushes.

8.6 Summary and Outlook

In conclusion, we demonstrated substantial differences between spin-coated polymers and polymer brushes during high loading force AFM lithography. Polymer brushes with a thickness of 20-30 nm can be reproducibly structured and scratched down to the substrate (silicon oxide layer of the wafer) even with single scan lines without dragging of material in the vicinity. Equally distanced line structures with 100 nm resolution were achieved in such a simple lithography process. Higher resolution is expected by further parameter optimization (polymer brush system, AFM tip, loading force etc.). Parallel pattern writing by cantilever

arrays is considered for future experiments to enable patterning of larger surface areas in shorter time. The possibility of cleaning the structured polymer brushes by sonication and removing the excavated material without altering non-scratched areas results in lithographic pattern with well defined rims. Furthermore, the stability against solvents allows us to further process the structured wafers in solution. As first examples dye molecules were site selectively immobilized into the structured brushes either into the polymeric region or on the scratched part of the structured wafer. The two different regions of the wafer can be selectively addressed by tuning the chemical structure of the dye. By choosing suitable pairs and modifications different dyes can be immobilized in separate areas (i.e., one in the polymeric and the other in the scratched areas) on the same sample.

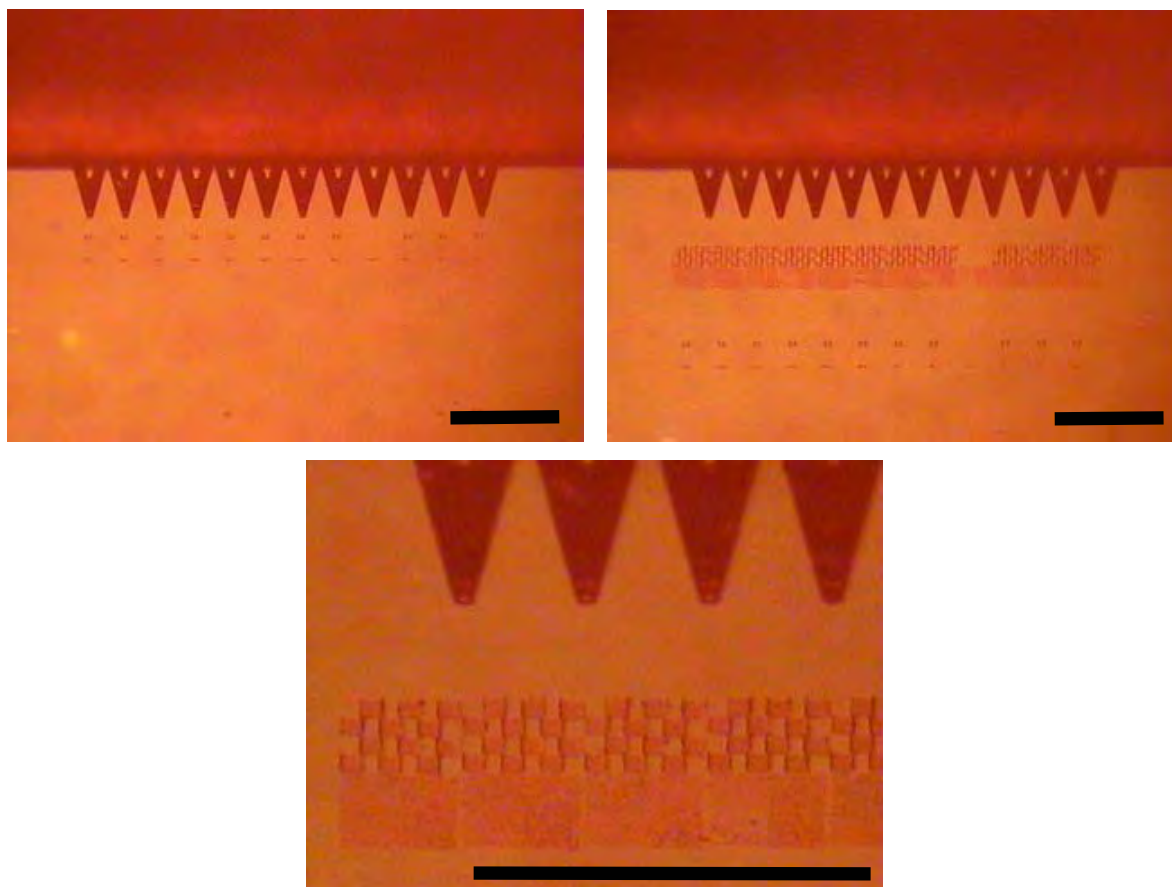


Figure 70. Parallel pattern writing with a one dimensional cantilever array. Black bars represent 200 μ m.

Some preliminary experiments* with cantilever arrays demonstrate the feasibility of parallel pattern writing to achieve large area patterning. This is one of the key requirements for the use of such substrates in cell culture experiments which usually require a large area patterning not accessible in a reasonable time scale with sequential writing. Figure 70 shows a one dimensional array of twelve v-shaped cantilevers before and after writing a chessboard pattern (with squares of 10 μm , 1 μm and 500 nm edge length in a 60 x 80 μm^2 field for each cantilever). A fluorescent microscopy micrograph of one the chessboard patterns after deposition of NBD into the polymer brushes is shown in Figure 71b. The writing performance is already quite good because of the much better position control on this closed loop instrument that enables the precise positioning of elements and well defined lines over large areas (Figure 71a). A problem that still remains is that the cantilever arrays are designed for contact mode application and therefore exhibit a small k constant of 0.5 N/m. To reliably reach the high loading forces needed for the presented type of AFM lithography it would be nice to obtain high k cantilever arrays made from hard materials like silicon oxide. Together with a better force feedback control this would enable an excellent and maximum reproducible method towards the large area patterning of polymer brushes. The functionalizing options of selective deposition of bioactive molecules into the brushes open up an interesting road to produce chemically defined substrates for cell culture experiments.

* These experiments were done at the KIT at the research centre Karlsruhe under the guidance of Dr. Steven Lenhart.

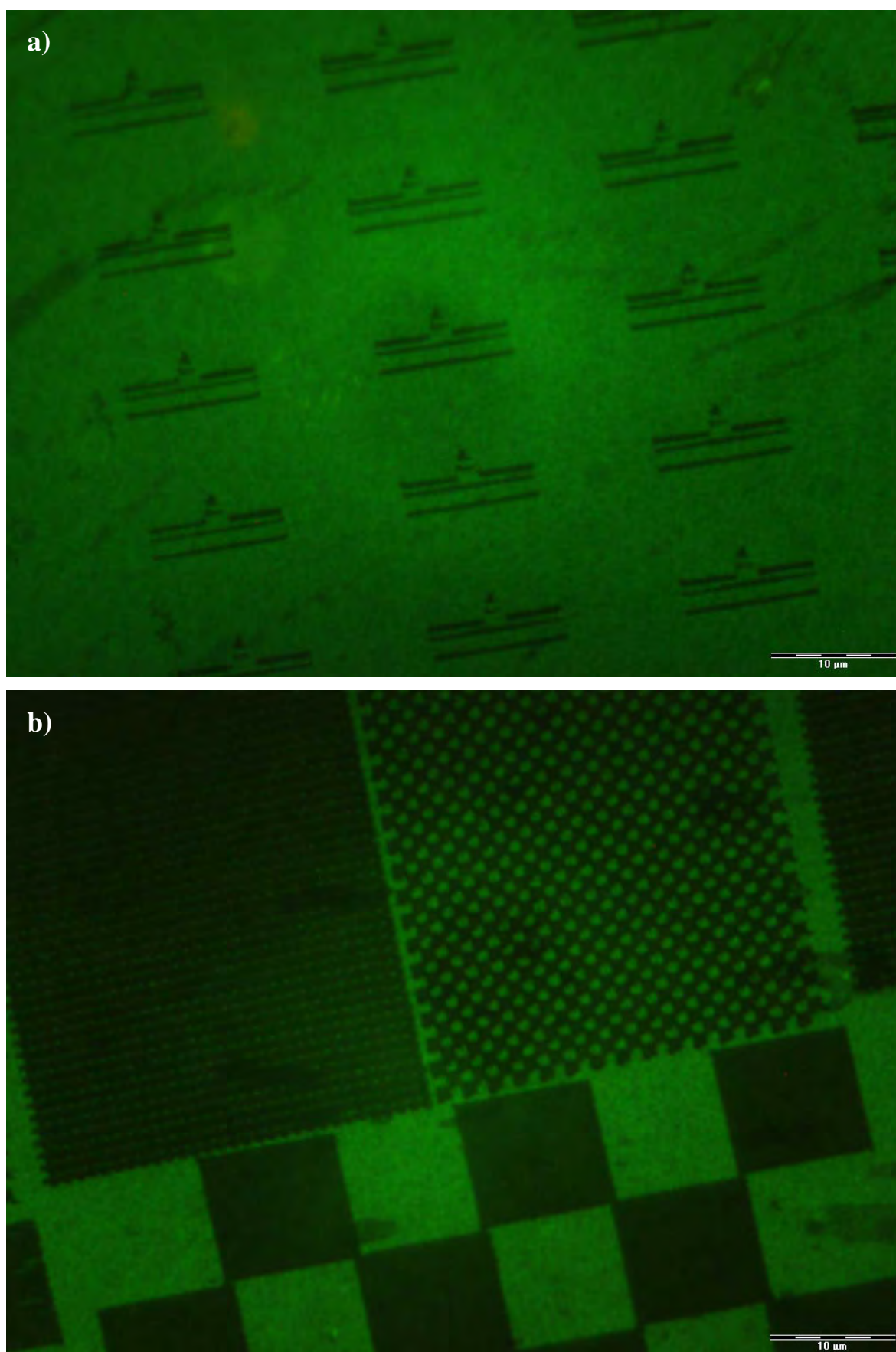


Figure 71. Fluorescent microscopy images of NBD stained PS brushes. (a) Logo of Münster University (b) Parallel written chessboard pattern.

9 MD Simulation of Adenin-C₂₀ on Graphite

9.1 Introduction

The self-assembly of molecules at the solid-liquid or solid-vacuum interface has drawn much interest. They offer an excellent possibility to study the influence of binding force balances and binding networks on pattern formation as well as to investigate interesting surface patterns for further or future use. Here we present our MD simulations on the specific self-assembly system of adenine-C₂₀ on graphite that shows interesting phase transitions upon heating and cooling. Our aim is to elucidate the validity of different structural propositions for the different observed phases and also to shed some light on the thermal stability of the crystal structures.

9.2 The Experimental System

The experiments described in this section were conducted by Dr. Zhongcheng Mu and are not published yet. The overall experiments involved the self-assembly of different alkyl derivatives of thymine and adenine. Here we will only discuss the experiments with adenine-C₂₀ on HOPG where we elucidated the phase behavior with MD simulations. For the self-assembly process a saturated solution of adenine-C₂₀ in phenyloctane was applied onto a freshly cleaved surface of HOPG at room temperature.

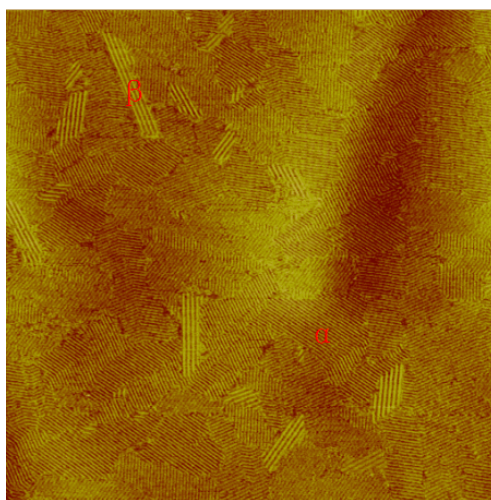


Figure 72. Ordered adenine-C₂₀ structures on HOPG (area 500 × 500 nm²) with narrow-stripe domains (α phase) and wide-stripe domains (β phase).

Figure 72 shows a typical result of such a self-assembly process. Ordered structures in form of a stripe pattern are visible over a wide area of the substrate. Two different kinds of domains can be observed: a narrow-striped one (termed α phase from now on) with a stripe distance of about 3.3 nm and a wide-striped one (termed β phase from now on) with an increased inter-stripe distance of 4.9 nm.

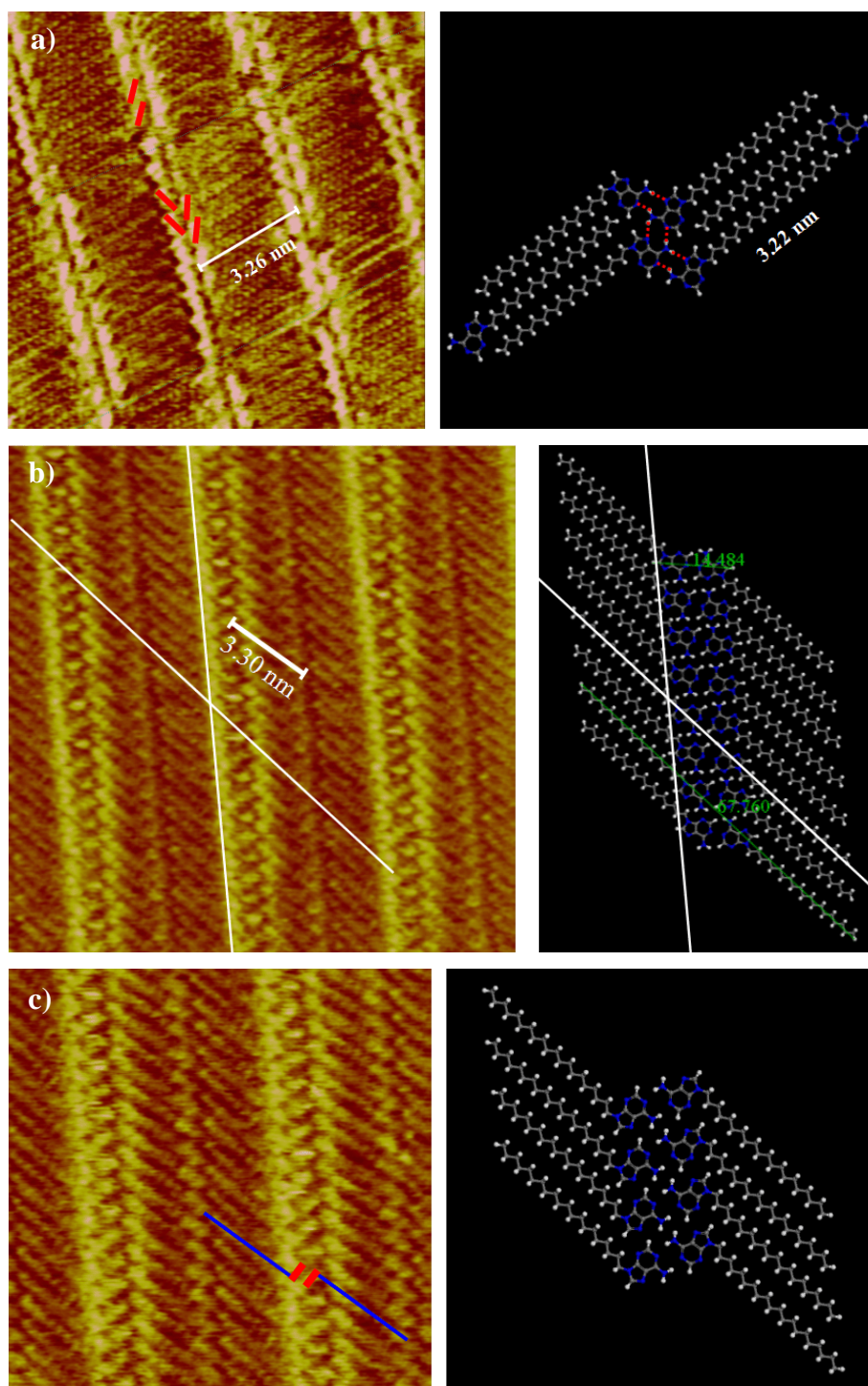


Figure 73. STM close ups and corresponding structural model propositions for (a) α phase (STM image $12 \times 12 \text{ nm}^2$), (b) β_1 phase (STM image $15 \times 15 \text{ nm}^2$), and (c) β_2 phase (STM image $10 \times 10 \text{ nm}^2$).

Taking into account the spatial information obtained by the STM images and the homopairing possibilities of adenine^[175] structural propositions for the two observed phases were developed and are shown in Figure 73. The α phase can be best described by an interdigitated structure depicted in Figure 73a. For the β phase two equally well fitting propositions were made that will be referred to as β_1 phase (Figure 73b) and β_2 phase (Figure 73c), respectively. One of our targets was to find indications to judge which on of the proposals for the β phase should be favored.

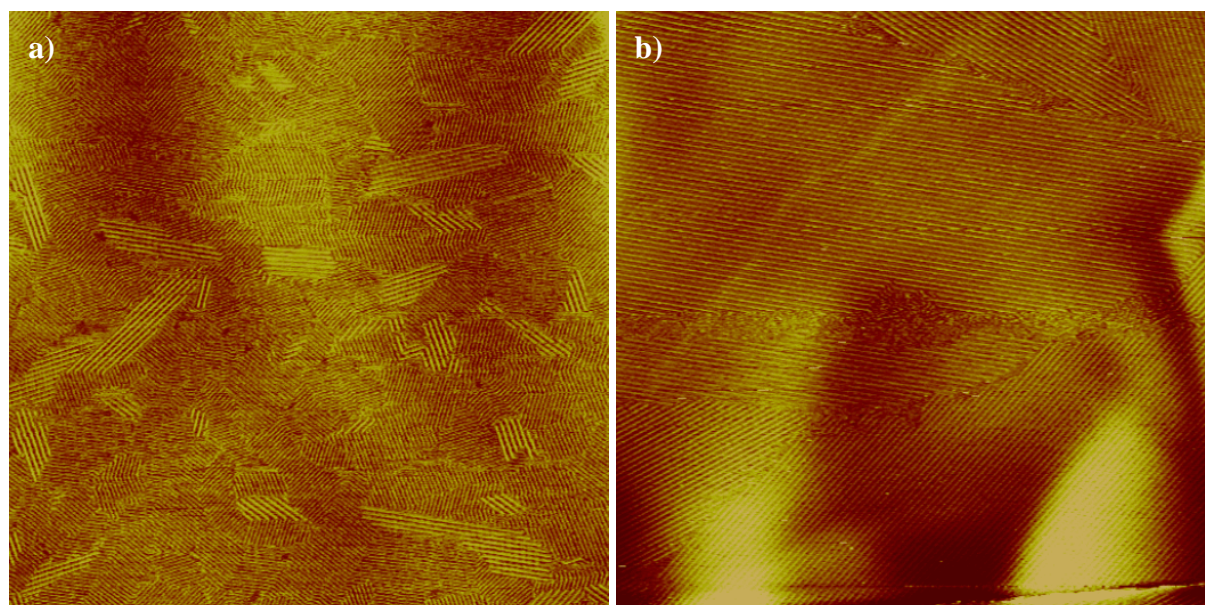


Figure 74. Structural transformation of adenine- C_{20} layer by heating: (a) layer as prepared, (b) after 10 min at 50 °C (image area 500 × 500 nm²).

An interesting feature of the adenine- C_{20} layers is that they undergo a phase transition over heating. Figure 74a shows an adenine- C_{20} layer as prepared; α phase and β phase are coexisting. Heating-up the sample to 50 °C for 10 min. transforms the whole layer into β phase (Figure 74b). This phase transition is reversible: Letting the layer rest at room temperature for several hours one can observe recurrence of the α phase and shrinkage of β phase domains (Figure 75).

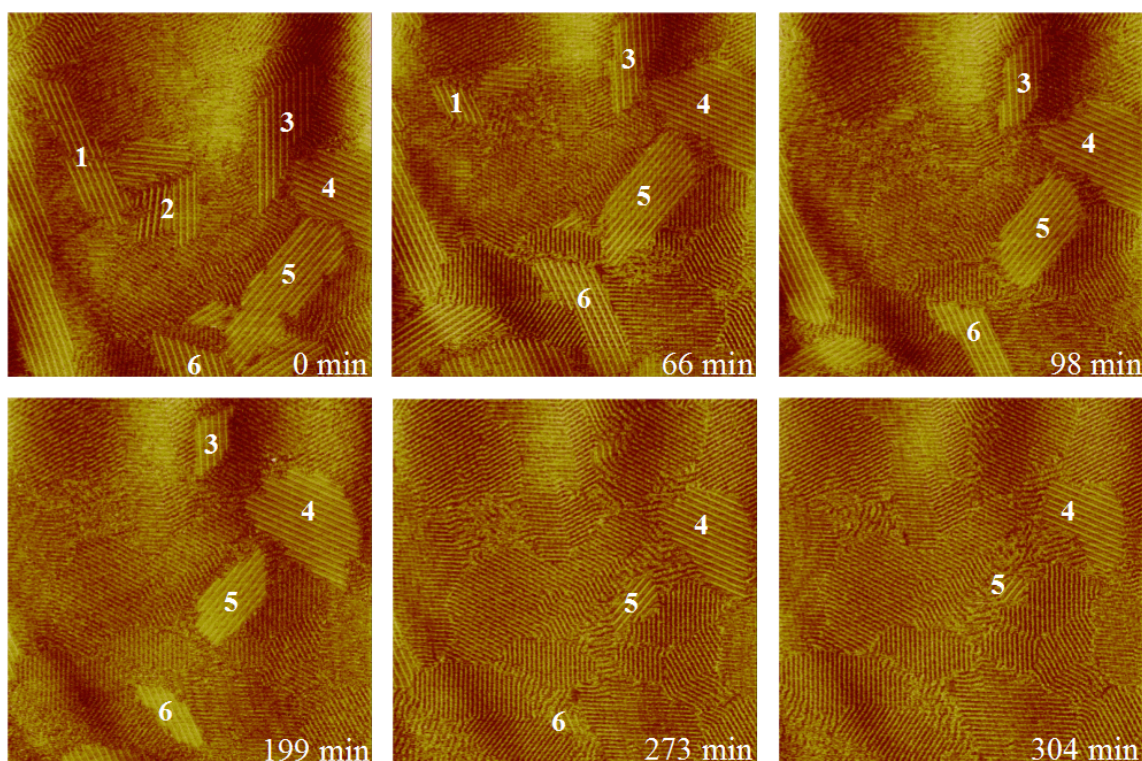


Figure 75. Reoccurrence of α phase and shrinking of β phase domains over time (image areas $250 \times 250 \text{ nm}^2$).

The timescales of phase transfer (especially in the latter case) observed in these experiments are far out of reach for the current MD simulations. Nevertheless, the simulations can give indications for the stability of films over heating and the mechanism behind phase transfer in the adenine- C_{20} films.

9.3 Modelling of the System in GROMACS

For a successful modelling of the described experimental system in GROMACS a description of the graphite substrate and the adenine- C_{20} molecules must be established. The initial structure for the graphite substrate was generated by the Inorganic Builder plug-in of the visualization software package VMD.^[176] Three layers of graphite were kept ensuring a substrate thicker than the VdW cutoff radius of the simulations. The lateral size of the substrate was adjusted to the need of the respective simulation, which demands periodic continuation to enable full periodic boundary conditions. The force field parameters for the substrate were taken from literature.^[177,178]

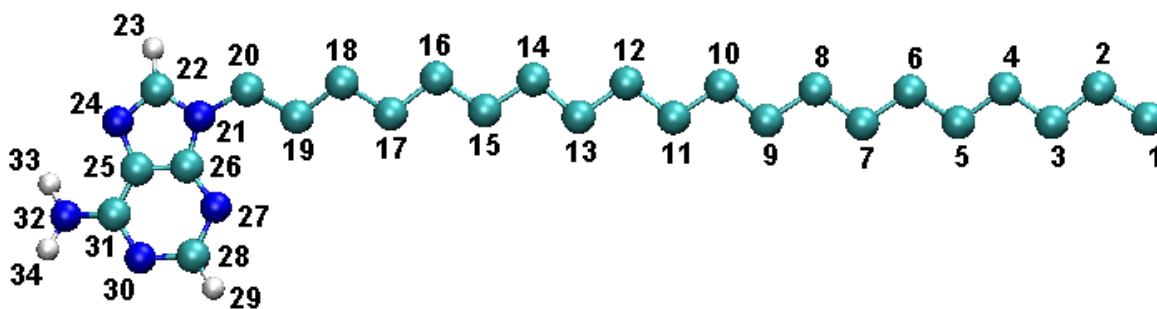


Figure 76. Topology for adenine-C₂₀. Numbers correspond to the atom number in Table 5.

Table 5. Atom type, charge group and charge by atom number for the used adenine-C₂₀ topology.

Atom Number	Atom Type	Charge Group	Charge (e)	Atom Number	Atom Type	Charge Group	Charge (e)
1	CH3	1	-0.047	18	CH2	8	+0.027
2	CH2	1	+0.024	19	CH2	8	-0.020
3	CH2	1	+0.023	20	CH2	8	-0.064
4	CH2	2	0	21	NR	8	+0.119
5	CH2	2	0	22	CR1	8	+0.241
6	CH2	3	0	23	HC	8	-0.147
7	CH2	3	0	24	NR	8	-0.146
8	CH2	4	0	25	C	8	+0.022
9	CH2	4	0	26	C	9	+0.171
10	CH2	5	0	27	NR	9	-0.183
11	CH2	5	0	28	CR1	9	+0.463
12	CH2	6	0	29	HC	9	-0.299
13	CH2	6	0	30	NR	9	-0.207
14	CH2	6	0	31	C	10	+0.084
15	CH2	7	0	32	NT	10	+0.121
16	CH2	7	0	33	H	10	-0.110
17	CH2	8	-0.021	34	H	11	-0.095

The basic topology for the adenine-C₂₀ was obtained from the Dundee PRODRG2.5 Server,^[179] a website* that can generate valid topologies for different molecular dynamics packages based on given coordinates (e.g., PDB files) or even simple drawings for small molecules. To enhance the partial charges on the molecule we obtained a charge distribution

* http://davapc1.bioch.dundee.ac.uk/cgi-bin/prodrgr_beta

by DFT calculations* and derived the atom bound charges of the MD topology by a modified restrained electrostatic potential (RESP) fitting^[180] with the method published by Hu, Lu and Yang.^[181] The final topology parameters are listed in Table 5.

Since the detailed structure of the adenine-C₂₀ phases was unknown we followed a multi-step approach to obtain a starting structure for the bulk crystal simulation. Firstly, we assembled “nanocrystals” of 64 adenine-C₂₀ molecules each according to the aforementioned structural propositions for the different phases on a much bigger graphite substrate of $19.6 \times 17.0 \text{ nm}^2$. The structures were allowed to relax in a 200 ps simulation at 50 K (the low temperature was chosen to prevent additional thermal perturbations). After stabilization of the structures they were transferred onto graphite substrates cut into the right size to fit the crystal structure and enable a periodic continuation. This allowed for the simulation of a bulk layer of adenine-C₂₀ in the different phases. The bulk layers underwent a simulated annealing with linear raising temperature from 50 K to 300 K for the first 500 ps and then cooling down to 50 K again within the next 500 ps and staying stationary at 50 K for last 200 ps of the simulation. All simulations were run in GROMACS version 3.3.1^[74,182] using either the GROMOS96 43B1^[183] or 53A6^[184] force field parameter. Temperature control was maintained by a Berendsen thermostat.^[185] For the nanocrystal simulations coulomb forces were shifted to zero from 0 nm to a cutoff radius of 1.2 nm. In the bulk simulations Particle-mesh Ewald^[85,86] was used for long range coulomb interactions and a cutoff of 1.4 nm was applied for the short range interactions. The Van der Waals forces were modified by a shift function switching from 0.9 nm to a cutoff of 1.2 nm. The bonds to hydrogen atoms were constrained using the LINCS algorithm^[186] and a timestep of 2 fs was used.

9.4 Simulation Results and Discussion

Since the detailed structure of the different phases was not known we first modeled “nanocrystals” of 64 adenin-C₂₀ molecules on a bigger graphite substrate. With this the molecules were allowed to slide into their preferable positions within the crystal lattice from a rough starting structure. As an example the relaxation of the α phase nanocrystal is shown in Figure 77.

* Conducted by Jörn-Holger Franke.

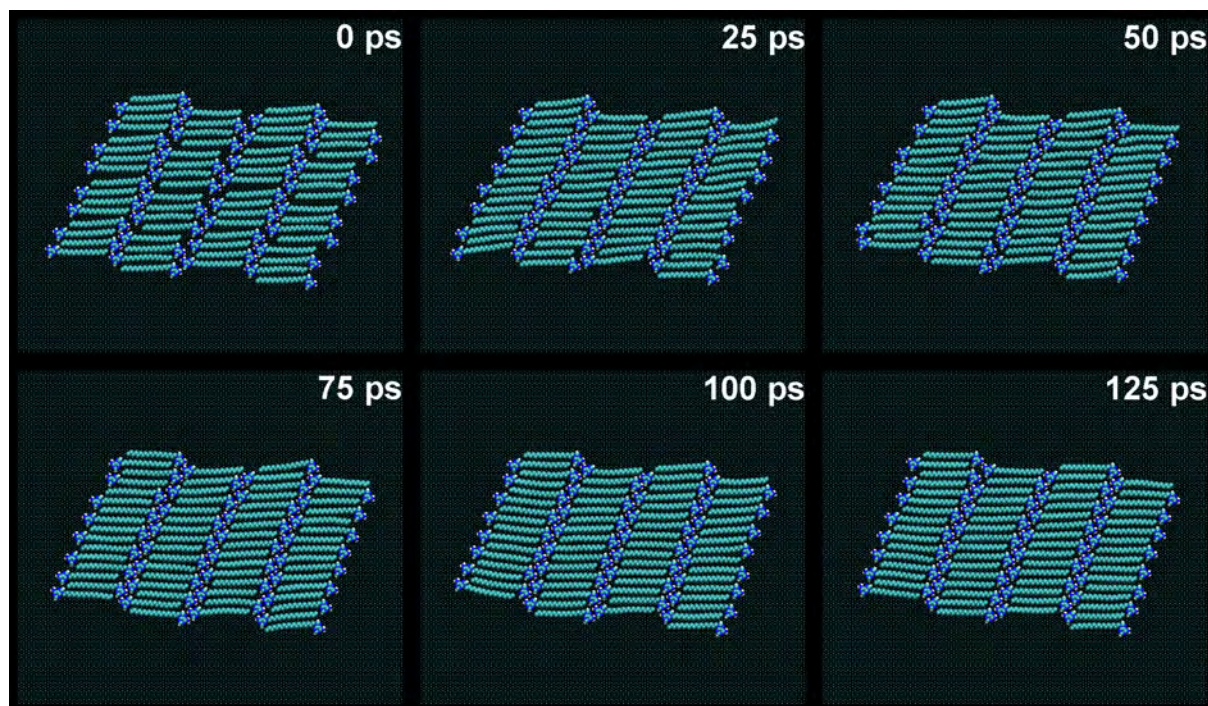


Figure 77. Relaxation of an α phase “nanocrystal” on a graphite substrate (not shown) over 125 ps.

The starting structure is composed of eight smaller subsets that were obtained by previous auxiliary simulations consisting of eight adenine- C_{20} molecules each. The overall structure already resembles the α phase structural proposition. The structural defects vanish within a few picoseconds and a stable crystal structure is reached after 100 ps. Stable nanocrystals of the two β phase structural propositions were obtained in the same manner. The different stable nanocrystals are shown in the first row of Figure 78. The structural proposition for the β_1 phase evolves into a slightly different stable structure where the adenine- C_{20} molecules are shifted a little bit along the stripe direction without any change in the angle of the adenine headgroups toward the hydrocarbon tails. Another interesting observation is that the β_1 phase shows a strain at the corners where the hydrocarbon tails are drawn into the direction of the neighboring “bulk” tails. This leads to a slightly lower tilting angle of the hydrocarbon tails with respect to the adenine headgroups at the top left and bottom right corner and a considerable increase in the tilting angle at the top right and bottom left corner of the nanocrystal. The α phase and the β_2 phase nanocrystals do not show any notable edge deviations. They could be readily continued by a simple copy and translate procedure while the distortion at the corners of the β_1 phase nanocrystal prevented a direct periodic continuation. A compilation of the crystal structure parameters measured in the different nanocrystals is given in Table 6.

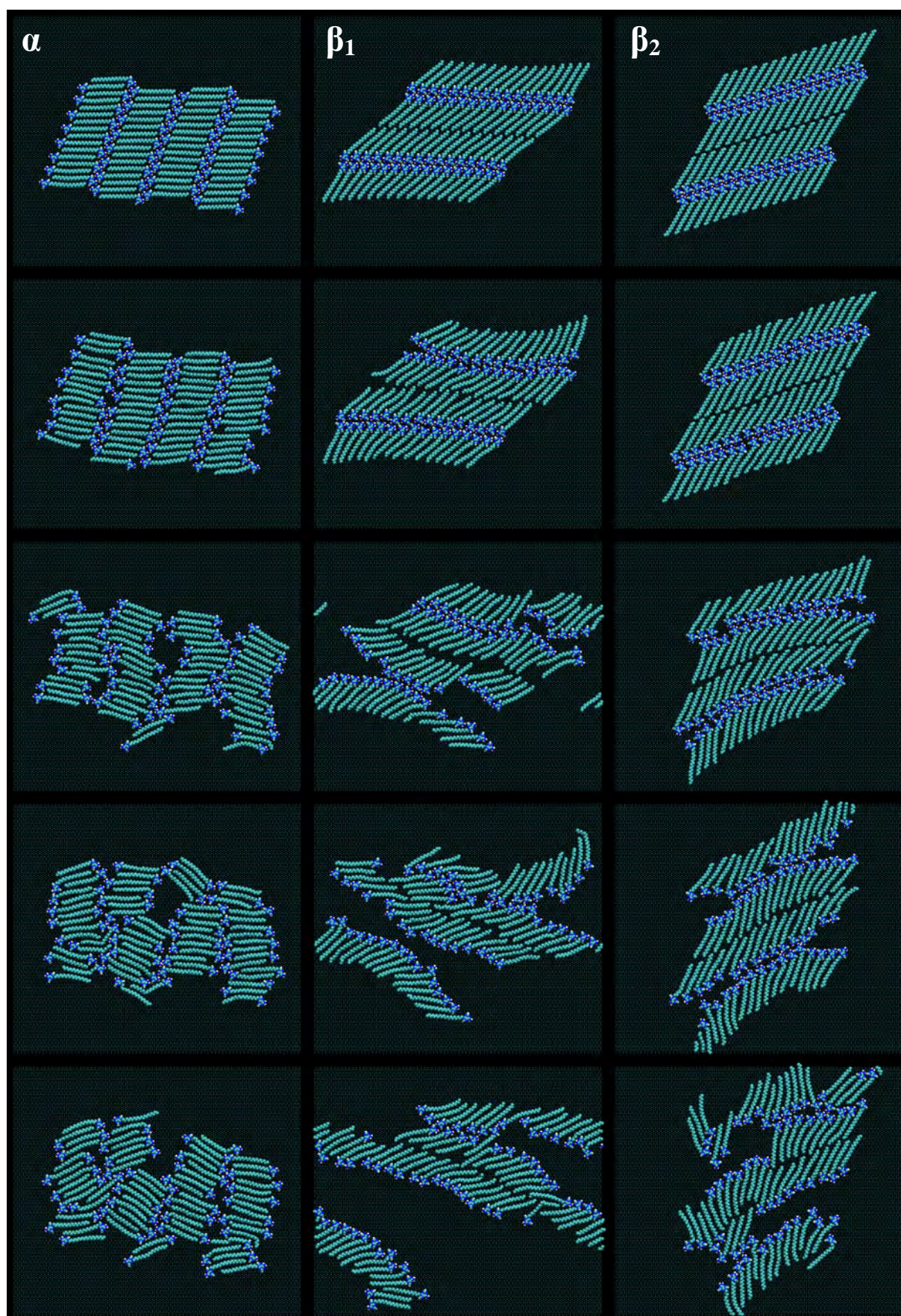


Figure 78. Heating of nanocrystals of α phase (left column), β_1 phase (middle column) and β_2 phase (right column).

Figure 78 shows a sequence of snapshots from the heating simulation of the different nanocrystals. None of the nanocrystals remains stable upon heating which is not surprising since the modelled crystals are way too small to reach a thermodynamic equilibrium with the (empty) surrounding substrate. The α and β_1 phase crystals suffer a severe structural collapse at roughly the same time into the simulation, the β_2 phase crystal remains stable a little longer.

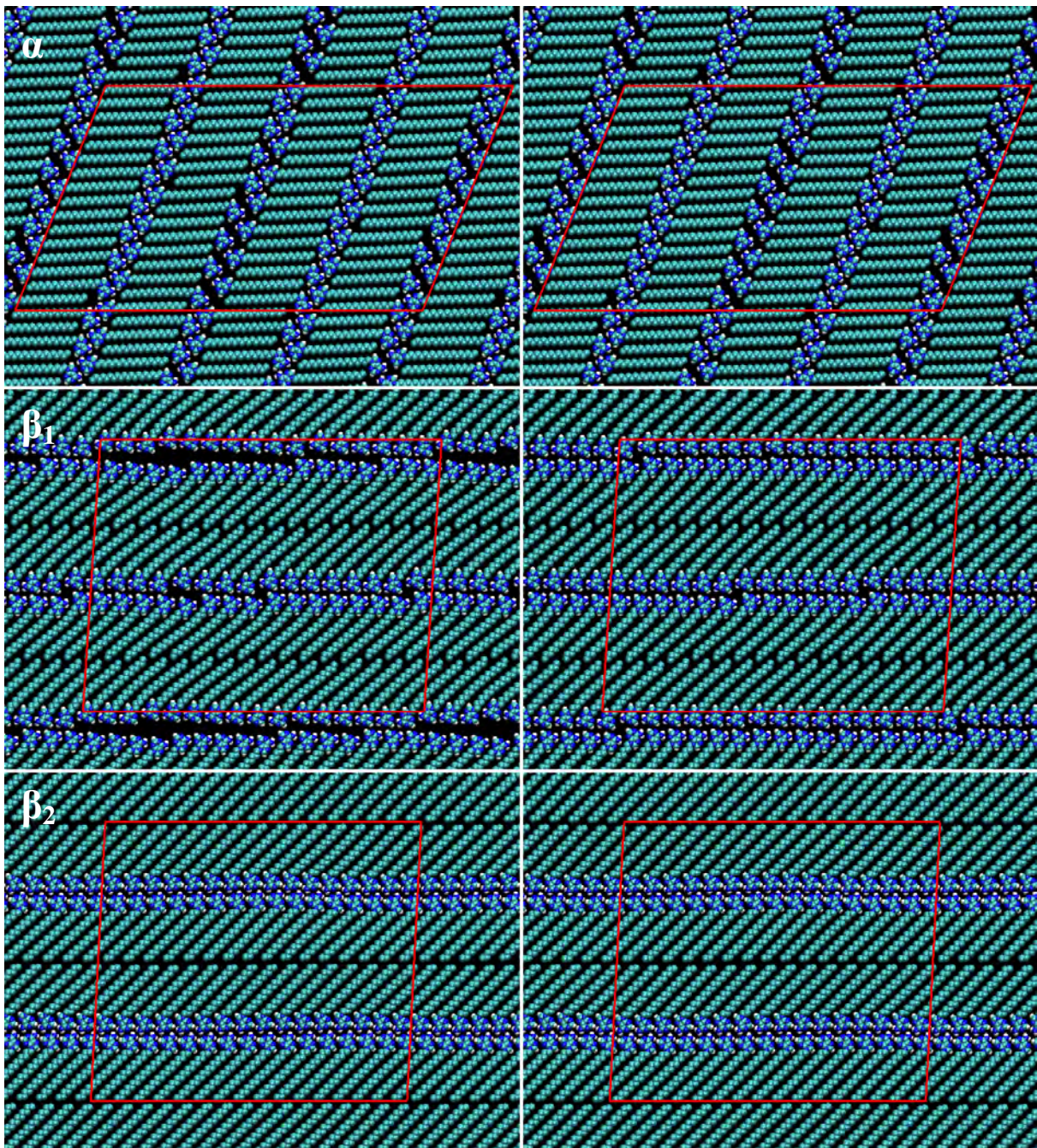


Figure 79. 2D bulk crystal structure of α phase (top row), β_1 phase (middle row) and β_2 phase (bottom row) for parameter set 43B1 (left column) and 53A6 (right column), simulation unit cells are marked in red.

It is interesting to note that all crystals break up at positions involving inter-adenine bonding. The attractive forces between the hydrocarbon chains are obviously much stronger: fragments of the particular stripe of the crystal connected by the interactions of the hydrocarbon chains remain bound throughout the heating process.

Table 6. Structural parameters of the adenin-C₂₀ nanocrystals.

	α phase	β_1 phase	β_2 phase
Crystal area (± 0.5 nm ²)	108.5 nm ²	110.1 nm ²	105.5 nm ²
$ \vec{a} , \vec{b} , \varphi$ (± 0.1 nm, $\pm 0.5^\circ$)	8.1 nm, 13.9 nm, 74.5°	12.9 nm, 11.5 nm, 48.0°	11.9 nm, 11.1 nm, 53.0°
Inter-chain distance (± 0.01 nm)	0.47 nm	0.48 nm	0.48 nm
Inter-stripe distance (± 0.1 nm)	3.3 nm	4.7 nm	4.7 nm
Chain-Stripe angle ($\pm 0.5^\circ$)	68.5°	43.0°	43.0°

Table 7. Structural parameters of the adenin-C₂₀ bulk crystals.

	α phase	β_1 phase	β_2 phase
	43B1 / 53A6	43B1 / 53A6	43B1 / 53A6
Unit cell area (± 0.5 nm ²)	109.8 nm ²	111.9 nm ²	106.6 nm ²
$ \vec{a} , \vec{b} , \varphi$ (± 0.1 nm, $\pm 0.5^\circ$)	8.4 nm, 14.1 nm, 68.0°	9.5 nm, 11.8 nm, 87.0°	9.7 nm, 11.0 nm, 87.0°
Inter-chain distance (± 0.01 nm)	0.48 nm / 0.48 nm	0.50 nm / 0.50 nm	0.49 nm / 0.49 nm
Inter-stripe distance (± 0.1 nm)	3.3 nm / 3.3 nm	4.8 nm / 4.8 nm	4.9 nm / 4.9 nm
Chain-Stripe angle ($\pm 0.5^\circ$)	67.0° / 67.0°	42.0° / 44.0°	44.0° / 44.0°

For the simulation of 2d bulk crystals the obtained crystal structures of the nanocrystal simulations were transferred onto a graphite substrate matching the unit cell defined by the respective nanocrystal allowing for a periodic continuation yielding the desired bulk crystal. These structures were allowed to fully relax in a 200 ps simulation at 0 K; for comparison the

simulations were conducted additionally with the 53A6 force field parameters, the results are shown in Figure 79. The α and β_2 phase bulk crystals relax into a stable structure virtually identical to the ones of the nanocrystals for both force fields (structural data given in Table 7). The case of the β_1 phase bulk crystal is more complicated. The β_1 phase nanocrystal was not suitable for a direct continuation due to corner distortions. Hence, the bulk crystal was compiled by cutting smaller pieces out of the nanocrystal and duplicating them to achieve a unit cell of 64 adenine-C₂₀ molecules adequate for the periodic continuation. The structure stabilizes in yet another relative position of the adenine headgroups of the different stripes while the tilt angle of the hydrocarbon tails remains constant. Even more intriguing is the fact that the stripes (formed by the adenine headgroups) itself break up after a few adenine-C₂₀ dimers. The straining force responsible for the distortion of the nanocrystal cannot alter the tilting angle of the hydrocarbon chains in the case of the bulk crystal. Therefore, they create a slight tilt in the headgroup stripe that leads to a parallel set off after a few adenine-C₂₀ dimers. Since the intra row binding between the hydrocarbon tails is bigger than the inter row binding of the adenine headgroups there is also some splitting of the headgroup bindings parallel to the stripe direction. The lateral offset is less defined but still visible in the case of the 53A6 force field but no inter row splitting is observed.

The time evolution graphs of the total binding energies and the parts contributed by Lennard-Jones interactions and Coulomb interactions for the simulations with parameter set 43B1 (Figure 80) as well as for the simulations with parameter set 53A6 (Figure 81) show a stable structure after several picoseconds of simulation. The stable binding energies are given in Table 8. The part of the binding energy originating in Lennard-Jones interactions is bigger than that by Coulomb interactions for all phases. The hydrocarbon chain of the adenine-C₂₀ is almost uncharged; therefore, virtually all electrostatic binding or repulsion is mediated by the adenine headgroups. This also makes it understandable why the crystals tend to break up at the headgroup bindings first: unlike the Lennard-Jones interactions that only become repulsive if the interacting particles come too close together, the Coulomb interactions additionally depend on the charge polarity. The hydrocarbon chains will have a certain distance of ideal binding energy (in the minima of the Lennard-Jones potential) and small perturbation of the position will always tend to move back into the ideal position. With the charge and polarity pattern of the headgroups small perturbations can already lead to instabilities and repulsive forces when corresponding charges come together (comparable to a

sodium chloride crystal bursting along a crystal axis by an induced displacement that places positive and negative charges next to each other).

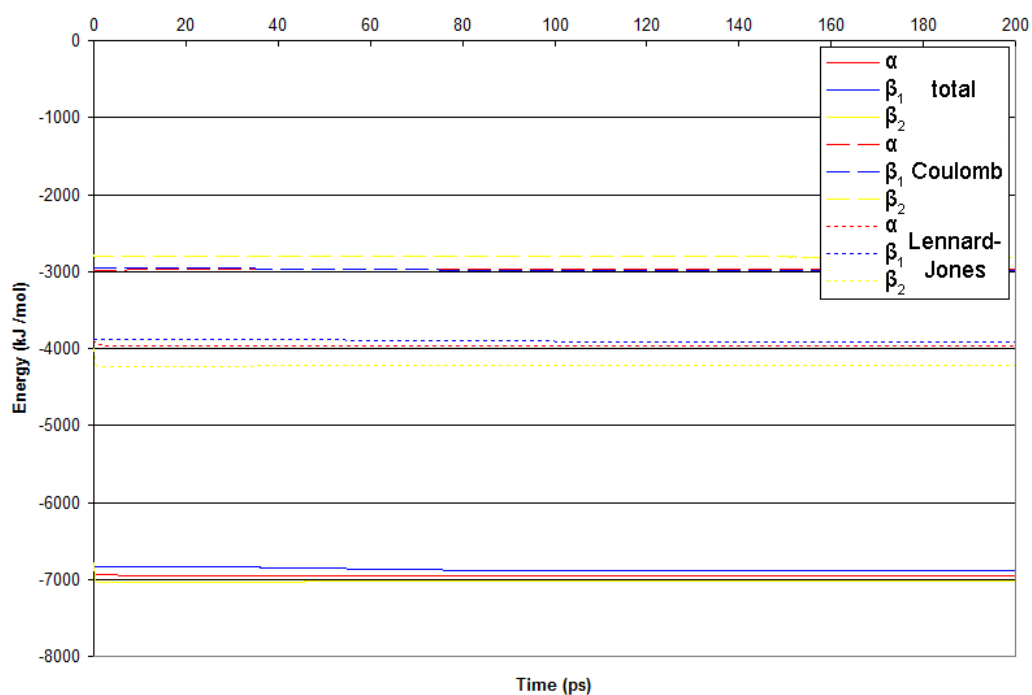


Figure 80. Total binding energy, Coulomb and Lennard-Jones part of the binding energy (43B1).

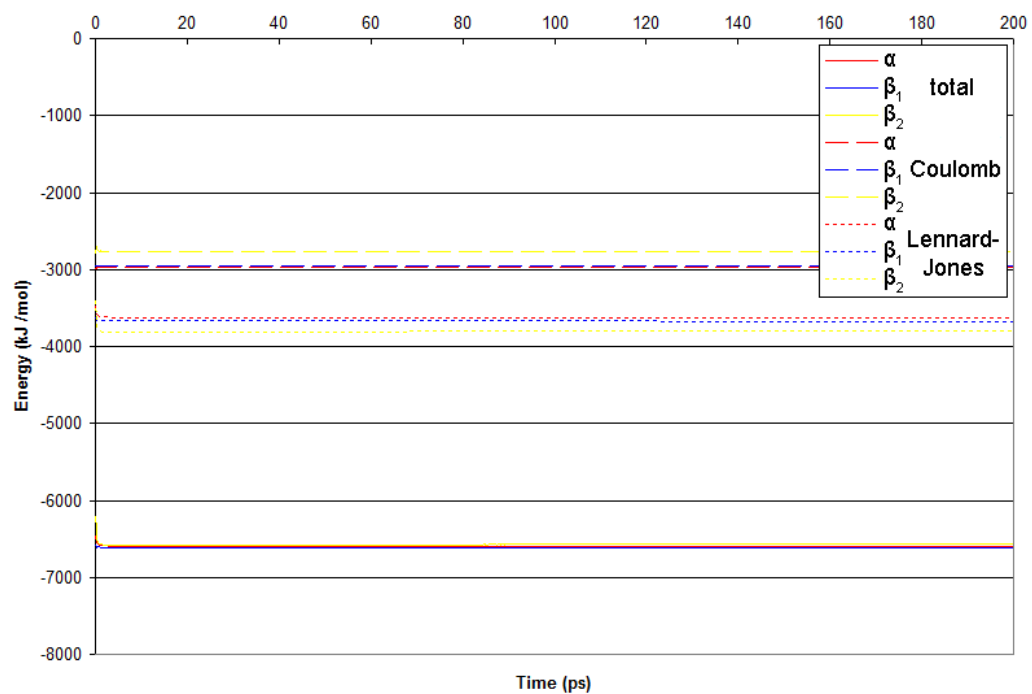


Figure 81. Total binding energy, Coulomb and Lennard-Jones part of the binding energy (53A6).

Table 8. Binding energies for the different bulk crystal phases.

	α phase	β_1 phase	β_2 phase
energies in kJ/mol	43B1 / 53A6	43B1 / 53A6	43B1 / 53A6
Coulomb energy	-2978.8 / -2971.6	-2985.5 / -2945.7	-2811.5 / -2772.2
Lennard-Jones energy	-3971.7 / -3627.0	-3908.4 / -3674.2	-4211.3 / -3798.2
Total energy	-6950.5 / -6598.6	-6893.9 / -6619.9	-7022.8 / -6570.4

The total binding energies do not vary greatly among the different phases. For the 43B1 parameter set the β_2 phase has the biggest binding energy, followed by the α phase. The β_1 phase is the least bound one but the overall binding energy varies only by 2%. The simulations with the 53A6 parameter set result in an overall decrease in binding energy. The β_1 phase becomes the most bound structure followed by the α phase and the β_2 phase is now the least bound one but the difference in binding energy among the different phases is not even 1%. Since the overall structure does not vary much between the different parameter sets the Coulomb energies do not change substantially because the charges stay the same in all simulations. Accordingly, the overall decrease in binding energy is caused by a decrease of the Lennard-Jones energy due to the different Lennard-Jones parameterization.

Table 9. Comparison of total binding energies per molecule of MD and DFT calculations.

Energies in eV	α phase	β_1 phase	β_2 phase
MD (43B1)	-1.126	-1.116	-1.137
MD (53A6)	-1.069	-1.072	-1.064
DFT*	-	-1.299	-1.094

Table 9 gives a comparison of the total binding energy per molecule from the MD simulations with DFT calculations made for the β phases, α phase calculations would be prohibitive for the required system size. The magnitude of the binding energies from MD fits to the (probably more precise) ones obtained by DFT calculations. The main difference is the significantly stronger binding (about 20%) of the β_1 phase compared to the β_2 phase in the DFT calculations.

* Received by personal reference from Jörn-Holger Franke. Calculations were done in VASP^[212] with the revPBE^[213,214] functional and semi-empirical dispersion corrections.^[215]

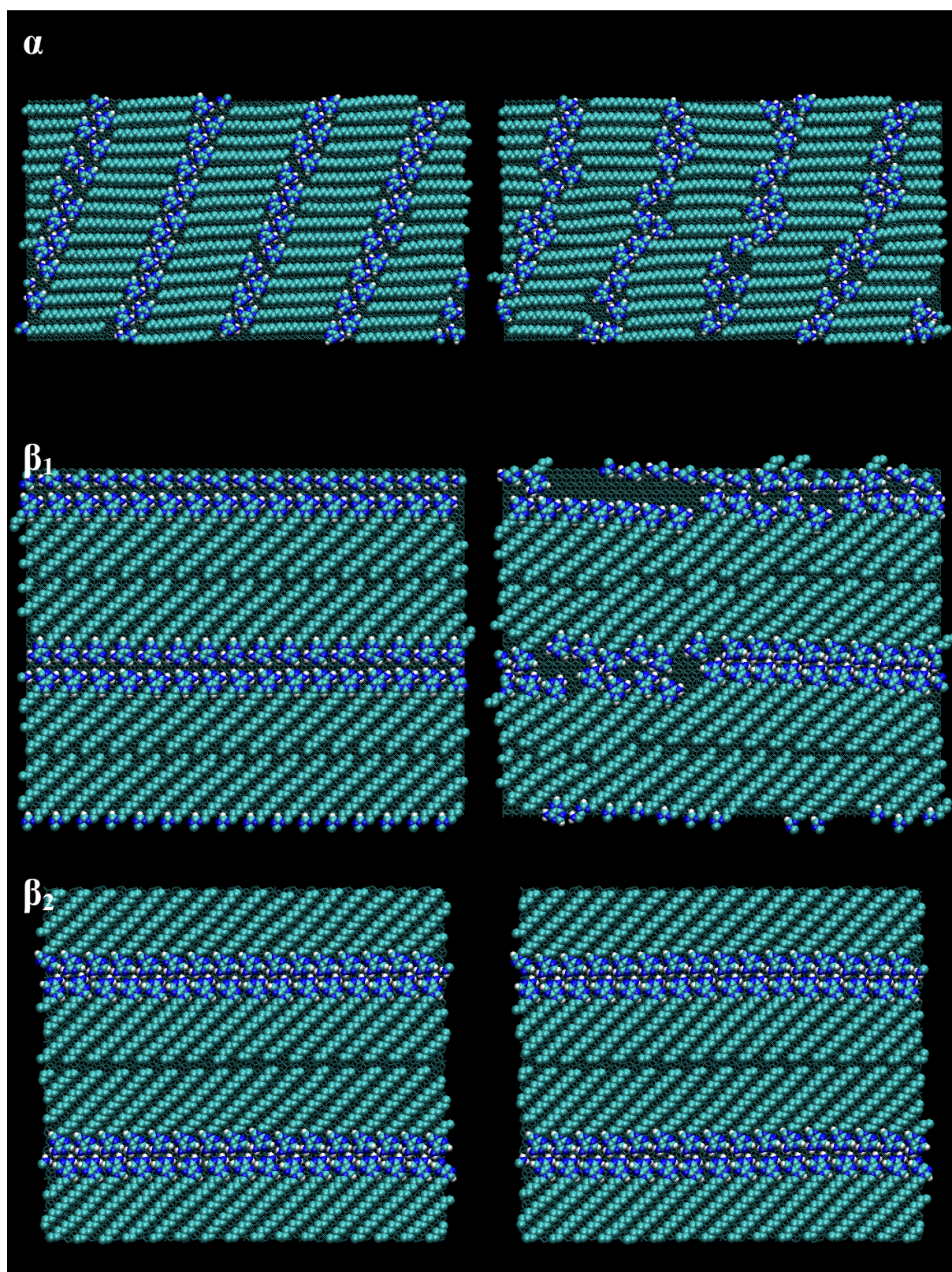


Figure 82. 2D bulk crystal α phase (top row), β_1 phase (middle row) and β_2 phase (bottom row) before (left column) and after (right column) annealing.

The results of the annealing simulations of the bulk crystals are shown in Figure 82. Only the 43B1 parameter simulations were stable under annealing. Heating under 53A6 parameters led 120

to film breaks with adenine headgroups leaving the substrate plane and sticking out of the monolayer. The left column shows the initial structures, the right column the resulting structures after the annealing cycle. The α phase is somewhat disturbed after annealing, although not completely destroyed. The β_2 phase is completely stable and survives the annealing process without any deviation in the crystal structure. In contrast, the β_1 phase structure is severely deranged by the annealing cycle. It is especially striking that a considerable part of the simulation unit cell is transformed into β_2 phase. This strongly suggests an increased stability of the β_2 phase structure as compared to β_1 phase structure. The energy differences (Table 8) seem to be much too small to account for such a distinct difference in stability on heating. But we can understand this difference by considering the observation of the relative position change in opposed adenine headgroups of the β_1 phase in the different simulations: in all simulations of the β_1 phase we observed adjustments in the relative positions of opposed adenine headgroups parallel to the stripe direction. This relative ease of sliding the half stripes against each other implies a multitude of similar β_1 phases, sharing the overall parameters of stripe distance and chain tilt angle while the relative position of opposed adenine headgroups is different. This makes the β_1 phase susceptible to random perturbations because if combined the different relative headgroup positions are not compatible with the overall ordered structure. Another similar contribution to the enhanced stability of the β_2 phase may be a better interlocking of the charge pattern of the adenine headgroups. The α and β_2 phase seem to lack nearby stable configurations forcing them back into the initial crystal structure after thermal random fluctuations, especially the latter one exhibiting good thermal stability. The overall better stability of the β_2 phase over the α phase for higher temperatures is also reflected in the different area requirements that are higher for the α phase. This means additional stress for the crystal structure during heating because of thermal expansion that can be avoided by evading into the β_2 phase. Notably, the β_1 phase needs even more area than the α phase which constitutes yet another argument for the better stability of the β_2 phase.

9.5 Summary

Extensive simulations on the stability of three different structural propositions (α , β_1 , and β_2 phase) for self-assembled monolayers of adenine-C20 molecules on a graphite substrate were conducted. Although the sole consideration of MD binding energies remains indecisive and DFT calculations clearly indicate a stronger binding in the case of β_1 phase MD

simulations strongly suggest a superior stability of the β_2 phase structure. Taking into account the different structural parameters (especially area requirements) it can also be understood why the β_2 phase is prevailing in high temperature environments while α phase could be predominating at lower temperatures. All in all we conclude that the β_2 phase is most probably the actual crystal structure of the broad stripe β phase on the samples and that the structural proposition for the α phase is excellent for the observed narrow stripe phase.

10 MD Simulation of Molecular Diffusion on DPPC

10.1 Introduction

The site-selective patterning of luminescent organic materials into ordered micro to nanoscale arrangements has become a major research interest due to its broad potential application in many areas, e.g., photonics,^[187,188] optoelectronics,^[188-191] biochip-based detection,^[192] and biosensor arrays.^[193] Current strategies to achieve large-area site-selective patterning usually involve various combinations of top-down and bottom-up methods, such as nanoimprinting^[194] or microcontact printing (μ CP).^[195-198] Within these approaches the substrate surfaces are chemically modified to generate binding sites specific for the material to be patterned by tuning energetically and/or chemically properties of these areas (templated self-assembly). Usually the templated self-assembly of organic material is conducted in wet-chemical environments. Until recently much less effort has been spent on site-selective patterning of luminescent organic molecules via gas-phase deposition.^[198-200]

Before this we and others have shown that our DPPC stripe pattern can be utilized as a template to pattern nanocrystals^[151,124,125] or proteins.^[123] Recently the DPPC stripe pattern was introduced as a template for luminescent organic molecules like 3(5)-(9-anthryl) pyrazole (ANP)^[201] and perylene (publication in preparation). In this work we use molecular dynamics simulations to clarify the mechanism behind the selective deposition of these organics molecules onto the DPPC stripe pattern.

10.2 The Experimental System

This chapter gives a quick overview over the experimental findings investigated in our molecular dynamics study. *Hao* et. al. introduced a DPPC stripe pattern as a template for the selective deposition of ANP.^[201] The ANP is deposited by thermal evaporation under a vacuum of 5×10^{-4} Pa and a sublimation temperature of only 43°C. The amount of deposited ANP is quantified by a quartz crystal microbalance (QCM). The film thickness read from the QCM sensor corresponds to the film thickness on the sample if the deposited molecules would constitute a smooth film. On the contrary it is found that the molecules first deposit

* Part of the work contained in this chapter was submitted for publication, a complete account with additional simulations that expand and deepen the findings presented here is in preparation for publication.

exclusively onto the LE-phase areas of the stripe pattern for lower occupancy and decorate the LC-phase areas only on further evaporation (Figure 83).

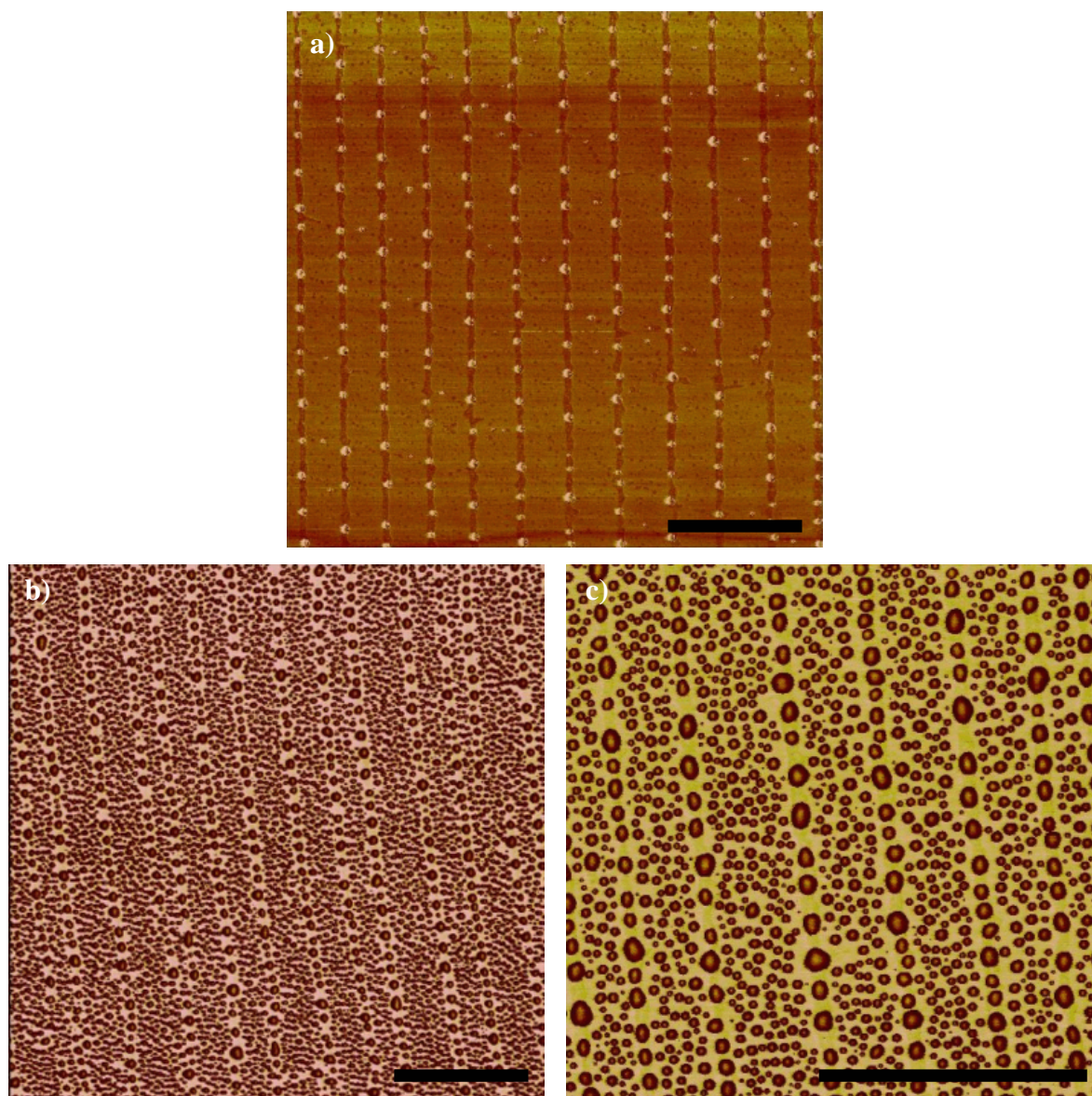


Figure 83. DPPC stripe pattern with evaporated ANP, (a) lower occupancy (1 nm), (b) higher occupancy (7 nm), (c) higher occupancy (7 nm, close up). Bars equal 5 μm .

The comparison of the nucleation on the LE- and LC-phase reveals another striking difference: the nucleation sites are smaller on average and more numerous on the LC-phase areas compared to the LE-phase areas. This observation is true not only for the mixed phase stripe pattern but was also verified for pure phase substrates. *Hao et. al.* explain their findings in the following way: first the preferred deposition of the organic molecules onto the LE-phase areas may be attributed to their higher surface energy, which drives, for example, the preferred deposition of nanocrystals as well.^[125] The difference in size and distribution of the nucleation

sites strongly suggest a smaller diffusion length of the ANP molecules on the LC-phase compared to the LE-phase. On first sight this may seem inconsistent to the preferred deposition onto the LE-phase, because a better diffusion on the LE phase should also lead to a flow of material from the LE-phase areas to the LC-phase areas where it should accumulate. To solve this contradiction Hao et. al. postulate a difference in the energy barrier for molecules crossing from LC- to LE-phase and vice versa. If the energy barrier is higher for the case of crossing from LE- to LC-phase this would result in a lower rate constant preserving the preferred deposition on LE-phase areas. Consistent with this notion the preferred nucleation onto LE-phase areas is lost when the LC-stripes become too large.

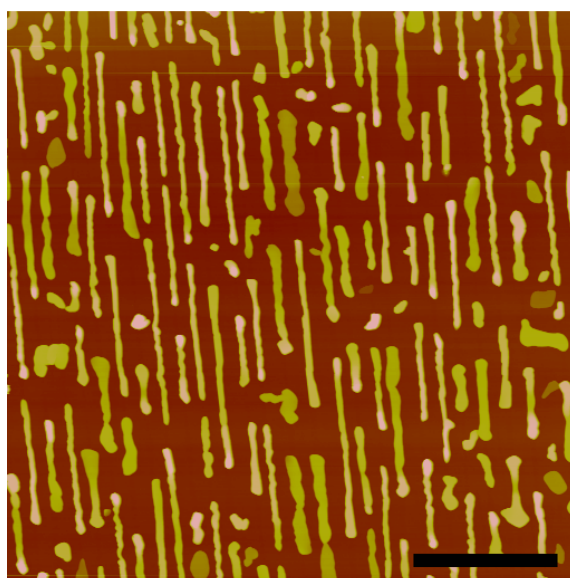


Figure 84. DPPC stripe pattern with evaporated perylene. Bar equals 5 μm .

A second model system with similar behavior is the evaporation of perylene molecules onto DPPC stripe pattern (Figure 84). The results of these experiments are not yet published but were relayed to the author by personal communication.

10.3 Modelling of the System in GROMACS

To model the experimental system into GROMACS several subtasks had to be achieved: topologies for the silicon oxide substrate, DPPC, and for the molecules to be deposited on the surface (ANP and Perylene) had to be written and a suitable equilibrated DPPC monolayer had to be obtained.

The silicon oxide substrate was modelled in an approach similar to that used by *Wensink et. al.* in their study on water bridging effects between two surfaces.^[202] The modelling of amorphous silicon oxide would be much more complicated probably without notable improvement of the results. Hence, we decided to use an easier to handle substrate with a regular crystal lattice, namely α -quartz. As a starting point an α -quartz crystal of desired size was produced by the Inorganic Builder plug-in of the visualisation package VMD.^[176] The crystal was cut and rotated to expose the (1,0,-1) Miller plane as the surface lying parallel to the x-y-plane of the coordinate system. The surface was then saturated with silanol groups by adding a hydrogen atom to each surface oxygen atom. Finally the crystal was cut at two planes perpendicular to the x-y-plane with respect to the periodic boundary conditions and in parallel to the x-y-plane to a thickness of about 1.4 nm to ensure a substrate thicker than the cutoff radius of typical simulations. This procedure resulted in a silanol terminated silicon oxide slab of the dimensions 9.6 nm \times 9.8 nm \times 1.4 nm suitable for periodic continuation in the x-y-plane (Figure 85).

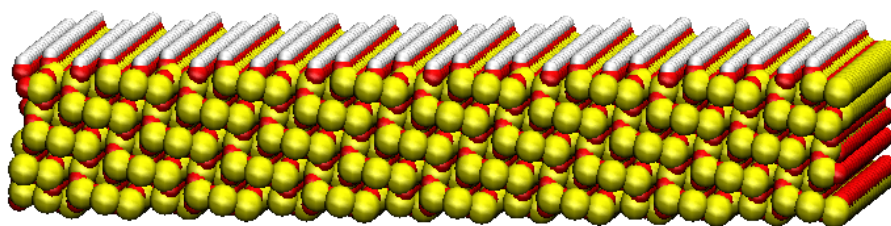


Figure 85. Silicon oxide in α -quartz configuration with surface silanol groups.

The force field parameters for the silicon oxide substrate were taken from literature^[202-204] and are summarized in Table 10.

Table 10. Force field parameters for the silicon oxide substrate.

Atom Type	$C^{(6)}$ (kJ nm ¹² /mol)	$C^{(12)}$ (kJ nm ⁶ /mol)	q (e)
Hydrogen	-	-	+0.40
Oxygen (bulk)	0.22617×10^{-2}	0.74158×10^{-6}	0
Oxygen (surface)	0.22617×10^{-2}	0.15062×10^{-5}	-0.71
Silicon (bulk)	0.22617×10^{-2}	0.22191×10^{-4}	0
Silicon (surface)	0.22617×10^{-2}	0.22191×10^{-4}	+0.31

Table 11. Atom type, charge group and charge by atom number for the used DPPC topology.

Atom Number	Atom Type	Charge Group	Charge (e)	Atom Number	Atom Type	Charge Group	Charge (e)
1	CH3	0	+0.4	26	CH2	12	0
2	CH3	0	+0.4	27	CH2	13	0
3	CH3	0	+0.4	28	CH2	14	0
4	N	0	-0.5	29	CH2	15	0
5	CH2	0	+0.3	30	CH2	16	0
6	CH2	1	+0.4	31	CH3	17	0
7	OA	1	-0.8	32	CH2	18	+0.50
8	P	1	+1.7	33	OA	18	-0.70
9	OM	1	-0.8	34	C	18	+0.80
10	OM	1	-0.8	35	O	18	-0.60
11	OA	1	-0.7	36	CH2	19	0
12	CH2	2	+0.4	37	CH2	20	0
13	CH1	2	+0.3	38	CH2	21	0
14	OA	2	-0.7	39	CH2	22	0
15	C	2	+0.7	40	CH2	23	0
16	O	2	-0.7	41	CH2	24	0
17	CH2	3	0	42	CH2	25	0
18	CH2	4	0	43	CH2	26	0
19	CH2	5	0	44	CH2	27	0
20	CH2	6	0	45	CH2	28	0
21	CH2	7	0	46	CH2	29	0
22	CH2	8	0	47	CH2	30	0
23	CH2	9	0	48	CH2	31	0
24	CH2	10	0	49	CH2	32	0
25	CH2	11	0	50	CH3	33	0

The topology for the DPPC molecules was adapted from available topologies for the GROMOS96 45A3 parameter set^[205] and transcribed into the current GROMOS96 53A6 force field scheme.^[184] The obtained topology is shown in Figure 86, the force field parameter are tabulated in Table 11. Only very recently (after completion of most simulations) a detailed study on slightly differing DPPC topologies for the GROMOS96 53A6 force field was published by *Kukol*.^[206] Our topology corresponds to the model termed DPPC2 therein. The model favored by this author matches our current model except for the use of a different estercarbonyl carbon atom type, “CH0” instead of “C”. The van der Waals radius for the carbonyl-ester is therefore increased from 0.336 nm for atom type “C” to 0.664 nm for atom type “CH0”.^[206] The repetition of some of our simulations with the newly suggested topology

revealed no differences relevant to our considerations. Nevertheless, we suggest switching to the new topology for future simulations because eventually it will become the standard for DPPC bilayer simulations based on the thorough investigation presented by *Kukol*.

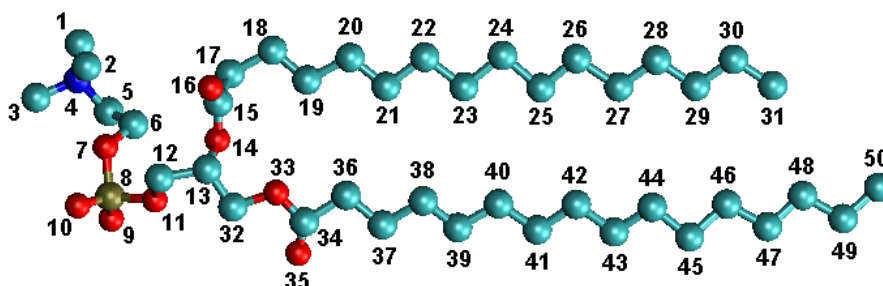


Figure 86. Topology for DPPC. Numbers correspond to the atom number in Table 11.

The molecular topologies for ANP and perylene were obtained from the Dundee PRODRG2.5 Server.^[179] This website* allows to generate valid topologies for different molecular dynamics packages based on given coordinates (e.g., PDB files) or even simple drawings for small molecules.

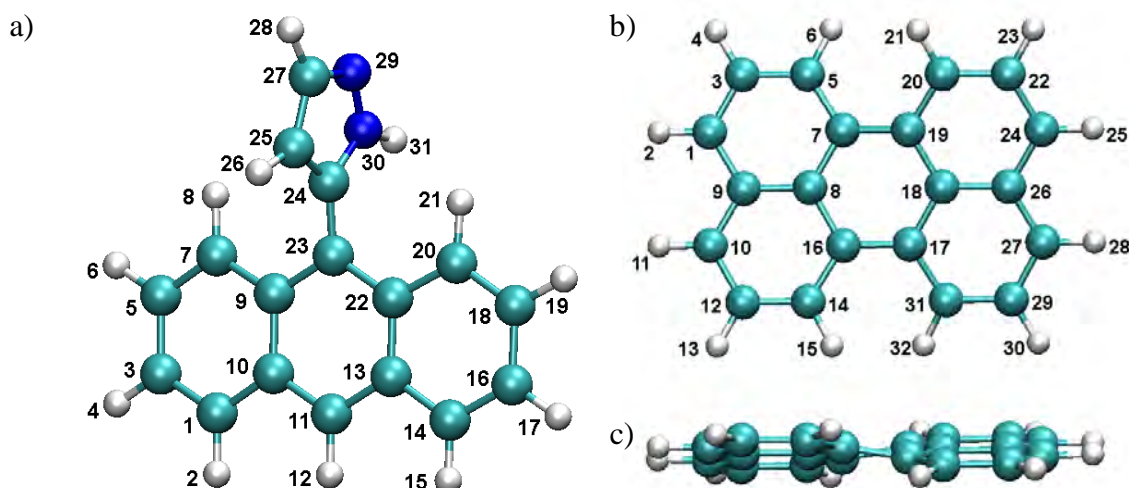


Figure 87. Topologies of (a) ANP, (b) perylene (top view), and (c) perylene (side view). Numbers correspond to the atom number in Table 12 and Table 13, respectively.

The obtained topologies for ANP and perylene are shown in Figure 87. Tabulated values for the force field atom type and partial charges are given in Table 12 and Table 13, respectively.

* http://davapc1.bioch.dundee.ac.uk/cgi-bin/prodrgr_beta

Table 12. Atom type, charge group and charge by atom number for the used ANP topology.

Atom Number	Atom Type	Charge Group	Charge (e)	Atom Number	Atom Type	Charge Group	Charge (e)
1	CR1	1	-0.007	17	HC	4	+0.007
2	HC	1	+0.007	18	CR1	5	-0.007
3	CR1	2	-0.003	19	HC	5	+0.007
4	HC	2	+0.013	20	CR1	6	-0.007
5	CR1	2	-0.003	21	HC	6	+0.007
6	HC	2	+0.013	22	C	7	-0.010
7	CR1	2	-0.003	23	C	7	-0.010
8	HC	2	+0.013	24	C	7	+0.092
9	C	2	-0.013	25	CR1	7	-0.003
10	C	2	-0.014	26	HC	7	+0.018
11	CR1	2	-0.003	27	CR1	7	-0.003
12	HC	2	+0.013	28	HC	7	+0.018
13	C	2	-0.013	29	NR	7	-0.265
14	CR1	3	-0.007	30	NR	7	+0.161
15	HC	3	+0.007	31	H	7	+0.002
16	CR1	4	-0.007				

Table 13. Atom type, charge group and charge by atom number for the used perylene topology.

Atom Number	Atom Type	Charge Group	Charge (e)	Atom Number	Atom Type	Charge Group	Charge (e)
1	CR1	0	-0.004	17	C	2	-0.012
2	HC	0	+0.014	18	C	2	-0.012
3	CR1	0	-0.005	19	C	2	-0.012
4	HC	0	+0.014	20	CR1	2	-0.004
5	CR1	0	-0.005	21	HC	2	+0.016
6	HC	0	+0.015	22	CR1	2	-0.004
7	C	0	-0.013	23	HC	2	+0.016
8	C	0	-0.012	24	CR1	2	-0.004
9	C	0	-0.013	25	HC	2	+0.016
10	CR1	0	-0.005	26	C	3	-0.016
11	HC	0	+0.014	27	CR1	3	-0.006
12	CR1	1	-0.005	28	HC	3	+0.011
13	HC	1	+0.013	29	CR1	3	-0.006
14	CR1	1	-0.005	30	HC	3	+0.012
15	HC	1	+0.012	31	CR1	3	-0.006
16	C	1	-0.015	32	HC	3	+0.011

A self developed program was used to set up the simulation geometries and to combine the different system constituents (i.e., water, DPPC, silicon oxide substrate, ANP and perylene, respectively) into the desired quantity and starting positions. The single point charge (SPC) water model^[207] integrated in GROMACS served as model for the water molecules. To achieve a pseudo two-dimensional simulation geometry a big z dimension of 30 nm was applied which sufficiently separates the periodical images of the system in z direction. The MD simulations ran in GROMACS version 4.0.3.^[75] If not stated differently, all simulations are conducted with constant volume and temperature (Berendsen thermostat^[185] at 300 K) and the number of particles is not changing during simulation (NVT ensemble). Particle-mesh Ewald^[85,86] is used for long range coulomb interactions and a cutoff of 1.4 nm was applied for the short range interactions. Van der Waals settings included a shift function switching from 0.9 nm to a cutoff of 1.2 nm. The bonds to hydrogen atoms were constraint using the LINCS algorithm.^[186] A timestep of 2 fs was used for the simulation of DPPC on water and of 1 fs in the simulations involving the silicon oxide substrate.

10.4 Simulation Results and Discussion

To obtain equilibrated DPPC monolayers in a different phase (LE and LC respectively) for the diffusion simulations first a simulated compression of a DPPC monolayer on a small water slab was carried out. For this purpose a system consisting of 100 DPPC molecules in a regular grid on a water slab of $12 \times 12 \text{ nm}^2$ area and an initial thickness of about 1 nm (6,501 molecules) was simulated under a semi-isotropic Berendsen pressure coupling^[185] with a compressibility of 5×10^{-5} in x-y-direction and 0 in z-direction. During the course of the 2,000 ns simulation of the film compression the x-y plane area was reduced from $12 \times 12 \text{ nm}^2$ to $5.3 \times 5.3 \text{ nm}^2$ yielding molecular areas from 1.44 nm^2 to 0.28 nm^2 . Figure 88 shows snapshots of the first 1,100 ps of the simulation in top and side view. The progressive reduction in the surface area is clearly visible and accompanied by a straightening up of the hydrocarbon chains of the DPPC molecules. After about 900 ps of the simulation (at a molecular area of about 0.53 nm^2) buckling of the DPPC monolayer occurs. Eventually this leads to a later film collapse or the emerging of vesicles from the film into the water slab.

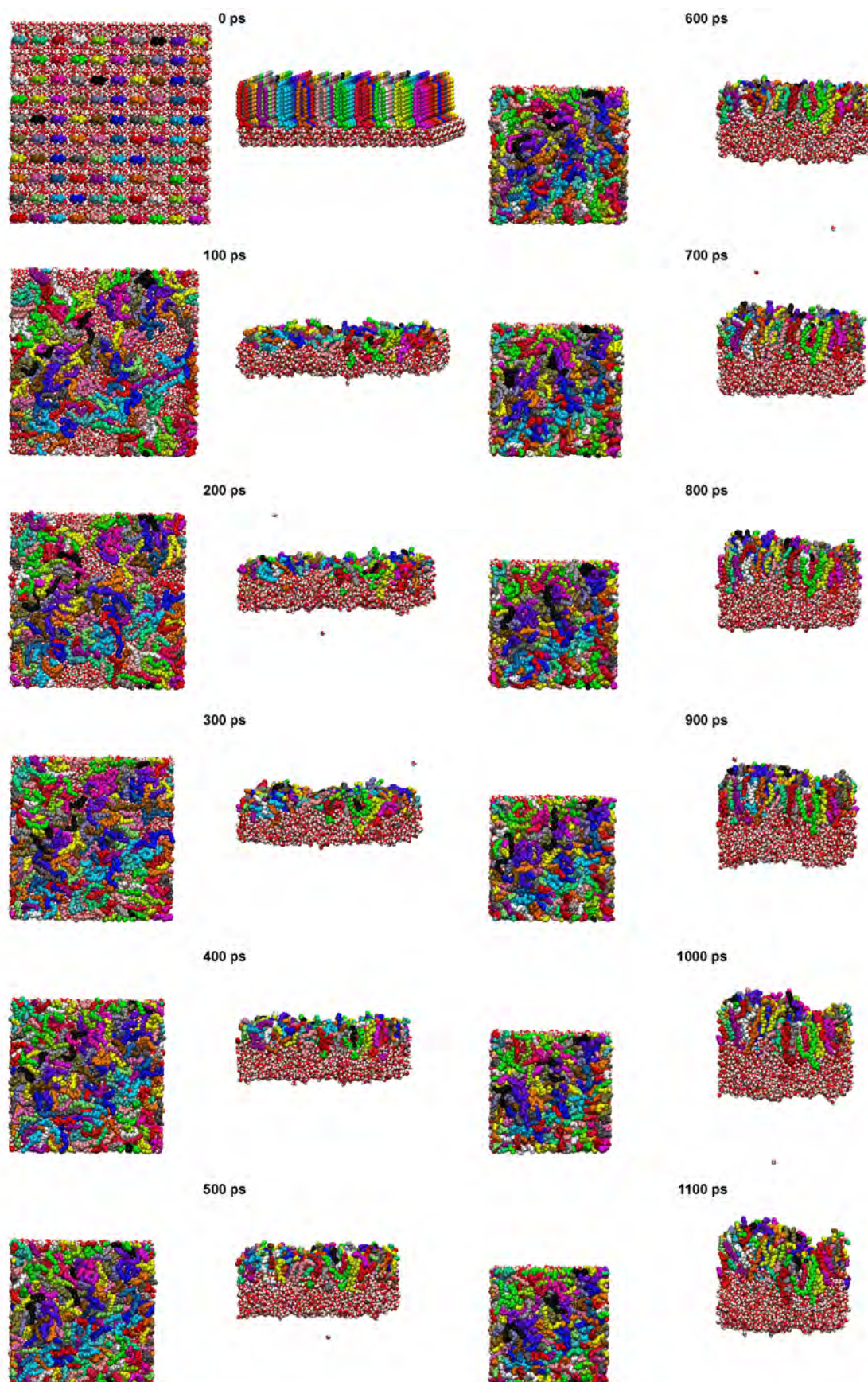


Figure 88. Snapshots (top view/side view) of a simulated compression of a DPPC film on a thin water slab at different simulation times.

In a second step the system snapshots after 0 ps, 100 ps, 200 ps, 300 ps, 400 ps, 500 ps, 600 ps, 700 ps, and 800 ps served as start configurations of simulations for additional 2,000 ps with constant volume condition (NVT ensemble). This yielded an equilibration on the respective molecular area (1.44 nm^2 , 1.25 nm^2 , 1.08 nm^2 , 0.94 nm^2 , 0.83 nm^2 , 0.72 nm^2 , 0.66 nm^2 , 0.59 nm^2 , and 0.56 nm^2 respectively) without further compression. In the case of 1.44 nm^2 and 1.25 nm^2 the water slab is not sufficiently stabilized by the overlying monolayer and collapses under its own surface tension (Figure 89). This behavior is in good agreement with the observation that a DPPC film in GA phase should not substantially alter the surface tension of water. All other monolayers are stable under further simulation.

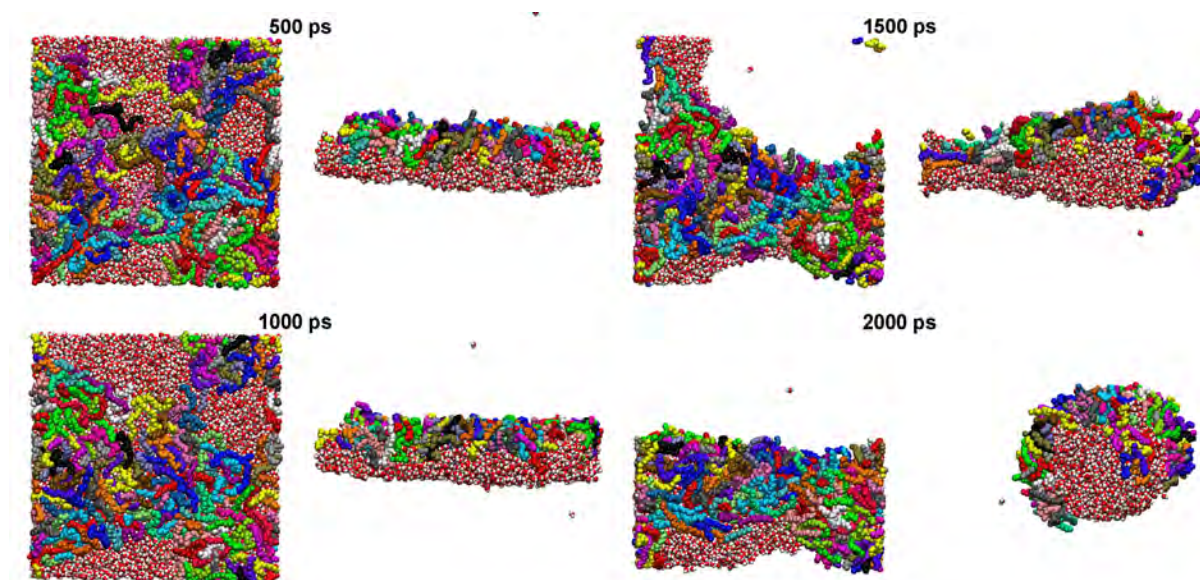


Figure 89. Disruption of a thin water slab covered with DPPC at a molecular area of 1.25 nm^2 . Snapshots at four different times of simulation in top and side view each. Side length of the simulation box is about 11 nm.

Figure 90 shows the order parameter S_z of the DPPC molecules after the additional 2,000 ps equilibration run (the values for 1.44 nm^2 and 1.25 nm^2 were taken at some time before the break up of the water slab). Considering the clustering of the order parameter graphs and keeping in mind the isotherm data for DPPC obtained by experiments we can conclude that the areas of 1.44 nm^2 and 1.25 nm^2 correspond to the gas analogues (GA) phase fading into the liquid expanded (LE) phase at about 1.08 nm^2 and 0.94 nm^2 . With an area per molecule of 0.83 nm^2 the film is still in LE phase. Therefore, it is still clustering together with the latter two but on the verge of the coexistence domain. The molecular areas of 0.72 nm^2 and 0.66 nm^2 delimit the coexistence region of the isotherm. Therefore, they are not clustering well with the other order parameter graphs. With areas of 0.59 nm^2 and 0.56 nm^2 clearly the

liquid condensed (LC) phase is reached, further compression is not considerably changing the order parameter anymore. By periodic continuation of one monolayer for each phase (0.59 nm² monolayer for LC, 0.83 nm² monolayer for LE, and 0.94 nm² monolayer for GA phase respectively) sufficiently large areas were constructed to cut out an area of appropriate size and transfer it onto the silicon oxide substrate. During this process the water film was thinned out to about 0.5 nm in between the DPPC monolayer and the silicon oxide substrate as well. We chose to include this thin water film into the simulation geometry because previous experiments strongly suggest some remaining water after film transfer.^[208] After the transfer onto the silicon oxide substrate the systems were simulated an additional 2,000 ps to allow for a new equilibration. After this the order parameters were determined again (also shown in Figure 90). The molecular areas differs a little bit from the source monolayers due to mismatch of molecules during the cutting out of the periodic continued monolayers and the new imposed periodic boundaries of the silicon oxide substrate containing simulation box. Nevertheless, the order parameters of the monolayers on the silicon oxide substrates clearly correspond to the LC, LE and border of GA phase as intended.

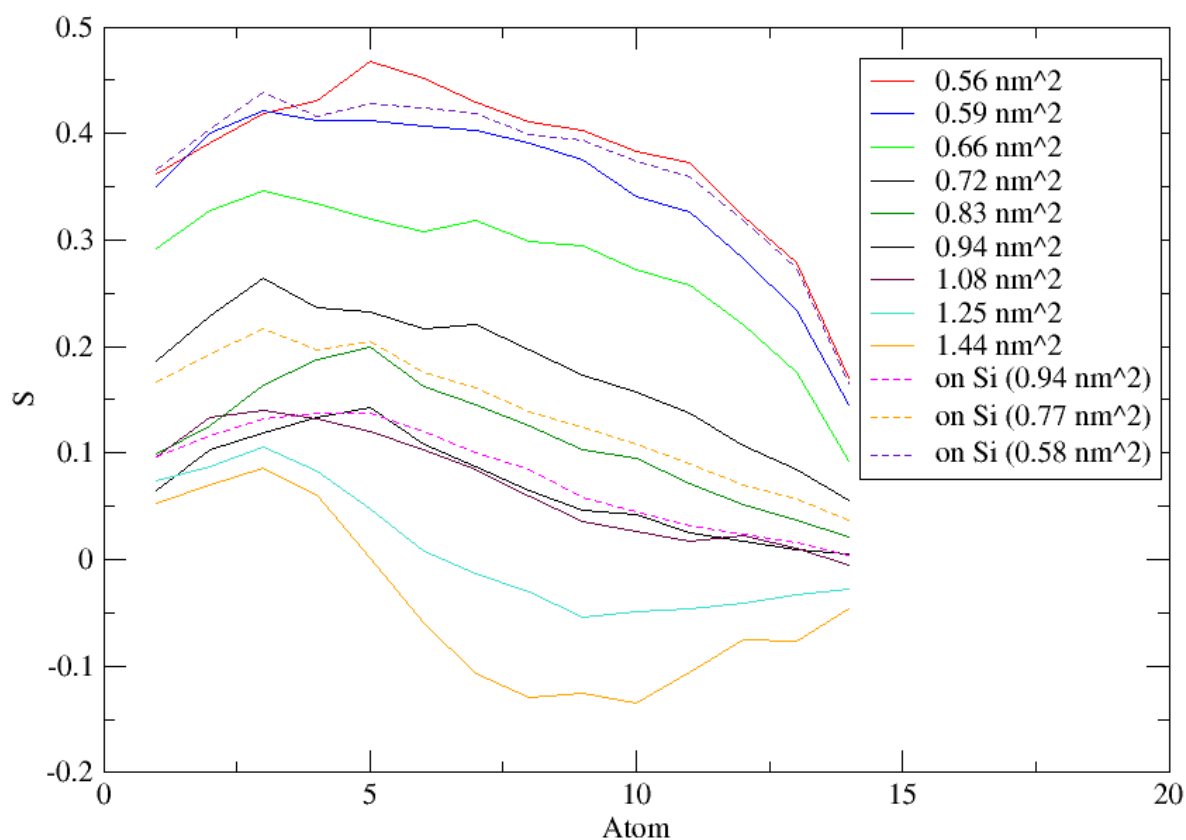


Figure 90. Order parameter S_z of the DPPC molecules in films with different molecular area, averaged over both hydrocarbon chains.

Having obtained suitable substrate systems with silicon oxide covered by a thin water layer and a DPPC monolayer in LC, LE or GA phase respectively, the actual diffusion simulations could be set up. For this one molecule of ANP and perylene respectively was brought into close vicinity (ca. 0.3 nm) to the monolayer and for each phase four different simulations with different start positions of the molecule in the x-y-plane were performed, again for 2,000 ps each. Snapshots from a typical simulation are shown in Figure 91.

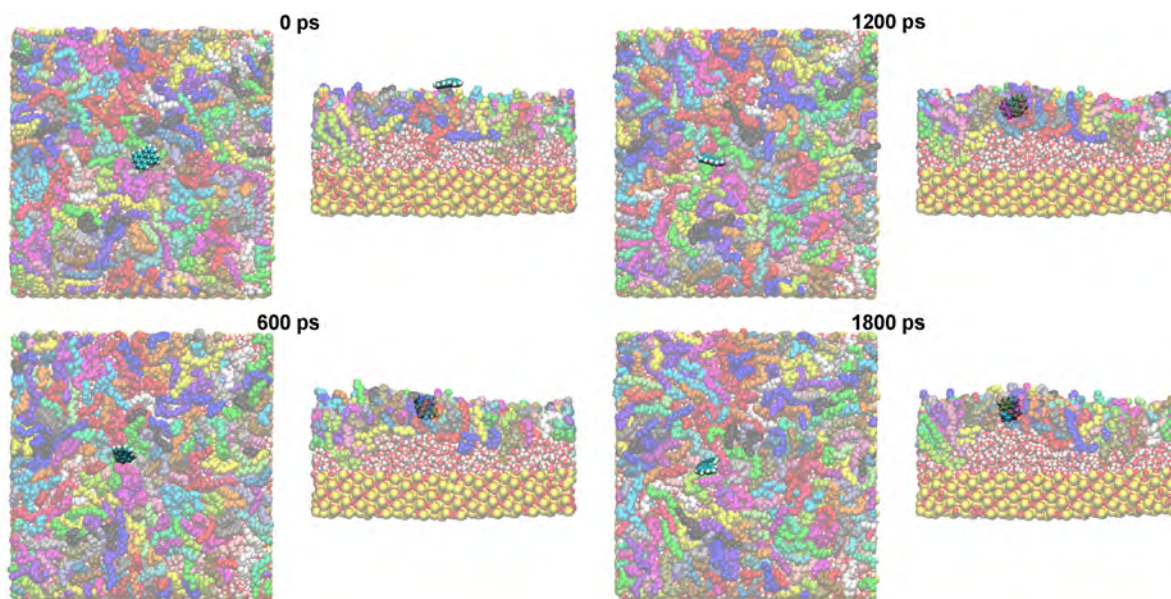


Figure 91. Snapshots of the simulation of a perylene molecule on a LE-phase DPPC substrate at different simulation times (top view/side view). The substrate system is depicted transparent for better visibility of the perylene molecule.

After completion of the simulations the mean square displacement (MSD) in the x-y-plane for the respective molecule was calculated by the program `g_msd`^[78] of the GROMACS suite and the MSD was averaged over the four simulations for each substrate. Graphs of the resulting MSD versus time are given in Figure 92 for ANP and Figure 93 for perylene.

The diffusion of ANP as well as perylene molecules is higher on the LE phase DPPC than on LC phase underground. This fits well with the experimental finding of fewer but bigger domains on LE phase compared to LC phase for ANP as well as perylene. This can be explained by a higher mobility of the molecules on the LE phase.

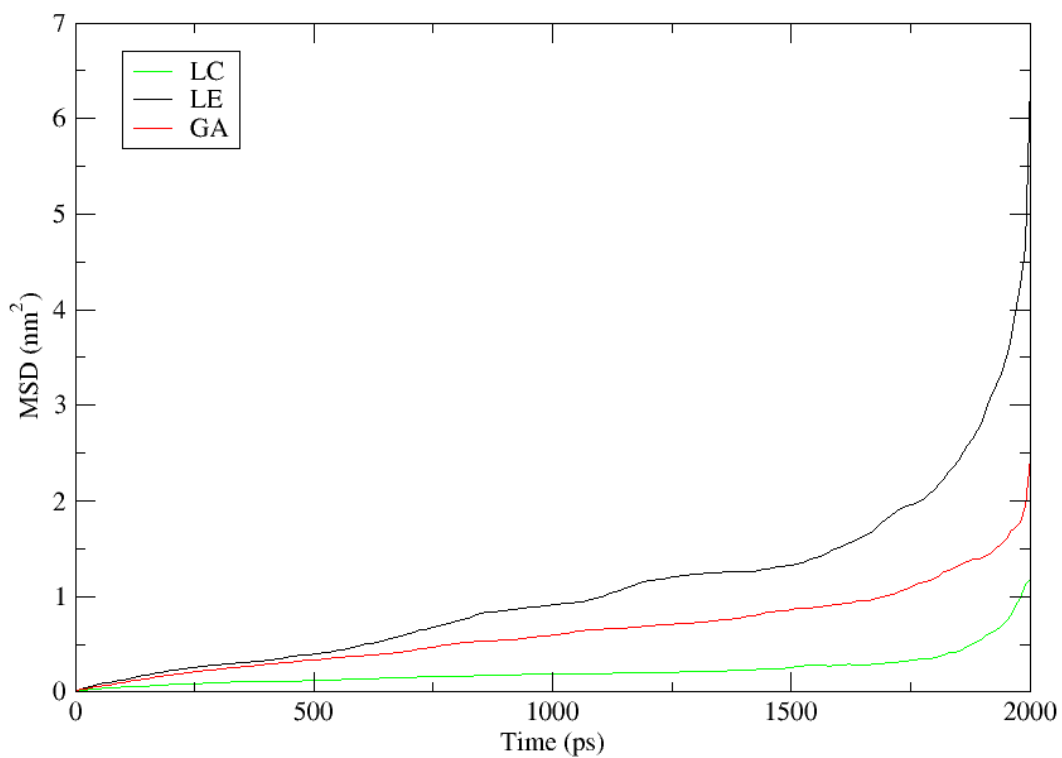


Figure 92. Graph of mean square displacement versus time for ANP.

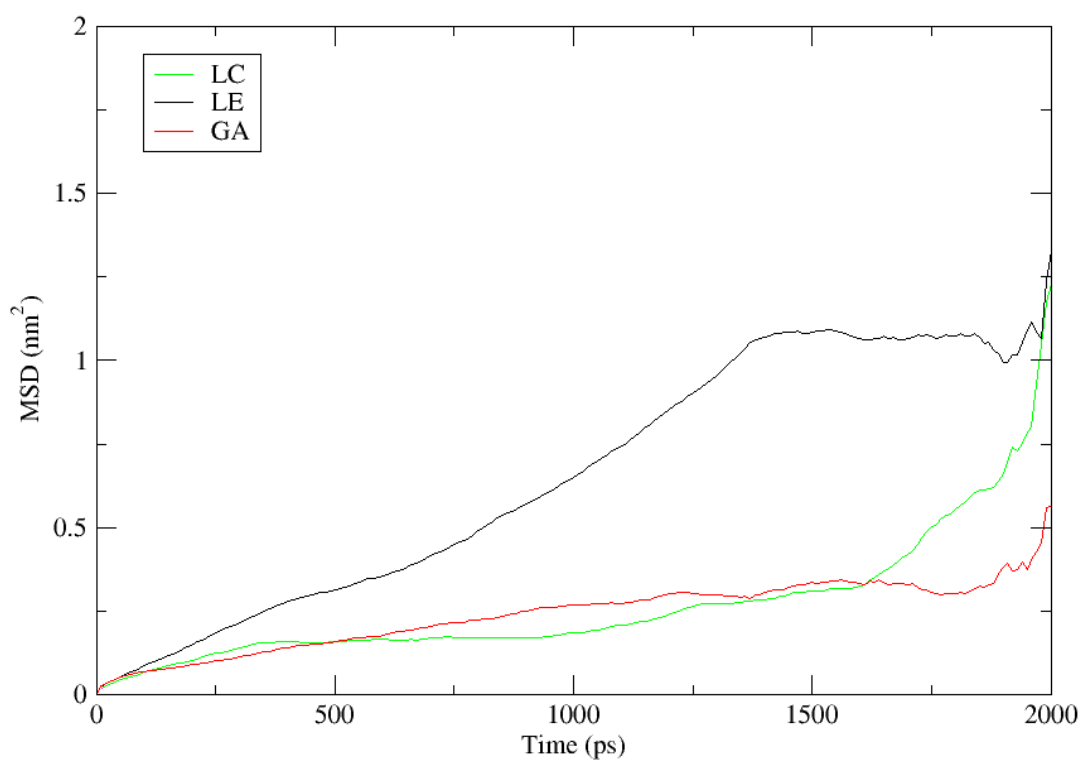


Figure 93. Graph of mean square displacement versus time for perylene.

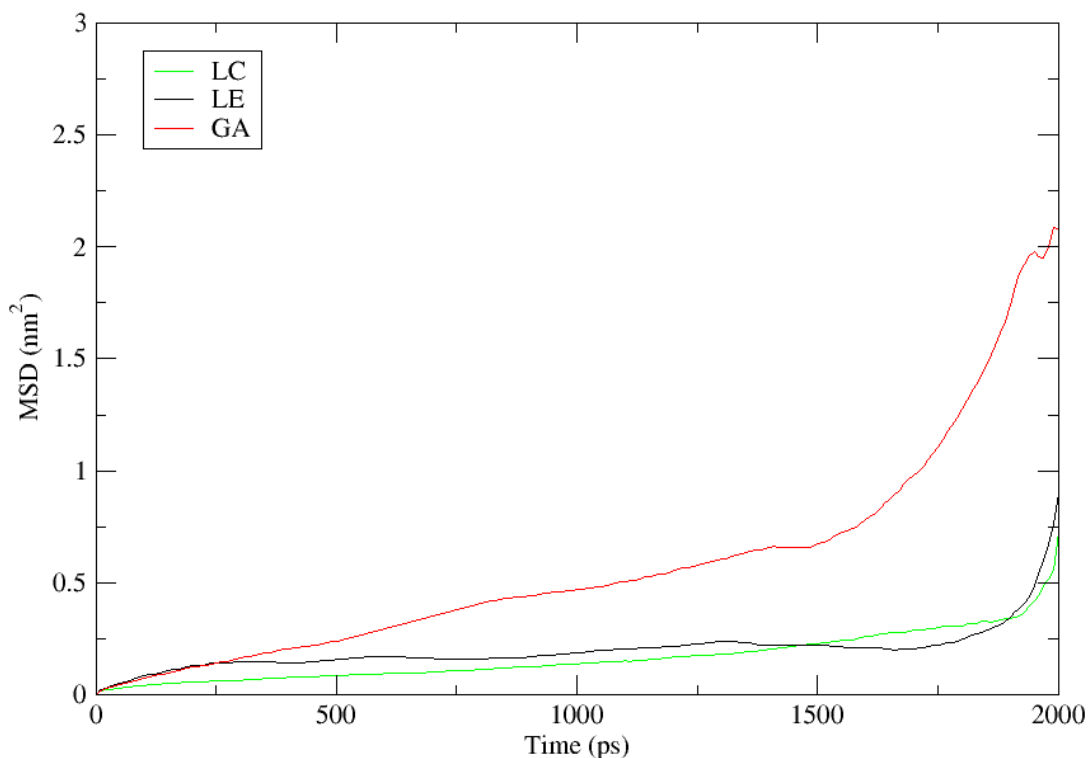


Figure 94. Graph of mean square displacement versus time for perylene NCs.

For comparison we also performed simulations of the diffusion of perylene nanocrystals (NCs) consisting of three perylene molecules. These simulations showed a lower diffusion for the perylene NCs on LC- and LE-phase (Figure 94). The diffusion constants in Table 14 are derived by a linear fit to the averaged MSDs in the middle time segment (from 500 s to 1,500 s) to avoid edge artefacts.

Table 14. Lateral diffusion coefficients by molecule and phase.

	Lateral Diffusion Coefficient (10^{-6} cm ² /s)		
	LC-phase	LE-phase	GA-phase
ANP	1.13 ± 0.02	9.70 ± 0.12	5.09 ± 0.04
Perylene	1.60 ± 0.06	8.64 ± 0.09	1.63 ± 0.03
Perylene NCs	1.37 ± 0.02	0.86 ± 0.04	4.24 ± 0.04

The molecules do not stay on top of the DPPC film but rather submerge into the hydrocarbon chains of the DPPC monolayer during diffusion. Taking this into account we can identify a plausible mechanism for the difference in diffusion as well as the bigger energy barrier for crossing from LE- to LC phase in comparison to the opposite way. The difference in plasticity

and chain movement of the DPPC film becomes quite obvious when looking at a trajectory. But to introduce a measure easier to communicate we calculated the root mean square deviation (RMSD) for the DPPC films of the ANP simulations with the tool `g_rmsdist` of the GROMACS simulation suite.^[78] The first frame of each simulation was taken as a reference and the deviation in the distance of all possible atom pairs within the DPPC film compared to the respective reference structure versus time was calculated. This allows for judging of the plasticity of the film. Figure 95 shows the RMSD averaged over the different simulations.

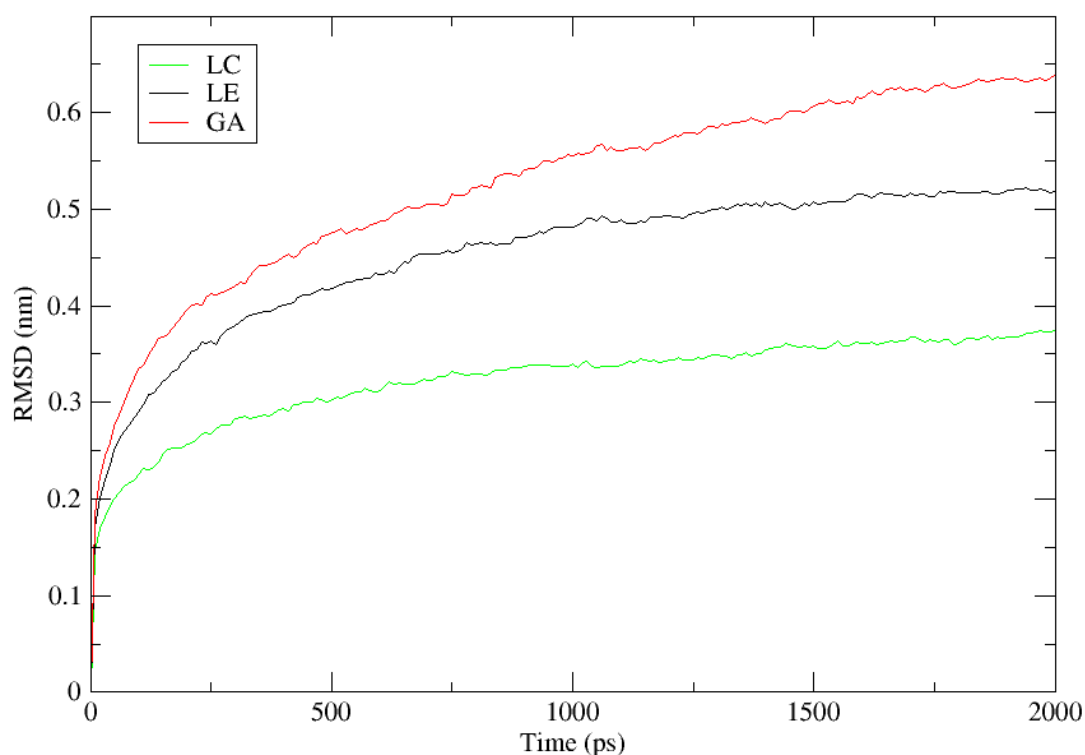


Figure 95. Averaged RMSD of the DPPC films in different phases.

As expected, the packing density of the DPPC films is directly reflected in the structural plasticity, therefore yielding higher RMSD from LC- to LE- to GA-phase. When the molecule is submerged into the DPPC film (as in the case for LC- and LE-phase) its diffusion will be hindered according to the plasticity of the surrounding DPPC chains. Therefore the diffusion becomes slower on LC-phase DPPC with respect to LE-phase areas, yielding the observed increase in number and decrease in size of the domains on the LC-phase. The same difference in diffusion drag can also account for the asymmetric energy barrier between LC- and LE-phase. Recognizing the higher density and lower plasticity of the LC-phase it should be easier for diffusing molecules to pass over from the LC-phase to the LE-phase than the other way around. This behavior still allows for a preferential deposition of molecules onto the LE-phase

even when there is a higher diffusion associated with the LE-phase area. The higher RMSD of the GA-phase does not directly translate into even higher diffusion of the single molecules on GA-phase DPPC. But we observed an intermediate diffusion constant for ANP and an almost LC-phase-like one for perylene. We attribute this to the very unordered structure of the GA-phase film that yields a high RMSD but nevertheless may be harder to cross for the molecules because the hydrocarbon chains of the DPPC are more entangled and tilted than it is the case for the other phases. This notion is also supported by the diffusion of the perylene NCs that is lower compared to single molecule diffusion on LC- and LE-phase but higher on the GA-phase, because the NC will not tumble like single perylene molecules on the rough GA-phase. The NC's incomplete submergence in the case of GA-phase film yields even a higher diffusion than for the single molecules on LC- or LE-phase.

10.5 Summary and Outlook

We conducted a series of MD simulations to elucidate the diffusion and deposition of organic molecules ANP and perylene onto phase-separated DPPC samples. The lower diffusion on LC-phase DPPC observed in experiments could be replicated in the simulation. The mechanism behind the diffusion hindrance in our simulations was identified as an increased drag onto molecules submerged into the hydrocarbon chains of the DPPC film by a denser and less plastic character of the LC-phase compared to the LE-phase. This mechanism can account both for the observed difference in diffusion as well as the postulated asymmetric energy barrier for crossing LC-/LE-phase boundaries which are necessary to explain preferred deposition of molecules onto LE-phase in the light of lower diffusion on the LC-phase. There are additional unpublished experimental results on the organic molecule sexiphenyl (6P) which show a temperature dependant selective assembly onto the DPPC stripe pattern template. Preliminary results suggest that the presented simulations can be applied to this system, too. Therefore ongoing effort is made to run simulations onto this temperature dependant behavior and expand the findings presented here to gain further understanding of the selective deposition of organic molecules onto the DPPC stripe pattern template for different types of molecules.

11 Closing Remarks

During the course of the present work we adventured into many interesting topics in the field of nanotechnology. New insights into the self-organized patterning of DPPC were gained and some novel ways of employing this process for the generation of chemical and topographic patterned surfaces were developed. The combination of the bottom-up process constituted by the DPPC pattern formation with top-down methods like electron beam lithography to generate prestructures that influence the pattern formation lays the foundation for future work on topographic and chemical prestructures with the aim to gain more control over the pattern shape and distribution. Another promising approach to functionalized patterned surfaces for the life sciences is embodied by the enhanced mechanical properties of polymer brushes. This enables structuring by AFM lithography with subsequent selective deposition of chemical compounds into the structured polymer brushes. Preliminary experiments with cantilever arrays for the structuring of large surface areas and the employment of dip pen nanolithography for additional functionalization have been conducted and will be continued in the future. The molecular dynamics simulations gave an additional insight into two model systems: one (domain structure and stability of adenine-C20 on graphite) being a typical example for pattern formation by self-assembly, the other (diffusion and selective deposition of ANP and perylene on DPPC stripe pattern) a likewise typical example for a template guided selective deposition process. The results of the simulations encourage future modelling of similar systems to gain deeper insight into the molecular mechanisms behind the experimental findings. The prospect of ever-growing computational power makes these kinds of calculations more and more feasible even for bigger and more complex systems.

Science is always a collaborative process and I am glad that I was able to be a part in this process together with my colleagues. Hopefully we added a grain of useful knowledge to the ever-growing body of science and I would be more than glad to be able to continue to do so in the future.

References

- (1) Moore, G. E. *Electronics* **1965**, 38.
- (2) Bettinger, C.; Robert Langer; Jeffrey T. Borenstein *Angew. Chem. Int. Ed.* **2009**, 48, 5406-5415.
- (3) Neinhuis, C.; Barthlott, W. *Ann. Bot.* **1997**, 79, 667-677.
- (4) Shalaev, V. M. *Nat. Photonics* **2007**, 1, 41-48.
- (5) Schmelmer, U.; Paul, A.; Küller, A.; Steenackers, M.; Ulman, A.; Grunze, M.; Götzhäuser, A.; Jordan, R. *Small* **2007**, 3, 459-65.
- (6) Steenackers, M.; Küller, A.; Ballav, N.; Zharnikov, M.; Grunze, M.; Jordan, R. *Small* **2007**, 3, 1764-73.
- (7) Garno, J. C.; Yang, Y.; Amro, N. A.; Cruchon-Dupeyrat, S.; Chen, S.; Liu, G. *Nano Lett.* **2003**, 3, 389-395.
- (8) Geissler, M.; Xia, Y. *Adv. Mater.* **2004**, 16, 1249-1269.
- (9) Thompson, L. F.; Willson, C. G.; Bowden, M. J. *Introduction to microlithography*; ACS Symposium Series; American Chemical Society: Washington, DC, 1983.
- (10) Eigler, D. M.; Schweizer, E. K. *Nature* **1990**, 344, 524-526.
- (11) Crommie, M. F.; Lutz, C. P.; Eigler, D. M. *Science* **1993**, 262, 218-220.
- (12) Hla, S.; Bartels, L.; Meyer, G.; Rieder, K. *Phys. Rev. Lett.* **2000**, 85, 2777.
- (13) Piner, R. D.; Zhu, J.; Xu, F.; Hong, S.; Mirkin, C. A. *Science* **1999**, 283, 661-663.
- (14) Xia, Y.; George M. Whitesides *Angew. Chem. Int. Ed.* **1998**, 37, 550-575.
- (15) Chou, S. Y.; Krauss, P. R.; Renstrom, P. J. *Science* **1996**, 272, 85-87.
- (16) Whitesides, G. M.; Kriebel, J. K.; Love, J. C. *Sci. Prog.* **2005**, 88, 17-48.
- (17) Cox, J. K.; Eisenberg*, A.; Lennox, R. B. *Curr. Opin. Colloid Interface Sci.* **1999**, 4, 52-59.
- (18) Lyuksyutov, I.; Naumovets, A. G.; Pokshishevsky, V. V. *Two-Dimensional Crystals*; Academic Pr Inc, 1992.
- (19) Seeman, N. C.; Lukeman, P. S. *Rep. Prog. Phys.* **2005**, 68, 237-270.
- (20) Fischer, U. C.; Heimel, J.; Maas, H.; Hartig, M.; Höppener, S.; H. Fuchs, H. *Surf. Interface Anal.* **2002**, 33, 75-80.
- (21) Ariga, K.; Hill, J. P.; Lee, M. V.; Vinu, A.; Charvet, R.; Acharya, S. *Sci. Technol. Adv. Mater.* **2008**, 9, 014109.
- (22) Camazine, S.; Deneubourg, J.; Franks, N. R.; Sneyd, J.; Theraulaz, G.; Bonabeau, E. *Self-Organization in Biological Systems*; Princeton University Press, 2001.
- (23) Ball, P. *The Self-Made Tapestry: Pattern Formation in Nature*; Oxford University Press, USA, 2001.
- (24) Epstein, I. R.; Showalter, K. *J. Phys. Chem.* **1996**, 100, 13132-13147.
- (25) Gleiche, M.; Chi, L. F.; Fuchs, H. *Nature* **2000**, 403, 173-175.
- (26) Moraille, P.; Badia, A. *Langmuir* **2002**, 18, 4414-4419.
- (27) Chen, X.; Lenhert, S.; Hirtz, M.; Lu, N.; Fuchs, H.; Chi, L. *Acc. Chem. Res.* **2007**, 40, 393-401.
- (28) Franklin, B. *Phil. Trans.* **1774**, 64, 445-460.
- (29) Rayleigh, J. W. S. *Philos. Mag.* **1890**, 30, 285-298, 465-475.
- (30) Pockels, A. *Nature* **1891**, 43, 437-439.
- (31) Langmuir, I. *J. Am. Chem. Soc.* **1917**, 39, 1848-1906.
- (32) Blodgett, K. B. *J. Am. Chem. Soc.* **1934**, 56, 495.
- (33) Blodgett, K. B. *J. Am. Chem. Soc.* **1935**, 57, 1007-1022.
- (34) Blodgett, K. B.; Langmuir, I. *Phys. Rev.* **1937**, 51, 964.
- (35) Kuhn, H. *Thin Solid Films* **1983**, 99, 1-16.

-
- (36) Paloheimo, J.; Kuivalainen, P.; Stubb, H.; Vuorimaa, E.; Yli-Lahti, P. *Appl. Phys. Lett.* **1990**, *56*, 1157-1159.
- (37) Heath, J. R. *Annu. Rev. Mater. Res.* **2009**, *39*, 1-23.
- (38) Tedeschi, C.; Polli, M.; Fontana, M.; Pieroni, O. *Thin Solid Films* **1996**, *284-285*, 174-176.
- (39) Agbor, N. E.; Cresswell, J. P.; Petty, M. C.; Monkman, A. P. *Sens. Actuators B* **1997**, *41*, 137-141.
- (40) Kusano, H.; Kitagawa, M. *IEICE Trans. Electron.* **2008**, *E91-C*, 1876-1880.
- (41) Huang, J.; Kim, F.; Tao, A. R.; Connor, S.; Yang, P. *Nat. Mater.* **2005**, *4*, 896-900.
- (42) Huang, J.; Tao, A. R.; Connor, S.; He, R.; Yang, P. *Nano Lett.* **2006**, *6*, 524-529.
- (43) Li, X.; Zhang, L.; Wang, X.; Shimoyama, I.; Sun, X.; Seo, W.; Dai, H. *J. Am. Chem. Soc.* **2007**, *129*, 4890-4891.
- (44) Cote, L. J.; Kim, F.; Huang, J. *J. Am. Chem. Soc.* **2009**, *131*, 1043-1049.
- (45) Chechel, O. V.; Nikolaev, E. N. *Instrum. Exp. Tech.* **1991**, *34*, 750-762.
- (46) Kaganer, V. M.; Möhwald, H.; Dutta, P. *Rev. Mod. Phys.* **1999**, *71*, 779.
- (47) Adam, N. K. *Proc. R. Soc. Lond. A* **1922**, *101*, 516-531.
- (48) Young, T. *Phil. Trans.* **1805**, *95*, 65-87.
- (49) Petrov, P. G.; Petrov, J. G. *Langmuir* **1995**, *11*, 3261-3268.
- (50) Petrov, J. G.; Radoev, B. P. *Colloid. Polym. Sci.* **1981**, *259*, 753-760.
- (51) Blake, T. D.; Haynes, J. M. *J. Colloid Interf. Sci.* **1969**, *30*, 421-423.
- (52) Lenhert, S.; Gleiche, M.; Fuchs, H.; Chi, L. *ChemPhysChem* **2005**, *6*, 2495-2498.
- (53) Hönig, D.; Möbius, D. *J. Phys. Chem.* **1991**, *95*, 4590-4592.
- (54) Hénon, S.; Meunier, J. *Rev. Sci. Instrum.* **1991**, *62*, 936-939.
- (55) Hell, S. W. *Nat. Biotechnol.* **2003**, *21*, 1347-1355.
- (56) Schönle, A.; Hell, S. W. *Nat. Biotechnol.* **2007**, *25*, 1234-1235.
- (57) Binnig, G.; Quate, C. F.; Gerber, C. *Phys. Rev. Lett.* **1986**, *56*, 930-933.
- (58) Binnig, G.; Rohrer, H.; Gerber, C.; Weibel, E. *Phys. Rev. Lett.* **1982**, *49*, 57-61.
- (59) Binnig, G.; Rohrer, H.; Gerber, C.; Weibel, E. *Phys. Rev. Lett.* **1983**, *50*, 120-123.
- (60) Klehn, B.; Kunze, U. *J. Appl. Phys.* **1999**, *85*, 3897-3903.
- (61) Heyde, M.; Rademann, K.; Cappella, B.; Geuss, M.; Sturm, H.; Spangenberg, T.; Niehus, H. *Rev. Sci. Instrum.* **2001**, *72*, 136-141.
- (62) Cappella, B.; Sturm, H.; Weidner, S. M. *Polymer* **2002**, *43*, 4461-4466.
- (63) Cappella, B. *Dynamic Plowing Lithography und Kraft-Abstands-Kurven Indentation als lithographische Methoden für die Modifizierung von Polymeroberflächen.*, Technischen Universität Berlin, 2002.
- (64) Wang, Y.; Xiaodong Hong; Jun Zeng; Baoquan Liu; Bin Guo; Honghua Yan *Small* **2009**, *5*, 477-483.
- (65) Alder, B. J.; Wainwright, T. E. *J. Chem. Phys.* **1959**, *31*, 459-466.
- (66) Freddolino, P. L.; Arkhipov, A. S.; Larson, S. B.; McPherson, A.; Schulten, K. *Structure* **2006**, *14*, 437-449.
- (67) Marrink, S. J.; Risselada, H. J.; Yefimov, S.; Tieleman, D. P.; de Vries, A. H. *J. Phys. Chem. B* **2007**, *111*, 7812-24.
- (68) Xing, C.; Faller, R. *J. Phys. Chem. B* **2008**, *112*, 7086-7094.
- (69) Baoukina, S.; Monticelli, L.; Marrink, S. J.; Tieleman, D. P. *Langmuir* **2007**, *23*, 12617-12623.
- (70) Case, D. A.; III, T. E. C.; Darden, T.; Gohlke, H.; Luo, R.; Jr, K. M. M.; Onufriev, A.; Simmerling, C.; Wang, B.; Woods, R. J. *J. Comput. Chem.* **2005**, *26*, 1668-1688.
- (71) Brooks, B. R.; Brucoleri, R. E.; Olafson, B. D.; States, D. J.; Swaminathan, S.; Karplus, M. *J. Comput. Chem.* **1983**, *4*, 187-217.
- (72) MacKerell, Jr., A. D.; Brooks, B.; Brooks, III, C. L.; Nilsson, L.; Roux, B.; Won, Y.; Karplus, M. In *The Encyclopedia of Computational Chemistry* (ed. P. von Raqué-Schleyer); John Wiley & Sons Ltd: Chichester, 1998; Bd. 1, S. 271-277.

-
- (73) Brooks, B. R.; III, C. L. B.; Jr, A. D. M.; Nilsson, L.; Petrella, R. J.; Roux, B.; Won, Y.; Archontis, G.; Bartels, C.; Boresch, S.; Caflisch, A.; Caves, L.; Cui, Q.; Dinner, A. R.; Feig, M.; Fischer, S.; Gao, J.; Hodosecek, M.; Im, W.; Kuczera, K.; Lazaridis, T.; Ma, J.; Ovchinnikov, V.; Paci, E.; Pastor, R. W.; Post, C. B.; Pu, J. Z.; Schaefer, M.; Tidor, B.; Venable, R. M.; Woodcock, H. L.; Wu, X.; Yang, W.; York, D. M.; Karplus, M. *J. Comput. Chem.* **2009**, *30*, 1545-1614.
- (74) van der Spoel, D.; Lindahl, E.; Hess, B.; Groenhof, G.; Mark, A. E.; Berendsen, H. J. C. *J. Comput. Chem.* **2005**, *26*, 1701-1718.
- (75) Hess, B.; Kutzner, C.; van der Spoel, D.; Lindahl, E. *J. Chem. Theory Comput.* **2008**, *4*, 435-447.
- (76) Phillips, J. C.; Braun, R.; Wang, W.; Gumbart, J.; Tajkhorshid, E.; Villa, E.; Chipot, C.; Skeel, R. D.; Kalé, L.; Schulten, K. *J. Comput. Chem.* **2005**, *26*, 1781-1802.
- (77) van der Spoel, D.; Lindahl, E.; Hess, B.; van Buuren, A. R.; Apol, E.; Meulenhoff, P. J.; Tieleman, D. P.; Sijbers, A. L. T. M.; Feenstra, K. A.; van Drunen, R.; Berendsen, H. J. C. *Gromacs User Manual version 4.0*; www.gromacs.org, 2005.
- (78) van der Spoel, D.; Lindahl, E.; Hess, B.; van Buuren, A. R.; Apol, E.; Meulenhoff, P. J.; Tieleman, D. P.; Sijbers, A. L. T. M.; Feenstra, K. A.; van Drunen, R.; Berendsen, H. J. C. *Gromacs User Manual version 4.0*; www.gromacs.org, 2005.
- (79) van Gunsteren, W. F.; Billeter, S. R.; Eising, A. A.; Hünenberger, P. H.; Krüger, P.; Mark, A. E.; Scott, W. R. P.; Tironi, I. G. *Biomolecular Simulation: The GROMOS96 Manual and User Guide*; Verlag der Fachvereine Hochschulverlag AG an der ETH Zurich: Zürich, 1996.
- (80) Allen, M. P.; Tildesley, D. J. *Computer Simulation of Liquids*; Oxford University Press, USA, 1989.
- (81) Yonetani, Y. *J. Chem. Phys.* **2006**, *124*, 204501-11.
- (82) Berendsen, H. J. C. In *Computer Simulation of Biomolecular Systems: Theoretical and Experimental Applications* (eds. Van Gunsteren, W. ; Weiner, P.; Wilkinson, A. T.); ESCOM: Leiden, 1993; Bd. 2, S. 161-181.
- (83) Anezo, C.; de Vries, A. H.; Holtje, H.; Tieleman, D. P.; Marrink, S. J. *Phys. Chem. B* **2003**, *107*, 9424-9433.
- (84) Ewald, P. P. *Ann. Phys.* **1921**, *369*, 253-287.
- (85) Darden, T.; York, D.; Pedersen, L. *J. Chem. Phys.* **1993**, *98*, 10089-10092.
- (86) Essmann, U.; Perera, L.; Berkowitz, M. L.; Darden, T.; Lee, H.; Pedersen, L. G. *J. Chem. Phys.* **1995**, *103*, 8577-8593.
- (87) van Gunsteren, W. F.; Berendsen, H. J. C. *Gromos-87 manual. Biomos BV Nijenborgh 4, 9747 Groningen, The Netherlands*; 1987.
- (88) Lawrence, C. P.; Skinner, J. L. *Chem. Phys. Lett.* **2003**, *372*, 842-847.
- (89) Moss, G. P. *Pure Appl. Chem.* **1996**, *68*, 2193-2222.
- (90) Spratte, K.; Chi, L. F.; Riegler, H. *Europhys. Lett.* **1994**, *25*, 211-217.
- (91) Chen, X.; Hirtz, M.; Fuchs, H.; Chi, L. *Adv. Mater.* **2005**, *17*, 2881-2885.
- (92) Brinks, M.; Hirtz, M.; Chi, L.; Fuchs, H.; Studer, A. *Angew. Chem. Int. Ed.* **2007**, *46*, 5231-5233.
- (93) Wang, L.; Cruz, A.; Flach, C. R.; Perez-Gil, J.; Mendelsohn, R. *Langmuir* **2007**, *23*, 4950-4958.
- (94) Schultz, J.; Tsutsumi, K.; Donnet, J. J. *Colloid Interface Sci.* **1977**, *59*, 272-276.
- (95) Schultz, J.; Tsutsumi, K.; Donnet, J. J. *Colloid Interface Sci.* **1977**, *59*, 277-282.
- (96) Zhuravlev, L. T. *Langmuir* **1987**, *3*, 316-318.
- (97) Peterson, I. R.; Brzezinski, V.; Kenn, R. M.; Steitz, R. *Langmuir* **1992**, *8*, 2995-3002.
- (98) Chen, X. *Emergence and Complexity in Interfacial Self-organization of Lipids* (Doctoral Thesis), Westfälische Wilhelms-Universität Münster, 2006.

- (99) Loh, K. K.; Saxena, A.; Lookman, T.; Parikh, A. In *Technical Proceedings of the 2002 International Conference on Computational Nanoscience and Nanotechnology*; Computational Pubns, 2002; Bd. 2, S. 409-410.
- (100) Baier, H.; Bonhoeffer, F. *Science* **1992**, *255*, 472-475.
- (101) Dertinger, S. K. W.; Jiang, X.; Li, Z.; Murthy, V. N.; Whitesides, G. M. *PNAS* **2002**, *99*, 12542-12547.
- (102) Ruardy, T. G.; Schakenraad, J. M.; Mei, H. C. V. D.; Busscher, H. J. *Surf. Sci. Rep.* **29**, 3-30.
- (103) Fossier, K. A.; Nuzzo, R. G. *Anal. Chem.* **2003**, *75*, 5775-5782.
- (104) Jeon, N. L.; Dertinger, S. K. W.; Chiu, D. T.; Choi, I. S.; Stroock, A. D.; Whitesides, G. M. *Langmuir* **2000**, *16*, 8311-8316.
- (105) Jiang, X.; Xu, Q.; Dertinger, S. K. W.; Stroock, A. D.; Fu, T.; Whitesides, G. M. *Anal. Chem.* **2005**, *77*, 2338-2347.
- (106) Chaudhury, M. K.; Whitesides, G. M. *Science* **1992**, *256*, 1539-1541.
- (107) Liedberg, B.; Tengvall, P. *Langmuir* **1995**, *11*, 3821-3827.
- (108) Riepl, M.; Ostblom, M.; Lundstrom, I.; Svensson, S. C. T.; Denier van der Gon, A. W.; Schaferling, M.; Liedberg, B. *Langmuir* **2005**, *21*, 1042-1050.
- (109) Choi, S.; Zhang Newby, B. *Langmuir* **2003**, *19*, 7427-7435.
- (110) Bhangale, S.; Tjong, V.; Wu, L.; Yakovlev, N.; Moran, P. *Adv. Mater.* **2005**, *17*, 809-813.
- (111) von Philipsborn, A. C.; Lang, S.; Loeschinger, J.; Bernard, A.; David, C.; Lehnert, D.; Bonhoeffer, F.; Bastmeyer, M. *Development* **2006**, *133*, 2487-2495.
- (112) Dalby, M. J. *Med. Eng. Phys.* **2005**, *27*, 730-742.
- (113) Cao, H.; Tegenfeldt, J. O.; Austin, R. H.; Chou, S. Y. *Appl. Phys. Lett.* **2002**, *81*, 3058-3060.
- (114) Fuierer, R.; Carroll, R.; Feldheim, D.; Gorman, C. *Adv. Mater.* **2002**, *14*, 154-157.
- (115) Boncheva, M.; Whitesides, G. M. *MRS Bull.* **2005**, *30*, 736-742.
- (116) Chen, X.; Lu, N.; Zhang, H.; Hirtz, M.; Wu, L.; Fuchs, H.; Chi, L. *J. Phys. Chem. B* **2006**, *110*, 8039-8046.
- (117) Ghosh, M.; Fan, F.; Stebe, K. J. *Langmuir* **2007**, *23*, 2180-2183.
- (118) Langmuir, I.; Schaefer, V. J. *J. Am. Chem. Soc.* **1938**, *60*, 1351-1360.
- (119) Lenhert, S.; Zhang, L.; Mueller, J.; Wiesmann, H. P.; Erker, G.; Fuchs, H.; Chi, L. *Adv. Mater.* **2004**, *16*, 619-624.
- (120) Gleiche, M.; Chi, L.; Gedig, E.; Fuchs, H. *ChemPhysChem* **2001**, *2*, 187-191.
- (121) Lu, N.; Gleiche, M.; Zheng, J.; Lenhert, S.; Xu, B.; Chi, L.; Fuchs, H. *Adv. Mater.* **2002**, *14*, 1812-1815.
- (122) Purrucker, O.; Fortig, A.; Ludtke, K.; Jordan, R.; Tanaka, M. *J. Am. Chem. Soc.* **2005**, *127*, 1258-1264.
- (123) Moraille, P.; Badia, A. *Angew. Chem. Int. Ed.* **2002**, *41*, 4303-4306.
- (124) Lu, N.; Chen, X.; Molenda, D.; Naber, A.; Fuchs, H.; Talapin, D. V.; Weller, H.; Muller, J.; Lupton, J. M.; Feldmann, J.; Rogach, A. L.; Chi, L. *Nano Lett.* **2004**, *4*, 885-888.
- (125) Chen, X.; Hirtz, M.; Rogach, A. L.; Talapin, D. V.; Fuchs, H.; Chi, L. *Nano Lett.* **2007**, *7*, 3483-3488.
- (126) Lenhert, S.; Meier, M.; Meyer, U.; Chi, L.; Wiesmann, H. P. *Biomaterials* **2005**, *26*, 563-570.
- (127) Zhang, M.; Lenhert, S.; Wang, M.; Chi, L.; Lu, N.; Fuchs, H.; Ming, N. B. *Adv. Mater.* **2004**, *16*, 409-413.
- (128) Chen, X.; Hirtz, M.; Fuchs, H.; Chi, L. *Langmuir* **2007**, *23*, 2280-2283.
- (129) Zhao, B.; Brittain, W. J. *Prog. Polym. Sci.* **2000**, *25*, 677-710.
- (130) Jennings, G.; Brantley, E. *Adv. Mater.* **2004**, *16*, 1983-1994.
- (131) Edmondson, S.; Osborne, V. L.; Huck, W. T. S. *Chem. Soc. Rev.* **2004**, *33*, 14-22.
- (132) Prucker, O.; Ruhe, J. *Macromolecules* **1998**, *31*, 592-601.
- (133) Prucker, O.; Ruhe, J. *Macromolecules* **1998**, *31*, 602-613.
- (134) Hawker, C. J.; Bosman, A. W.; Harth, E. *Chem. Rev.* **2001**, *101*, 3661-3688.
- (135) Matyjaszewski, K.; Xia, J. *Chem. Rev.* **2001**, *101*, 2921-2990.

-
- (136) Kamigaito, M.; Ando, T.; Sawamoto, M. *Chem. Rev.* **2001**, *101*, 3689-3746.
- (137) Rizzardo, E.; Chiefari, J.; Mayadunne, R. T. A.; Moad, G.; Thang, S. H. In *Controlled/Living Radical Polymerization (Ed: K. Matyjaszewski)*; ACS Symposium Series; Oxford University Press: Washington DC, 2000; S. 278.
- (138) Jones, D.; Smith, J.; Huck, W.; Alexander, C. *Adv. Mater.* **2002**, *14*, 1130-1134.
- (139) von Werne, T. A.; Germack, D. S.; Hagberg, E. C.; Sheares, V. V.; Hawker, C. J.; Carter, K. R. *J. Am. Chem. Soc.* **2003**, *125*, 3831-8.
- (140) Edmondson, S.; Huck, W. T. S. *Adv. Mater.* **2004**, *16*, 1327-1331.
- (141) Zhou, F.; Huck, W. T. S. *Chem. Commun.* **2005**, 5999-6001.
- (142) Husemann, M.; Morrison, M.; Benoit, D.; Frommer, J.; Mate, C. M.; Hinsberg, W. D.; Hedrick, J. L.; Hawker, C. J. *J. Am. Chem. Soc.* **2000**, *122*, 1844-1845.
- (143) Zhou, F.; Jiang, L.; Liu, W.; Xue, Q. *Macromol. Rapid Commun.* **2004**, *25*, 1979-1983.
- (144) Xu, F. J.; Song, Y.; Cheng, Z. P.; Zhu, X. L.; Zhu, C. X.; Kang, E. T.; Neoh, K. G. *Macromolecules* **2005**, *38*, 6254-6258.
- (145) Schmelmer, U.; Jordan, R.; Geyer, W.; Eck, W.; Götzhäuser, A.; Grunze, M.; Ulman, A. *Angew. Chem. Int. Ed.* **2003**, *42*, 559-563.
- (146) Brack, H.; Padeste, C.; Slaski, M.; Alkan, S.; Solak, H. H. *J. Am. Chem. Soc.* **2004**, *126*, 1004-1005.
- (147) Ahn, S. J.; Kaholek, M.; Lee, W.; LaMattina, B.; LaBean, T. H.; Zauscher, S. *Adv. Mater.* **2004**, *16*, 2141-2145.
- (148) Kaholek, M.; Lee, W.; Feng, J.; LaMattina, B.; Dyer, D. J.; Zauscher, S. *Chem. Mater.* **2006**, *18*, 3660-3664.
- (149) Park, M.; Harrison, C.; Chaikin, P. M.; Register, R. A.; Adamson, D. H. *Science* **1997**, *276*, 1401-1404.
- (150) Haynes, C. L.; Van Duyne, R. P. *J. Phys. Chem. B* **2001**, *105*, 5599-5611.
- (151) Chen, X.; Rogach, A. L.; Talapin, D. V.; Fuchs, H.; Chi, L. *J. Am. Chem. Soc.* **2006**, *128*, 9592-9593.
- (152) Studer, A. *Chem. Soc. Rev.* **2004**, *33*, 267-73.
- (153) Matyjaszewski, K.; Woodworth, B. E.; Zhang, X.; Gaynor, S. G.; Metzner, Z. *Macromolecules* **1998**, *31*, 5955-5957.
- (154) Wetter, C.; Gierlich, J.; Knoop, C. A.; Müller, C.; Schulte, T.; Studer, A. *Chem. Eur. J.* **2004**, *10*, 1156-1166.
- (155) Schulte, T.; Siegenthaler, K. O.; Luftmann, H.; Letzel, M.; Studer, A. *Macromolecules* **2005**, *38*, 6833-6840.
- (156) Devaux, C. *Eur. Phys. J. E* **2002**, *7*, 345.
- (157) Tsujii, Y.; Ohno, K.; Yamamoto, S.; Goto, A.; Fukuda, T. In *Surface-Initiated Polymerization I (Ed. Rainer Jordan)*; Advances in Polymer Science; Springer: Berlin, 2006; Bd. 197, S. 1.
- (158) Yoshikawa, C.; Goto, A.; Tsujii, Y.; Fukuda, T.; Kimura, T.; Yamamoto, K.; Kishida, A. *Macromolecules* **2006**, *39*, 2284-2290.
- (159) Bhat, R.; Chaney, B.; Rowley, J.; Liebmann-Vinson, A.; Genzer, J. *Adv. Mater.* **2005**, *17*, 2802-2807.
- (160) Andruzzi, L.; Senaratne, W.; Hexemer, A.; Sheets, E. D.; Ilic, B.; Kramer, E. J.; Baird, B.; Ober, C. K. *Langmuir* **2005**, *21*, 2495-2504.
- (161) Charest, J. L.; Eliason, M. T.; García, A. J.; King, W. P. *Biomaterials* **2006**, *27*, 2487-94.
- (162) Lenhart, S.; Sesma, A.; Hirtz, M.; Chi, L.; Fuchs, H.; Wiesmann, H. P.; Osbourn, A. E.; Moerschbacher, B. M. *Langmuir* **2007**, *23*, 10216-10223.
- (163) Motornov, M.; Minko, S.; Eichhorn, K.; Nitschke, M.; Simon, F.; Stamm, M. *Langmuir* **2003**, *19*, 8077-8085.
- (164) Steenackers, M.; Lud, S. Q.; Niedermeier, M.; Bruno, P.; Gruen, D. M.; Feulner, P.; Stutzmann, M.; Garrido, J. A.; Jordan, R. *J. Am. Chem. Soc.* **2007**, *129*, 15655-61.
- (165) Liu, X.; Guo, S.; Mirkin, C. A. *Angew. Chem.* **2003**, *115*, 4933-4937.

- (166) Dronavajjala, K. D.; Rajagopalan, R.; Uppili, S.; Sen, A.; Allara, D. L.; Foley, H. C. *J. Am. Chem. Soc.* **2006**, *128*, 13040-1.
- (167) Diegoli, S.; Hamlett, C. A. E.; Leigh, S. J.; Mendes, P. M.; Preece, J. A. *Proc. Inst. Mech. Eng. G J. Aerosp. Eng.* **2007**, *221*, 589-629.
- (168) Hu, Y.; Das, A.; Hecht, M. H.; Scoles, G. *Langmuir* **2005**, *21*, 9103-9.
- (169) Liang, J.; Scoles, G. *Langmuir* **2007**, *23*, 6142-7.
- (170) Berger, R.; Cheng, Y.; Förch, R.; Gotsmann, B.; Gutmann, J. S.; Pakula, T.; Rietzler, U.; Schärfl, W.; Schmidt, M.; Strack, A.; Windeln, J.; Butt, H. *Langmuir* **2007**, *23*, 3150-6.
- (171) Szoszkiewicz, R.; Okada, T.; Jones, S. C.; Li, T.; King, W. P.; Marder, S. R.; Riedo, E. *Nano Lett.* **2007**, *7*, 1064-9.
- (172) Studer, A.; Schulte, T. *Chem. Rec.* **2005**, *5*, 27-35.
- (173) Headrick, J. E.; Armstrong, M.; Cratty, J.; Hammond, S.; Sheriff, B. A.; Berrie, C. L. *Langmuir* **2005**, *21*, 4117-22.
- (174) Lee, M. V.; Nelson, K. A.; Hutchins, L.; Becerril, H. A.; Cosby, S. T.; Blood, J. C.; Wheeler, D. R.; Davis, R. C.; Woolley, A. T.; Harb, J. N.; Linfood, M. R. *Chem. Mater.* **2007**, *19*, 5052-5054.
- (175) Kelly, R. E. A.; Lee, Y. J.; Kantorovich, L. N. *J. Phys. Chem. B* **2005**, *109*, 11933-11939.
- (176) Humphrey, W.; Dalke, A.; Schulten, K. *J. Mol. Graphics* **1996**, *14*, 33-38.
- (177) Rappe, A. K.; Casewit, C. J.; Colwell, K. S.; Goddard, W. A.; Skiff, W. M. *J. Am. Chem. Soc.* **1992**, *114*, 10024-10035.
- (178) Shi, X.; Kong, Y.; Zhao, Y.; Gao, H. *Acta. Mech. Sin.* **2005**, *21*, 249-256.
- (179) Schüttelkopf, A. W.; van Aalten, D. M. F. *Acta Cryst.* **2004**, *D60*, 1355-1363.
- (180) Bayly, C. I.; Cieplak, P.; Cornell, W.; Kollman, P. A. *J. Phys. Chem.* **1993**, *97*, 10269-10280.
- (181) Hu, H.; Lu, Z.; Yang, W. *J. Chem. Theory Comput.* **2007**, *3*, 1004-1013.
- (182) Lindahl, E.; Hess, B.; van der Spoel, D. *J. Mol. Model.* **2001**, *7*, 306-317.
- (183) Daura, X.; Mark, A. E.; Gunsteren, W. F. V. *J. Comput. Chem.* **1998**, *19*, 535-547.
- (184) Oostenbrink, C.; Villa, A.; Mark, A. E.; Gunsteren, W. F. V. *J. Comput. Chem.* **2004**, *25*, 1656-1676.
- (185) Berendsen, H. J. C.; Postma, J. P. M.; van Gunsteren, W. F.; DiNola, A.; Haak, J. R. *J. Chem. Phys.* **1984**, *81*, 3684-3690.
- (186) Hess, B.; Bekker, H.; Berendsen, H. J. C.; Fraaije, J. G. E. M. *J. Comput. Chem.* **1997**, *18*, 1463-1472.
- (187) Gaal, M.; Gadermaier, C.; Plank, H.; Moderegger, E.; Pogantsch, A.; Leising, G.; List, E. *Adv. Mater.* **2003**, *15*, 1165-1167.
- (188) Kallinger, C.; Hilmer, M.; Haugeneder, A.; Perner, M.; Spirkl, W.; Lemmer, U.; Feldmann, J.; Scherf, U.; Müllen, K.; Gombert, A.; Wittwer, V. *Adv. Mater.* **1998**, *10*, 920-923.
- (189) Koide, Y.; Wang, Q.; Cui, J.; Benson, D. D.; Marks, T. J. *J. Am. Chem. Soc.* **2000**, *122*, 11266-11267.
- (190) Lee, T.; Zaumseil, J.; Bao, Z.; Hsu, J. W. P.; Rogers, J. A. *PNAS* **2004**, *101*, 429-433.
- (191) Veinot, J. G. C.; Yan, H.; Smith, S. M.; Cui, J.; Huang, Q.; Marks, T. J. *Nano Lett.* **2002**, *2*, 333-335.
- (192) Cheek, B. J.; Steel, A. B.; Torres, M. P.; Yu, Y.; Yang, H. *Anal. Chem.* **2001**, *73*, 5777-5783.
- (193) Lingerfelt, B. M.; Mattoussi, H.; Goldman, E. R.; Mauro, J. M.; Anderson, G. P. *Anal. Chem.* **2003**, *75*, 4043-4049.
- (194) Hu, W.; Lu, N.; Zhang, H.; Wang, Y.; Kehagias, N.; Reboud, V.; Sotomayor Torres, C. M.; Hao, J.; Li, W.; Fuchs, H.; Chi, L. *Adv. Mater.* **2007**, *19*, 2119-2123.
- (195) Choi, H. Y.; Kim, S. H.; Jang, J. *Adv. Mater.* **2004**, *16*, 732-736.
- (196) Briseno, A. L.; Aizenberg, J.; Han, Y.; Penkala, R. A.; Moon, H.; Lovinger, A. J.; Kloc, C.; Bao, Z. *J. Am. Chem. Soc.* **2005**, *127*, 12164-12165.
- (197) de la Fuente, J. M.; Andar, A.; Gadegaard, N.; Berry, C. C.; Kingshott, P.; Riehle, M. O. *Langmuir* **2006**, *22*, 5528-5532.

-
- (198) Briseno, A. L.; Mannsfeld, S. C. B.; Ling, M. M.; Liu, S.; Tseng, R. J.; Reese, C.; Roberts, M. E.; Yang, Y.; Wudl, F.; Bao, Z. *Nature* **2006**, *444*, 913-917.
- (199) Plain, J.; Pallandre, A.; Nysten, B.; Jonas, A. *Small* **2006**, *2*, 892-897.
- (200) Wang, W. C.; Zhong, D. Y.; Zhu, J.; Kalischewski, F.; Dou, R. F.; Wedeking, K.; Wang, Y.; Heuer, A.; Fuchs, H.; Erker, G.; Chi, L. F. *Phys. Rev. Lett.* **2007**, *98*, 225504-4.
- (201) Hao, J.; Lu, N.; Wu, Q.; Hu, W.; Chen, X.; Zhang, H.; Wu, Y.; Wang, Y.; Chi, L. *Langmuir* **2008**, *24*, 5315-5318.
- (202) Wensink, E. J. W.; Hoffmann, A. C.; Apol, M. E. F.; Berendsen, H. J. C. *Langmuir* **2000**, *16*, 7392-7400.
- (203) von Alftan, S.; Kuronen, A.; Kaski, K. *Phys. Rev. B* **2003**, *68*, 073203.
- (204) Lee, S. H.; Rossky, P. J. *J. Chem. Phys.* **1994**, *100*, 3334-3345.
- (205) Chandrasekhar, I.; Kastenholz, M.; Lins, R. D.; Oostenbrink, C.; Schuler, L. D.; Tieleman, D. P.; van Gunsteren, W. F. *Eur. Biophys. J.* **2003**, *32*, 67-77.
- (206) Kukol, A. *J. Chem. Theory Comput.* **2009**, *5*, 615-626.
- (207) Berendsen, H. J. C.; Postma, J. P. M.; van Gunsteren, W. F.; Hermans, J. In *Intermolecular Forces* (ed. Pullman, A.); D. Reidel Publishing Company: Dordrecht, 1981; S. 331-342.
- (208) Hirtz, M.; Fuchs, H.; Chi, L. *J. Phys. Chem. B* **2008**, *112*, 824-827.
- (209) Hirtz, M. Selbstorganisierte Musterbildung von DPPC auf Plasma- und RCA-behandeltem Silizium (Diploma Thesis), Westfälische Wilhelms-Universität Münster, 2005.
- (210) Brinks, M.; Hirtz, M.; Chi, L.; Fuchs, H.; Studer, A. *Angew. Chem.* **2007**, *119*, 5324-5326.
- (211) Hirtz, M.; Brinks, M. K.; Miele, S.; Studer, A.; Fuchs, H.; Chi, L. *Small* **2009**, *5*, 919-923.
- (212) Kresse, G.; Furthmüller, J. *Phys. Rev. B* **1996**, *54*, 11169.
- (213) Perdew, J. P.; Burke, K.; Ernzerhof, M. *Phys. Rev. Lett.* **1996**, *77*, 3865.
- (214) Zhang, Y.; Yang, W. *Phys. Rev. Lett.* **1998**, *80*, 890.
- (215) Grimme, S. *J. Comput. Chem.* **2006**, *27*, 1787-1799.

Publications

Articles in peer-reviewed Journals:

1. H. Gan, K. Tang, T. Sun, **M. Hirtz**, Y. Li, L. F. Chi, S. Butz, H. Fuchs: Selective Adsorption of DNA on Chiral Surfaces: Supercoiled or Relaxed Conformation (Angew. Chem. Int. Ed., 48, 5282-5286, 2009)
2. **M. Hirtz**, M. K. Brinks, S. Miele, A. Studer, H. Fuchs, L. F. Chi: Structured Polymer Brushes by AFM Lithography (Small, 5(8), 919-923, 2009)
3. D. Y. Zhong, **M. Hirtz**, W. C. Wang, R. F. Dou, L. F. Chi, H. Fuchs: Kinetics of island formation in organic film growth (Phys. Rev. B, 77, 113404, 2008)
4. **M. Hirtz**, H. Fuchs, L. F. Chi: Influence of Substrate Treatment on Self-Organized Pattern Formation by Langmuir-Blodgett Transfer (J. Phys. Chem. B, 112 (3), 824-827, 2008)
5. X. Chen, **M. Hirtz**, A. L. Rogach, D. V. Talapin, H. Fuchs, L. F. Chi: Correlating Dynamics and Selectivity in Adsorption of Semiconductor Nanocrystals onto a Self-Organized Pattern (Nano Lett., 7, 3483-3488, 2007)
6. S. Lenhart, A. Sesma, **M. Hirtz**, L. F. Chi, H. Fuchs, H. P. Wiesmann, A. E. Osbourn, B. M. Moerschbacher: Capillary-Induced Contact Guidance (Langmuir, 23, 10216-10223, 2007)
7. M. Brinks, **M. Hirtz**, L. F. Chi, H. Fuchs, A. Studer: Site-selective surface-initiated Polymerization by Langmuir-Blodgett Lithography (Angew. Chem. Int. Ed., 46, 5231-5233, 2007) / (Angew. Chem., 119, 5324-5326, 2007)
8. X. Chen, S. Lenhart, **M. Hirtz**, N. Lu, H. Fuchs, L. F. Chi: Langmuir-Blodgett Patterning: A bottom-up Way to build Mesostructures over large Areas (Acc. Chem. Res., 40(6), 393-401, 2007)
9. X. Chen, **M. Hirtz**, H. Fuchs, L. F. Chi: Fabrication of Gradient Mesostructures by Langmuir-Blodgett Rotating Transfer (Langmuir, 23, 2280-2283, 2007)

10. X. Chen, N. Lu, H. Zhang, **M. Hirtz**, L. Wu, H. Fuchs, L. F. Chi:
Langmuir-Blodgett Patterning of Phospholipid Microstripes: Effect of the Second Component
(J. Phys. Chem. B, 110 (15), 8039-8046, 2006)
11. X. Chen, **M. Hirtz**, H. Fuchs, L. F. Chi:
Self-Organized Patterning: Regular and Spatially Tunable Luminescent Submicrometer Stripes Over Large Areas
(Adv. Mater., 17, 2881–2885, 2005)

Articles Submitted or in Preparation:

1. J. Hao, N. Lu, L. Li, **M. Hirtz**, L. Gao, W. Wang, C. Du, H. Fuchs, L. F. Chi:
Anisotropic organic field effect transistor
(submitted)
2. **M. Hirtz**, N. Kumar, J. Hao, N. Lu, H. Fuchs, L. F. Chi:
Template-Guided Deposition of Organic Molecules studied by MD Simulations
(in preparation)

Talks on Conferences and Workshops:

1. Structuring Polymer Brushes by LB- and AFM-Lithography with Subsequent Site-Selective Immobilization of Functionalized Molecules
(13.07.09 CeNTech-Day 2009)
2. Structured Polymer Brushes by AFM-Lithography
(25.03.09 DPG-Conference 2009)
3. Structured Polymer Brushes by AFM-Lithography
(16.09.08 MNE08)
4. Multi-Component Langmuir-Blodgett Transfers for Chemical and Structural Surface Patterning
(12.03.08 FRONTIERS Workshop Bio Nano 08)
5. Multi-Component Langmuir-Blodgett Transfers for Chemical and Structural Surface Patterning
(04.07.07 LB-12)
6. Multi-Component Langmuir-Blodgett Transfers for Chemical and Structural Surface Patterning
(26.03.07 DPG-Conference 2007)
7. Selbstorganisation von DPPC auf Vorstrukturierten Substraten
(27.03.06 Raith Lithography User-Meeting)

Poster Presentations on Conferences and Workshops:

1. **M. Hirtz**, M. K. Brinks, S. Miele, A. Studer, H. Fuchs, L. F. Chi:
AFM Lithography on Polymer Brushes and Spin-Coated Polymer Films
(DPG-Conference 2008)
2. **M. Hirtz**, M. Kahl, H. Fuchs, L. F. Chi:
Simulation of Exposure and Development Process in 3D Electron Beam
Lithography
(NNT'07)
3. **M. Hirtz**, X. Chen, H. Fuchs, L. F. Chi:
The Influence of prestructured Substrates on self-organized LB Patterning
(LB-12 2007)
4. **M. Hirtz**, X. Chen, M. K. Brinks, A. Studer, H. Fuchs, L. F. Chi:
LB-Transfer of Mixed Monolayers for Structural Surface Patterning
(SFB 424 Symposium 2007)
5. X. Chen, **M. Hirtz**, H. Fuchs, L. F. Chi:
Complex Surface Patterning by Dynamic Molecular Self-Organization
(International Symposium on Nonlinear Dynamics in Nanosystems 2006)
6. **M. Hirtz**, X. Chen, S. Lenhert, N. Lu, H. Fuchs, L. F. Chi:
Self-Organized Surface Patterning
(DPG-Conference 2006)
7. **M. Hirtz**, X. Chen, M. K. Brinks, A. Studer, H. Fuchs, L. F. Chi:
LB-Transfer of Mixed Monolayers for Structural Surface Patterning
(SFB 424 Symposium 2006)
8. **M. Hirtz**, L. F. Chi, H. Fuchs:
Self-Organized Nanostructuring of Organic Monolayers
(DPG-Conference 2005)
9. L. F. Chi, X. Chen, **M. Hirtz**, Z. Mu, D. Zhong, W. Wang, H. Fuchs
Ordnungsphänomene und ihre Modellierung in funktionalen
organischen/anorganischen Grenzflächen
(SFB 424 Symposium 2005)

Acknowledgements

A lot of people helped me over the course of my PhD study – some with work-related issues, others by being a friend and most pleasing many of them by being both good comrades and skilled colleagues.

First of all I have to thank Prof. Dr. Lifeng Chi for her excellent supervision of my PhD study. While setting me on interesting and fruitful aspects in the field of self-organized surface structuring and guiding me into the right direction, she nevertheless always had an open mind for my ideas. Thus she created a very unique environment for my research where I always felt the comfort of professional input and guidance while still being able to find my own personal way and realize many of my own ideas for experiments. After years of working for and with her I also feel a deep personal connection that makes me hope to stay in touch – I would be more than glad to have some joint projects in the future.

I want to thank Prof. Dr. Harald Fuchs for offering me the opportunity to do my PhD in his working group. I admire him for his tremendous competence in the field of nanoscience and his ability to create such an extraordinary research environment as I could experience here. Despite his busy agenda he nevertheless still found time for discussions and gave fruitful suggestions at many points during the course of my work.

I am grateful for the close collaboration with Prof. Dr. Armido Studer in the parts of my work connected to polymer brushes. I have seldom met a person that is so enthusiastic about his work and cheerfully spreads this mood to everyone nearby. It is always a pleasure to discuss with him and I always felt energized and ready for new actions after talking to him. The very close and fruitful collaboration with his former PhD student Dr. Marion Brinks and his (almost former) PhD student Saskia Miele was one of the most pleasant experiences during my work. I want to thank both of them for the excellent teamwork and the many discussions “from chemist to physicist” that brought me a better insight of the chemistry of polymers. Thanks also to Julia Hederer (also PhD student at the Studer group) who synthesized some of the compounds used in this work.

Although he left our group during the first year of my PhD I will always remember Dr. Xiadong Chen and want to thank him for the very productive collaboration. I always enjoyed working with him and he also became a good friend (since our baking marathon at the very latest).

Many thanks to Dr. Nan Lu who made my stay in China an unforgettable experience by being a perfect host. In addition to the nice work in the lab she introduced more facets of China to me (tourist sights as well as the everyday life) than I would have ever expected to get to know in the limited time of my stay. Owing to her I will also never mix up *tóufà* and *máo* again for the rest of my life.

I also want to thank “my” research intern Naresh Kumar who visited our group for some months. He was really helpful in the work involving molecular dynamics simulations and additionally became a good friend rapidly. I hope that I not only introduced a bit of everyday lab work to him, but that he also enjoyed the trip to Bremen and surrounding sights as much as I did. I am looking forward to visit him in India as soon as possible.

Many thanks are entitled to our technician Reinhold Arends for invaluable help with all kinds of technical problems occurring in all the years. The same is true for our secretary Jutta Marquardt who was constantly helping me in the neverending struggle against the shallows of the university’s administrative proceedings. Martin Leweling should be thanked for the extremely fast and competent support in respect to the high performance computing facilities used for the molecular dynamics simulations.

This work would have been impossible without my fellow PhD students – they can lighten up grey days by a short chat and it is great to have some “friendly neighboring office” to go to whenever one needs a timeout. So many thanks to Jörn-Holger Franke and Dr. Felix Kalischewski (DPG conferences will never be the same without these two!), Jens Falter, Daniel Braun, Daniel Ebeling, and Lars Janßen. All in all I should thank all the group members for generating an overall comfortable atmosphere were I always liked to work.

Many thanks to my friends and colleagues who volunteered for proof-reading my thesis: Jörn-Holger Franke, Martin Had, Alexander Höink, Dieter Kerkfeld, Naresh Kumar, and Dr.

Liqiang Li – without them there would be many more “gems” of funny germanisms and blunt typing errors than, I fear, are still lurking in this document.

There are so many more people I would like to thank for their collaboration and support during my work, like Dr. Steven Lenhart, Dr. Zhongcheng Mu, Dr. Wenchong Wang, Dr. Dingyong Zhong, Dr. Taolei Sun, Dr. Ulrich Fischer, Dr. Martin Bühner, Dr. Jiang Lin, Dr. Ruifen Dou, Dr. Marcus Schäfer, Dr. Liqiang Li, Dr. Xing Wang, Dr. Xiaochun Wu, Hui Gan, Juanyuan Hao, Fei Pan, Chuan Du, and Johannes Sondhauß. Finally, my sincere apologies to everyone I may have forgotten in this list.

Last but not the least I want to thank my mother Margret Hirtz and my friend Bastian Beck for their constant support over all these years. I would never be where I am right now without you.

Best wishes to all of you!

Michael

Lebenslauf

Persönliche Daten

Name: Dr. rer. medic. Michael Hirtz, Dipl.-Phys.
Geburtsdatum/-ort: 07.03.1979 in Coesfeld
Staatsangehörigkeit: deutsch
Eltern: Hugo Hirtz
Margret Hirtz, geb. Ripperda

Schulische Ausbildung

08/1985-06/1989 Martinschule Brink, Coesfeld
08/1989-06/1998 Städtisches Heriburg-Gymnasium Coesfeld,
Abschluss: Abitur

Zivildienst

07/1998-07/1999 Zivildienst im Altersheim St.-Laurentius-Stift Coesfeld

Studium

10/1999-03/2005 Studium der Physik an der Westfälischen Wilhelms-Universität Münster, Abschluss: Diplom
Thema der Diplomarbeit:
„Selbstorganisierte Musterbildung von DPPC auf Plasma- und RCA-behandeltem Silizium“
06/2005-03/2008 Promotion zum Dr. rer. medic. in der Poliklinik für Kieferorthopädie des Universitätsklinikums Münster
Thema der Dissertation:
„Computergestützte Zahnbogenformberechnungen zur Verbesserung der Ergebnisqualität in der Orthodontie“
Seit 06/2005 Promotion zum Dr. rer. nat. am Physikalischen Institut der WWU Münster
Thema der Dissertation:
„Surface Structuring by Bottom-Up and Top-Down Approaches“

Beruflicher Werdegang und Praktika

02/2002-03/2005	Studentische Hilfskraft in der Poliklinik für Kieferorthopädie des Universitätsklinikums Münster
08/2003-10/2003	Praktikum im Bereich Simulationsprogrammierung bei der Gesellschaft für Schwerionenforschung mbH, Darmstadt
04/2005-05/2005	Praktikum an der Jilin-Universität, Changchun, China
06/2005-11/2005	Wissenschaftliche Hilfskraft am Physikalischen Institut der WWU Münster
Seit 12/2005	Wissenschaftlicher Mitarbeiter am Physikalischen Institut der WWU Münster

Bremen, den 29.07.2009,